

# **Quantum Waveguide Theory**

This thesis is presented for the degree of

Doctor of Philosophy of Physics

of The University of Western Australia.

Stuart Midgley BSc (Hons)

Department of Physics

University of Western Australia

2003

# **Declaration of Originality**

I declare that the contents of this thesis,  
except where specified, is my original work.

Stuart Midgley

November 2003

# Acknowledgments

Where do I start. The number of people who have provided help, assistance and motivation for the duration of the PhD and Thesis is extremely large.

My wife, Gem, has endured my endeavors to complete a PhD for many years now. She has been tolerant, helpful and constructive. More over, she has helped me keep my eye on the ball and to finish.

A/Prof. Jingbo Wang, primary supervisor, has provided a huge amount of academic support. Her strong analytic skills and attention to detail kept the project on track and focused on both the short and long term goals. Without Jingbo the papers, thesis and conference presentations would never have been possible.

Prof. Jim Williams, secondary supervisor, has provided moral and academic support throughout.

Dr Paul Abbott for putting up with my continual Mathematica questions.

Dr Colin Taylor. What can I say, he provided me with a massive amount of moral support, academic discussion and acted as a mentor throughout the entire experience. The fact that he was an experimentalist meant he saw my work in a slightly different light to my supervisor. Without Colin, my time at UWA would not have been half of what it was.

The “River Rats” (canoe polo team): Ken, Sean, Ian, Mal and Mark. They provided just the right amount of distraction (or possible too much) to my studies. They kept me sane, a little fit and certainly entertained.

Numerous people living in Canberra during the time of my write up. Without their continual nagging, I would not have completed the thesis. Quickly, they were: Adele, David, James, Judy, Julia, Matt, Michelle, Sandra, Sarah and everyone at ANUSF.

The calculations performed throughout this thesis would not have been possible without the generous support of the Australian Partnership for Advanced Computing (APAC) National Facility and the Interactive Virtual Environments Centre (IVEC) High Performance Computing Facility.

Finally, I would like to thank Dr Bob Gingold. He employed me while I was trying to write up. Thankfully, he turned a blind eye every now and again in the hope that I would finish. Well, I did.

# Abstract

The study of nano-electronic devices is fundamental to the advancement of the semiconductor industry. As electronic devices become increasingly smaller, they will eventually move into a regime where the classical nature of the electrons no longer applies. As the quantum nature of the electrons becomes increasingly important, classical or semi-classical theories and methods will no longer serve their purpose.

For example, the simplest non-classical effect that will occur is the tunnelling of electrons through the potential barriers that form wires and transistors. This results in an increase in noise and a reduction in the device's ability to function correctly. Other quantum effects include coulomb blockade, resonant tunnelling, interference and diffraction, coulomb drag, resonant blockade and the list goes on.

This thesis develops both a theoretical model and computational method to allow nano-electronic devices to be studied in detail. Through the use of computer code and an appropriate model description, potential problems and new novel devices may be identified and studied. The model is as accurate to the physical realisation of the devices as possible to allow direct comparison with experimental outcomes.

Using simple geometric shapes of varying potential heights, simple devices are readily accessible: quantum wires; quantum transistors; resonant cavities; and coupled quantum wires. Such devices will form the building blocks of future complex devices and thus need to be fully understood. Results obtained studying the connection of a quantum wire with its surroundings demonstrate non-intuitive behaviour and the importance of device geometry to electrical characteristics.

The application of magnetic fields to various nano-devices produced a range of interesting phenomenon with promising novel applications. The magnetic field can be used to alter the phase of the electron, modifying the interaction between the electronic potential and the transport electrons. This thesis studies in detail the Aharonov-Bohm oscillation and impurity characterisation in quantum wires.

By studying various devices considerable information can be added to the knowledge base of nano-electronic devices and provide a basis to further research. The computational algorithms developed in this thesis are highly accurate, numerically efficient and unconditionally stable, which can also be used to study many other physical phenomena in the quantum world. As an example, the computational algorithms were applied to positron-hydrogen scattering with the results indicating positronium formation.

# Publications

The following papers were published during studies for this thesis:

J. B. Wang and S. Midgley, *Quantum waveguide theory: a direct solution to the time dependent Schrödinger equation*, Phys. Rev. B **60**, 13668 (1999)

J. B. Wang, N. Riste, S. Midgley, A. T. Stelbovics and J. F. Williams, *Time-dependent approach to s-wave positron-hydrogen scattering*, Aust. J. Phys. **52**, 595 (1999)

S. Midgley and J. B. Wang, *Complex Absorbing Potential and Chebyshev propagation scheme*, Phys. Rev. E **61**, 920 (2000)

S. Midgley and J. B. Wang, *Time-dependent quantum waveguide theory : a study of nano ring structures*, Aust. J. Phys. **53**, 77 (2000)

J. B. Wang and S. Midgley, *Time-dependent approach to electron scattering in nano structures*, Physica B **284**, 1962 (2000)

S. Midgley and J. B. Wang, *Single electron transport through 2D quantum wires with flanges*, Phys. Rev. B **64**, 153304 (2001)

S. Midgley and J. B. Wang, *Quantum dynamics under the influence of external magnetic fields*, Phys. Rev. E **67**, 046702 (2003)

S. Midgley and J. B. Wang, *Impurity scanning in a quantum wave guide*, Phys. Rev. Let., Under preparation (2003)

S. Midgley and J. B. Wang, *Single electron transport using the Chebyshev propagation scheme*, Comp. Phys. Comm., Under preparation (2003)

The following papers were presented at conferences:

S. Midgley and J. B. Wang, *Time dependent approach to quantum transport in nanostructures*, The 13th National Congress of the Australian Institute of Physics (September 1998, Perth, Australia)

J. B. Wang and S. Midgley, *Quantum transport in nano electronic devices*, The Advanced Research Workshop on Nanostructures: Quantum Confine-ments (December 1998, Canberra, Australia)

J. B. Wang and S. Midgley, *Time dependent approach to electron transport in nano electronic devices*, The 22nd International Conference on Low Temperature Physics (August 1999, Helsinki, Finland)

J. B. Wang, S. Midgley and P. Falloon, *Quantum waveguide theory*, International Conference on Electron Transport in Mesoscopic Systems (August 1999, Gotenberg, Sweden)

The following papers were published during studies for this thesis, however, their content is not directly related:

G. V. Bicknell, C. J. Saxton, R. S. Sutherland, S. Midgley and S. J. Wagner, *Jets: An Environmental Impact Statement*, New Astronomy Reviews, in press (2003)

S. Midgley, *2000 International Physics Olympiad Leicester, UK*, The Physi-cist **38**, 47 (2000)

# Preface

This thesis is divided into chapters, sections and subsections to aid the reader in understanding the material contained and the topic in general.

Chapter 1 provides an introduction to nano-electronic devices, why they are of interest and a brief description of the position of this thesis amongst previous and current work. The reader will be guided through the history of nano-electronic devices and the current state of both experimental and theoretical research. By introducing basic concepts, a setting for the research outlined in the remainder of the thesis is provided.

Chapter 2 is the start of the original work undertaken during this PhD study. The basic theoretical model used will be presented and discussed. Justification for proceeding with this model will also be presented against the background of previous and current work in the field. The various limitations and applications of the model will also be discussed.

Chapter 3 details the computational work. Important features of the computer program will be highlighted along with problems encountered, how these problems were resolved and how those solutions evolved with time.

Chapter 4 investigates several physical systems using the theoretical model and computational scheme described in Chapters 2 and 3. The application of the computer program is outlined, allowing the results to be understood in terms of the inputs. Many of the systems studied and results obtained are original work that have been published or submitted for publication.

Chapter 5 presents a study of positron-hydrogen scattering that utilised the model and computational code produced as part of this thesis. This work was developed primarily in Niel Riste's Honours project, of which I was a co-supervisor.

The concluding Chapter 6 highlights the important outcomes of the research.

The appendices contain a complete description of the format for the input file. A complete copy of the computer code is not included, however it is available upon request.

# Contents

<b>1</b>	<b>Introduction</b>	<b>1</b>
1.1	Physical realisation of nano-electronic devices . . . . .	3
1.1.1	GaAs-AlGaAs Heterojunctions . . . . .	4
1.1.2	Quantum dots . . . . .	6
1.1.3	Quantum point contact and quantum wires . . . . .	7
1.2	Theoretical progress and position of this thesis . . . . .	10
<b>2</b>	<b>Theoretical model</b>	<b>14</b>
2.1	Single electron approximation . . . . .	14
2.2	Effective mass approximation . . . . .	15
2.3	Electronic potentials . . . . .	16
2.4	Magnetic potentials . . . . .	18
2.5	Time independent methods . . . . .	18
2.5.1	Mode matching . . . . .	20
2.5.2	Time independent Green's functions . . . . .	21
2.5.3	Finite element . . . . .	22
2.6	Time dependent methods . . . . .	23
2.6.1	Finite difference . . . . .	24
2.6.2	Higher order methods . . . . .	25
2.6.3	Split operator . . . . .	26
2.6.4	Time dependent Green's functions . . . . .	27
2.7	Time dependent Chebyshev propagation scheme . . . . .	28
2.7.1	Chebyshev approximation . . . . .	28
2.7.2	Time dependent potentials . . . . .	30
2.7.3	Derivatives and the Fast Fourier Transform . . . . .	31

### **3 Computational realisation**

---

3.1	Overview of computation . . . . .	33
3.1.1	Program flow . . . . .	34
3.1.2	Storage of arrays . . . . .	35
3.2	Computation of Chebyshev polynomials . . . . .	37
3.3	Computation of derivatives . . . . .	38
3.3.1	What FFTW computes . . . . .	40
3.3.2	Parallel algorithm . . . . .	41
3.4	Initial wave functions . . . . .	43
3.4.1	Gaussian wave packet . . . . .	43
3.4.2	Fermi wave packet . . . . .	44
3.5	Optimisation of the code . . . . .	47
3.5.1	Propagation of free waves . . . . .	47
3.5.2	Wave function splitting algorithm . . . . .	48
3.5.3	Complex potential . . . . .	50
3.5.4	Optimal grid spacing and size . . . . .	58
3.6	Computation of electronic potentials . . . . .	62
3.6.1	Gaussian blur . . . . .	65
3.6.2	Recursive averaging . . . . .	65
3.7	Computation of magnetic potential . . . . .	68
3.7.1	Comparison of different gauges . . . . .	69
3.8	Computational accuracy and stability . . . . .	74
3.8.1	Comparison to known solutions . . . . .	74
3.8.2	Conservation of energy and norm . . . . .	82
3.8.3	Time reversal propagation . . . . .	82
<b>4</b>	<b>Systems studied and results</b>	<b>87</b>
4.1	Double barrier . . . . .	87
4.1.1	Transmission coefficient . . . . .	90
4.1.2	Momentum spectrum . . . . .	96
4.1.3	Resonant tunnelling . . . . .	97
4.1.4	Effects of magnetic fields . . . . .	97
4.1.5	Time reversal . . . . .	100

4.2	Nano-rings . . . . .	105
4.2.1	Electron propagation in a nano-ring . . . . .	105
4.2.2	The Aharonov-Bohm ring . . . . .	107
4.3	Quantum wire . . . . .	112
4.3.1	Length . . . . .	112
4.3.2	Width and quantised conductance . . . . .	115
4.3.3	Flange angle . . . . .	117
4.4	Quantum transistor . . . . .	123
4.5	Resonant cavities . . . . .	127
4.6	Quantum wire impurity . . . . .	132
<b>5</b>	<b>Positron-hydrogen scattering</b>	<b>140</b>
5.1	Multi-electrons . . . . .	140
5.2	Background . . . . .	141
5.3	Theory . . . . .	144
5.4	Results . . . . .	146
<b>6</b>	<b>Conclusion</b>	<b>147</b>
<b>A</b>	<b>Format of input file</b>	<b>150</b>

# List of Figures

1.1	The first transistor built in 1947 ( <a href="http://www.bell-labs.com/history/physicscomm/transistor.html">http://www.bell-labs.com/history/physicscomm/transistor.html</a> ) . . . . .	1
1.2	Conduction band profile in a heterojunction (Ferry & Goodnick 1997, page 37). The large energy difference between the two levels $E_1$ and $E_2$ and the low thermal energy of the electrons results in an accumulation of electrons at $E_1$ . Consequently, motion in the $z-$ direction is prohibited. . . . .	4
1.3	Example layout of a GaAs-AlGaAs heterojunction with 2 degree electron gas (Ferry & Goodnick 1997, page 26). . . . .	5
1.4	Example layout of a GaAs heterostructure with 2 degree electron gas (Kane et al. 1998). . . . .	6
1.5	Quantum dots, nano-pillars and cavities (Kouwenhoven 1998). . . . .	8
1.6	Quantum point contact (Dr Ryan Held, Nanophysics at ETH); quantum wire (Kane et al. 1998); 70 nm bent quantum wires or quantum elbows and 100 nm quantum circuits (Naulleau et al. (2002), Lawrence Berkeley National Laboratories). . . . .	8
1.7	(a) Quantisation of conductance through a quantum wire (Ferry & Goodnick 1997). (b) Quantised conduction through a single atom wide wire (Lang & Avouris 1998)	9
1.8	Representation of Hard-walled and Soft-walled potentials. . . . .	12
2.1	A quantum wire potential with boundary potential height 0.11 eV. A typical cal- culation would use an initial wave function with median energy 0.054 eV, well below the potential height. . . . .	17
2.2	A double barrier potential with an external electric field. . . . .	17
2.3	The potential is split into different regions for computation . . . . .	20
3.1	General program flow. . . . .	36

3.2	Parallel scaling of computational program as the number of CPU's is increased. The near linear scaling allows large calculations to be performed in a reasonable time. The grid size was 2048 square for all calculations, with both an electronic and magnetic potential. Single CPU memory requirements were approximately 1400 <i>MB</i> , which increased to approximately 2000 <i>MB</i> for the 32 CPU case. . . . .	42
3.3	Typical initial wave function: (a) $ \psi(x,y) ^2$ in real space; (b) $ \Psi(p_x,p_y) ^2$ in momentum space; (c) real component; (d) imaginary component of $\psi(x,y)$ . . . . .	45
3.4	Wave function with a Fermi distribution for $T = 32\text{ K}$ : (a) $ \psi(x,y) ^2$ in real space; (b) $ \Psi(p_x,p_y) ^2$ in momentum space; (c) real component; (d) imaginary component of $\psi(x,y)$ . Note, that the top of the momentum space wave function (b) is flat, due to the Fermi energy cut-off $E_{Fermi}$ in Equation 3.14 . . . . .	46
3.5	By using a function $S$ the real space can be split into 3 regions as depicted. . . . .	49
3.6	Potentials used to absorb the wave function at the boundary of the space . . . . .	54
3.7	Propagation of an electron wave packet in free space with the exponential complex potential at the right end of the grid. The probability function $P(t) = \psi^*(x,y,t)\psi(x,y,t)$ is plotted in logarithm scale. Flow of time $t$ is left to right and top to bottom with time step satisfying Equation 3.40. The spatial units ( $x$ and $y$ axes) are $\times 1000a.u..$	56
3.8	Massive errors are introduced by the complex potential when Equation 3.40 no longer holds (same units as Figure 3.7). . . . .	57
3.9	(a) Absorption of system energy (a.u.) when Equation 3.40 is satisfied; (b) Energy (a.u.) diverges otherwise. . . . .	59
3.10	Propagation of an electron wave packet under the influence of a double barrier with exponential complex potentials at both end of the grid. Flow of time is left to right and top to bottom with time step satisfying Equation 3.41 (same units as Figure 3.7). . . . .	60
3.11	Absolute errors between the results shown in Figure 3.10 and the results obtained without the complex potentials but using a larger numerical grid (same units as Figure 3.7). . . . .	61
3.12	Collection of objects which can be used to construct potentials. . . . .	64
3.13	(a) Hard-walled potential; (b) Gaussian smoothed soft-walled potential; (c) Recursive averaging smoothed soft-walled potential. . . . .	66
3.14	Smoothing stencil for the point $(x_0,y_0)$ , which is averaged by the points about it (weighted by the number of points in the appropriate ring). . . . .	67

3.15 Parts (a) and (b) show the $x$ - and $y$ - components of the vector potential $A = \frac{b}{2}(-y, x, 0)$ to produce an approximately uniform magnetic field in the $z$ - direction. Part (c) shows the magnetic field produced from the vector potential $A = \frac{b}{2}(-y, x, 0)$ . In the main region of propagation it is constant, $b = 0.1$ , and zero along the boundary. The spatial size of the simulation is $8 \mu\text{m}$ in each dimension.	70
3.16 Part (a) shows the theoretical solution, while parts (b)-(d) show the absolute error for the three different gauges: $b(-y, 0, 0)$ ; $b/2(-y, x, 0)$ ; and $b/2(x - y, x - y, 0)$ respectively. The applied magnetic field is $0.3T$ with the initial wave function having energy $0.81 \text{ eV}$ and a momentum spread of $4.0\%$ .	72
3.17 Part (a) shows the ring potential, while part (b) shows the final wave function for the Landau gauge $b/2(-y, x, 0)$ . Parts (c) and (d) show the absolute error between the final wave functions for the gauges $b(-y, 0, 0)$ , $b/2(x - y, x - y, 0)$ , and the Landau gauge shown in part (b). The applied magnetic field is $0.02T$ with the initial wave function having energy $0.041 \text{ eV}$ energy and a momentum spread of $15\%$ .	73
3.18 The Gaussian wave packet propagates for a time $t = 1.6 \text{ ps}$ , spreading as expected.	76
3.19 Comparison of numerical solution for the propagation of a Gaussian to analytic solution for free space.	77
3.20 The Fermi wave packet propagates for a time $t = 1.6 \text{ ps}$ .	78
3.21 Propagation of an electron (Gaussian wave packet) under the influence of an approximately constant, uniform, magnetic field $B = 0.1T$ . Part (a) shows the propagation of the electron while the circles above the wave packet indicate the classical particle trajectory. The wave packet initially has energy $0.082 \text{ eV}$ in the $x$ -direction and momentum spread $2.3\%$ , corresponding to the Larmor frequency $0.13 \times 10^{12}$ . Part (b) shows the error between the computational propagation and analytic results. The error is approximately 6 to 7 orders of magnitude smaller than the wave packet.	81
3.22 Propagation of a fermi wave packet, for $1.6 \text{ ps}$ , under an approximate uniform constant magnetic field $B = 0.4T$ .	83
3.23 Comparison of the forward and backward propagation of the wave function to the initial wave function, (a) Gaussian wave packet (b) fermi wave packet.	85
3.24 Relative error for the forward and backward propagation of a (a) Gaussian and (b) fermi wave packet under the influence of an approximate uniform constant magnetic field.	86

4.1	Double barrier potential of height 0.082 eV, barrier spacing 160 nm with spatial size 2.6 $\mu m$ in both the $x-$ and $y-$ dimensions. . . . .	88
4.2	Propagation through the double barrier depicted in Figure 4.1. (a) is the initial wave function, $t = 0$ (b) is the propagated wave function at 0.4 ps; (c) 0.8 ps; (d) 1.2 ps; (e) 1.6 ps and (f) at 2.0 ps. . . . .	89
4.3	Momentum space propagation for the wave function propagation shown in Figure 4.2. The coordinate units shown are $10^{-26} \text{ kg m s}^{-1}$ , where $7.2 \times 10^{-26} \text{ kg m s}^{-1}$ is the maximum momentum in the $x-$ dimension and $3.3 \times 10^{-26} \text{ kg m s}^{-1}$ is the maximum momentum in the $y-$ dimension. . . . .	91
4.4	Propagation through a double barrier similar to that depicted in Figure 4.1, except the potential barrier height is 0.11 eV. (a) is the initial wave function, $t = 0$ (b) is the propagated wave function at 0.4 ps; (c) 0.8 ps; (d) 1.2 ps; (e) 1.6 ps and (f) at 2.0 ps. . . . .	92
4.5	Momentum space propagation for the wave function propagation shown in Figure 4.4. The coordinate units shown are $10^{-26} \text{ kg m s}^{-1}$ , where $7.2 \times 10^{-26} \text{ kg m s}^{-1}$ is the maximum momentum in the $x-$ dimension and $3.3 \times 10^{-26} \text{ kg m s}^{-1}$ is the maximum momentum in the $y-$ dimension. . . . .	93
4.6	Final wave function for propagation through a double barrier with varying height. For these calculations, the wave function had median energy 0.082 eV and was propagated from left to right. The extent of the propagation space is $-1.3 \mu m$ to $1.3 \mu m$ . The potential height of and transmission through the double barrier was: (a) 0.027 eV and 1.0; (b) 0.054 eV and 0.96; (c) 0.082 eV and 0.36; (d) 0.11 eV and 0.0081 (e) 0.14 eV and $8.4 \times 10^{-6}$ (f) 0.16 eV and $7.3 \times 10^{-8}$ . . . . .	94
4.7	(a) Doubler barrier formed by walls with a potential height of 0.11 eV, while the double barrier is of height 0.081 eV; (b) Momentum spectrum for the double barrier. The wave function peak momentum was $4.00 \times 10^{-26} \text{ kg m s}^{-1}$ with a momentum spread of 20% in both the $x-$ and $y-$ dimensions. The momentum distribution of the initial and final wave functions were integrated over $p_y$ to provide information about the $x-$ dimension propagation. . . . .	98
4.8	Comparison of resonant and non-resonant tunnelling. The initial momentum of each wave function is (a) $3.97 \times 10^{-26} \text{ kg m s}^{-1}$ , (b) $4.03 \times 10^{-26} \text{ kg m s}^{-1}$ , (c) $4.06 \times 10^{-26} \text{ kg m s}^{-1}$ and (d) $4.13 \times 10^{-26} \text{ kg m s}^{-1}$ . The transmission for each of these cases is (a) 0.057, (b) 0.87, (c) 0.80 and (d) 0.97. . . . .	99

4.9 Propagation through the double barrier depicted in Figure 4.1 with a strong applied magnetic field of $0.4 T$ .. (a) is the initial wave function, $t = 0$ (b) is the propagated wave function at $0.4 ps$ ; (c) $0.8 ps$ ; (d) $1.2 ps$ ; (e) $1.6 ps$ and (f) at $2.0 ps$ . . . . .	101
4.10 Momentum space propagation for the wave function propagation shown in Figure 4.9. The coordinate units shown are $10^{-26} kg m s^{-1}$ , where $7.2 \times 10^{-26} kg m s^{-1}$ is the maximum momentum in the $x-$ dimension and $3.3 \times 10^{-26} kg m s^{-1}$ is the maximum momentum in the $y-$ dimension. . . . .	102
4.11 Propagation of the wave packet to a final state and then back to the initial state under time reversal. This is under a strong applied magnetic field of $0.4 T$ and a double barrier electrostatic potential. . . . .	104
4.12 Relative error between initial wave function and the wave function propagated forward and then backward in time. This is for the propagation displayed in Figure 4.11.105	105
4.13 (a) The side and top view of the device. The dark grey regions are negatively charged metal gates and the light grey area is positively charged. (b) The confinement potential. The middle metal gate (i.e. the light grey area) is biased positively to induce conduction electrons in the semiconductor layer. The side and central gates (i.e. the dark grey area) are biased negatively to confine the conduction electrons in a narrow tunnel. . . . .	106
4.14 Propagation of the wave function through the potential. (a) Initial wave function. (b)-(f) Wave function at the end of each time step. . . . .	108
4.15 Error between forward and reversed propagation. (a) Error between the initial and the final time-reversed wave function. (b)-(f) Error between the wave function at the end of each time step and the wave function propagated backwards to the same time. . . . .	109
4.16 Ring potential used to study Aharonov Bohm oscillations. . . . .	110
4.17 Aharonov Bohm oscillations for the transmission of an electron through a ring with an applied magnetic field, varying between $-0.05T$ to $0.05T$ . Such oscillations are in line with those seen experimentally (van der Wiel. et al. 2001). . . . .	110
4.18 Propagation of an electron through the ring potential with no magnetic field applied.111	111
4.19 Propagation of an electron through the ring potential with an applied magnetic field of $0.018T$ . . . . .	111
4.20 Transmission through wires of three different widths. As the length of the wire is increased, the transmission becomes constant. . . . .	113

4.21 (a) Short quantum wire with flange, length of wire without flange is $0.21 \mu m$ and the potential height is $0.11 eV$ . (b) Long quantum wire with flange, length of wire without flange is $0.74 \mu m$ . . . . .	113
4.22 (a) Final wave function after propagation through the short quantum wire. The final transmission coefficient is 0.4023. (b) Final wave function after propagation through the long quantum wire. The final transmission coefficient is 0.4023. . . . .	114
4.23 (a) Conductance as the width of the wire increases and (b) Conductance as the energy of the electron increases. . . . .	116
4.24 Confinement potential and initial wave packet used in the calculations. The wave packet has been scaled to enable visualisation. . . . .	118
4.25 Conductance for different flange angles from $5^\circ$ to $85^\circ$ . Results for three different wire widths are shown: $14.8 nm$ ; $23.3 nm$ ; $46.6 nm$ ; and $46.6 nm$ with a smooth-wall potential. . . . .	119
4.26 Propagation of the electron wave packet for a flange angle of $18^\circ$ . Top to bottom, left to right $t = 0, 0.356, 0.712, 1.068, 1.424$ and $1.78 ps$ . . . . .	121
4.27 Propagation of the electron wave packet for a flange angle of $45^\circ$ . Top to bottom, left to right $t = 0, 0.356, 0.712, 1.068, 1.424$ and $1.78 ps$ . . . . .	122
4.28 $V_S$ is the source, $V_D$ is the drain and $V_G$ is the gate voltage. By reducing the gate voltage, the electron will be drawn into the stub, path A, inducing a phase shift with respect to path B. By tuning the voltage of $V_G$ the transmission can be altered anywhere between zero and one. . . . .	123
4.29 (a) Quantum transistor potential with no bias applied to small side gate, (b) is the density plot of the same potential. The potential height is $0.082 eV$ with the total space being $4.0 \mu m$ in the $x-$ dimension and $0.53 eV$ in the $y-$ dimension. (c) The same quantum transistor potential with a $-0.22 eV$ bias on the small side gate, (d) is the density plot of the same potential, highlighting the effect of the side gate. . . . .	125
4.30 (a) Shows the transmission of the wave function when no side gate bias is applied while (b) demonstrates that nearly the entire wave function is reflected with a $-0.22 eV$ bias on the small side gate. The transmission coefficients are 0.99 and 0.13 respectively. . . . .	126

4.31 Potential and wave function for (a)-(b) minimum transmission $T = 0.49$ for cavity size $0.87 \times 0.21 \mu m$ , and (c)-(d) maximum transmission $T = 0.89$ for cavity size $0.58 \times 0.21 \mu m$ . The wave function had initial energy $0.0049 eV$ and the potential height was $0.13 eV$ . The actual space size is $8.5 \times 3.2 \mu m$ which has been cropped to show the region of interest. . . . .	128
4.32 Transmission through a single cavity, of width $0.21 \mu m$ , as the length of the cavity is increased. The wave function had initial energy $0.0049 eV$ and the potential height was $0.13 eV$ . . . . .	128
4.33 Potential with 1 and 3 resonant cavities. The single cavity is $0.16 \times 0.21 \mu m$ , while the triples cavities are: $0.13 \times 0.21 \mu m$ ; $0.26 \times 0.21 \mu m$ ; and $0.40 \times 0.21 \mu m$ respectively. . . . .	129
4.34 Propagation through a single resonant cavity. Approximately 40% of the wave function is resonantly reflected. . . . .	130
4.35 Propagation through a triple resonant cavity. Each cavity is tuned to a slightly different energy. Approximately 90% of the wave function is resonantly reflected. . . . .	131
4.36 Experimental and semi-classical theoretical results obtained by Koonen et al. (2000). Simulations curves are denoted ‘S’, ‘S1’ and ‘S2’, while the other curves, some denoted ‘E1’ and ‘E2’, are results of experiments for different bias voltages and conditions. The distance between the electron source and detector was $4.0 \mu m$ with the impurity between $0.6 \mu m$ and $2.0 \mu m$ from the electron injection point. The impurity was between $0.08 \mu m$ and $0.42 \mu m$ off axis. The system was cooled to approximately $1.8K$ with a wave function width ranging between $0.08 \mu m$ and $0.14 \mu m$ . . . . .	134
4.37 Transmission curves as the magnetic field is swept from $-0.03T$ to $0.03T$ . The impurity is a small rectangular block of size $0.074 \times 0.037 \mu m$ , with potential height $0.82 eV$ , while the electron has mean energy $0.27 eV$ . (a) is the unobstructed conductance (no impurity). (b) the impurity is located on the x- axis ( $y = 0$ ) while (c) is $0.037 \mu m$ off axis, (d) $0.074 \mu m$ off axis, (e) $0.111 \mu m$ off axis and (f) $0.48 \mu m$ off axis. For all calculations the slit in the screen is $0.074 \mu m$ wide. . . . .	135

4.38	Transmission curves as the magnetic field is swept from $-0.03T$ to $0.03T$ . The impurity is a small rectangular block of size $0.074 \times 0.074 \mu m$ , with potential height $0.82 eV$ , while the electron has mean energy $0.27 eV$ . (a) is the the unobstructed conductance (no impurity). (b) the impurity is located on the x- axis ( $y = 0$ ) while (c) is $0.037 \mu m$ off axis, (d) $0.074 \mu m$ off axis, (e) $0.111 \mu m$ off axis and (f) $0.48 \mu m$ off axis. For all calculations the slit in the screen is $0.074 \mu m$ wide.	136
4.39	Transmission curves as the magnetic field is swept from $-0.03T$ to $0.03T$ . The impurity is a small rectangular block of size $0.074 \times 0.15 \mu m$ , with potential height $0.82 eV$ , while the electron has mean energy $0.27 eV$ . (a) is the the unobstructed conductance (no impurity). (b) the impurity is located on the x- axis ( $y = 0$ ) while (c) is $0.037 \mu m$ off axis, (d) $0.074 \mu m$ off axis, (e) $0.111 \mu m$ off axis and (f) $0.48 \mu m$ off axis. For all calculations the slit in the screen is $0.074 \mu m$ wide.	137
4.40	Typical propagation probing the impurity. No magnetic field is applied, hence only the central component of the wave function is sampled. The impurity is $0.074 \times 0.15 \mu m$ in size with the slit in the screen $0.074 \mu m$ wide. (a) Shows the potential while (b)-(f) show the propagation.	138
4.41	Typical propagation probing the impurity. A magnetic field of $-0.0132T$ is applied. The portion of the transmitted wave function sampled by the screen has changed due to the wave function being swung by the magnetic field. The impurity is $0.074 \times 0.15 \mu m$ in size with the slit in the screen $0.074 \mu m$ wide. (a) Shows the potential while (b)-(f) show the propagation.	139
5.1	Time evolution of the positron-hydrogen system wave function through the collision interaction. The dominant energy of the incident positron is $3.4 a.u.$	145

# List of Tables

3.1	Number of arrays required to represent different components of the computational model. . . . .	37
3.2	Allowed values for the array size $N \leq 2000$ as described in Equation 3.7. . . . .	39
3.3	Example input file to produce various potential objects as shown in Figure 3.12. . .	63

# Chapter 1

## Introduction

In the early 1950's the semi-conductor electronic industry was born. Pieces of semi-conductor roughly millimetres in size were used to construct basic transistors and connecting wires (ie. tracks of semi-conductor). Figure 1.1 shows the first transistor built by Brattain, Shockley and Bardeen of the AT&T Laboratories in 1947.

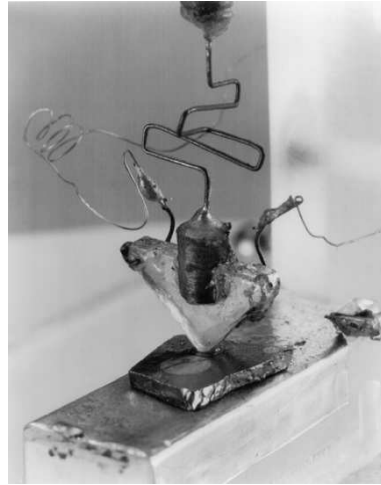


Figure 1.1: The first transistor built in 1947 (<http://www.bell-labs.com/history/physicscomm/transistor.html>).

Since then, the semi-conductor industry has been halving the size of transistors and wires every 18 months; today typical sizes referred to are approximately 130 nanometres (*nm*). If the current rate of reduction in size continues over the next 10 years, the size of components will reach the 1 *nm* scale. At which point, the size and arrangement of the atoms

in the semi-conductor and the wavelength of the transport electrons will determine the properties of the device being constructed.

The purpose of studying such nano-structured electronic devices is two-fold: to gain a greater understanding of quantum physics and its applications; and to advance the commercial semi-conductor industry into the nanometre technology age, allowing higher density and faster operating devices.

The term *nano-electronic devices* refers to electronic structures, typically made out of silicon (Si), gallium arsenide (GaAs) or other semiconductor materials, whose size is of the order of 1 to 100 *nm*, or 1 to 100 millionths of a millimetre. Even simple structures of this size, such as straight wires, have very different electrical characteristics when compared to corresponding classical structures. To make sense of this size, consider a single atom of iron or silicon. The average radius of an iron atom is of the order of 0.14 nanometres (*nm*) while silicon is of the order of 0.11 *nm*. So, a device 10 *nm* in size is approximately equivalent to 100 atoms.

As electronic circuits approach the nanometre scale, analysis based on semi-classical transport theories, such as the Boltzmann rate equation, eventually fails. The characteristic dimensions of nanometre structures are comparable to the wavelength of an electron with energy from millielectron volts (*meV*) to a few electron volts (*eV*), thus the quantum wave nature of the electrons plays a dominant role. For instance, the wavelength of an electron with energy of 1 *meV* is about 40 *nm*. An electron with energy of 1 *eV* has a wavelength of approximately 1.2 *nm*.

Very recent advances in semi-conductor fabrication technology have already allowed construction of mesoscopic structures from 100 *nm* to 1 *nm* in size with the transport electrons confined to zero, one or two-dimensions. For an overview of such devices see (Sohn 1998); quantum dots (Kouwenhoven 1998, Kouwenhoven et al. 2001); carbon nanotube (Tans et al. 1998); single-atom-chain nanowire (Yanson et al. 1998); parallel nano wires and elbows (Naulleau et al. 2002). As an example, it has been demonstrated that a single electron can be pumped around a circuit using a tunable double barrier potential (Jensen & Martinis 1992, Martinis & Nahum 1994, Fonseca et al. 1996). Nano-structures are also studied with external static or oscillating magnetic fields (Barticevic

et al. 2002, Sugaya et al. 2002), which yield interesting results and demonstrate fundamental quantum phenomena. Such devices are expected to become the building blocks of the next generation of electronics.

Unavoidably, the next generation of ultrafast computers with lower power consumption and more compact circuits will need to take advantage of quantum mechanical phenomena. One of the possibilities is for the devices to operate by controlling the phase of a few electrons rather than the electron density as in present day devices. In this way, less energy is required and fast switching time can be achieved. Another possibility is to establish communications between quantum wires and quantum dot cells through the non-locality nature of the electron waves without the need of traditional wires to propagate information.

## 1.1 Physical realisation of nano-electronic devices

Typically, nano-electronic devices are made up of many layers of semi-conductor material with metallic gates used to form the potential barriers. Depending on the semiconductors used and the layout of the metallic gates, devices with different properties can be constructed. The most common semi-conductors in use are Gallium Arsenide (GaAs), Aluminium Gallium Arsenide (AlGaAs) and to a lesser extent Silicon (Si). Gallium Arsenide and Aluminium Gallium Arsenide are often used due to the high mobility that can be achieved. Silicon offers much higher purity with no doping atoms, resulting in more uniform lattices and less scattering at the expense of mobility.

Most nano-devices currently being studied are concerned with the conductance or electron flow through them. These structures range from approximately zero to two-dimensions with various interactions and properties. Many of the devices developed and studied operate at milli Kelvin temperatures. At such temperatures the mean free path of the electrons is considerably larger than the devices being studied. However, for devices to be readily usable they will need to operate at considerably higher temperatures (liquid nitrogen and above). Already a single  $C_{60}$  molecule has been operated as an amplifier (Whittington et al. 1995) and a single carbon nano-tube has been used to make a transistor, both work at

room temperature (Tans et al. 1998, Sohn 1998). More recently, a semiconducting single-walled nanotube transistor has been used to construct a nonvolatile charge-storage memory element operating at room temperature (Fuhrer et al. 2002). An array of nanowires has been used to create photoluminescence, again at room temperature, where the wavelength is dependent on the diameter of the nanowires (Lyons et al. 2002). As fabrication techniques improve it will be possible to construct larger devices that have smaller features and the ability to operate at higher temperatures. A brief discussion of the various types of nano-structured devices is given below.

### 1.1.1 GaAs-AlGaAs Heterojunctions

GaAs-AlGaAs Heterojunctions result in a two-dimensional electron gas (2DEG) between the GaAs and AlGaAs layers. The Fermi energy of AlGaAs is initially higher than the GaAs causing electrons to spill from the AlGaAs into the GaAs. This deforms the band energies in the GaAs and causes a local increase in the electron density about the junction as shown in Figures. 1.2 and 1.3. These electrons are trapped in the triangular well and their motion is confined effectively to two-dimensions, giving rise to the name *two-dimension electron gas* (2DEG).

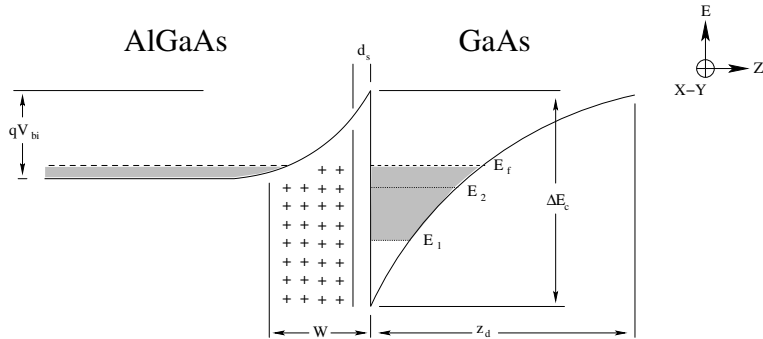


Figure 1.2: Conduction band profile in a heterojunction (Ferry & Goodnick 1997, page 37). The large energy difference between the two levels  $E_1$  and  $E_2$  and the low thermal energy of the electrons results in an accumulation of electrons at  $E_1$ . Consequently, motion in the  $z-$  direction is prohibited.

Carrier concentration typically ranges from  $2 \times 10^{11} / cm^2$  to  $2 \times 10^{12} / cm^2$  which is  $0.002 / nm^2$  to  $0.02 / nm^2$ . Devices approximately  $10nm \times 10nm$  in size are often referred to as single

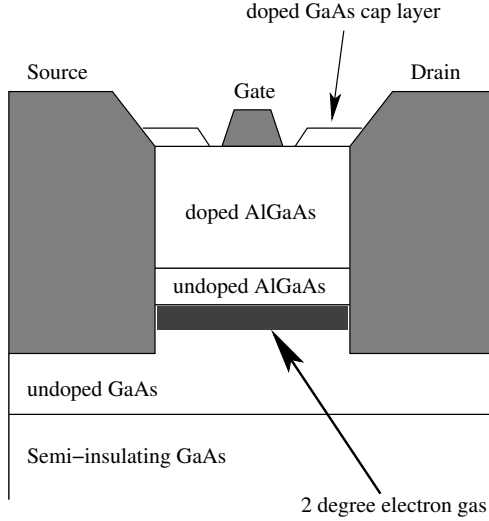


Figure 1.3: Example layout of a GaAs-AlGaAs heterojunction with 2 degree electron gas (Ferry & Goodnick 1997, page 26).

electron devices since, on average, only 1 to 2 electrons are within the device at any given time (Datta 1995, Ferry & Goodnick 1997, O'Brien 1999).

To create various structures, the conduction band can be depleted by applying a negative voltage to a metallic gate deposited on the surface of the AlGaAs. By controlling the bias on the gates, potentials of varying strengths can be constructed.

Enhancement mode field effect transistors (FETs) in high mobility GaAs heterostructures replace the dopant layer adjacent to the band electrons with an undoped layer, as shown in Figure 1.4. This design reduces the disorder seen by the 2DEG (less scattering) allowing for a smaller spacing between the gate and the conduction band, in turn allowing structures with finer detail to be manufactured. Devices can be constructed with an electron density ranging from  $10^{10}/cm^2$  to  $5 \times 10^{11}/cm^2$ . At  $0.1K$  propagation electrons have a mean free path exceeding  $100\mu m$ , which is considerably larger than the size of the devices being studied (Kane et al. 1998).

With this layout, the gate draws electrons into the propagation channel, in the undoped GaAs, from the contacts. Other gates can then be biased to produce a potential of the desired shape. Due to the requirement that the electrons must be drawn from the contacts, while not shorting to the gates, these devices are difficult to construct. However, recent advances in semi-conductor fabrication techniques have allowed this to occur, with

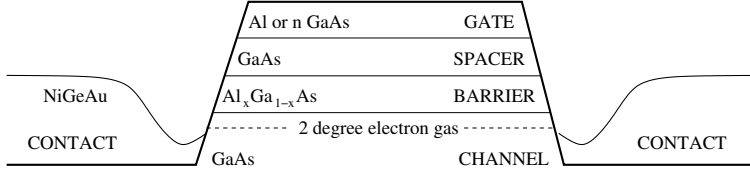


Figure 1.4: Example layout of a GaAs heterostructure with 2 degree electron gas (Kane et al. 1998).

structures of the order of  $25\text{ nm}$  being constructed and studied (Kane et al. 1995, Kane et al. 1998).

### 1.1.2 Quantum dots

Quantum dots are devices where the electrons are effectively confined in all dimensions. That is, they have no degrees of freedom and are often thought of as zero dimensional. Most research in quantum dots is concerned with the electron configuration within the dot and how dots interact. Quantum dots have many realisations, ranging from nano-pillars to cavities (see Figure 1.5).

With an appropriately designed dot, the contained electrons will arrange themselves in shell-like structures in two dimensions. These shell-like structures possess some of the properties of an atom and are often referred to as *artificial atoms* (Kastner 1993, Kouwenhoven 1998).

By adjusting the confining potential, electrons can be ejected or added individually, allowing a single electron *turnstile* to be developed. Dots demonstrate charge and energy quantisation and allow fundamental atomic physics experiments to be performed on a simplified system. For example, the effect of a magnetic field on shell structure can be examined in detail.

Since these dots can be manufactured in the laboratory to almost arbitrary shapes and sizes, artificial atoms with greatly differing properties can be constructed. An atom with desired characteristics can be made and the effects of different external potentials tested. By making the dots non-symmetric a whole new range of possibilities is available; such

as tunable atoms which may be used to generate lasers with previously unavailable wavelengths.

By placing several dots side-by-side artificial molecules can be constructed and the properties studied. Placement of the dots can be accurately controlled, allowing the coupling between the atoms in the molecule to be finely adjusted. The interactions between atoms in a molecule can be studied in a systematic way and on an individual basis.

Quantum dots also allow easier access to and control over crystal structures where band structures are dominant. Dots have also been suggested as a possible mechanism for implementing a quantum computer, principally based upon their quantum and artificial atomic nature.

### **1.1.3 Quantum point contact and quantum wires**

Quantum point contacts and quantum wires are often considered to be one dimensional structures. The electrons can flow from source to drain, but their motion is restricted to approximately one dimension only (see Figure 1.6).

The conductance through such devices is demonstrated both experimentally and theoretically to be quantised (Szafer & Stone 1989, Katine et al. 1997, Alamo et al. 1998, Kane et al. 1998). Figure 1.7(a) shows the quantisation of conduction through a quantum wire as the applied voltage is increased. This is mainly due to the number of energy levels available for conduction increasing in quantised steps as the voltage is increased. When the size of the wire is reduced to several atoms in a line (1 atom wide wire), (Lang & Avouris 1998), the conductance is observed to be highly dependent on the number of atoms forming the wire (see Figure 1.7(b) ).

The basic operation of quantum wires and quantum transistors will play an ever-increasingly important role in future semiconductor products. However, with the construction of such devices becoming possible within the last decade, many new and novel devices have been developed. For example, a quantum wire has been operated as a low threshold, small red-shift laser with single mode stability (Hayamizu et al. 2002). The application to quantum

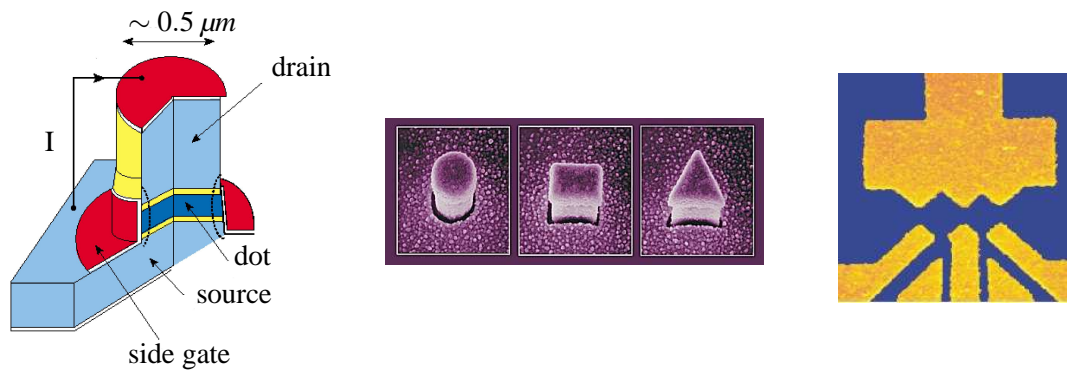


Figure 1.5: Quantum dots, nano-pillars and cavities (Kouwenhoven 1998).

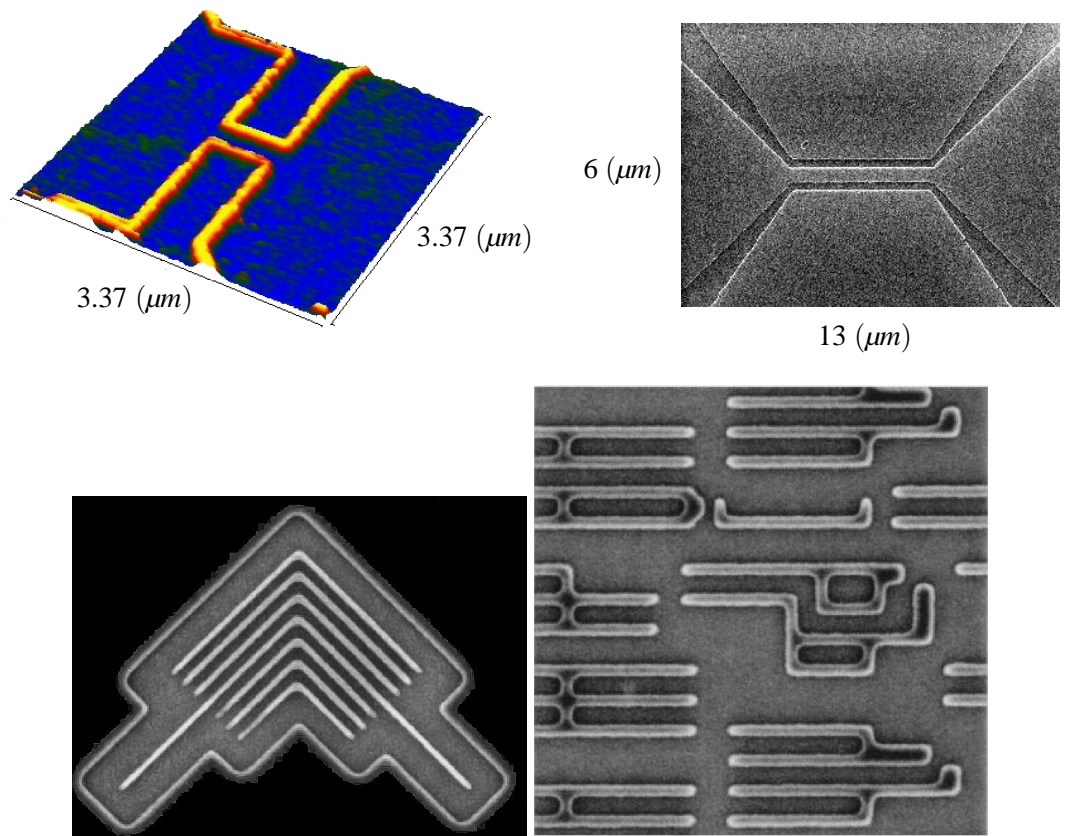
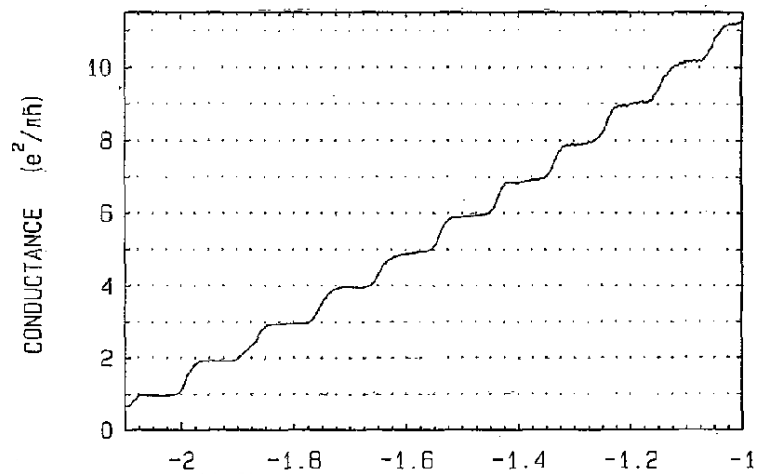
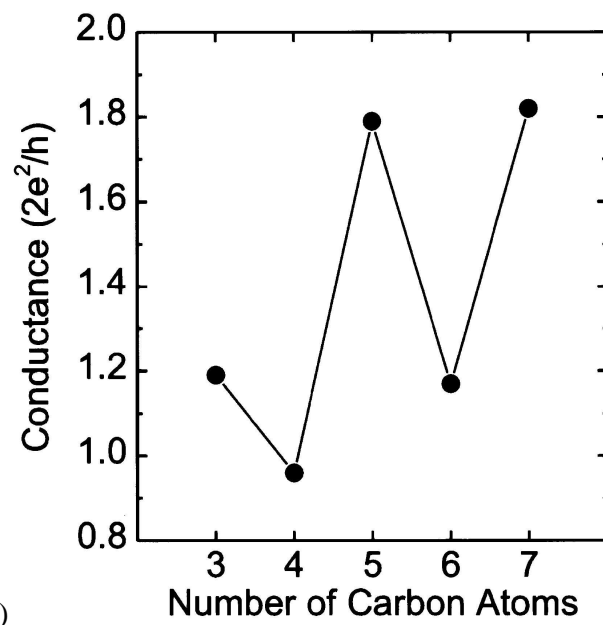


Figure 1.6: Quantum point contact (Dr Ryan Held, Nanophysics at ETH); quantum wire (Kane et al. 1998); 70 nm bent quantum wires or quantum elbows and 100 nm quantum circuits (Naulleau et al. (2002), Lawrence Berkeley National Laboratories).



(a) GATE VOLTAGE (V)



(b) Number of Carbon Atoms

Figure 1.7: (a) Quantisation of conductance through a quantum wire (Ferry & Goodnick 1997). (b) Quantised conduction through a single atom wide wire (Lang & Avouris 1998)

computing has been suggested by Akis & Ferry (2001), whereby a quantum waveguide array allows the computation of Fourier transforms using a parallel quantum approach. Bertoni et al. (2000) have shown that the universal set of quantum logic gates can be realised using solid-state quantum bits based on coherent electron transport in quantum wires. Similarly, Harris et al. (2001) and Gilbert et al. (2002) examined the implementation of a quantum controlled-not gate using magnetically switched quantum waveguide qubits. They demonstrated that a quantum waveguide inverter gate, under the application of an appropriate magnetic field, shows promise for a semiconductor realisation of quantum computing.

Moving away from the semiconductor industry and quantum computing, quantum waveguides have the potential to separate the spin and charge components of the one dimensional electron wave function forming quasiparticles, leading to spatial separation of these properties, as proposed by Luttinger (1963). Intriguing electronic properties have been discovered experimentally, such as a splitting of one dimensional electron band structure into two states, symmetrically positioned at the Fermi wave vector of a half-filled band (Robinson et al. 2002).

## 1.2 Theoretical progress and position of this thesis

A pressing challenge to theorists is to provide an accurate prediction of quantum transport and interference in these nano-structures, including: resonant tunnelling; low dimensionality effects; Aharonov-Bohm interference; effect of magnetic and electronic fields and the coupling to classical systems. In fact, the size of electronic components cannot be scaled down much further without a proper understanding of the quantum effects that emerge at the nanometre scale. A detailed theoretical study will provide the essential quantum mechanical basis for the design and analysis of quantum devices at the nanometre scale.

Since the characteristic dimensions of nanometre scale electronic devices are comparable to the wavelength of an electron with energy from *meV* to a few *eV*, a classical “billiard-ball” description of their motion is no longer valid. Theoretical calculation of device properties requires a full quantum mechanical treatment, that is, solving the time depen-

dent Schrödinger equation

$$i\hbar \frac{\partial \psi(\mathbf{r},t)}{\partial t} = \mathcal{H}\psi(\mathbf{r},t) \quad (1.1)$$

$$\mathcal{H} = -\frac{1}{2m}(-i\hbar\nabla - e\mathbf{A})^2 + e\mathcal{V} \quad (1.2)$$

where  $\mathbf{r}$  represents the spatial coordinates,  $\mathcal{H}$  is the system Hamiltonian,  $\mathcal{V}$  is the electronic potential and  $\mathbf{A}$  is the magnetic vector potential where the magnetic field  $\mathbf{B} = \nabla \times \mathbf{A}$ .

Current theoretical work on quantum waveguides is predominantly based on the separability of time and spatial variables  $\psi(\mathbf{r},t) = \phi(\mathbf{r})\tau(t)$ , which leads to the time independent Schrödinger equation (Olendski & Mikhailovska 2002, Csontos & Xu 2002, Xu & Gu 2001, Jin et al. 1999, Varshini 1998, Nikolic & Sodan 1998, Gu et al. 1998, Carini et al. 1997, Clark & Bracken 1996, Tachibana & Totsuji 1996, Popov & Popova 1996).

The time independent Schrödinger equation is of the form of an eigenvalue problem

$$\mathcal{H}\psi(\mathbf{r}) = E\psi(\mathbf{r}), \quad (1.3)$$

where  $E$  and  $\psi$  are the eigenenergies and eigenfunctions of the system respectively.

However, there are severe limitations for the time independent methods to provide information on transient behaviours of the system under study. Consequently, much remains to be studied in the temporal response of quantum electronic devices, which is of particular importance for analysing high-speed quantum transistors and quantum switches. In principle, the general solution of the time dependent Schrödinger equation can be constructed by a complete expansion of all allowed stationary energy eigenfunctions, since the time dependent part is simply  $\tau(t) = c\exp(-\frac{i}{\hbar}Et)$ . However this often requires a very large number of discrete eigenstates as well as an integration over the continuous part of the energy spectrum, ie.

$$\psi(\mathbf{r},t) = \sum_E \psi_E(\mathbf{r}) \exp\left(-\frac{i}{\hbar}Et\right). \quad (1.4)$$

In terms of accuracy and efficiency, the time independent methods cannot compete with the time dependent approach presented in this thesis, as shown in Chapters 2 and 3. In addition, the separation of time and spatial variables implies explicitly time independent Hamiltonian  $\mathcal{H}$  and thus the electronic transportation properties can be analysed only under steady-state conditions if the time independent Schrödinger equation is used.

Another difficulty in solving the time independent Schrödinger equation lies in the explicit boundary conditions imposed by the various quantum cavities. In some cases, special transformations are carried out to obtain simpler boundaries in the new coordinate system, but this normally gives rise to more complicated differential equations (Clark & Bracken 1996). The inclusion of *soft-walled* potentials again increases the difficulty of defining the boundary. Soft-walled potentials more accurately model physical systems as sharp changes in the potential are smeared out (see Figure 1.8).

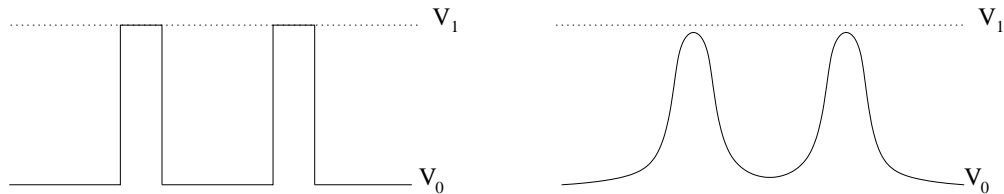


Figure 1.8: Representation of Hard-walled and Soft-walled potentials.

For this reason, only quantum waveguides with very simple geometry have been studied. One can employ the finite element method and the boundary element methods to treat irregular boundaries, by dividing the system into scattering and probe regions and then matching the wave functions at the boundaries (Frohne et al. 1989, Wang et al. 1994, Amemiya & Kawamura 1995, Knipp & Reinecke 1996, Amemiya 1999). In this way, the quantum scattering problem is simplified to the solution of a set of algebraic equations. A major difficulty is then the inversion of large matrices, which can be prohibitively expensive in terms of computer memory and CPU time (Wang et al. 1994).

This thesis develops a highly accurate and effective time dependent approach, by which a complete knowledge of the system, including transient information, can be obtained. This approach was originally developed by quantum chemists to study a variety of gas-phase reactive scattering and related chemical processes (Tal-Ezer & Kosloff 1984, Cerjan & Kulander 1991, Kroes & Neuhauser 1996, Balakrishnan et al. 1997, Gray & Balintkurti 1997). This work extends their methods to investigate quantum transport phenomena in nano-electronic structures.

Undoubtedly, the time dependent approach has a more natural correspondence to reality, that is, starting from an initial state of the system and following the events through time. It gives a direct solution of the quantum equations of motion and consequently has many

distinct advantages over the traditional time independent methods. For example, it provides information on transient behaviours and allows direct visualisation of the transport process, in which one can “watch” a system evolve in real time and as a result monitor intermediate stages of the process of interest. As an initial value problem, it is also comparatively easy to implement, flexible and versatile in treating a large variety of quantum problems. It can be applied to study quantum waveguides with arbitrarily complex boundaries and thus free of the difficulties encountered by time independent methods. Another very important attribute of this approach is that it can be applied to a time-varying Hamiltonian. This is achieved by breaking the propagation into small time steps such that the system Hamiltonian changes slowly with respect to the time interval.

Due to its broad application, such a time dependent approach is easily adaptable to many other problems including scattering, band structure, multi-device potentials and multi-scattering phenomena. The development of the theoretical model and computational techniques forms the majority of the original work undertaken during studies for this thesis.

Many of the results shown in following chapters have not been produced theoretically prior to this thesis. The theoretical inclusion of magnetic fields in the time dependent Schrödinger equation and results produced are entirely original and demonstrate the power and adaptability of the model developed in this work. The development and understanding of the complex potential presented in Section 3.5.3 is also original work, providing a bound on the use of complex potentials to reduce computation. The results obtained when varying the lead flange angle of a quantum wire allow direct improvement of transmission through quantum wires. The inclusion of a magnetic field is demonstrated to allow the detection and partial characterisation of impurities in quantum wires. The treatment used is a full quantum mechanical solution with no semi-classical adjustments made to the wave function. The oscillations observed from the Aharonov-Bohm ring match those seen experimentally and demonstrate clearly the phase modification due to a magnetic field.

# **Chapter 2**

## **Theoretical model**

Before a detailed study of nano-structured electronic devices can be undertaken an appropriate theoretical model must be developed. As outlined in the introduction, classical and semi-classical methods are not adequate for studying electronic devices at the nano-metre scale, leaving quantum mechanics as the only viable description. A full quantum mechanical solution to the Schrödinger equation provides both spatial and phase information of the system at all times, and thus a complete knowledge of all possible observables of the system under study.

This chapter details the theoretical model utilised in the remainder of the thesis and discusses various methods for solving the corresponding Schrödinger equation. Certain approximations are made by taking into account physically the most important aspects of the system. Guidance is taken from previous and current experimental results as to which effects can be neglected and which are important, with attempts made to understand the effects on the final solution.

### **2.1 Single electron approximation**

The dynamical properties of a quantum system is governed by the time dependent Schrödinger equation Equation 1.1. However, solving this equation for all electrons and particles in

the semi-conductor is not practical. Devices currently constructed, as described in Section 1.1.1, statistically contain only 1 conduction electron at any given instant. Consequently, theoretical modelling of single electron transport through such devices closely matches the reality of experiments. This approximation allows theoreticians to model the most important aspects of experiments without taking into account every minute detail. As eluded to by Webb (1998), who quotes Rolf Landauer as saying ‘*Yes, in the vast phase space between heaven and hell there are undoubtedly some corners where Tomonaga–Luttinger liquids, Wigner crystals and Unicorns flourish. But you have to hunt for them!*’.

The resultant wave function from the single-electron model will have probability amplitude that reflects the statistical nature of a large number of single electrons propagating through the device. By studying the transmission and reflection, experimental quantities such as conductance and energy spectrum can be inferred as detailed in Chapter 4.

## 2.2 Effective mass approximation

As commented on in the introduction, the systems being studied are of the order of only a few hundred atoms in size and of the same order as the wavelength of an electron with a few eV of energy. It is quite conceivable that the potential felt by the transport electron would be very complicated and more lattice like in its structure. However, it has been shown in theory and by experimentation (Pang & Louie 1990, Tanner 1995) that such lattice effects and other local effects can be approximated by a ground state electron with a reduced or effective mass, which is material and temperature dependent. For homogeneous Gallium Arsenide at a few kelvin the reduced mass  $m^*$  is approximately 0.0667  $m_e$  (Kittel 1986). The energy dependent effective mass is given by

$$m^*(E) = (0.0665 + 0.436E + 0.236E^2 - 0.147E^3) m_e \quad (2.1)$$

(Pang & Louie 1990) where  $E$  is the single-particle energy above the band edge in eV.

The Schrödinger equation then becomes

$$i\hbar \frac{\partial \psi(\mathbf{r},t)}{\partial t} = \left( -\frac{1}{2m^*}(-i\hbar\nabla - e\mathbf{A})^2 + e\mathcal{V} \right) \psi(\mathbf{r},t), \quad (2.2)$$

where  $\mathcal{V}$  represents the effective electronic potential and  $\mathbf{A}$  represents the magnetic vector potential.

A number of assumptions are made about the lattice: it is uniform; its interaction with the propagation electron is incorporated into the effective mass; and it is non-deforming due to screening (ie. the presence of the conduction electron does not alter the shape of the lattice potential). Since the electrons and their conjugate ‘exchange-correlation holes’ in the Fermi gas are free to move, the conjugate exchange-correlation holes move toward the propagation electron. This leads to a surplus of positive charge near the propagation electron, thus screening the lattice potential from the propagation electron at some distance from the electron. Elliot (1998) demonstrates that the Thomas-Fermi screening length is typically of the order of  $1\text{\AA}$ , which is considerably smaller than the structures considered in this thesis, which have finest detail around  $1\text{ nm}$  to  $10\text{ nm}$  in size.

## 2.3 Electronic potentials

The main confinement potential is the *electronic potential*,  $\mathcal{V}(\mathbf{r})$ . This is modelled by setting the potential height  $\mathcal{V}(\mathbf{r})$  to different values, which represent the different features of a device. For example, a quantum wire is formed by setting the boundaries of the wire to  $V$ , much greater than the incident energy of the electron, and the conduction area of the wire to 0. Consequently, the electron will conduct through the potential where it is zero, reflecting from the boundaries. In this fashion, the electron travels along the wire, as shown in Figure 2.1.

If required, an additional electric field can be applied across the devices. This results in the whole potential pattern described above being tilted in accordance with  $\mathcal{V} = Ed$  for distance  $d$  along the device and electric field strength  $E$ , as shown in Figure 2.2.

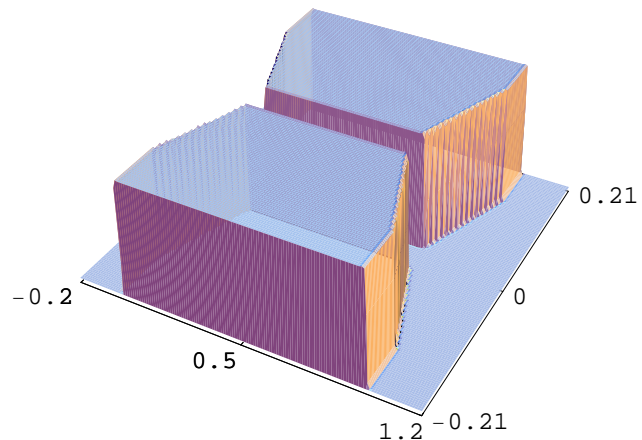


Figure 2.1: A quantum wire potential with boundary potential height  $0.11\text{ eV}$ . A typical calculation would use an initial wave function with median energy  $0.054\text{ eV}$ , well below the potential height.

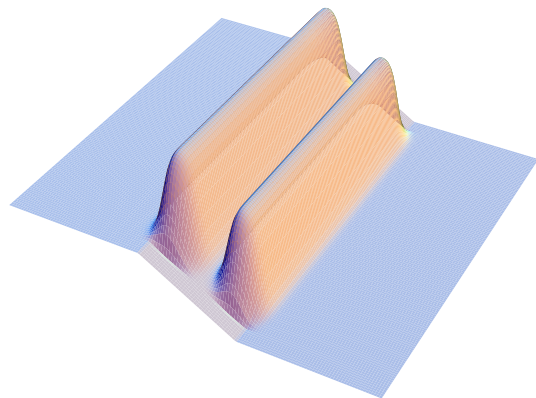


Figure 2.2: A double barrier potential with an external electric field.

## 2.4 Magnetic potentials

With the main device structure being formed by the electric potential  $\mathcal{V}$ , more subtle quantum effects can be probed by applying an external magnetic field  $\mathbf{B}$ . The application of a weak magnetic field allows the phase of the wave function to be altered without affecting the overall electron density distribution. For example, by applying a magnetic field to the *Aharonov-Bohm Ring* (van der Wiel. et al. 2001), the transmission through the ring can be made to undergo oscillations as the electron wave function constructively and destructively interferes in the output lead.

As described earlier, the magnetic field enters the Hamiltonian via the vector potential  $\mathbf{A}$ , i.e.

$$\mathcal{H} = -\frac{1}{2m}(-i\hbar\nabla - e\mathbf{A})^2 + e\mathcal{V}, \quad (2.3)$$

where  $\mathbf{A}$  is defined by

$$\mathbf{B} = \nabla \times \mathbf{A}. \quad (2.4)$$

For a given magnetic field  $\mathbf{B}$ , there are an infinite number of ways to form the magnetic vector potentials  $\mathbf{A}$  (namely the different gauges), all of which provide the same results for physically measurable quantities.

There are many ways of solving the Schrödinger equation. Their strength and limitations are reviewed in the following sections.

## 2.5 Time independent methods

Time independent methods aim to solve the time independent Schrödinger equation given by Equation 1.3, in which the system being studied is defined by the Hamiltonian  $\mathcal{H}$ . The most naive approach is to attempt to solve the eigen value and eigen vector problem directly. However, this can lead to the inversion of poorly conditioned matrices, rendering them ineffective.

The discretisation of the space often results in a matrix representation of the Laplacian  $\nabla^2$

which is poorly conditioned (see below). Coupled with a potential  $\mathcal{V}$  of arbitrary shape and magnetic fields  $\mathbf{B} = \nabla \times \mathbf{A}$  the matrix representation of  $\mathcal{H}$  is very poorly conditioned. Moving to a higher order method only serves to make the condition number of the matrix representation for  $\mathcal{H}$  even worse. Depending on the type of method implemented (iterative or direct), a poorly conditioned matrix leads to either many iterative steps, or a direct solution which requires a large number of computations to converge.

The condition number is the ratio of the maximum and minimum eigen values  $\kappa = \frac{E_{max}}{E_{min}}$ .

Now in one dimension we want

$$-\nabla^2 u(x) = E u(x) , \quad (2.5)$$

when discretised

$$u(x_i) = \frac{1}{\sqrt{n}} \sum_{j=0}^{n-1} U(p_j) \exp\left(2\pi i \frac{p_j x_i}{n}\right) \quad (2.6)$$

and

$$-\nabla^2 u(x_i) = -\frac{1}{\sqrt{n}} \sum_{j=0}^{n-1} \left(2\pi i \frac{p_j}{n}\right)^2 U(p_j) \exp\left(2\pi i \frac{p_j x_i}{n}\right) . \quad (2.7)$$

If  $u(x)$  is carefully chosen such that

$$u(x_i) = \frac{1}{\sqrt{n}} U(p_j) \exp\left(2\pi i \frac{p_j x_i}{n}\right) , \quad (2.8)$$

for a particular  $p_j$ , then the eigenvalues are simply

$$E_j = \frac{4\pi^2 p_j^2}{n^2} , \quad (2.9)$$

for  $j = 0$  to  $n - 1$ . It is maximum for  $j = n - 1$  and minimum for  $j = 0$ , giving

$$E_{max} = \frac{4\pi^2 p_{n-1}^2}{n^2} , \quad (2.10)$$

$$E_{min} = \frac{4\pi^2 p_0^2}{n^2} , \quad (2.11)$$

so the condition number is

$$\kappa = \frac{p_{max}^2}{p_{min}^2} . \quad (2.12)$$

Now each frequency component of  $U(p_j)$  has angular frequency  $\omega = 2\pi\nu = p_x x$ . Consequently, the maximum momentum is given by  $p_{max} = \frac{\pi}{x_{min}}$  where  $h = 2x_{min}$  is the grid

spacing. The minimum momentum is  $p_{min} = \frac{\pi}{x_{max}}$  where  $n h = x_{max}$ . This gives the condition number as

$$\kappa = n^2 . \quad (2.13)$$

As the accuracy of the model is increased (by decreasing the grid spacing and increasing the number of grid points) the condition number increases as  $n^2$ .

The following methods outline several typical methods used to solve the time independent Schrödinger equation. However, like with the simplistic eigen problem approach, they often result in hard to solve equations, which renders them useful only in a restricted subset of problems.

### 2.5.1 Mode matching

By splitting the potential up into regions, known analytical or numerical solutions can be used to derive a total solution for the potential, see Figure 2.3 as an example. By obtaining a general solution to each region and then matching the solutions at the boundaries between regions, a solution to the Schrödinger equation can be found (Schult et al. 1989, Tachibana & Totsuji 1996, Yiu & Wang 1996, Carini et al. 1997, Wang 1997, Olendski & Mikhailovska 2002).

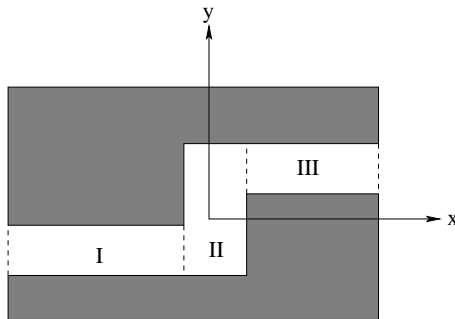


Figure 2.3: The potential is split into different regions for computation

For example, the solution to the Schrödinger equation in each region  $j = I, II$  or  $III$  in Figure 2.3 is obtained by solving for  $\mathcal{V}_I = \mathcal{V}_{II} = \mathcal{V}_{III} = 0$  with infinite boundary walls

$$-\frac{\hbar^2}{2m^*} \left( \frac{\partial^2}{\partial x^2} + \frac{\partial^2}{\partial y^2} \right) \psi^j(x, y) = E \psi^j(x, y) \quad (2.14)$$

$$\psi^j(x, y) = \sum_n \left[ a_n^j \exp\left(\frac{i}{\hbar} p_n^j x\right) + b_n^j \exp\left(-\frac{i}{\hbar} p_n^j x\right) \right] \phi_n^j(y), \quad (2.15)$$

where  $\phi_n^j(y)$  are a set of transverse eigenstates in the region  $j$  in the channel. The constants  $a_n^j$  and  $b_n^j$  are determined by the boundary conditions and by matching the functions at the boundaries to the regions.

Unfortunately, the number of known solutions is small (step function, top hat function, quantum wire and a small number of others), which greatly restricts which shapes can be studied using this method. Also, most known solutions are for hard-walled potentials, which do not accurately model the physical device. The lack of known solutions for the inclusion of a magnetic field applied to these simple systems also limits the method's usefulness in work carried out in this thesis.

The solution obtained is also the equilibrium or steady state solution and contains no information about transient states. This method does not work for time varying potentials nor for more than a single electron.

### 2.5.2 Time independent Green's functions

Green's function methods transform a system of differential equations and boundary conditions into integral equations over the internal boundaries of the system, which can then be discretised and solved numerically (Knipp & Reinecke 1996). Simple systems can be analysed using the single particle Green's function  $G(\mathbf{r}, \mathbf{r}'; E)$  for the time dependent Schrödinger equation and discretising it, a general wave function propagator can be obtained

$$[E - \mathcal{H}] \psi = 0, \quad (2.16)$$

$$[E - \mathcal{H}] G(\mathbf{r}, \mathbf{r}'; E) = \delta(\mathbf{r} - \mathbf{r}'). \quad (2.17)$$

The time independent wave function is obtained by integrating over the boundary  $S$  with normal  $\mathbf{n}(\mathbf{r})$  (Saito et al. 1992, Knipp & Reinecke 1996, Koonen et al. 2000), ie.

$$\psi(\mathbf{r}') = \frac{i}{2m} \int_S \mathbf{n}(\mathbf{r}) [-i\hbar\psi(\mathbf{r}) \nabla_{\mathbf{r}} G(\mathbf{r}, \mathbf{r}'; E)] dS. \quad (2.18)$$

With an appropriate discretisation of the space and a representation of the potential and Laplacian (contained in  $\mathcal{H}$ ) the matrix  $E - \mathcal{H}$  is inverted yielding the propagator  $G(\mathbf{r}, \mathbf{r}'; E)$ . Unfortunately, the matrix given by  $E - \mathcal{H}$  is poorly conditioned and can not be easily factorised.

### 2.5.3 Finite element

The finite element method allows a potential of almost arbitrary shape to be studied. By choosing a suitable set of basis functions (often piecewise polynomials, nonzero only in a local region of space), the potential, Laplacian and wave function can be discretised. This replaces the partial differential equations by algebraic equations, approximate functions locally, and formulates the problem as functional evaluations on grid points on the boundary of each element.

Once an appropriate basis set is chosen and the potential, Laplacian and wave function discretised, standard time independent methods can be used. By ensuring that the solution is continuous across the boundary of each element, a complete solution can be obtained (Beck 2000).

As an alternate discretisation to simply taking the values of the function at grid points, it still leads to poorly conditioned matrices to invert. Consequently, the method suffers the same problems as generic eigenvalue or finite difference methods (Knipp & Reinecke 1996).

The space is usually divided up into triangles with their size and density varied according to the potential shape and boundary conditions. In this fashion, areas in which the potential is changing rapidly can be computed with higher accuracy while areas in which it changes very little (eg. free space) can be computed with fewer triangles, thus increasing the speed of the calculation. If the size and density of the triangles is modified during the calculation, increasing accuracy in areas where it is needed, a fast, flexible and efficient algorithm is obtained.

However, the solution on each element is only an approximation to the actual wave func-

tion, often resulting in extremely small elements being used to obtain accurate spatial and phase information. Changing the size of the elements and their density will produce high frequency noise, which can introduce considerable error into the phase of the wave function.

## 2.6 Time dependent methods

The time dependent Schrödinger equation has many advantages over the time independent equation. It is stated as an initial value problem rather than a boundary condition problem, which allows an arbitrary initial wave packet to be used as the input wave function  $\psi(x, y, t = 0)$  and advances it in time under the application of a potential. By stopping the code at regular intervals, a time-slice movie of the evolution can be obtained. It removes the need for boundary conditions, which can be difficult to implement for arbitrarily shaped potentials.

The time dependent Schrödinger equation is simply expressed in Equation 1.1 where the system being studied is defined by the Hamiltonian  $\mathcal{H}$ . For a two dimensional system the form is given by

$$\begin{aligned} i\hbar \frac{\partial \psi(x, y, t)}{\partial t} &= -\frac{1}{2m} \left( -\hbar^2 \frac{\partial^2}{\partial x^2} - \hbar^2 \frac{\partial^2}{\partial y^2} + i\hbar q \frac{\partial}{\partial x} A_x + i\hbar q \frac{\partial}{\partial y} A_y + q^2 A_x^2 + q^2 A_y^2 \right) \psi(x, y, t) \\ &+ \mathcal{V}(x, y) \psi(x, y, t), \end{aligned} \quad (2.19)$$

where  $\mathcal{V}(x, y)$  is the electronic potential defining the nano-device being studied and  $\mathbf{A} = (A_x, A_y)$  is the magnetic vector potential.

The time dependent approach aims to obtain a full solution of the time dependent Schrödinger equation directly. The formal solution has been known for a long time (Goldberger & Watson 1964, Taylor 1972)

$$\psi(x, y, t + \Delta t) = \exp \left( -\frac{i}{\hbar} \mathcal{H} \Delta t \right) \psi(x, y, t), \quad (2.20)$$

but computational techniques for treating the exponential time propagator  $\exp(-\frac{i}{\hbar} \mathcal{H} \Delta t)$  have been slow to develop and practical calculations have had to await the arrival of powerful computers. Different approximations to the exponential time propagator  $\exp(-\frac{i}{\hbar} \mathcal{H} \Delta t)$ ,

along with the technique used to evaluate the action of the Laplacian  $\nabla^2$  on the wave function, lead to different time evolution schemes.

### 2.6.1 Finite difference

Many different methods have been employed to solve the time dependent Schrödinger equation. Perhaps the simplest is the first-order finite-difference approximation to the exponential operator in Equation 2.20

$$\psi(x, y, t + \Delta t) = \psi(x, y, t) - \frac{i}{\hbar} \mathcal{H} \Delta t \psi(x, y, t) \quad (2.21)$$

with an appropriate numerical solution for  $\frac{\partial \psi(x, y, t)}{\partial t}$ . Such methods require a large number of very small time steps  $\Delta t$  (typically of the order of  $10^6$  time steps) to develop a complete time evolution. This scheme scales  $O(m)$  (where  $m$  is the number of spatial grid points used to represent the system), is not symmetric with respect to time (therefore unstable) and is not unitary, rendering it unsuitable except for simple cases.

To avoid the instability, McCullough & Wyatt (1971) used the following first-order difference (FOD) scheme combined with a unitarised approximation to the time evolution propagator

$$\psi(\mathbf{r}, t + \Delta t) = \frac{2 - \frac{i}{\hbar} \mathcal{H} \Delta t}{2 + \frac{i}{\hbar} \mathcal{H} \Delta t} \psi(\mathbf{r}, t) , \quad (2.22)$$

which is often called the Crank-Nicolson method. This method scales as  $O(m)$  and is unitary and unconditionally stable. However, large poorly conditioned matrices need to be inverted which can be prohibitively expensive in terms of computer memory and CPU time.

To overcome this problem, Asker & Cakmak (1978) developed an explicit second-order differencing (SOD) scheme

$$\psi(\mathbf{r}, t + \Delta t) - \psi(\mathbf{r}, t - \Delta t) = -2 \frac{i}{\hbar} \mathcal{H} \Delta t \psi(\mathbf{r}, t) . \quad (2.23)$$

The SOD method scales as  $O(m)$ , is unitary, symmetric in time and demonstrated to be conditionally stable.

The drawback of these finite difference type of methods is that the associated truncation error is proportional to  $(\mathcal{H}\Delta t)^2$ . For this reason, the time step  $\Delta t$  for each propagation has to be extremely small and, therefore, the number of steps required for modeling a complete scattering event is very large. For example, an electron-atom scattering event with incident energy of 10 eV would require the same time propagation operator repeatedly acting upon the system wave function a few hundreds of thousand times. Although both the FOD and SOD schemes conserve the norm and energy, errors will accumulate in the phase.

There are other existing explicit and implicit propagation schemes based on a Taylor expansion of the time evolution operator, for example Pindzola & Schultz (1996). However, all these methods require small time steps and thus suffer the same problem of error accumulation, which may cause severe distortion of the wave packets.

### 2.6.2 Higher order methods

Due to the slow convergence of the approximately single order finite difference methods, higher order methods can be used,  $O(\Delta t^n)$  where  $n > 2$ . These allow larger time steps to be used, thus advance through the propagation faster. However, they usually involve greater computational complexity which can, in turn, slow down the calculation at each time step.

Buffington et al. (1999) utilised a high order terminated Taylor expansion to solve the time dependent Schrödinger equation for hydrogen electron scattering. They expanded the unitary propagator  $\mathcal{U} = \exp(-\frac{i}{\hbar} \mathcal{H}\Delta t)$  as

$$\mathcal{U}(\Delta t) = \sum_{n=0}^{\infty} \frac{1}{n!} \left[ -\frac{i}{\hbar} \mathcal{H}\Delta t \right]^n. \quad (2.24)$$

With a sufficient number of terms and a small enough time step  $\Delta t$ , the Taylor expansions of the propagator  $\mathcal{U}$  can be computed to the required accuracy. This often requires very small time steps and a large number of terms, though can be applied to systems with unbounded energies.

Rau & Unnikrishnan (1996) developed a method utilising the *Baker-Campbell-Hausdorff* formula to expand Equation 2.20 as

$$\begin{aligned}\psi(x, y, t + \Delta t) &= \exp\left(-\frac{i}{\hbar}\mathcal{H}\Delta t\right)\exp\left(-\frac{i}{\hbar}\mathcal{V}\Delta t\right) \\ &\times \exp\left(-\frac{i}{2\hbar^2}[\mathcal{H}, \mathcal{V}]\Delta t^2 + \frac{1}{6\hbar^3}[\mathcal{H}, [\mathcal{H}, \mathcal{V}]]\Delta t^3\right. \\ &\left.+ \frac{i}{3\hbar^3}[\mathcal{V}, [\mathcal{V}, \mathcal{H}]]\Delta t^3 \dots\right) \psi(x, y, t).\end{aligned}\quad (2.25)$$

For certain potentials the expansion terminates, while for some potentials the expansion can be terminated after a certain number of terms with reasonable convergence. For those systems that the expansion converges or terminates, the solution obtained is exact and easily computed numerically. Unfortunately, the expansion does not generally converge or terminate and is not practical when used in computations for arbitrarily shaped electronic and constant magnetic potentials as studied in this thesis.

### 2.6.3 Split operator

Another notable propagation scheme is the split operator (SPO) method devised by Feit et al. (1982), which was later used by Zhang et al. (1994) to study electron-pair wave packets. This scheme splits the exponential function into three parts

$$\psi(\mathbf{r}, t + \Delta t) = \exp\left(-\frac{i\nabla^2}{2\hbar}\Delta t\right)\exp\left(-\frac{i}{\hbar}\mathcal{V}\Delta t\right)\exp\left(-\frac{i\nabla^2}{2\hbar}\Delta t\right)\psi(\mathbf{r}, t)\quad (2.26)$$

and thus takes advantage of the ease of treating operators in their diagonal representations. Note that the kinetic  $\nabla^2$  and potential  $\mathcal{V}$  energy operators are diagonal in momentum and configuration space, respectively. The expansion error is determined by the next higher commutator between the potential and the kinetic energy operators and will vary with the value of these terms. This method is unconditionally stable and norm preserving since only unitary operators are involved. It has been used widely and, in some cases, successfully in propagating wave packets under the influence of system Hamiltonians. Nevertheless, this scheme neglects the commutators between the potential and kinetic energy operators and thus introduces error in both energy and phase of the wave function. The magnitude of the inaccuracy depends strongly on the system under investigation (Braun et al. 1996).

## 2.6.4 Time dependent Green's functions

Similar to the time independent Green's functions described in Section 2.5.2, Green's functions can be used to study the time dependent Schrödinger equation. A general formulation can be derived where the final solution is given by

$$\psi(\mathbf{r}, t) = \int d^3\mathbf{r}' \int_{t'}^t dt' K(\mathbf{r}, t; \mathbf{r}', t') \psi(\mathbf{r}', t') . \quad (2.27)$$

$K(\mathbf{r}, t; \mathbf{r}', t')$  is the propagator or kernel, where the Green's function  $G(\mathbf{r}, t; \mathbf{r}', t') = -iK(\mathbf{r}, t; \mathbf{r}', t')$ .

In the absence of any interactions, the equations of motion for the Green's function are

$$\left( i\hbar \frac{\partial}{\partial t} - \mathcal{H}(\mathbf{r}) - \mathcal{V}(\mathbf{r}) \right) G(\mathbf{r}, t; \mathbf{r}'; t') = \hbar \delta(\mathbf{r} - \mathbf{r}') \delta(t - t') , \quad (2.28)$$

$$\left( -i\hbar \frac{\partial}{\partial t'} - \mathcal{H}(\mathbf{r}') - \mathcal{V}(\mathbf{r}') \right) G(\mathbf{r}, t; \mathbf{r}'; t') = \hbar \delta(\mathbf{r} - \mathbf{r}') \delta(t - t') . \quad (2.29)$$

A Fourier transform in both space and time yields

$$G(\mathbf{p}, \omega) = \frac{\hbar}{\hbar\omega - E(\mathbf{p})} \quad (2.30)$$

where  $\mathbf{p}$  is the momentum,  $\omega$  is the frequency and  $E(\mathbf{p})$  is the energy eigenvalue of  $\mathcal{H} + \mathcal{V}$ . The inclusion of interactions such as impurity scattering, system-surrounding and phonons is also possible. For a more detailed discussion of this method applied to study the electron transport in nanostructures, see “Transport in Nanostructures” (Ferry & Goodnick 1997).

Again, computation of these eigenvalues proves prohibitive for quantum systems with complicated boundaries. The spatial Fourier transform allows easy representation of derivatives in  $\mathcal{H}$ . However, the representation of spatial potentials can lead to the summation of a large number of polynomials in  $\mathbf{p}$ . For simple potentials with a simple integrable representation, solutions can be obtained quickly. However, arbitrarily shaped potentials, possibly with soft-walls, often lead to infinite sums of polynomials. Consequently, the problem is transformed from one where the Laplacian is difficult to model to a situation where the potential is difficult to model.

## 2.7 Time dependent Chebyshev propagation scheme

Direct solution of partial differential equations requires  $O(N^3)$  operations and use  $O(N^2)$  memory (where  $N = N_x N_y$  is the total number of grid points). Iterative solvers require  $O(N^2)$  operations and use  $O(N)$  memory (Golub & Loan 1989). This can be improved with a preconditioned conjugate gradient or a multi-grid method which reduces the number of operations to  $O(N \log(N))$ . Fourier methods, utilising fast Fourier transforms, require  $O(N \log(N))$  operations and use  $O(N)$  memory, making them a fast, efficient use of memory and they are easy to program.

The computational model developed in this thesis is based on Fourier methods, which produce a wave function propagated an amount  $t$  from an initial wave function. The wave function contains all spatial and phase quantum information. The single electron effective mass approximation is adopted as described in Sections 2.1 and 2.2. From the final wave function, the transmission through the device, the conductance, an energy spectrum, and a momentum spectrum can be obtained. These quantities can be used to study and develop nano-devices and provide insight into the phenomena such as resonant tunnelling, interference and other geometric effects.

### 2.7.1 Chebyshev approximation

To solve the time dependent Schrödinger equation, Equation 2.20, the Chebyshev scheme was used. This method is little used in physics but extensively used in quantum chemistry (Tal-Ezer & Kosloff 1984, Cerjan & Kulander 1991, Kroes & Neuhauser 1996, Balakrishnan et al. 1997, Gray & Balintkurti 1997). This has been proven to provide an efficient and accurate method to study such nano structured electronic devices (Wang & Scholz 1998, Wang & Midgley 1999, Midgley & Wang 2000).

The Chebyshev scheme approximates the exponential time propagator by a Chebyshev polynomial expansion (Tal-Ezer & Kosloff 1984)

$$\psi(x, y, t) = \exp\left(-\frac{i}{\hbar}(\mathcal{E}_{max} + \mathcal{E}_{min})t\right) \sum_{n=0}^N a_n(\alpha) \phi_n(-i\tilde{\mathcal{H}}) \psi(x, y, 0), \quad (2.31)$$

where  $\mathcal{E}_{min}$  and  $\mathcal{E}_{max}$  are the minimum and maximum energy eigen values of the system Hamiltonian,  $\alpha = \frac{\mathcal{E}_{max} - \mathcal{E}_{min}}{2\hbar}t$ ,  $a_n(\alpha) = 2J_n(\alpha)$  except for  $a_0(\alpha) = J_0(\alpha)$ ,  $J_n(\alpha)$  are the Bessel functions of the first kind,  $\phi_n$  are the Chebyshev polynomials, and the normalised Hamiltonian is defined as

$$\tilde{\mathcal{H}} = \frac{1}{\mathcal{E}_{max} - \mathcal{E}_{min}} [2\mathcal{H} - \mathcal{E}_{max} - \mathcal{E}_{min}] . \quad (2.32)$$

The above normalisation ensures that the expansion of the Chebyshev polynomials is convergent. Since the Bessel functions fall to zero exponentially as  $n$  increases beyond  $\alpha$ , it follows that terminating the expansion at  $N > \alpha$  would yield accurate results. Note that  $\alpha$  is proportional to the time step  $t$  and so is the number of terms required in the expansion. Since the time step  $t$  can be arbitrarily large, this scheme is often used as a one-step propagator to cover the complete interaction.

The action of the operator  $\phi_n(-i\tilde{\mathcal{H}})$  on the initial wave function  $\psi(x, y, 0)$  can be evaluated using the following recurrence relation:

$$\phi_{n+1}(-i\tilde{\mathcal{H}})\psi(x, y, 0) = -2i\tilde{\mathcal{H}}\phi_n(-i\tilde{\mathcal{H}})\psi(x, y, 0) + \phi_{n-1}(-i\tilde{\mathcal{H}})\psi(x, y, 0) , \quad (2.33)$$

with

$$\phi_1(-i\tilde{\mathcal{H}})\psi(x, y, 0) = -i\tilde{\mathcal{H}}\psi(x, y, 0) \quad (2.34)$$

$$\phi_0(-i\tilde{\mathcal{H}})\psi(x, y, 0) = \psi(x, y, 0) . \quad (2.35)$$

The calculation therefore boils down to a series of calculations of the scaled Hamiltonian  $\tilde{\mathcal{H}}$  acting on some initial wave function  $\psi(x, y, 0)$ .

The major draw back of the Chebyshev scheme is the requirement of the Hamiltonian to be normalised. For single electron transport through electronic and magnetic potentials, this requirement is not a large restriction, because its energy eigen values are bound. That is, for a given initial energy of the wave function and shape of the potential, the maximum energy experienced by the wave function is bounded. The minimum energy is generally assumed to be zero. The larger the energy difference between the maximum and minimum energy eigen values, the more terms need to be included in the scheme and the slower the calculation.

If the energy eigen values are not bound, as in the case with a multi-electron system where the coulomb potential is present, then this method is not readily applicable. To allow this scheme to be used soft-core type approximations can be made to bound the energy or the energy can simply be truncated at some large value. See Chapter 5 for an application of these methods.

The major advantages are: single time step propagation; finite number of terms in summation; recurrence law easy to implement; no restriction on the potential (other than time independent); no boundary conditions; and an arbitrary initial wave function can be used.

### 2.7.2 Time dependent potentials

As mentioned above, the Chebyshev propagation scheme produces a solution to the time dependent equation, however it is not a solution for time dependent potentials. This can be overcome in some cases by assuming the potential does not change from time step to time step (i.e. propagate for only small time steps) and vary it gradually over many time step propagations.

If the potential varies slowly compared to the time step used, the assumption that it is constant for any single time step is reasonably good. In this way, by splitting the propagation up into many time steps, the potential can be varied from one time step to another, but assumed to be constant for any single step.

As the time steps get smaller, the approximation to the actual case gets increasingly better. Using this method, it should be possible to study a time varying potential of any frequency, with an appropriate number of time steps.

Initial investigation of time dependent potentials using the Chebyshev propagation scheme have been made as part of the work undertaken for an Honours Thesis by Hines (2000). This study was motived by analytical work by Rau & Unnikrishnan (1996) where the height of a double barrier was made to oscillate. The Chebyshev propagation scheme was modified to propagate the wave function for many small time steps for a time varying Hamiltonian  $\mathcal{H}(t)$ . In this way, many of the features analytically obtained by Rau

& Unnikrishnan (1996) were reproduced. Most importantly, the results show that the transmission spectrum is dependent on the frequency of the oscillations applied.

### 2.7.3 Derivatives and the Fast Fourier Transform

The application of the Hamiltonian on the wave function can be carried out in two stages for the electronic potentials and three for the inclusion of the magnetic field. In both cases, the difficult part is the computation of the derivatives. Wang & Scholz (1998) discussed the advantages and disadvantages of various methods and concluded that using Fourier transforms produced more accurate results and did not suffer some of the convergence problems of finite difference methods. However, as discussed, there are some restrictions placed on the model.

The Fourier transform method makes use of the fact that the wave function can be expressed as

$$\psi(x, y) = \int_{-\infty}^{\infty} \Psi(p_x, p_y) \exp(-i p_x x - i p_y y) dp_x dp_y , \quad (2.36)$$

for some function  $\Psi(p_x, p_y)$  called the Fourier transform of  $\psi(x, y)$ . Derivatives can then be computed as

$$\frac{\partial}{\partial x} \psi(x, y) = \int_{-\infty}^{\infty} -i p_x \Psi(p_x, p_y) \exp(-i p_x x - i p_y y) dp_x dp_y \quad (2.37)$$

$$\frac{\partial}{\partial y} \psi(x, y) = \int_{-\infty}^{\infty} -i p_y \Psi(p_x, p_y) \exp(-i p_x x - i p_y y) dp_x dp_y \quad (2.38)$$

$$\nabla^2 \psi(x, y) = \int_{-\infty}^{\infty} (-p_x^2 - p_y^2) \Psi(p_x, p_y) \exp(-i p_x x - i p_y y) dp_x dp_y . \quad (2.39)$$

By calculating the Fourier transform of the wave function and multiplying it by the momentum, derivatives become a matter of multiplication and can be computed very quickly.

With the use of the Fourier transform, the wave function across the boundaries must be continuous. If this condition is not met, then large oscillations occur in the function and produce large numerical errors. The other constraint on the model is that a wave function that travels past a boundary reappears on the opposite boundary (it wraps around the space). Thus a sufficiently large space must be used so that the wave function never

reaches a boundary. This applies a subsequent constraint that the wave function must now be localised.

The use of Fourier transforms has an extra benefit. The computation of both first and second order derivatives requires only one forward transform. The transformed wave function  $\Psi$  is then multiplied by the appropriate momentum function (for the respective order derivatives) and then a backward transform for each order derivative. The reduction in Fourier transforms leads to a saving in computation.

# Chapter 3

## Computational realisation

With a theoretical model for the nano structured systems and strategy to solve the corresponding time dependent Schrödinger equation, the actual implementation on a computer will be considered in this chapter. There are many optimisations that can be performed while writing the computer code to increase performance and decrease memory usage.

### 3.1 Overview of computation

The computation starts by defining a space for the wave function  $\psi(x,y)$  to propagate in. This consists of an array of value of size  $(N_x, N_y)$  with  $N_x$  columns and  $N_y$  rows. Each value in the array,  $\psi'(x_i, y_j)$ , is a complex floating point number  $z = x + iy$  which represents the wave function. The  $\psi'(x_i, y_j)$  is a discretised approximation of the actual wave function  $\psi(x,y)$  to some arbitrary precision. To achieve a closer approximation, a larger number of grid points with closer spatial separation would be used.

The wave function, electric potential, magnetic vector potential and derivatives are defined and computed on this discretised space. For example, an array will be defined,  $\mathcal{V}(x_i, y_j)$ , where the value on the grid defines the height of the potential at the point  $(x_i, y_j)$ . To multiply the potential  $\mathcal{V}(x,y)$  by the wave function  $\psi(x,y)$  the values on the discretised space are multiplied respectively, i.e.  $\mathcal{V}(x_i, y_j) \psi(x_i, y_j)$ .

The derivatives are computed in momentum space as discussed in Section 2.7.3. The momentum space wave function is also defined on a discretised grid, with an equal number of points to the spatial discretisation. Each point now represents a momentum value  $\Psi'(p_i, p_j)$ , where the momentum space is defined over  $-\frac{2\pi}{\Delta x} \leq p \leq \frac{2\pi}{\Delta x}$ .

Initially the wave function  $\psi'(x_i, y_j)$  will be seeded with initial values, usually in the distribution of a Gaussian. As the computation proceeds, the values of  $\psi'(x_i, y_j)$  will be updated to represent the propagation of the wave function. After the propagation, the distribution will represent the final state of the wave function allowing various diagnostics to be performed.

### 3.1.1 Program flow

As depicted in Figure 3.1 the program flow is quite simple and starts out reading an input file, initialising model parameters, defining dynamic variables and initialising the wave function. The program then constructs the potential, magnetic fields and allows the identification of any optimisations to be performed. After this, various preparations are made for the full propagation, including saving the initial wave function and potential to disk, calculating the initial system energy and normalisation.

A loop over the number of time steps is initiated (which can be 1 for the Chebyshev propagation scheme) with the propagation for each time step computed. Prior to the propagation of a time step, the wave function is saved to disk for possible later retrieval. The propagation for each time step proceeds, according to Section 2.7, until the Chebyshev summation converges or diverges. If the summation diverges, the wave function state, initially saved to disk, is reloaded and some dynamic parameters altered. The propagation is then computed again.

When computing the Chebyshev summation, it is possible to alter the values of  $E_{min}$  and  $E_{max}$  in Equation 2.31, which in turn alters the number of terms in the summation. By increasing  $E_{max}$  the summation can be computed more accurately at the cost of computational time. As described above, if the summation diverges, the code increases  $E_{max}$  and recomputes the time step. In this fashion, the computational code is able to be setup for

a minimum number of terms in the summation (thus decreasing the time of the computation) and increase the number as required to maintain accuracy.

Once the propagation for the time step is complete, the wave function energy, norm, transmission and reflection are computed and displayed with the intermediate wave function saved to disk as required. The propagation continues for further time steps or proceeds to post processing if the total time of propagation is reached.

## Model parameters

The input file allows for a vast number of parameters to be set. A considerable number of these parameters are dependent on other parameters. For example the grid spacing is dependent on the maximum momentum required to be supported, which is dependent on the initial energy given to the wave function as well as the strength of the external potentials. The code dynamically assigns values to these parameters as required to maintain computational accuracy and stability. If parameters are defined in conflict with what the code would dynamically assign, warning messages are displayed. Also, if a number of parameters are not defined, the code provides sensible default values.

More details on the parameters that can be defined and layout of the input file can be found in Section 3.6 and Appendix A.

### 3.1.2 Storage of arrays

Each double precision complex number consumes 16 bytes ( $B$ ) of computer memory so an array of size (1000,500) would consume  $1000 * 500 * 16 = 8000000$  bytes or 7.63 mega bytes ( $MB$ ). The larger the space, the more memory required to represent the wave function, Hamiltonian and potentials to the same degree of precision.

Along side the wave function up to 12 arrays of the same size are needed to represent the electronic potential and the various components for the magnetic potential as listed in Table. 3.1. The memory requirements are now  $12 * 7.63 = 91.56 MB$  just to represent

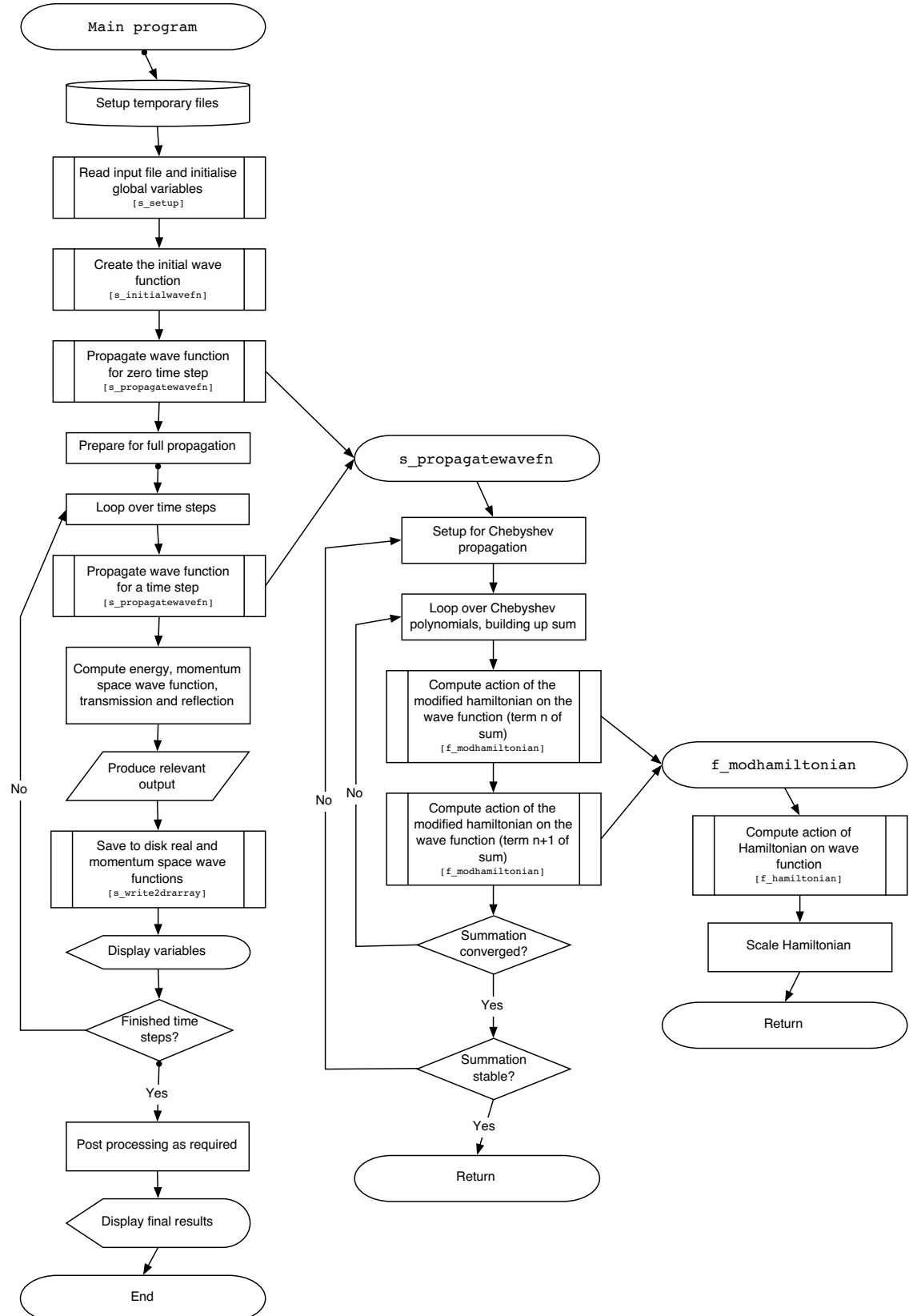


Figure 3.1: General program flow.

the wave function and potential. Couple to this several other temporary arrays and work arrays, the memory requirements quickly grow. Typical calculations in this thesis are performed on a grid of  $500 \times 500$  to  $2000 \times 2000$  requiring between  $70\text{ MB}$  and  $750\text{ MB}$  of memory respectively. Therefore, efficient memory management is obligatory.

Table 3.1: Number of arrays required to represent different components of the computational model.

Wave function	1
Electric potential	1
Computation of first order derivatives	2
Computation of laplacian (second order derivatives)	1
Magnetic vector potential and derivatives	up to 5
Temporary arrays for Chebyshev method	2

## 3.2 Computation of Chebyshev polynomials

The Chebyshev polynomials are easily computed using the recurrence relation Equations 2.33-2.35, which can be simplified as

$$\phi_{n+1}(\eta) = 2x\phi_n(\eta) + \phi_{n-1}(\eta) \quad (3.1)$$

$$\phi_1(\eta) = \eta \quad (3.2)$$

$$\phi_0(\eta) = 1. \quad (3.3)$$

A simple approach would be to use 3 arrays, one for each  $\phi_{n+1}(\eta)$ ,  $\phi_n(\eta)$  and  $\phi_{n-1}(\eta)$ , then roll the arrays and compute  $\phi_{n+1}(\eta)$  using the new values. At each iteration, the  $\phi_{n+1}(\eta)$  can be added to a total sum  $\sum_{i=1,n} a_i \phi_i$ , thus building the Chebyshev expansion as required by Equation 2.31. This process requires 3 arrays along with 10 arrays to define

the wave function and potential. The computational steps are:

$$\begin{aligned}
 \text{Step 1} \quad & 2\eta\phi_n(\eta) + \phi_{n-1}(\eta) \longrightarrow \phi_{n+1}(\eta) \\
 \text{Step 2} \quad & \sum_{i=1}^n a_i\phi_i(\eta) + a_{n+1}\phi_{n+1}(\eta) \longrightarrow \sum_{i=1}^{n+1} a_i\phi_i \\
 \text{Step 3} \quad & \phi_n(\eta) \longrightarrow \phi_{n-1}(\eta) \\
 \text{Step 4} \quad & \phi_{n+1}(\eta) \longrightarrow \phi_n(\eta) \\
 \text{Step 5} \quad & \text{Exit if finished, otherwise go to Step 1.}
 \end{aligned} \tag{3.4}$$

A more memory efficient method would be to do away with the  $\phi_{n+1}(\eta)$ . That is

$$\begin{aligned}
 \text{Step 1} \quad & \sum_{i=1}^n a_i\phi_i(\eta) + a_{n+1}(2\eta\phi_n(\eta) + \phi_{n-1}(\eta)) \longrightarrow \sum_{i=1}^{n+1} a_i\phi_i(\eta) \\
 \text{Step 2} \quad & \phi_n(\eta) \longrightarrow \phi_{n-1}(\eta) \\
 \text{Step 3} \quad & 2\eta\phi_n(\eta) + \phi_{n-1}(\eta) \longrightarrow \phi_n(\eta) \\
 \text{Step 4} \quad & \text{Exit if finished, otherwise go to Step 1.}
 \end{aligned} \tag{3.5}$$

However, this method results in the quantity  $2\eta\phi_n(\eta) + \phi_{n-1}(\eta)$  being computed twice, increasing computational time. The best method is to roll two iterations into one thus reducing both memory and computational time

$$\begin{aligned}
 \text{Step 1} \quad & 2\eta\phi_n(\eta) + \phi_{n-1}(\eta) \longrightarrow \phi_{n-1}(\eta) \\
 \text{Step 2} \quad & \sum_{i=1}^n a_i\phi_i(\eta) + a_{n+1}\phi_{n-1}(\eta) \longrightarrow \sum_{i=1}^{n+1} a_i\phi_i(\eta) \\
 \text{Step 3} \quad & 2\eta\phi_{n-1}(\eta) + \phi_n(\eta) \longrightarrow \phi_n(\eta) \\
 \text{Step 4} \quad & \sum_{i=1}^{n+1} a_i\phi_i(\eta) + a_{n+2}\phi_n(\eta) \longrightarrow \sum_{i=1}^{n+2} a_i\phi_i(\eta) \\
 \text{Step 5} \quad & \text{Exit if finished, otherwise go to Step 1,}
 \end{aligned} \tag{3.6}$$

which does away with the  $\phi_{n+1}(\eta)$  term and does not significantly increase computational time.

### 3.3 Computation of derivatives

The use of Fast Fourier Transforms (FFT) to compute derivatives has many computational advantages. Most platforms have a highly optimised FFT package with versions optimised for scalar, vector, parallel and massively parallel code. These packages are, in general, readily available. Since the computational model relies heavily on FFT's, the code should always perform well on any platform with an optimised FFT package.

Table 3.2: Allowed values for the array size  $N \leq 2000$  as described in Equation 3.7.

1, 2, 3, 4, 5, 6, 7, 8, 9, 10, 11, 12, 14, 15, 16, 18, 20, 21, 22, 24, 25, 27, 28, 30, 32, 33,
35, 36, 40, 42, 44, 45, 48, 49, 50, 54, 55, 56, 60, 63, 64, 66, 70, 72, 75, 77, 80, 81, 84,
88, 90, 96, 98, 99, 100, 105, 108, 110, 112, 120, 125, 126, 128, 132, 135, 140, 144,
147, 150, 154, 160, 162, 165, 168, 175, 176, 180, 189, 192, 196, 198, 200, 210, 216,
220, 224, 225, 231, 240, 243, 245, 250, 252, 256, 264, 270, 275, 280, 288, 294, 297,
300, 308, 315, 320, 324, 330, 336, 343, 350, 352, 360, 375, 378, 384, 385, 392, 396,
400, 405, 420, 432, 440, 441, 448, 450, 462, 480, 486, 490, 495, 500, 504, 512, 525,
528, 539, 540, 550, 560, 567, 576, 588, 594, 600, 616, 625, 630, 640, 648, 660, 672,
675, 686, 693, 700, 704, 720, 729, 735, 750, 756, 768, 770, 784, 792, 800, 810, 825,
840, 864, 875, 880, 882, 891, 896, 900, 924, 945, 960, 972, 980, 990, 1000, 1008,
1024, 1029, 1050, 1056, 1078, 1080, 1100, 1120, 1125, 1134, 1152, 1155, 1176,
1188, 1200, 1215, 1225, 1232, 1250, 1260, 1280, 1296, 1320, 1323, 1344, 1350,
1372, 1375, 1386, 1400, 1408, 1440, 1458, 1470, 1485, 1500, 1512, 1536, 1540,
1568, 1575, 1584, 1600, 1617, 1620, 1650, 1680, 1701, 1715, 1728, 1750, 1760,
1764, 1782, 1792, 1800, 1848, 1875, 1890, 1920, 1925, 1944, 1960, 1980, 2000

Most FFT packages are optimised for arrays of certain size. Compaq's Extended Math Library (for the Alpha platform) runs extremely fast for arrays with size close to a power of 2. However, if the array size is a large power of 2, say 1024, then cache thrashing can result. After much bench marking and performance testing, the package used in this work is the *FFTW* (Fastest Fourier Transform in the West) package developed at MIT by Matteo Frigo and Steven G. Johnson (Frigo & Johnson 1997, Frigo & Johnson 1998, Frigo 1999). This package has been carefully designed to compile in an optimised way on almost any scalar or parallel computer regardless of the compiler or architecture. It is versatile and performs well for almost any array size. The best performance can be obtained if the array size is of the form

$$N = 2^a \times 3^b \times 5^c \times 7^d \times 11^0 \text{ or } 1 , \quad (3.7)$$

for integers  $a, b, c$  and  $d$ . Table 3.2 contains a list of all allowed array sizes for  $N \leq 2000$ . For arrays sizes not of this form, the performance can be greatly reduced (by up to a factor of 100).

Equation 3.7 provides a large range of possible array sizes compared to  $2^n$  (required by

many other optimised packages) allowing for reduced memory usage and computational time. Consider a model which requires 1500 grid points. This would have to be rounded up to 2048 grid points to ensure computational accuracy (if a standard FFT package is used), leading to a substantial increase in memory and computational time. However, using FFTW this grid size is acceptable, requiring no extra memory or computational time.

Once the Fourier transform of the wave function has been computed, it needs to be multiplied by the momentum ( $-p_x^2 - p_y^2$ ), as indicated by Equations 2.37- 2.39. This term can be calculated once and stored in array form for further use, reducing computation time at the expense of memory.

### 3.3.1 What FFTW computes

FFTW computes an “in-order” un-normalised Fourier transform, which greatly increases its speed. This means that the momentum states are stored in an array with positive momentum first, followed by the negative momentum states. Care must be taken to ensure that any factors which multiply a transformed function are in the same format. This usually involves rotating the array by an amount  $n/2$ , where  $n$  is the size of the dimension.

The correct forward and reverse Fourier transforms are given by

$$\Psi(p_{x,a}, p_{y,b}) = \frac{1}{\sqrt{n_x n_y}} \sum_{i,j=0}^{n_x-1, n_y-1} \psi(x_i, x_j) \exp\left(-2\pi i \frac{p_{x,a} x_i}{n_x} - 2\pi i \frac{p_{y,b} y_i}{n_y}\right) \quad (3.8)$$

$$\psi(x_a, y_b) = \frac{1}{\sqrt{n_x n_y}} \sum_{i,j=0}^{n_x-1, n_y-1} \Psi(p_{x,i}, p_{y,j}) \exp\left(2\pi i \frac{p_{x,i} x_a}{n_x} + 2\pi i \frac{p_{y,j} y_b}{n_y}\right), \quad (3.9)$$

for  $a = -n_x/2, \dots, 0, \dots, n_x/2$  and  $b = -n_y/2, \dots, 0, \dots, n_y/2$ . Whereas, FFTW computes

$$\Psi(p_{x,a}, p_{y,b}) = \sum_{i,j=0}^{n_x-1, n_y-1} \psi(x_i, x_j) \exp\left(-2\pi i \frac{p_{x,a} x_i}{n_x} - 2\pi i \frac{p_{y,b} y_i}{n_y}\right), \quad (3.10)$$

for  $a = -1, \dots, -n_x/2, 0, \dots, n_x/2$  and  $b = -1, \dots, -n_y/2, 0, \dots, n_y/2$  and

$$\psi(x_a, y_b) = \sum_{i,j=0}^{n_x-1, n_y-1} \Psi(p_{x,i}, p_{y,j}) \exp\left(2\pi i \frac{p_{x,i} x_a}{n_x} + 2\pi i \frac{p_{y,j} y_b}{n_y}\right), \quad (3.11)$$

for  $a = -n_x/2, \dots, 0, \dots, n_x/2$  and  $b = -n_y/2, \dots, 0, \dots, n_y/2$ .

The forward and reverse transforms, as computed by FFTW, are required to be divided by  $\sqrt{n_x n_y}$  to maintain normalisation.

### 3.3.2 Parallel algorithm

An efficient implementation of the Chebyshev propagation scheme allows complicated system to be studied to a high degree of accuracy. However, for large enough problems the computational and memory resource requirements eventually exhaust those available on a single computer. To overcome this, use was made of the “Message Passing Interface” (MPI) to utilise the processing power and memory of many computers in a tightly coupled cluster.

The Fourier transform package FFTW has a parallel implementation easing the move to multiple processors (CPU’s). To use FFTW in this fashion, the arrays representing the potential (electrostatic and magnetic), wave function and the associated temporary variables are slab decomposed, with each portion distributed to a processor. That is, an array  $A$  of size  $N_x \times N_y$  would be distributed across  $n$  processors as follows

$$\begin{aligned} A\left(1 \rightarrow N_x, 1 \rightarrow \frac{N_y}{n}\right) &\longrightarrow \text{processor 1,} \\ A\left(1 \rightarrow N_x, (i-1)\frac{N_y}{n} + 1 \rightarrow i\frac{N_y}{n}\right) &\longrightarrow \text{processor } i, \\ A\left(1 \rightarrow N_x, (n-1)\frac{N_y}{n} + 1 \rightarrow N_y\right) &\longrightarrow \text{processor } n. \end{aligned} \quad (3.12)$$

Each process then reads in the input file describing the initial conditions and spatial information and initialise their respective slab of the distributed array. When information needs to be shared (say in computing the norm of the wave function, which requires a global sum) or swapped between processes (applying the recursive average smoothing Section 3.6.2, which requires the swapping of slab boundaries), the appropriate MPI call is made ensuring total distributed array is consistent and the computation proceeds correctly.

The success of this decomposition and algorithm relies on the minimal communication required to compute the Hamiltonian. That is, apart from the Fourier transforms, all the other numerical operations are completely local to the processor. Consequently, many

operations are performed between periods of high communication (where every process needs to communicate with every other process - all to all style communication).

### Scaling of the parallel algorithm

All the results using the parallel code were obtained using the Australian Partnership for Advanced Computing National Facility (APAC NF). The APAC Compaq SC has 127 ES45's (508 processors) with 1 Ghz chips (total peak speed of 1016 Gflops), each with at least 4 Gbytes of memory. Nodes are interconnected by a fat-tree low latency ( $4 \mu s$ ), high bandwidth ( $170 MB/s$ ) Quadrics switch.

The low latency, high bandwidth switch enables the parallel program to scale close to linearly with the number of CPU's, as shown in Figure 3.2. For up to four CPU's the messages are passed via shared memory segments, which are significantly faster than passing message via the network. A drop in performance is seen once the messages start transferring via the network, however from 8 to 32 CPU's the performance again scales linearly.

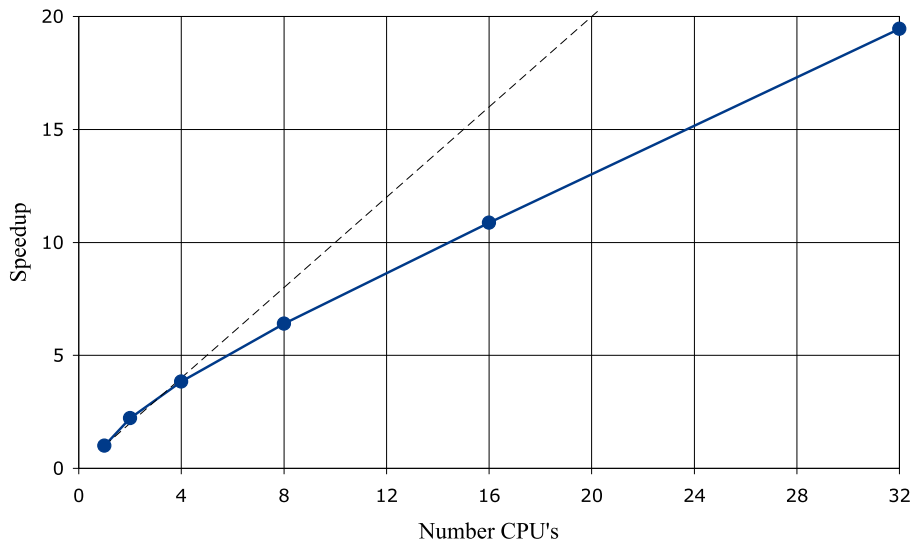


Figure 3.2: Parallel scaling of computational program as the number of CPU's is increased. The near linear scaling allows large calculations to be performed in a reasonable time. The grid size was 2048 square for all calculations, with both an electronic and magnetic potential. Single CPU memory requirements were approximately  $1400 MB$ , which increased to approximately  $2000 MB$  for the 32 CPU case.

## 3.4 Initial wave functions

The model developed in this thesis has little dependence on the shape or momentum spread of the initial wave function. As long as the initial wave function is localised, and an appropriate sized numerical grid is chosen, it can be propagated forward in time through an arbitrary potential.

The choice of initial wave function depends on the physical situation under study. Often, a simple Gaussian was sufficient. A wave packet with a Fermi distribution was also used for some calculations. The Fermi distributions dependence on temperature allows a wave packet to be constructed which closely represents the conduction electrons in physical devices, where the energy spread of the electrons is dependent on temperature.

### 3.4.1 Gaussian wave packet

For the majority of the calculations a Gaussian wave packet was used

$$\psi(x, y, 0) = \exp\left(-\frac{(x - x_0)^2}{2w_x^2} - \frac{(y - y_0)^2}{2w_y^2} + \frac{i}{\hbar}(p_x - p_0)(x - x_0) + \frac{i}{\hbar}p_y(y - y_0)\right), \quad (3.13)$$

where  $w_x$  and  $w_y$  are the half height maximum width of the wave packet,  $x_0$  and  $y_0$  are the initial starting position of the wave packet and  $p_0$  is the initial momentum in the  $x$  direction, see Figure 3.3.

The Gaussian has the unique property that it remains a Gaussian when propagated in free space and its momentum space representation is also a Gaussian. Also, many analytical solutions are known for Gaussians, allowing direct comparison to known solutions to be made. More importantly, it is a reasonable representation of a localised electron with certain energy and energy spread.

### 3.4.2 Fermi wave packet

For some calculations, a wave packet with a Fermi distribution of energy was required. This was constructed by computing the amplitude of the wave packet in momentum space

$$\Psi(p_x, p_y) = \frac{1}{\exp\left(\frac{p_x^2 + p_y^2}{2mkT} - \frac{E_{Fermi}}{kT}\right) + 1}, \quad (3.14)$$

where  $T$  is the temperature of the device,  $k$  is the Boltzmann constant and  $E_{Fermi}$  is the Fermi energy, see Figure 3.4.

To obtain the real space wave function, a Fourier transform is applied

$$\psi(x, y) = \int \Psi(p_x, p_y) \exp(-i p_x x - i p_y y) dp_x dp_y. \quad (3.15)$$

From Equation 3.14, it can be seen that a wave function with a Fermi distribution of energy is approximately bounded by a Gaussian with width

$$w = \sqrt{\frac{\hbar^2}{kmT}}. \quad (3.16)$$

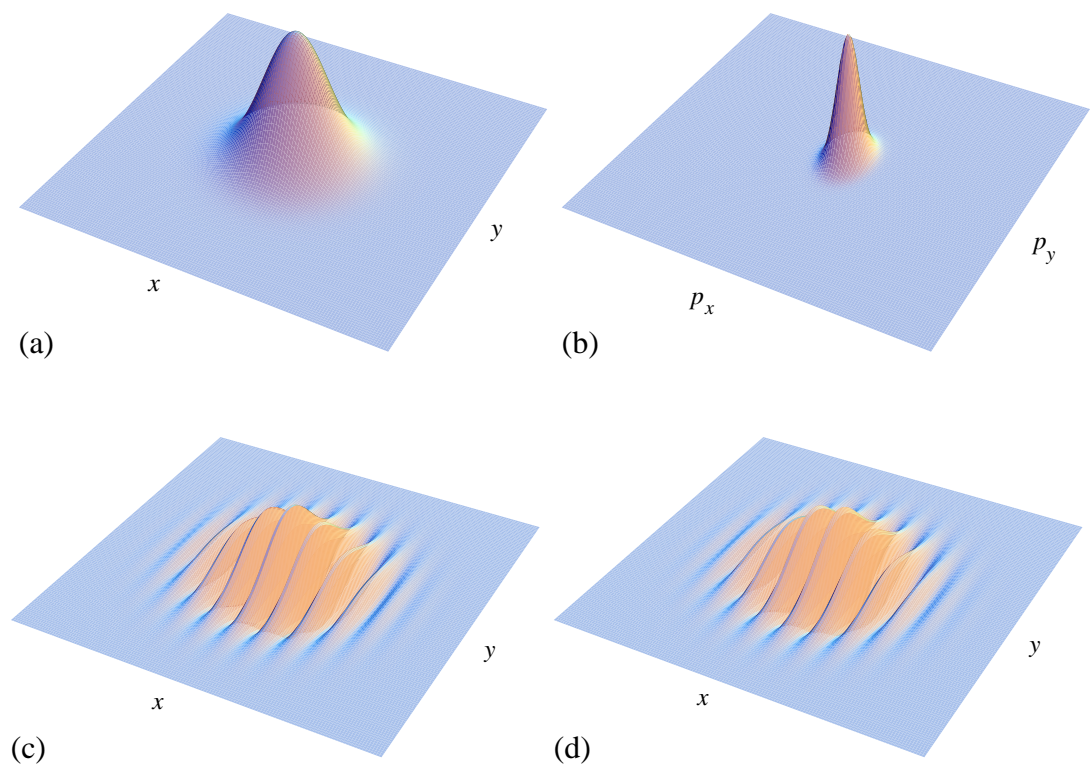


Figure 3.3: Typical initial wave function: (a)  $|\Psi(x,y)|^2$  in real space; (b)  $|\Psi(p_x,p_y)|^2$  in momentum space; (c) real component; (d) imaginary component of  $\Psi(x,y)$ .

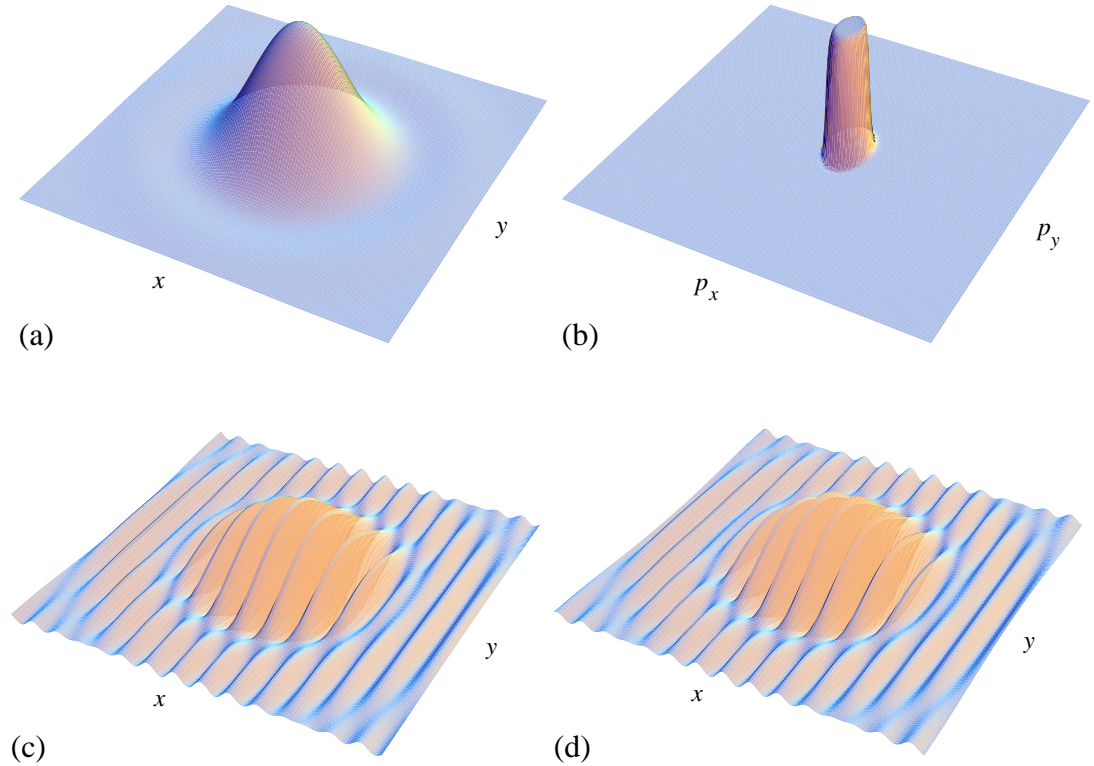


Figure 3.4: Wave function with a Fermi distribution for  $T = 32 \text{ K}$ : (a)  $|\psi(x,y)|^2$  in real space; (b)  $|\Psi(p_x,p_y)|^2$  in momentum space; (c) real component; (d) imaginary component of  $\psi(x,y)$ . Note, that the top of the momentum space wave function (b) is flat, due to the Fermi energy cut-off  $E_{Fermi}$  in Equation 3.14

## 3.5 Optimisation of the code

Numerically solving the time dependent Schrödinger equation often requires large numerical grids to represent the system Hamiltonian and the dynamics of its wave function. This can be prohibitively expensive in terms of memory and computational time. Several computational techniques can be used to reduce the effective propagation space size, which reduces the number of grid points required to represent the wave function and potentials. The effect on computation is two fold: the total memory required for computation is reduced; and the time to perform Fourier transforms and other such calculations is decreased. The following ideas work when the external potentials are localised, i.e. they are applied only to a small region.

One of the ideas is to split the wave function into an interaction part in the vicinity of the potential and a free space part, away from the potential. The wave function in the interaction region needs to be propagated using the full Hamiltonian, while the free space wave function can be propagated trivially over the larger grid using the free space propagator. Another idea is to remove those components of the wave function which have left the interaction region and are going to propagate further as free waves. By doing so, one can explore the time evolution of the slower components of the wave function still under the influence of the interaction potentials, without the complication arising from the reflection or wrap-around of the faster components at the grid boundaries. These techniques are described below in detail.

### 3.5.1 Propagation of free waves

For an electron propagating in free space, there is no need to use the Chebyshev propagation scheme. A far simpler propagation method exists.

With no external potential  $\mathcal{V}$ , the Hamiltonian becomes

$$\mathcal{H} = -\frac{\hbar^2}{2m} \left( \frac{\partial^2}{\partial x^2} + \frac{\partial^2}{\partial y^2} \right) \psi(x, y, t) \quad (3.17)$$

with solution

$$\psi(x, y, t + \Delta t) = \exp\left(i \frac{\hbar^2}{2m} \nabla^2 \Delta t\right) \psi(x, y, t). \quad (3.18)$$

In momentum space

$$\exp\left(i \frac{\hbar^2}{2m} \nabla^2 \Delta t\right) = \exp\left(i \frac{\hbar^2}{2m} (-p_x^2 - p_y^2) \Delta t\right), \quad (3.19)$$

thus we have

$$\psi(x, y, t + \Delta t) = \int \exp\left(i \frac{\hbar^2}{2m} (-p_x^2 - p_y^2) \Delta t\right) \Psi(p_x, p_y, t) \exp(ip_x x + ip_y y) dp_x dp_y \quad (3.20)$$

where  $\Psi(p_x, p_y, t)$  is the Fourier transform of  $\psi(x, y, t)$ , namely the momentum space wave function.

By multiplying  $\Psi(p_x, p_y, t)$  by  $\exp\left(i \frac{\hbar^2}{2m} (-p_x^2 - p_y^2) \Delta t\right)$  and taking the inverse Fourier transform, the fully propagated wave function in free space is computed for an arbitrary initial wave function. This method is comparable to the Green's Function method for a single particle (see Section 2.6.4).

### 3.5.2 Wave function splitting algorithm

One method to reduce the computational and memory overhead is to use the linearity of the Hamiltonian and split it into multiple parts as depicted in Figure 3.5. The first section is where the potential is zero, the second is where the potential is non-zero and the third is where it is zero again. Where the potential is zero, the wave function is propagated as a free wave using Equation 3.20, which can be calculated extremely quickly. Where the potential is non-zero, the Chebyshev scheme can be used, but this is operating on a much reduced grid leading to vast memory and speed improvements.

As depicted in Figure 3.5, the shaded regions (where the function  $S$  is in transition from 0 to 1) represent an overlap region. By overlapping the Chebyshev propagation grid with the free space propagation grid, the wave function is able to transition from one numerical grid to another. If the overlap between the two numerical grids is sufficiently large (large enough such that the fastest momentum component can not propagate through the overlap region in a single time step) then this method introduces little numerical error.

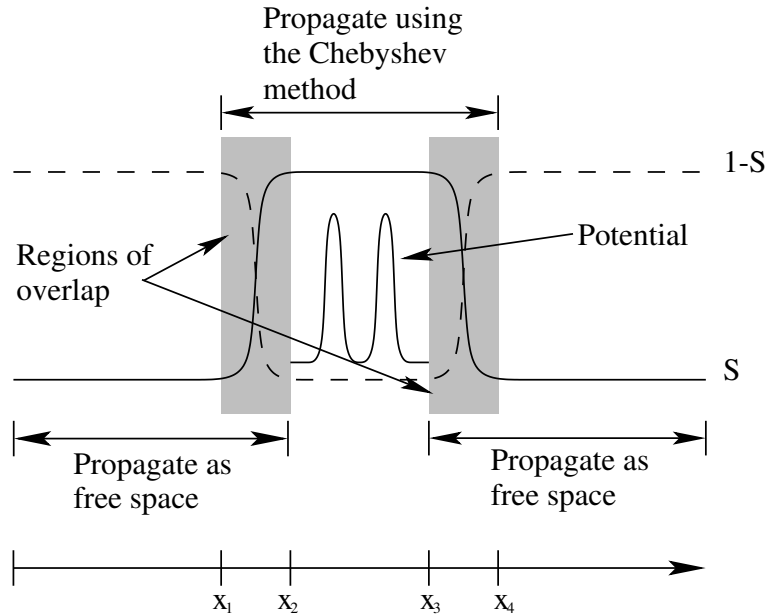


Figure 3.5: By using a function  $S$  the real space can be split into 3 regions as depicted.

Consider a function  $S(x)$  such that

$$S(x) = \begin{cases} 0 & \text{for } x < x_1, \text{ where } \mathcal{V}(x) = 0 \\ f(x) & \text{for } x_1 \leq x \leq x_2, f(x_1) = 1 \text{ and } f(x_2) = 0, \text{ defining the overlap region} \\ 1 & \text{for } x_2 < x < x_3, \text{ where } \mathcal{V}(x) > 0 \\ g(x) & \text{for } x_3 \leq x \leq x_4, g(x_3) = 1 \text{ and } g(x_4) = 0, \text{ defining the overlap region} \\ 0 & \text{for } x_4 < x, \text{ where } \mathcal{V}(x) = 0 \text{ again,} \end{cases} \quad (3.21)$$

where  $\mathcal{V}(x)$  is the system potential and the functions  $f(x)$  and  $g(x)$  vary smoothly from 0 to 1. The solution to the system Hamiltonian can be written as

$$\psi(x, t) = \exp\left(-\frac{i}{\hbar}\mathcal{H}t\right) [S(x)\psi(x, 0) - (S(x) - 1)\psi(x, 0)] \quad (3.22)$$

and the  $-\exp\left(-\frac{i}{\hbar}\mathcal{H}t\right)(S(x) - 1)\psi(x, 0)$  component is propagated using a free wave equation and the  $\exp\left(-\frac{i}{\hbar}\mathcal{H}t\right)S(x)\psi(x, 0)$  component is propagated using the Chebyshev scheme.

This method is particularly useful when a “long time” solution is required, demanding a large space to contain the fast components of the wave function. Most of this space is free of external potentials.

### 3.5.3 Complex potential

Methods used to remove the fast components of the wave function outside the interaction region have varied from using lines of no return, complex optical potentials in the Hamiltonian, and split operator Hamiltonian (Balakrishnan et al. 1997). The most attractive of these is the complex absorbing potential, which absorbs the wave function components just before they reach the grid boundaries (Child 1991). The complex potential is easy to implement, requires little extra computation power, and has been found to be very effective at absorbing the wave packet (Neuhauser & Baer 1990).

The main drawback of the complex potential is that the final wave function cannot be reconstructed. In other words, the absorbed components are effectively lost. It also produces artificial reflections, however these can be minimised due to the freedom in the design of complex potentials. Various schemes have been proposed, which vary the shape of the absorbing potential and adjust the slope and depth to reduce reflection while maximising the absorption (Seideman & Miller 1991, Vibók & Balint-Kurt 1992, Macias et al. 1994, Riss & Meyer 1995).

The introduction of a complex potential modifies the Schrödinger equation

$$i\hbar \frac{\partial \psi(\mathbf{r}, t)}{\partial t} = (\mathcal{H} - i\mathcal{U})\psi(\mathbf{r}, t) \quad (3.23)$$

and the solution

$$\psi(\mathbf{r}, t) = \exp\left(-\frac{i}{\hbar}\mathcal{H}t - \frac{1}{\hbar}\mathcal{U}t\right)\psi(\mathbf{r}, 0). \quad (3.24)$$

This is no longer a true Schrödinger equation, but if applied correctly, the complex potential  $\mathcal{U}$  only absorbs the wave function incident on it without affecting the wave function at other regions. Following is a discussion of how the complex potential works and then a limit is established for the maximum workable time step.

Using the *Baker-Campbell-Hausdorff* formula (Normand 1980)

$$\exp(A + B) = \exp(A)\exp(B)\exp\left(-\frac{1}{2}[A, B] + \frac{1}{6}[A, [A, B]] - \frac{1}{3}[B, [B, A]] + \dots\right), \quad (3.25)$$

one can expand Equation 3.24 as

$$\psi(\mathbf{r}, t) = \exp\left(-\frac{i}{\hbar}\mathcal{H}t\right)\exp\left(-\frac{1}{\hbar}\mathcal{U}t\right)\exp\left(-\frac{i}{2\hbar^2}[\mathcal{H}, \mathcal{U}]t^2 + \frac{1}{6\hbar^3}[\mathcal{H}, [\mathcal{H}, \mathcal{U}]]t^3\right)$$

$$+ \frac{i}{3\hbar^3} [\mathcal{U}, [\mathcal{U}, \mathcal{H}]] t^3 \dots \Big) \psi(\mathbf{r}, 0). \quad (3.26)$$

Since the interaction potential  $\mathcal{V}$  and the complex absorbing potential  $\mathcal{U}$  are defined non-zero in different regions, they can be considered separately. Now consider the non-interaction region where the complex potential  $\mathcal{U}$  is non-zero while  $\mathcal{V} = 0$ , we have

$$\begin{aligned} \psi(\mathbf{r}, t) &= \exp\left(-\frac{i}{\hbar} \mathcal{H}t\right) \exp\left(-\frac{1}{\hbar} \mathcal{U}t\right) \exp\left(-\frac{i}{4m} [\nabla^2, \mathcal{U}] t^2 + \frac{\hbar}{24m^2} [\nabla^2, [\nabla^2, \mathcal{U}]] t^3 \right. \\ &\quad \left. + \frac{i}{6m\hbar} [\mathcal{U}, [\mathcal{U}, \nabla^2]] t^3 \dots \right) \psi(\mathbf{r}, 0). \end{aligned} \quad (3.27)$$

For convenience, the following analysis is carried out using a linear ramp in the  $x$  direction as the complex potential defined by,

$$\mathcal{U}(x, y) = \begin{cases} ax + b & x > -b \\ 0 & \text{otherwise,} \end{cases} \quad (3.28)$$

where  $b$  is the starting point and  $a$  is the slope of the complex potential. In this case the commutator relations in Equation 3.27 are, for any arbitrary function  $\psi$ ,

$$[\nabla^2, x]\psi = 2\partial_x\psi, \quad (3.29)$$

$$[x, [x, \nabla^2]]\psi = -2[x, \partial_x]\psi = 2\psi, \quad (3.30)$$

$$[\nabla^2, [\nabla^2, x]]\psi = 2[\nabla^2, \partial_x]\psi = 0. \quad (3.31)$$

The higher order commutators in the expansion are zero as only constants, which commute with each other, are present. Equation 3.27 then becomes

$$\psi(\mathbf{r}, t) = \exp\left(-\frac{i}{\hbar} \mathcal{H}t\right) \exp\left(-\frac{1}{\hbar} (ax + b)t\right) \exp\left(-\frac{a^2 i}{2m} \partial_x t^2 + \frac{a^2 i}{3m\hbar} t^3\right) \psi(\mathbf{r}, 0). \quad (3.32)$$

Note that  $\exp\left(-\frac{a^2 i}{2m} \partial_x t^2\right)$  is exactly the Taylor expansion of  $\psi(x - \frac{a^2 i}{2m} t^2, y, z, 0)$ , so

$$\psi(\mathbf{r}, t) = \exp\left(-\frac{i}{\hbar} \mathcal{H}t\right) \exp\left(-\frac{1}{\hbar} (ax + b)t\right) \exp\left(\frac{a^2 i}{3m\hbar} t^3\right) \psi\left(x - \frac{a^2 i}{2m} t^2, y, z, 0\right). \quad (3.33)$$

From this equation, the normal propagation operator can be seen  $\exp\left(-\frac{i}{\hbar} \mathcal{H}t\right)$ . The following component  $\exp\left(-\frac{i}{\hbar} (ax + b)t\right)$  encapsulates the absorption of the wave function. For appropriately chosen  $a$  and  $b$  this function obviously decreases the amplitude of the wave function. The  $\exp\left(\frac{a^2 i}{3m\hbar} t^3\right)$  introduces a phase change and finally the wave function is translated  $\psi(x - \frac{a^2 i}{2m} t^2, y, z, 0)$ .

As described, the complex potential is only defined along the boundary of the space, so this absorption only occurs near the boundary. For all areas away from the boundary, the wave function propagates as expected.

According to Child (1991), the depth  $\mathcal{U}_0$  and the width  $\Delta r$  of the linear ramp complex potential should satisfy the following simple relation,

$$\frac{\hbar E}{\Delta r \sqrt{8m}} \ll \mathcal{U}_0 \ll \frac{\Delta r \sqrt{8m} E^{\frac{3}{2}}}{\hbar}, \quad (3.34)$$

where  $E$  is the translation energy and  $m$  is the mass. The slope of the complex potential is given by  $a = \mathcal{U}_0/\Delta r$ . The starting point for the complex potential is normally very close to the boundary. The choice of  $\mathcal{U}_0$  can be made such that

$$\beta \frac{\hbar E}{\Delta r \sqrt{8m}} = \mathcal{U}_0 = \frac{1}{\beta} \frac{\Delta r \sqrt{8m} E^{\frac{3}{2}}}{\hbar} \quad (3.35)$$

provided

$$\beta = \frac{\Delta r \sqrt{8m} E^{1/4}}{\hbar} \ll 1. \quad (3.36)$$

Elimination of  $\beta$  gives

$$\mathcal{U}_0 = E^{5/4}. \quad (3.37)$$

This is convenient as  $\mathcal{U}_0$  is independent of the width of the complex potential  $\Delta r$ , as long as Equation 3.36 is satisfied.

### Computational sensitivity of the complex potential

The complex potential introduces massive errors when naively implemented in the Chebyshev propagation scheme (Tal-Ezer & Kosloff 1984, Wang & Scholz 1998), where arbitrarily large time steps can be used. Previous work with complex potentials involved small time steps and did not experience the massive errors. It was pointed out by Vibók & Balint-Kurt (1992) that the complex potential must act adiabatically, which implies that it must not change by a large amount in any single time step. This is clearly not the case for the Chebyshev propagation scheme.

From the above solution Equation 3.33, it is clear that the wave function  $\psi(\mathbf{r}, t)$  can blow up rapidly if the time step  $t$  is too big. However, if  $t$  is chosen such that

$$\left\| \exp\left(\frac{a^2 i}{3m\hbar} t^3\right) \psi\left(x - \frac{a i}{2m} t^2, y, z, 0\right) \right\| \leq 1 \quad (3.38)$$

over the range of the complex potential, the complex potential would reduce exponentially the magnitude of the wave packet across the complex potential. For simplicity only the  $x$  dimension was considered, since the other dimensions can be included trivially. Assuming that the initial wave function is a Gaussian, i.e.  $\psi(x, 0) = \frac{1}{\sqrt{2\pi w}} \exp\left(\frac{-(x-x_0)^2}{2w^2} + \frac{i}{\hbar} p_x(x-x_0)\right)$ , then

$$\begin{aligned} & \left\| \exp\left(\frac{a^2 i}{3m\hbar} t^3\right) \psi\left(x - \frac{ai}{2m} t^2, 0\right) \right\| \\ &= \frac{1}{\sqrt{2\pi w}} \left\| \exp\left[-2\left(\frac{x - \frac{ai}{2m} t^2 - x_0}{2w}\right)^2 + \frac{i}{\hbar} p_x\left(x - \frac{ai}{2m} t^2 - x_0\right)\right] \right\| \\ &= \frac{1}{\sqrt{2\pi w}} \exp\left[-2\left(\frac{x - x_0}{2w}\right)^2 + \frac{2}{(2w)^2} \frac{a^2}{4m^2} t^4 + p_x \frac{a}{2m\hbar} t^2\right]. \end{aligned} \quad (3.39)$$

Because the time  $t$  can not be complex or negative, the only viable solution to the inequality Equation 3.38 is

$$t \leq \sqrt{\frac{2m}{a} \left( \sqrt{\frac{p_x^2 w^4}{\hbar^2} + 2 \log(\sqrt{2\pi w}) w^2 + (x - x_0)^2} - \frac{p_x w^2}{\hbar} \right)}, \quad (3.40)$$

which sets a limiting value for the maximum time step. If multiple time steps are required to complete a calculation,  $\psi(x, 0)$  would be the wave packet of the previous time step and will generally not be a Gaussian. In other words, its momentum will not be localised around  $p_x$  and its position expectation value will not be  $x_0$ . To overcome this, the above limit on  $t$  can be tightened by (1) substituting  $p_{max}$  for  $p_x$ , where  $p_{max}$  is the maximum momentum that the numerical grid can support, and (2) assuming that the wave packet has already reached the complex potential, i.e.  $x = x_0$ . This provides the smallest limit for  $t$ , i.e.

$$t \leq \sqrt{\frac{2m}{a} \left( \sqrt{\frac{p_{max}^2 w^4}{\hbar^2} + 2 \log(\sqrt{2\pi w}) w^2} - \frac{p_{max} w^2}{\hbar} \right)}, \quad (3.41)$$

that should then work for all cases.

Although this criterion is derived using the linear complex potential given by Equation 3.28, it is found to be applicable to other types of potentials as well, for example, a Gaussian edge and an exponential potential given by

$$i U_0 \left( \exp\left(-\frac{2(x-b)^2}{a^2}\right) - 1 \right) \quad (3.42)$$

and

$$-i \mathcal{U}_0 \exp(1) \exp\left(-\frac{a}{(x-b)^2}\right), \quad (3.43)$$

where  $\mathcal{U}_0$  and  $a$  define the height and the width of the complex potential, and  $b$  is where the potential starts. Figure 3.6 shows the three potentials.

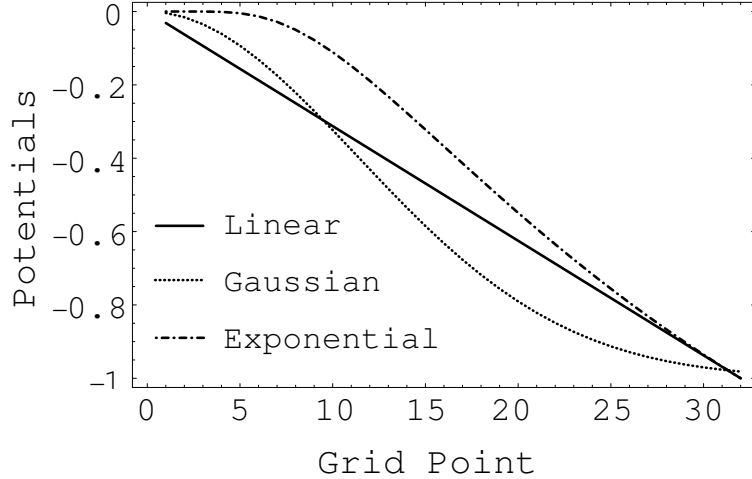


Figure 3.6: Potentials used to absorb the wave function at the boundary of the space

As expected, the maximum time given by Equation 3.40 is dependent on the distance from the complex potential to the initial position of the wave packet. If the complex potential was at infinity, it would have no effect on the local propagation of the wave packet and would then allow arbitrarily long time steps as predicted by Equation 3.40. Note that the maximum time step is not zero even when the wave packet is at the complex potential. This is attractive from a computation point of view, which means that there is always some finite time step that will produce the results required.

### Propagation with a complex potential

As an example of implementing the complex absorbing potential in the Chebyshev scheme, first consider an electron wave packet propagating in free space with exponential complex potential given by Equation 3.43. In this case  $x_0$  and  $p_x$  of the wave packet are well defined at all times and thus we can determine a maximum time step by using Equation 3.40, instead of the tighter limit set by Equation 3.41. The propagation of the electron is shown in Figure 3.7. The initial energy of the wave packet is arbitrarily chosen as  $0.0300a.u..$

The effective mass is taken as  $0.0667a.u.$  for GaAs. The numerical grid in use is found to support a maximum momentum of  $p_{max} = 0.0895a.u.$  The propagation of the wave packet is divided into 9 equally spaced time steps with  $t_{step} = 42.5fs$ , which satisfies the criterion given by Equation 3.40.

Figure 3.7(a-c) shows the wave packet approaching the edge of the grid space and gradually spreading as it travels. When it hits the boundary, the wave packet is absorbed by the complex potential and only a slight reflected wave packet is observed (see Figure 3.7(d-f)). The magnitude of the wave packet before the edge of the space and the reflected wave packet are about  $10^{-6}$  and  $10^{-15}$ , respectively. The reflected wave packet can introduce error into further calculations when it starts to interact with the slower components of the wave packet still in the interaction region. However, since the reflected wave packet is about  $10^9$  times smaller than the incident wave packet, this effect is very small.

Despite the small reflection and high accuracy of the method, it was found that the Chebyshev expansion scheme is very sensitive to the presence of a complex potential. A small change in the time step for each propagation gave rise to very different results as illustrated in Figure 3.8. In this calculation, the propagation of the wave packet was divided into 8 equally spaced time steps with  $t_{step} = 47.8fs$ , which no longer satisfies Equation 3.40. As shown, large errors are introduced by the complex potential placed at the right end of the numerical grid. It is interesting to note that the wave packet appears to propagate with little error in the first few time steps, even when Equation 3.40 is not held. It is not until the wave packet approaches the complex potential that large errors start to enter the calculations. This is supported by the dependence of Equation 3.40 on  $x - x_0$ .

Figure 3.9(a) illustrates how well the system energy  $E_{system} = \int \psi^*(\mathbf{r}, t) \mathcal{H} \psi(\mathbf{r}, t) d\mathbf{r}$  is absorbed by the complex potentials when Equation 3.40 holds. It demonstrates how for the first 5 time steps the system energy is conserved. Then over the following 3 time steps the majority of the energy is absorbed by the complex potential, leaving only the energy of the reflected wave packet. For the linear, Gaussian and exponential potentials, the energy of the reflected wave packet is respectively about  $10^{-6}$ ,  $10^{-8}$  and  $10^{-10}$  times smaller than the initial system energy. This is very close to complete absorption. Among the three complex potentials, the exponential potential given by Equation 3.43 appears to

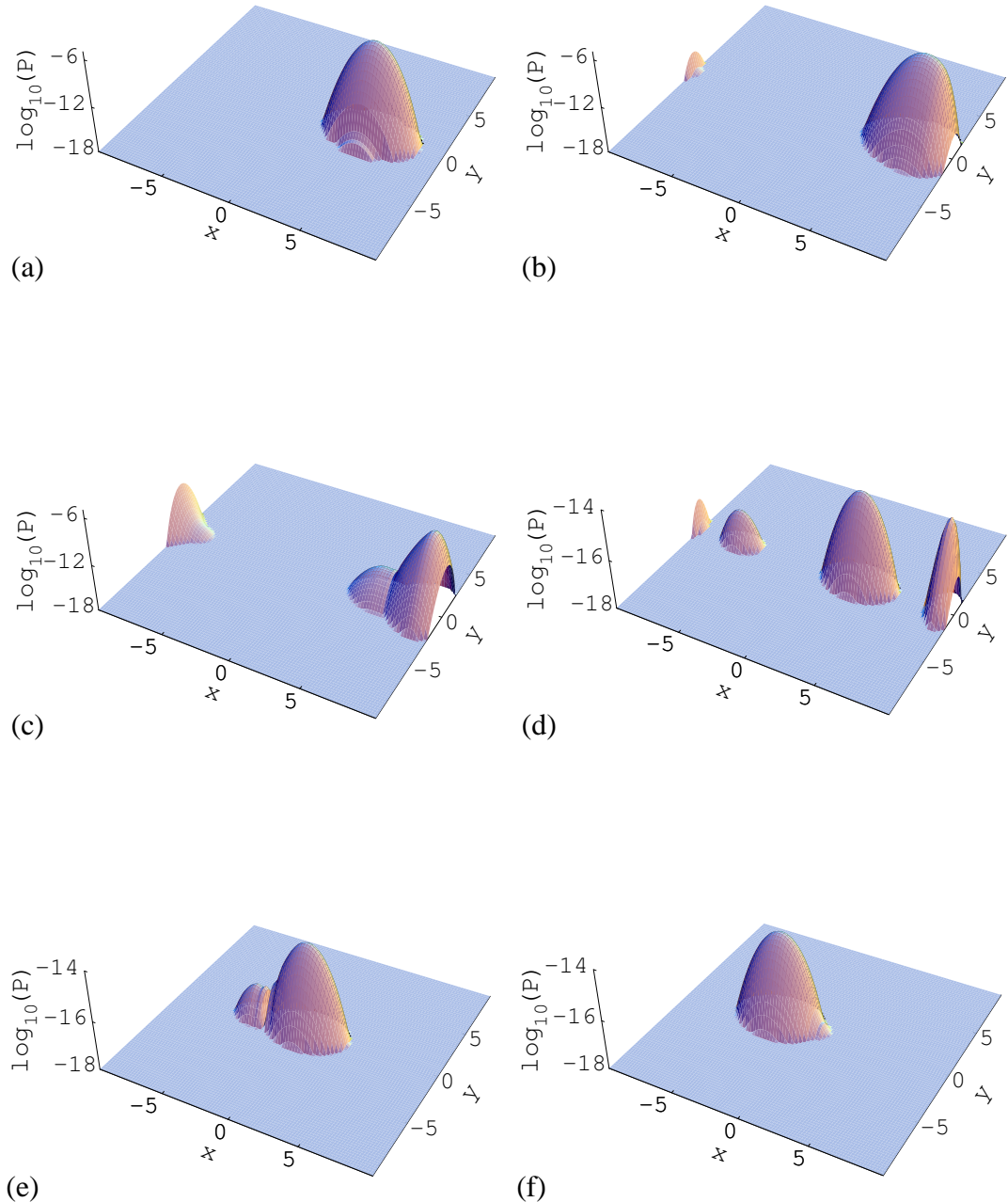


Figure 3.7: Propagation of an electron wave packet in free space with the exponential complex potential at the right end of the grid. The probability function  $P(t) = \psi^*(x,y,t)\psi(x,y,t)$  is plotted in logarithm scale. Flow of time  $t$  is left to right and top to bottom with time step satisfying Equation 3.40. The spatial units ( $x$  and  $y$  axes) are  $\times 1000a.u..$

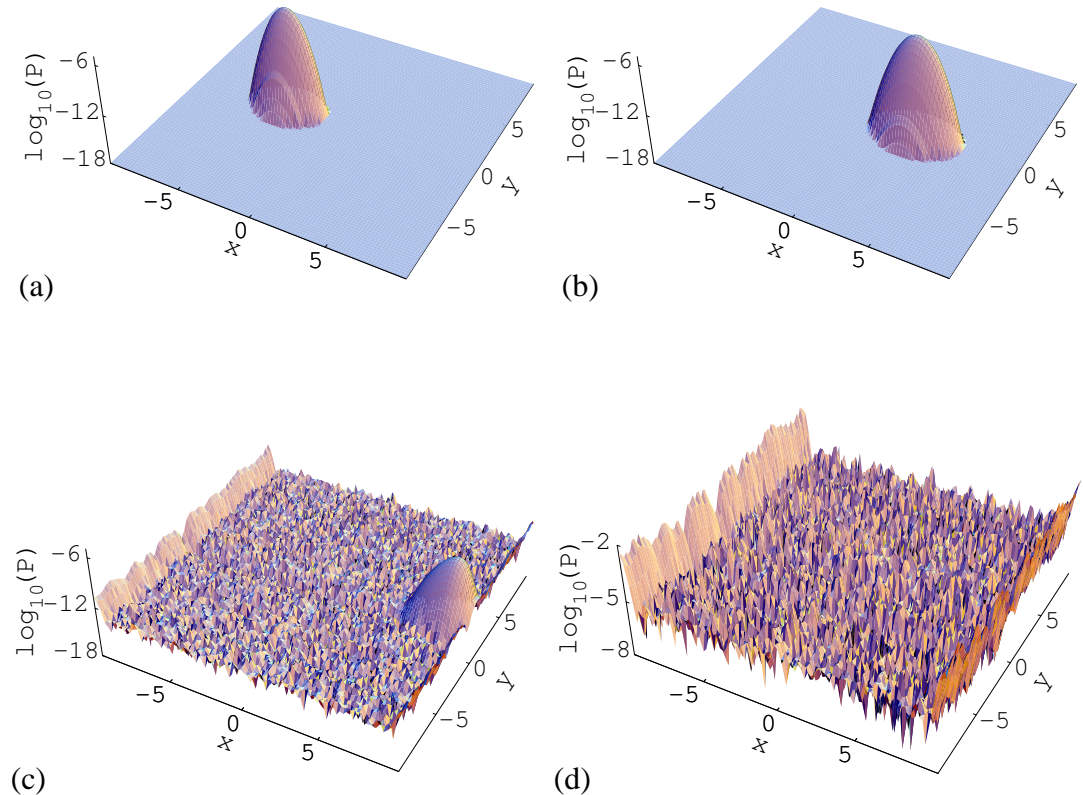


Figure 3.8: Massive errors are introduced by the complex potential when Equation 3.40 no longer holds (same units as Figure 3.7).

cause the least reflection, that is in agreement with Vib  k & Balint-Kurt (1992). However, for all three forms of complex potential, the system energy diverges when the time step is changed from  $42.5\text{fs}$  to  $47.8\text{fs}$ , as shown in Figure 3.9(b). This corresponds to the large errors introduced to the wave packet by the complex potential as shown in Figure 3.8. Alternatively, the norm of the wave function, as a function of time, could be plotted to show the absorption of flux by complex potentials. Almost identical behaviour was observed as that shown in Figure 3.9.

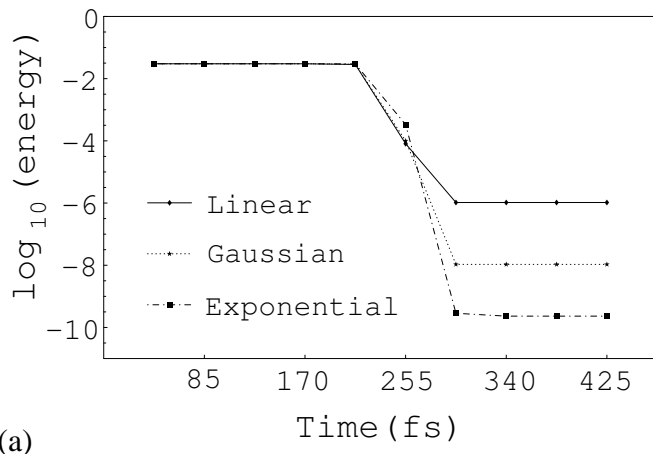
Figure 3.10 illustrates the propagation of an electron wave packet under the influence of a double barrier with complex potentials at both ends of the numerical grid. In this case a smaller grid spacing was adopted which supports a higher maximum momentum  $p_{max} = 0.171a.u..$  Also, since  $x_0$  and  $p_x$  of the wave packet are not well defined under the influence of the barrier potential, the tighter limit set by Equation 3.41 was used,  $t_{max} = 26.5\text{fs}$ . As shown in Figure 3.10, the reflection due to the complex potential does not visibly affect the wave packet propagation in the interaction region.

To quantify the errors introduced by the complex potentials, results shown in Figure 3.10 were compared with that obtained using a much larger numerical grid but without the complex potentials. The absolute errors are plotted in Figure 3.11. As shown, until the wave packet reaches the complex potential, the absolute errors are typically below  $10^{-15}$  (the magnitude of the norm was typically  $10^{-6}$  resulting in an approximately relative error of  $10^{-9}$ ), indicating that the complex boundary does not introduce significant error into the propagation. Once the wave packet reaches the complex potential, a slight reflection occurs giving rise to an error about 3 orders of magnitude smaller than the slower components of the wave packet still under the influence of the interaction potential.

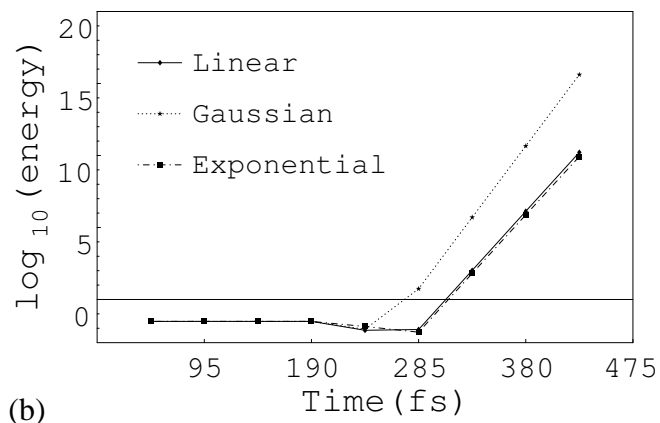
### 3.5.4 Optimal grid spacing and size

For a given potential and initial wave function, an optimal grid spacing can be determined. The Fourier transform method breaks the wave function up into its Fourier components

$$\Psi(x, y) = \int \Psi(p_x, p_y) e^{-ip_x x - ip_y y} dp_x dp_y . \quad (3.44)$$



(a)



(b)

Figure 3.9: (a) Absorption of system energy (a.u.) when Equation 3.40 is satisfied;  
(b) Energy (a.u.) diverges otherwise.

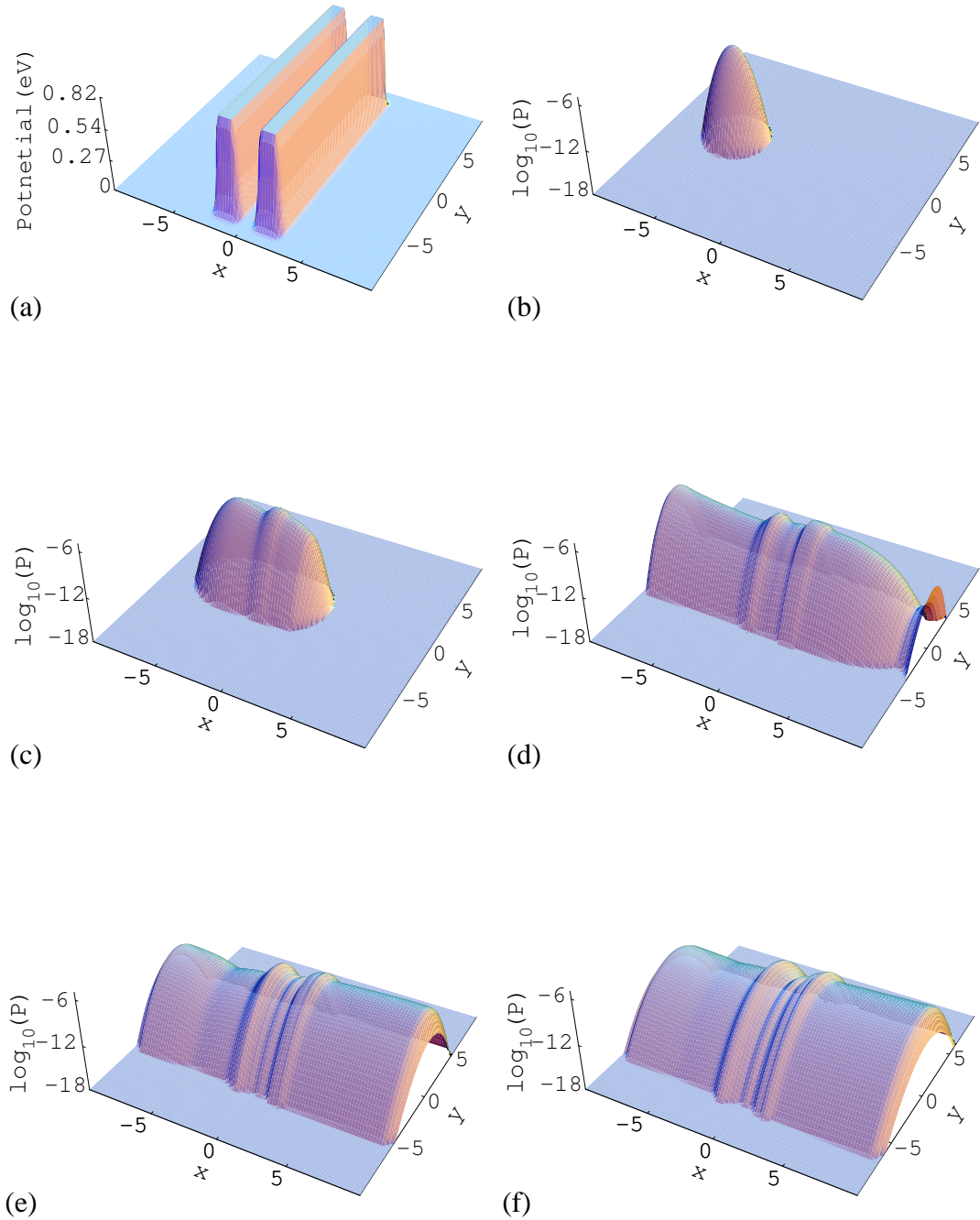


Figure 3.10: Propagation of an electron wave packet under the influence of a double barrier with exponential complex potentials at both end of the grid. Flow of time is left to right and top to bottom with time step satisfying Equation 3.41 (same units as Figure 3.7).

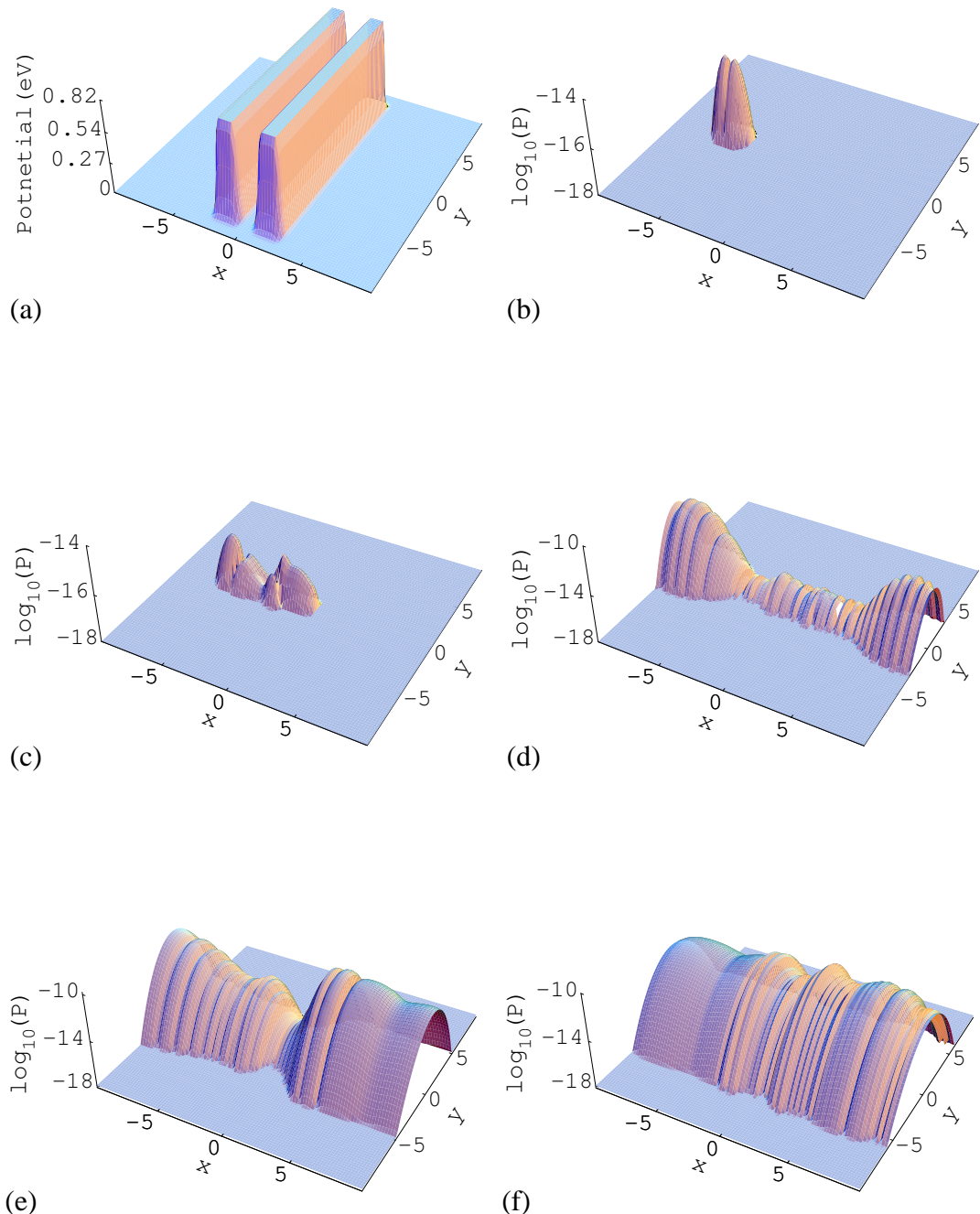


Figure 3.11: Absolute errors between the results shown in Figure 3.10 and the results obtained without the complex potentials but using a larger numerical grid (same units as Figure 3.7).

Each component  $\Psi(p_x)$  has an angular frequency  $\omega = p_x x$ . To accurately represent the momentum  $p_x$  it must be sampled at least twice, which corresponds to a grid spacing of  $x = \pi/p_x$ . For a maximum momentum of  $p_{max}$  a minimum grid spacing is given by  $\Delta x = \pi/p_{max}$ .

The maximum momentum  $p_{max}$  required for the given system can be estimated in the following way. First, the initial wave function, being a wave packet, will have a natural momentum spread. When the amplitude of the momentum packet falls below some small value, ie.  $\Psi(p_x) < \delta$ , the momentum state  $p_x$  will be the maximum momentum state required to represent the wave packet traveling through free space.

Second, if the potential has a negative component (or an external bias), this can be converted to kinetic energy of the wave function, increasing its linear momentum  $p$ . This can be approximated by taking the minimum of the potential  $\mathcal{V}_{min}$  and converting it to a momentum of  $p = \sqrt{2m\mathcal{V}_{min}}$  and adding it to the previous  $p_{max}$ .

Third, various aspects of the potential (eg. magnetic fields and reflecting potentials) can cause the wave packet to change direction, resulting in momentum from the  $x$ - dimension transferring into the  $y$ - dimension and vice-versa. To accommodate this, the maximum momentum in each dimension can be set to the maximum value of the momentum in both dimension.

Finally, to ensure that a large enough maximum momentum is obtained, the value of the maximum momentum can be multiplied by some scaling factor, increasing accuracy at the expense of computation time.

## 3.6 Computation of electronic potentials

The computation of the electronic potentials is based upon the geometric layout defined in the input file. The components making up the potential can consist of entities such as lines, circles, ellipses and polygons, all of which could be filled or open as shown in Figure 3.12. By defining the height of each component of the potential, complex struc-

tures can easily be layed out and studied. The code also has a function interpreter built in, which allows arbitrary potential functions to be defined, for example a parabola  $x^2 + y^2$ . The objects shown in Figure 3.12 are produced with the lines in the input file shown in Table. 3.3.

Table 3.3: Example input file to produce various potential objects as shown in Figure 3.12.

```

# aus = atomic unit for distance
# aue = atomic unit for energy

line                                # object type - line
1                                    # object number
-25000.0*aus -25000.0*aus          # point to start from
-15000.0*aus 1500.0*aus           # point to end at
2000.0*aus                           # width of line
5.0d-3*aue                          # potential energy of object

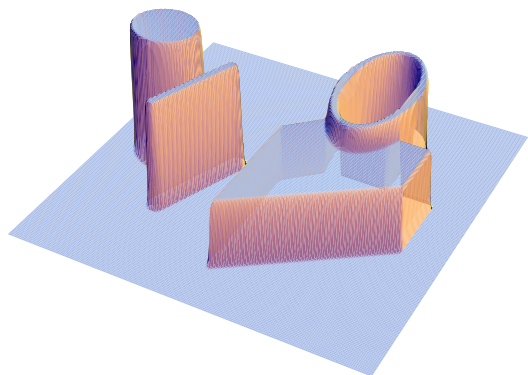
fillpolygon                         # object type - filled polygon
2                                    # object number
3.0d-3*aue                          # potential energy of object
0.0*aus -40000.0*aus                # start polygon point
40000.0*aus -10000.0*aus           # polygon point
40000.0*aus 10000.0*aus            # polygon point
10000.0*aus 10000.0*aus            # polygon point
0.0*aus 0.0*aus                     # polygon point
0.0*aus -40000.0*aus               # end/start polygon point

fillcircle                           # object type - filled circle
3                                    # object number
-35000.0*aus 0.0*aus                # centre point
10000.0*aus                           # radius
6.0d-3*aue                          # potential energy of object

ellipse                             # object type - ellipse
4                                    # object number
20000.0*aus 20000.0*aus             # centre point
20000.0*aus 10000.0*aus             # major and minor axes
2000.0*aus                            # width of line
4.0d-3*aue                          # potential energy of object

```

Once a potential is specified and the numerical array constructed, there are several post processing options available, which control the “smoothing” of the potential. This allows a more accurate model to the real device to be generated. The basic idea is to remove any sharp changes in the potential and make it smooth. Smoothing also increases numerical accuracy, since most numerical methods cannot handle delta-type functions.



(a)



(b)

Figure 3.12: Collection of objects which can be used to construct potentials.

### 3.6.1 Gaussian blur

The boundary between the wire and the walls can be smoothed using a Gaussian curve. This is done to replicate the quadratic nature of the electronic potentials formed in semiconductors. The smoothing operation was implemented by convolving the potential  $V(x,y)$  with a Gaussian function

$$FFT^{-1} \left[ FFT \left[ C \exp \left( -\frac{x^2}{2w_x^2} - \frac{y^2}{2w_y^2} \right) \right] \times FFT [V(x,y)] \right]. \quad (3.45)$$

By varying the width,  $w_x$  and  $w_y$ , of the Gaussian function, potentials with different amounts of smoothing can be generated, see Figure 3.13(a)-(b).

If the potential has extremely sharp discontinuities, the Gaussian blur method introduces considerable error (the FFT of the potential has extremely large high frequency components). The errors often result in a potential that is incorrectly scaled and has a considerable offset to the original potential. To counteract this effect, the potential is smoothed very slightly using a recursive averaging process described below, to remove extremely sharp discontinuities and then smoothed using the Gaussian blur. Figure 3.13 shows an example of a potential before and after the smoothing operation.

### 3.6.2 Recursive averaging

By applying an iterative averaging technique, a smooth potential can be constructed that maintains the overall shape of the original potential. This method does not suffer from the errors that can be introduced by using the Gaussian blur method described above.

Consider a lattice of grid points as shown in Figure 3.14, the new value for the point  $(x_0, y_0)$  is given by

$$\phi(x_0, y_0) = \frac{1}{n+1} \sum_{i=-n}^n \sum_{j=-n}^n \frac{\phi(x_i, y_j)}{\max(1, 8 \times |i|, 8 \times |j|)}, \quad (3.46)$$

where  $n$  defines how many grid points to include in the sum. This function produces a point  $\phi(X_0, y_0)$ , which is an average of the points in successive rings about it. If those points are co-planar, they will remain co-planar after the averaging.

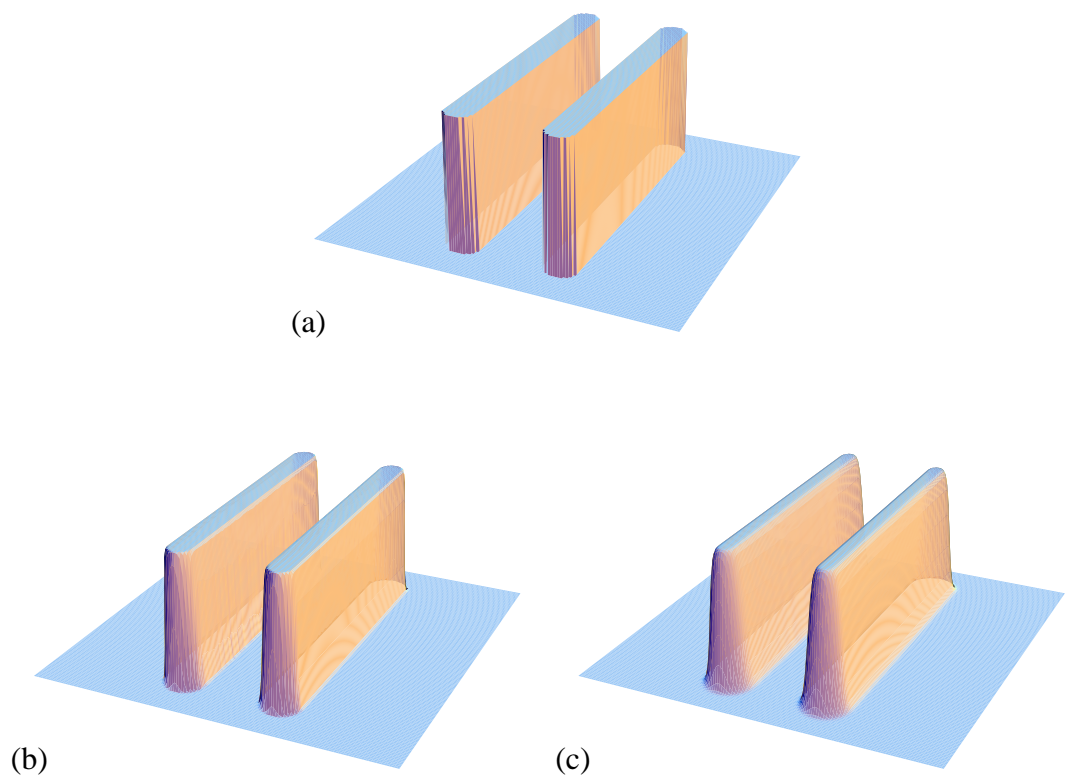


Figure 3.13: (a) Hard-walled potential; (b) Gaussian smoothed soft-walled potential;  
(c) Recursive averaging smoothed soft-walled potential.

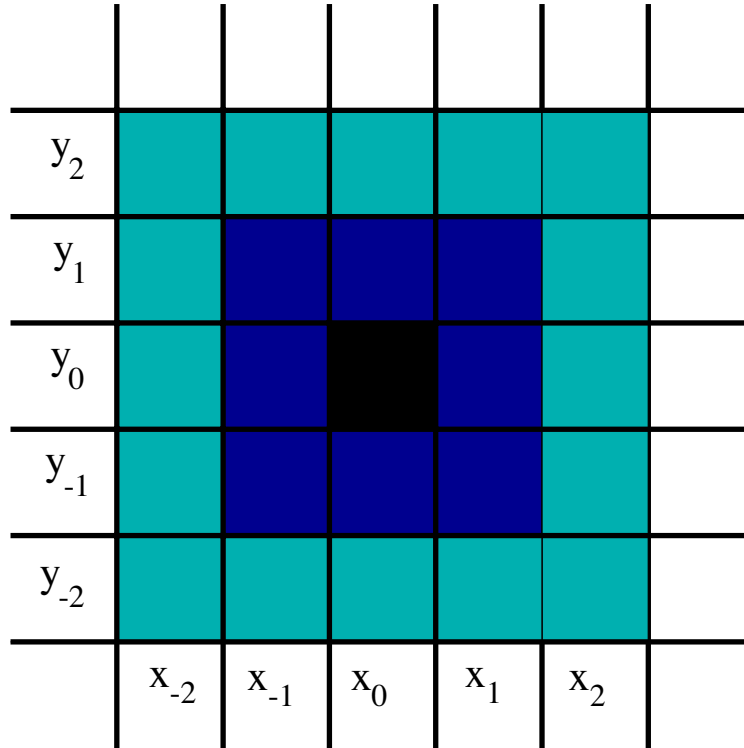


Figure 3.14: Smoothing stencil for the point  $(x_0, y_0)$ , which is averaged by the points about it (weighted by the number of points in the appropriate ring).

For  $n = 2$ , the equation becomes

$$\begin{aligned}
 \phi(x_0, y_0) &= \frac{1}{2}\phi(x_0, y_0) \\
 &+ \frac{1}{16}\{\phi(x_{-1}, y_{-1}) + \phi(x_0, y_{-1}) + \phi(x_1, y_{-1}) + \phi(x_{-1}, y_0) \\
 &+ \phi(x_1, y_0) + \phi(x_{-1}, y_1) + \phi(x_0, y_1) + \phi(x_1, y_1)\} \\
 &+ \frac{1}{32}\{\phi(x_{-2}, y_{-2}) + \phi(x_{-1}, y_{-2}) + \phi(x_0, y_{-2}) + \phi(x_1, y_{-2}) \\
 &+ \phi(x_2, y_{-2}) + \phi(x_{-2}, y_{-1}) + \phi(x_2, y_{-1}) + \phi(x_{-2}, y_0) \\
 &+ \phi(x_2, y_0) + \phi(x_{-2}, y_1) + \phi(x_2, y_1) + \phi(x_{-2}, y_2) \\
 &+ \phi(x_{-1}, y_2) + \phi(x_0, y_2) + \phi(x_1, y_2) + \phi(x_2, y_2)\} . \quad (3.47)
 \end{aligned}$$

By computing a new value for each point a relatively smooth potential results, taking into account points a distance  $n$  away. By applying the smoothing algorithm  $a$  times, points a distance  $a \times n$  are effectively used in the average (see Figure 3.13(c)).

### 3.7 Computation of magnetic potential

The computation of a magnetic potential can be quite costly in time and memory, though steps can be taken to reduce the computational overhead and temporary arrays needed. As described in Section 2.4, the magnetic field enters the Hamiltonian via the vector potential  $\mathbf{A}$ , i.e.

$$\mathcal{H} = -\frac{1}{2m}(-i\hbar\nabla - e\mathbf{A})^2 + e\mathcal{V}, \quad (3.48)$$

where  $\mathbf{A}$  is defined by

$$\mathbf{B} = \nabla \times \mathbf{A}. \quad (3.49)$$

The first concern is computing an appropriate vector potential  $\mathbf{A}$  from a constant magnetic field. This is made more difficult by the requirement that the potential be continuous across the boundaries and preferably zero along the boundary.

A suitable solution that produces the required magnetic field across the device but deviates from constant near the boundaries was found. This involved defining  $\mathbf{A}$  as

$$\mathbf{A} = \begin{cases} (A_x(x,y), A_y(x,y), 0) & x \text{ or } y \text{ not near a boundary} \\ 0 & x \text{ or } y \text{ near a boundary} \end{cases}, \quad (3.50)$$

which is then smoothed by convolution with a Gaussian function or via a local recursive averaging process. This magnetic vector potential,  $\mathbf{A}$ , produces a constant magnetic field across the nano structure under study but deviates from constant near the boundaries. In general, the vector potential can be expressed as

$$\mathbf{A} = (f(x,y), g(x,y), 0). \quad (3.51)$$

Expanding Equation 3.48 as

$$\mathcal{H} = -\frac{1}{2m}(-\hbar^2\nabla^2 + i\hbar e\nabla\mathbf{A} + i\hbar e\mathbf{A}\nabla + e^2\mathbf{A}^2) + e\mathcal{V} \quad (3.52)$$

leads to

$$\begin{aligned} \mathcal{H} = & -\frac{1}{2m} \left[ -\hbar^2\nabla^2 + 2i\hbar e \left( g(x,y)\frac{\partial}{\partial y} + f(x,y)\frac{\partial}{\partial x} \right) \right. \\ & \left. + i\hbar e \left( \frac{\partial f(x,y)}{\partial x} + \frac{\partial g(x,y)}{\partial y} \right) + e^2(f(x,y)^2 + g(x,y)^2) \right] + e\mathcal{V}, \end{aligned} \quad (3.53)$$

where  $f(x,y)$  and  $g(x,y)$  are smoothed functions, approximating the vector operator  $\mathbf{A}$  in the region where propagation occurs while being zero at the boundaries.

For speed of computation the components independent of  $\psi$ , that is

$$i\hbar e \left( \frac{\partial f(x,y)}{\partial x} + \frac{\partial g(x,y)}{\partial y} \right) + e^2 (f(x,y)^2 + g(x,y)^2), \quad (3.54)$$

can be computed once and stored. While the components dependent on  $\psi$ , that is

$$2i\hbar e \left( g(x,y) \frac{\partial}{\partial y} + f(x,y) \frac{\partial}{\partial x} \right), \quad (3.55)$$

must be computed each time the Hamiltonian is applied to  $\psi(x,y)$ .

Evaluation of the dependent components requires six arrays to be stored ( $f(x,y)$ ,  $g(x,y)$ ,  $\frac{\partial}{\partial y}$ ,  $\frac{\partial}{\partial x}$  and the application of each partial derivative on the wave function) and two reverse Fourier transforms to be applied to the wave function. The net result is an increase in memory space required by seven arrays (one independent and six dependent components) and two extra reverse Fourier transforms (and the associated increase in multiplications), doubling the number of Fourier transforms computed.

Figure 3.15 shows an example of a magnetic field and vector potentials typically used in a computation. In the region where a potential is defined, the magnetic field is equal to  $0.1 T$  and is zero and continuous along the boundaries.

### 3.7.1 Comparison of different gauges

It was found that certain gauges are computationally more favourable than others. For example, three solutions for the magnetic vector potential  $\mathbf{A}$  corresponding to a constant magnetic field  $\mathbf{B} = (0, 0, b)$  are

$$\mathbf{A} = b(-y, 0, 0), \quad (3.56)$$

$$\mathbf{A} = \frac{b}{2}(-y, x, 0), \quad (3.57)$$

$$\mathbf{A} = \frac{b}{2}(x-y, x-y, 0). \quad (3.58)$$

The symmetric vector potential, Equation 3.58, produces the least amount of numerical error and uses the least amount of memory. The error is less than Equation 3.56 due to

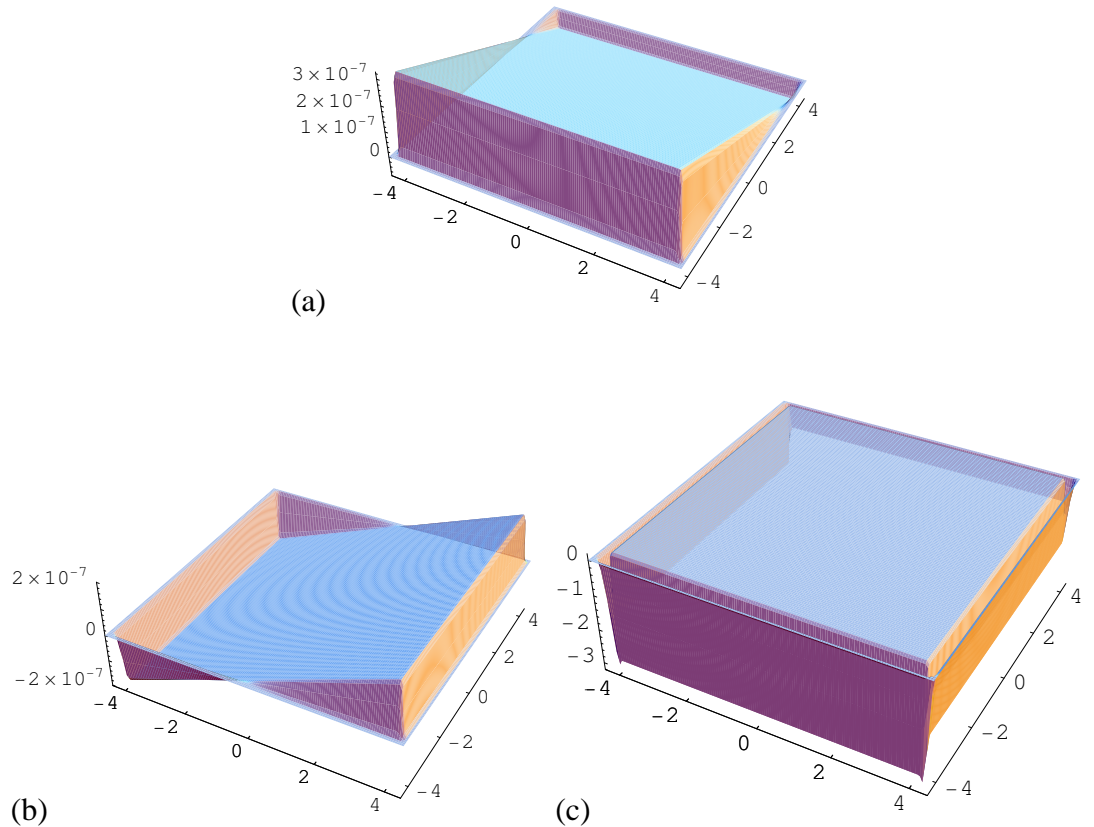


Figure 3.15: Parts (a) and (b) show the  $x$ - and  $y$ - components of the vector potential  $A = \frac{b}{2}(-y, x, 0)$  to produce an approximately uniform magnetic field in the  $z$ -direction. Part (c) shows the magnetic field produced from the vector potential  $A = \frac{b}{2}(-y, x, 0)$ . In the main region of propagation it is constant,  $b = 0.1$ , and zero along the boundary. The spatial size of the simulation is  $8 \mu\text{m}$  in each dimension.

the halving of the magnetic field in the equation. This results in half the error each time the Hamiltonian is applied. For the Chebychev scheme, where the Hamiltonian is used in a recursive summation hundreds to thousands of times, this causes a dramatically reduced error. Figure 3.16 demonstrates that each gauge produces the same final wave function with no noticeable error.

For a large magnetic field, the selection of the gauge makes a slight difference to the propagation error. However, with the application of a weak magnetic field, to control the phase of the electron rather than greatly altering its propagation, the difference between the gauges is indistinguishable.

Figure 3.17 shows the propagation of a single electron through a nano-ring for the three gauges under a weak magnetic field. The propagation proceeds as expected.

Care must be taken with magnetic fields to ensure that the minimum and maximum eigen energies used to scale the Hamiltonian in Equation 2.31 are chosen appropriately. The magnetic field affects all energy components and can result in large computational errors if the energy eigen value range is chosen too small (in an attempt to reduce computational time).

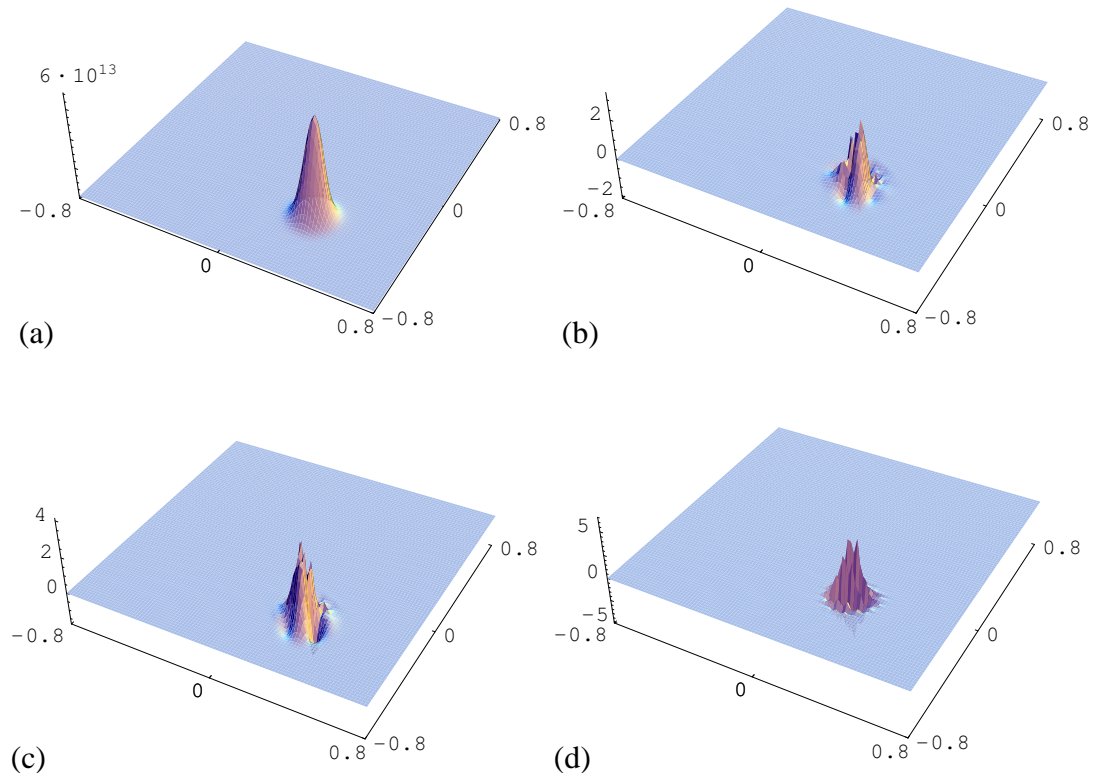


Figure 3.16: Part (a) shows the theoretical solution, while parts (b)-(d) show the absolute error for the three different gauges:  $b(-y, 0, 0)$ ;  $b/2(-y, x, 0)$ ; and  $b/2(x - y, x - y, 0)$  respectively. The applied magnetic field is  $0.3T$  with the initial wave function having energy  $0.81\text{ eV}$  and a momentum spread of  $4.0\%$ .

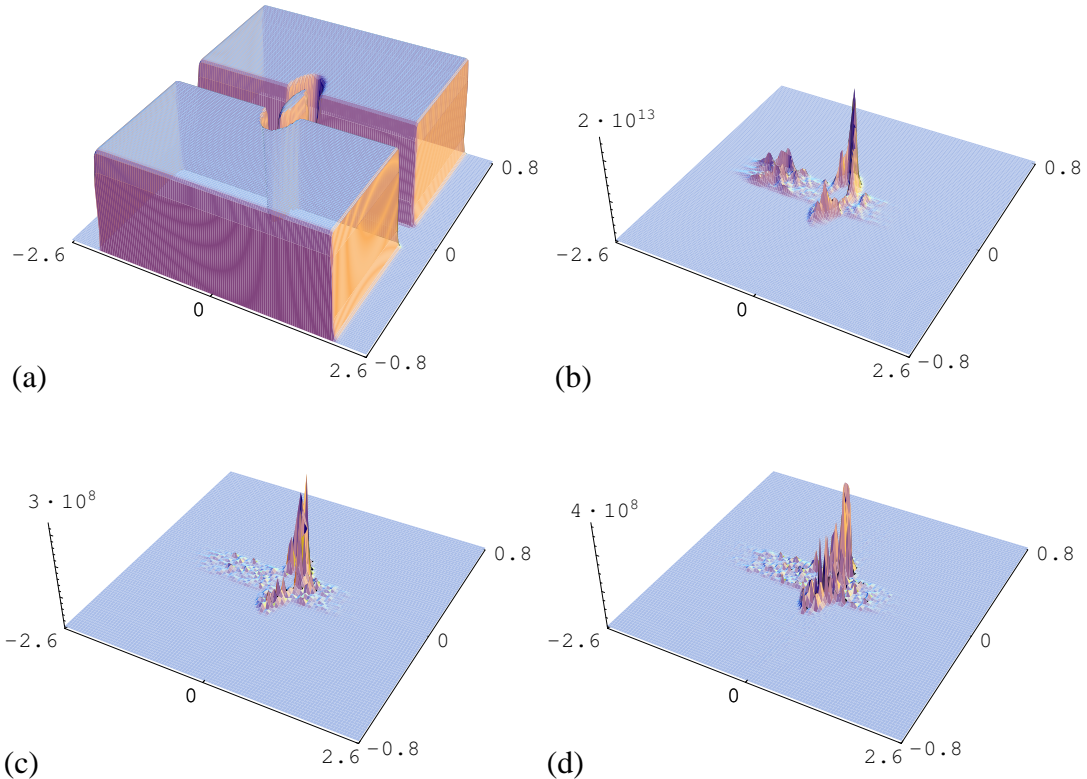


Figure 3.17: Part (a) shows the ring potential, while part (b) shows the final wave function for the Landau gauge  $b/2(-y, x, 0)$ . Parts (c) and (d) show the absolute error between the final wave functions for the gauges  $b(-y, 0, 0)$ ,  $b/2(x - y, x - y, 0)$ , and the Landau gauge shown in part (b). The applied magnetic field is  $0.02T$  with the initial wave function having energy  $0.041$  eV energy and a momentum spread of  $15\%$ .

## 3.8 Computational accuracy and stability

The largest criticism against computational methods is how accurately they model the physical system and how stable the solutions are. If the results obtained are not reliable or stable, then the program is of little use.

Many different test were applied to ensure that the results produced from the code were accurate. These were

- comparison to known solutions
- ensuring that energy is conserved
- ensuring that norm is conserved
- propagating forward and then backward in time to original wave function

### 3.8.1 Comparison to known solutions

By directly comparing the output from the computer code to known solutions for simple cases, the underlying operation of the model can be tested. Several known solutions exist, which are detailed below.

#### Electron propagation in free space

A classical particle in free space travels along with no change in its direction, velocity, or acceleration. A quantum particle in free space propagates with no change in direction, mean velocity or acceleration. It does, however, spread as it propagates. If a Gaussian wave packet is used as the initial wave function

$$\psi(x, y, 0) = \frac{1}{2\pi w_x w_y} \exp\left(-\frac{x^2}{2w_x^2} - \frac{y^2}{2w_y^2} + \frac{i}{\hbar} p_x x + \frac{i}{\hbar} p_y y\right), \quad (3.59)$$

the wave function some time later is given by (Cohen-Tannoudji et al. 1977, page 60)

$$\psi(x, y, t) = \left(\frac{16w_x^2 w_y^2}{\pi^2}\right)^{\frac{1}{4}} \exp(i\phi_1 + i\phi_2) \exp\left(i\frac{p_x x}{\hbar} + i\frac{p_y y}{\hbar}\right)$$

$$\times \exp \left\{ -\frac{\left[ x - \frac{p_x}{m} t \right]^2}{2w_x^2 + \frac{2i\hbar t}{m}} - \frac{\left[ y - \frac{p_y}{m} t \right]^2}{2w_y^2 + \frac{2i\hbar t}{m}} \right\}, \quad (3.60)$$

where  $\phi_1$  and  $\phi_2$  are real and independent of  $x$  and  $y$

$$\phi_1 = -\theta_1 - \frac{\hbar p_x^2}{2m} t \quad (3.61)$$

$$\phi_2 = -\theta_2 - \frac{\hbar p_y^2}{2m} t \quad (3.62)$$

$$\tan(2\theta_1) = \frac{2\hbar t}{mw_x^2} \quad (3.63)$$

$$\tan(2\theta_2) = \frac{2\hbar t}{mw_y^2}. \quad (3.64)$$

This allows direct comparison to the numerical results obtained using the Chebyshev scheme. Such a comparison is a strong indication that the computational model is valid and that the computer program written accurately reflects the model.

Figure 3.18 demonstrates how the wave function propagates in the direction of its initial momentum. Since the initial wave function was a Gaussian packet the numerical results correctly display the spreading of the wave packet and the decreasing of its height. Figure 3.19 shows the comparison of the probability distribution  $P = \psi\psi^*$  with the analytic solution. The results show that the numerical and analytical solutions agree to almost machine precision ( $10^{-15}$ ).

Figure 3.20 shows how a wave function with a Fermi distribution of energy (as described in Section 3.4.2) propagates in free space. As the wave function propagates, the peaks become more prominent and the wave function starts to form several distinct parts.

### **Electron propagation in free space with constant magnetic field**

A classical particle in a magnetic field undergoes circular motion. The same type of motion occurs for a wave packet in a constant uniform magnetic field, with its centre of mass following that of a classical particle. An analytical solution for the motion of a Gaussian wave packet in a uniform magnetic field can be derived. The derivation of an exact solution for the motion of a Gaussian electron wave packet follows the work by ter Haar (1975) as described below.

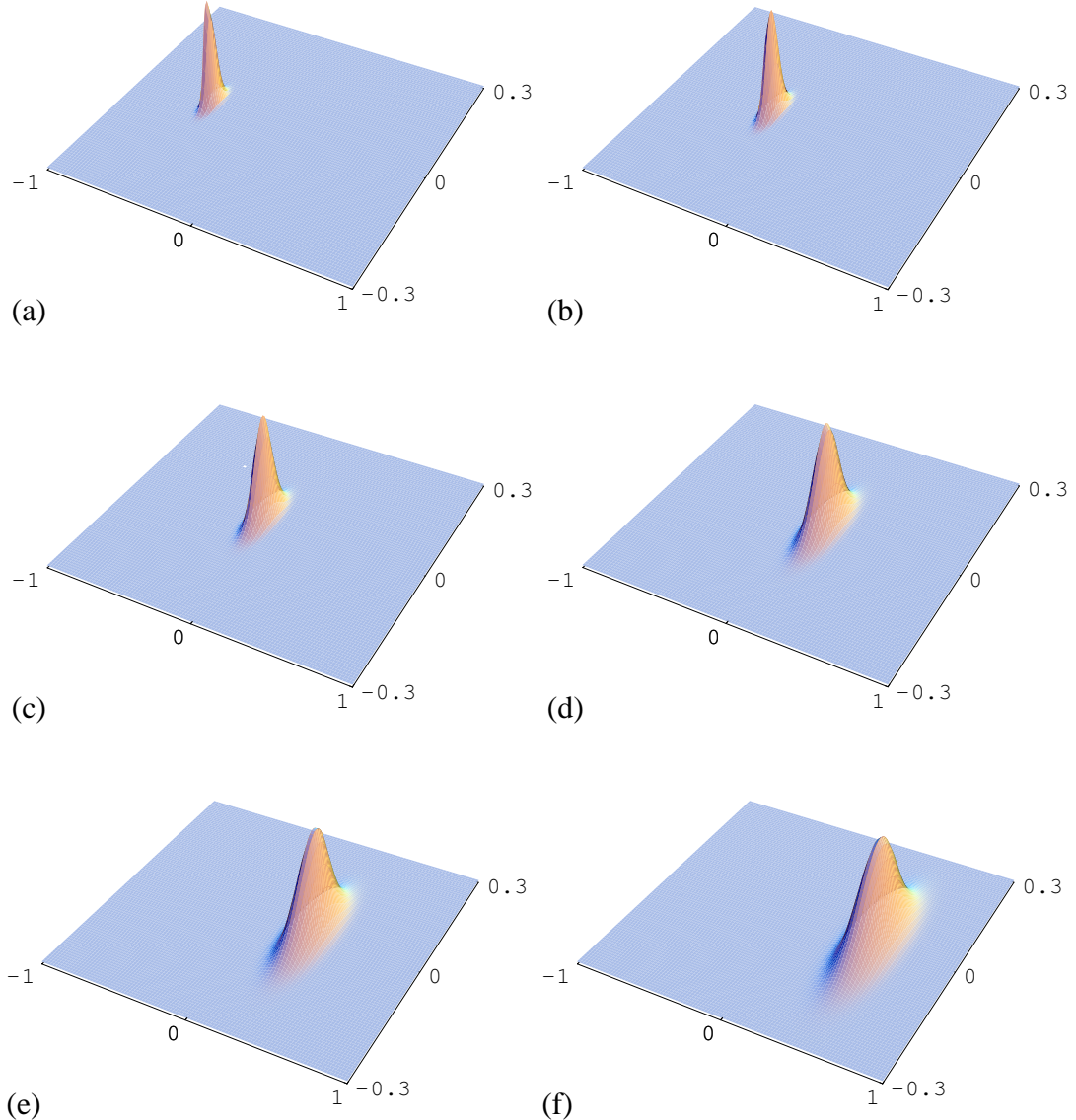


Figure 3.18: The Gaussian wave packet propagates for a time  $t = 1.6 \text{ ps}$ , spreading as expected.

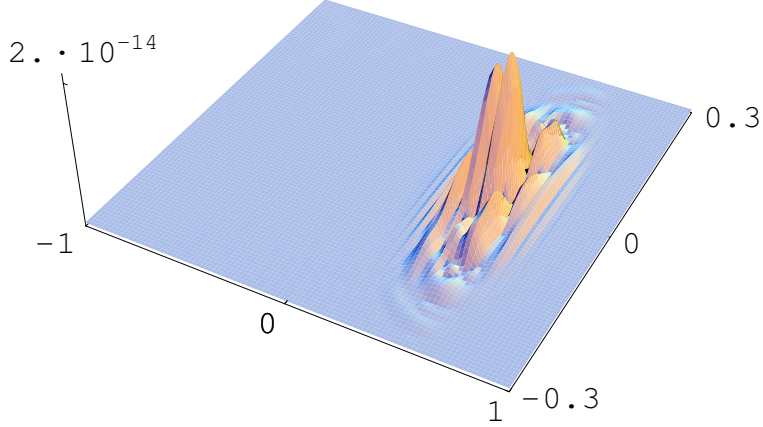


Figure 3.19: Comparison of numerical solution for the propagation of a Gaussian to analytic solution for free space.

The Schrödinger equation for a charged particle moving in a constant uniform magnetic field is given by

$$i\hbar \frac{\partial \Psi}{\partial t} = -\frac{\hbar^2}{2m} \nabla^2 \Psi + \frac{\hbar}{i} \omega_L \left( x \frac{\partial \Psi}{\partial y} - y \frac{\partial \Psi}{\partial x} \right) + \frac{1}{2} m \omega_L^2 (x^2 + y^2) \Psi, \quad (3.65)$$

where the magnetic vector potential used is  $\mathbf{A} = \frac{b}{2}(-y, x, 0)$  and  $\omega_L = \frac{eb}{2m}$  is the Larmor frequency. To find a solution, a rotating frame of reference is chosen

$$x = x' \cos(\omega_L t) + y' \sin(\omega_L t), \quad (3.66)$$

$$y = -x' \sin(\omega_L t) + y' \cos(\omega_L t), \quad (3.67)$$

$$t = t', \quad (3.68)$$

$$\Psi = \Psi'. \quad (3.69)$$

In this rotating frame of reference, the operators become

$$\frac{\partial}{\partial t'} = \frac{\partial}{\partial t} + \omega_L \left( x \frac{\partial}{\partial y} - y \frac{\partial}{\partial x} \right) \quad (3.70)$$

$$\nabla'^2 = \nabla^2. \quad (3.71)$$

With these substitutions, the Schrödinger equation is transformed to a simple harmonic oscillator

$$i\hbar \frac{\partial \Psi'}{\partial t'} = -\frac{\hbar^2}{2m} \nabla'^2 \Psi' + \frac{m\omega_L^2}{2} (x'^2 + y'^2) \Psi', \quad (3.72)$$

with well known solution. In two dimensions,

$$\Psi' \equiv \Psi(x', y', t) = C \sum_{n,l} A_{n,l} \chi_n(\alpha x') \chi_l(\alpha y') \exp(-i\omega_L(n+l+1)), \quad (3.73)$$

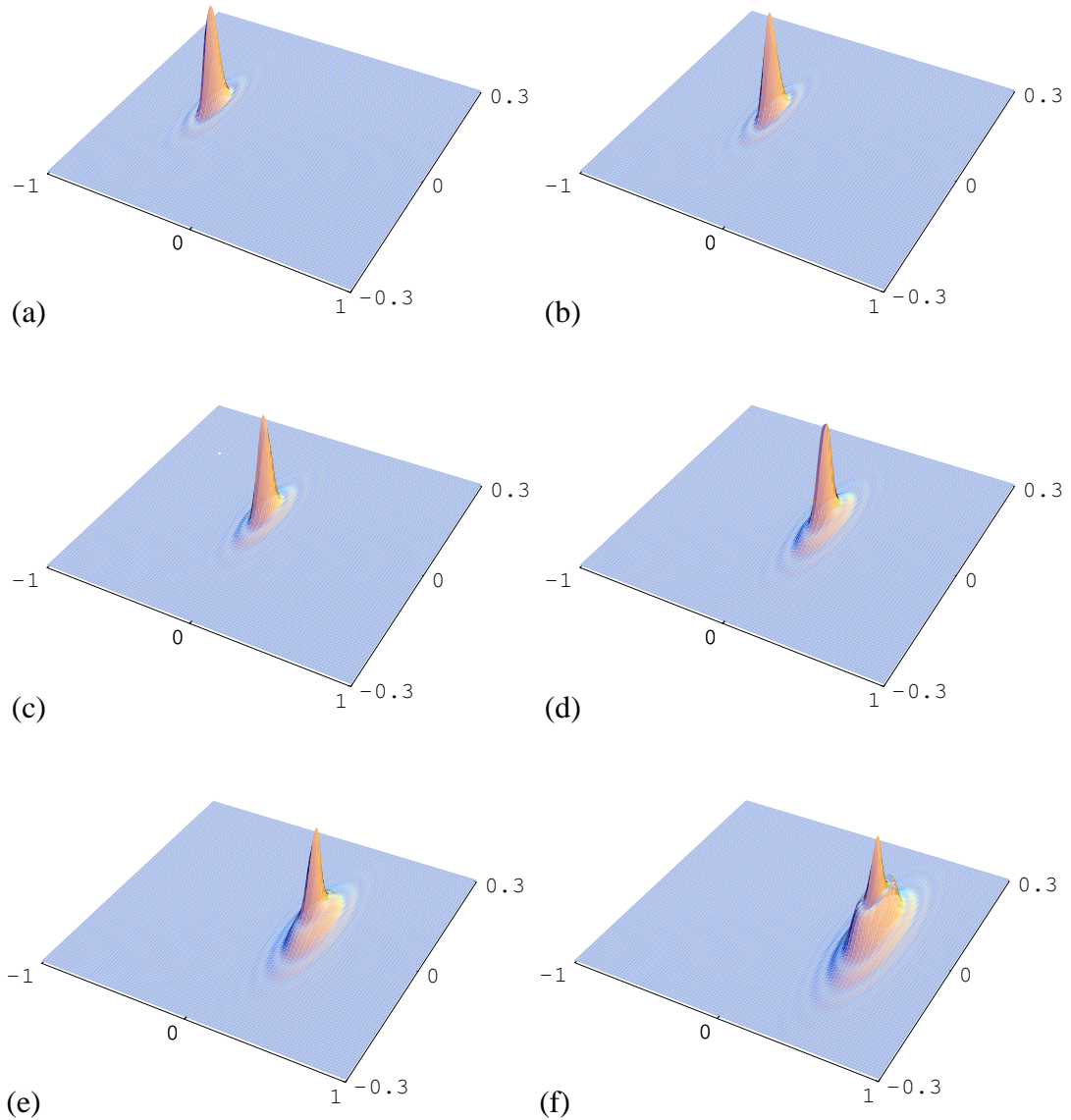


Figure 3.20: The Fermi wave packet propagates for a time  $t = 1.6$  ps.

where  $\chi_n(\alpha x) = c_n \exp\left(-\frac{\alpha^2 x^2}{2}\right) H_n(\alpha x)$  are the eigen functions of the simple harmonic oscillator,  $A_{n,l} = A_n^x A_l^y$  are chosen to satisfy the initial conditions with  $A_n^x$  and  $A_l^y$  referring to the  $x$  and  $y$  component of  $A_{n,l}$  respectively,  $H_n(\alpha x)$  are the Hermite polynomials,  $\alpha = \sqrt{\frac{m\omega_L}{\hbar}}$ , and  $c_n^2 = \frac{\alpha}{2^n n! \sqrt{\pi}}$ .

Using the generating function for the Hermite polynomials

$$\exp(-\lambda^2 + 2\lambda\eta) = \sum_n \frac{\lambda^n}{n!} H_n(\eta), \quad (3.74)$$

we have

$$\begin{aligned} \psi(x', y', 0) &= C \exp \left[ -(A_n^x c_n n!)^{\frac{2}{n}} + 2(A_n^x c_n n!)^{\frac{1}{n}} \alpha x' \right] \\ &\times \exp \left[ -\frac{\alpha^2 x'^2}{2} \right] \\ &\times \exp \left[ -(A_l^y c_l l!)^{\frac{2}{l}} + 2(A_l^y c_l l!)^{\frac{1}{l}} \alpha y' \right] \\ &\times \exp \left[ -\frac{\alpha^2 y'^2}{2} \right]. \end{aligned} \quad (3.75)$$

If the initial wave packet is given by a Gaussian

$$\psi(x', y', 0) = \frac{1}{\sqrt{w_x w_y \pi}} \exp \left( -\frac{x'^2}{2w_x^2} - \frac{y'^2}{2w_y^2} + \frac{i p_x x'}{\hbar} + \frac{i p_y y'}{\hbar} \right), \quad (3.76)$$

then equating the coefficients in Equations 3.75 and 3.76 gives

$$\frac{1}{\sqrt{w_x w_y \pi}} = C \exp \left[ -(A_n^x c_n n!)^{\frac{2}{n}} - (A_l^y c_l l!)^{\frac{2}{l}} \right], \quad (3.77)$$

$$-\frac{1}{2w_x^2} = -\frac{\alpha^2}{2}, \quad (3.78)$$

$$-\frac{1}{2w_y^2} = -\frac{\alpha^2}{2}, \quad (3.79)$$

$$\frac{i p_x}{\hbar} = 2(A_n^x c_n n!)^{\frac{1}{n}} \alpha, \quad (3.80)$$

$$\frac{i p_y}{\hbar} = 2(A_l^y c_l l!)^{\frac{1}{l}} \alpha. \quad (3.81)$$

From these, we obtain the following relations

$$w_x = w_y = \frac{1}{\alpha}, \quad (3.82)$$

$$A_n^x c_n = \frac{1}{n!} \left( \frac{i p_x}{2\hbar\alpha} \right)^n, \quad (3.83)$$

$$A_l^y c_l = \frac{1}{l!} \left( \frac{i p_y}{2\hbar\alpha} \right)^l, \quad (3.84)$$

$$C = \frac{\alpha}{\sqrt{\pi}} \exp \left[ - \left( \frac{p_x}{2\hbar\alpha} \right)^2 - \left( \frac{p_y}{2\hbar\alpha} \right)^2 \right]. \quad (3.85)$$

The evolution of the wave packet is therefore

$$\begin{aligned} \Psi(x', y', t) &= C \sum_{n,l} \frac{1}{n!} \left( \frac{ip_x}{2\hbar\alpha} \right)^n \frac{1}{l!} \left( \frac{ip_y}{2\hbar\alpha} \right)^l \\ &\times \exp \left( -\frac{\alpha^2 x'^2}{2} \right) \exp \left( -\frac{\alpha^2 y'^2}{2} \right) H_n(\alpha x') H_l(\alpha y') \\ &\times \exp(-i\omega_L t(n+l+1)). \end{aligned} \quad (3.86)$$

By using again the generating function for the Hermite polynomials, the above expression can be further simplified as

$$\Psi(x', y', t) = C \exp \left[ -\lambda_x^2 + 2\alpha\lambda_x x' - \frac{\alpha^2 x'^2}{2} - \lambda_y^2 + 2\alpha\lambda_y y' - \frac{\alpha^2 y'^2}{2} - i\omega_L t \right], \quad (3.87)$$

where

$$\lambda_x = \frac{ip_x}{2\hbar\alpha} \exp(-i\omega_L t), \quad (3.88)$$

$$\lambda_y = \frac{ip_y}{2\hbar\alpha} \exp(-i\omega_L t). \quad (3.89)$$

The simplest system with a magnetic field that can be studied is that of free space propagation with a constant uniform magnetic field. As stated in Section 3.7, the computation model and computer program developed does not quite reproduce a uniform magnetic field. However, by choosing a space large enough, a good approximation is obtained. As with the comparison to free space propagation, an analytical solution is available for propagation in free space with a uniform constant magnetic field (Section 3.8.1). Comparison to this analytical solution provides strong evidence that the model and computer code are accurate and that the approximation made is valid.

Figure 3.21 (a) shows the wave function propagating with an applied uniform constant magnetic field. The wave function is specially chosen to have a momentum spread corresponding to the Larmor frequency, which ensures that its shape is preserved while propagating. As expected, the wave function follows the same path as that of a classical electron in the same magnetic field. The difference between the analytical solution and the computational solution is shown in Figure 3.21 (b) and demonstrates the effectiveness of the computational method.

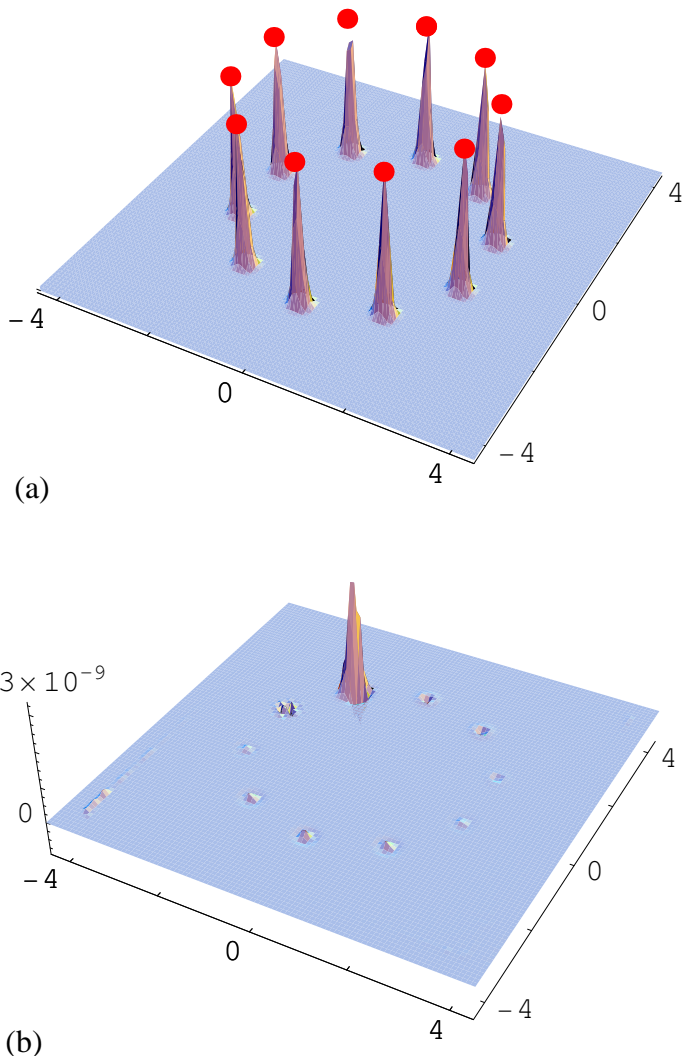


Figure 3.21: Propagation of an electron (Gaussian wave packet) under the influence of an approximately constant, uniform, magnetic field  $B = 0.1T$ . Part (a) shows the propagation of the electron while the circles above the wave packet indicate the classical particle trajectory. The wave packet initially has energy 0.082 eV in the  $x-$  direction and momentum spread 2.3%, corresponding to the Larmor frequency  $0.13 \times 10^{12}$ . Part (b) shows the error between the computational propagation and analytic results. The error is approximately 6 to 7 orders of magnitude smaller than the wave packet.

Figure 3.22 shows how a wave function with a Fermi distribution of energy (Section 3.4.2) propagates in free space with a magnetic field. As the wave function propagates, the peaks become more prominent and the wave function starts to form several distinct parts. Again, the norm, energy and momentum of the wave function were conserved to  $10^{-13}$ , which is approximately machine precision.

### 3.8.2 Conservation of energy and norm

For systems without exact analytical solutions, calculations were checked against the following set of criteria. First, the norm of the wave function must be conserved throughout the time evolution, because the exact time evolution operator is unitary. Second, the energy of the system should also remain constant throughout the time evolution. The preservation of norm and energy serve as a basic criteria to any propagation schemes. For the Chebyshev scheme these two attributes are particularly important, since the Chebyshev propagator is not by definition unitary and thus neither norm nor energy conserving. In this case, conservation of norm and energy puts forward a strong test to the propagation scheme and the computational model.

For three distinct cases: no potential; electrostatic potential only; and combined electrostatic and magnetic potential, both the norm and the energy was found to be conserved to  $10^{-8}$  and in many cases to below  $10^{-15}$ . By relaxing this stringent condition, faster convergence can be achieved, yielding results with no noticeable difference in macroscopic observables, such as the transmission coefficient and conductance.

### 3.8.3 Time reversal propagation

The solution to the time dependent Schrödinger equation, given by Equation 2.20, can be reorganised as

$$\exp\left(\frac{i}{\hbar}\mathcal{H}\Delta t\right)\psi(x,y,t+\Delta t)=\psi(x,y,t), \quad (3.90)$$

due to the Hamiltonian being hermitian. This represents the propagation of the final wave function  $\psi(x,y,t+\Delta t)$  an amount  $-\Delta t$  to the initial wave function  $\psi(x,y,t)$ . This can

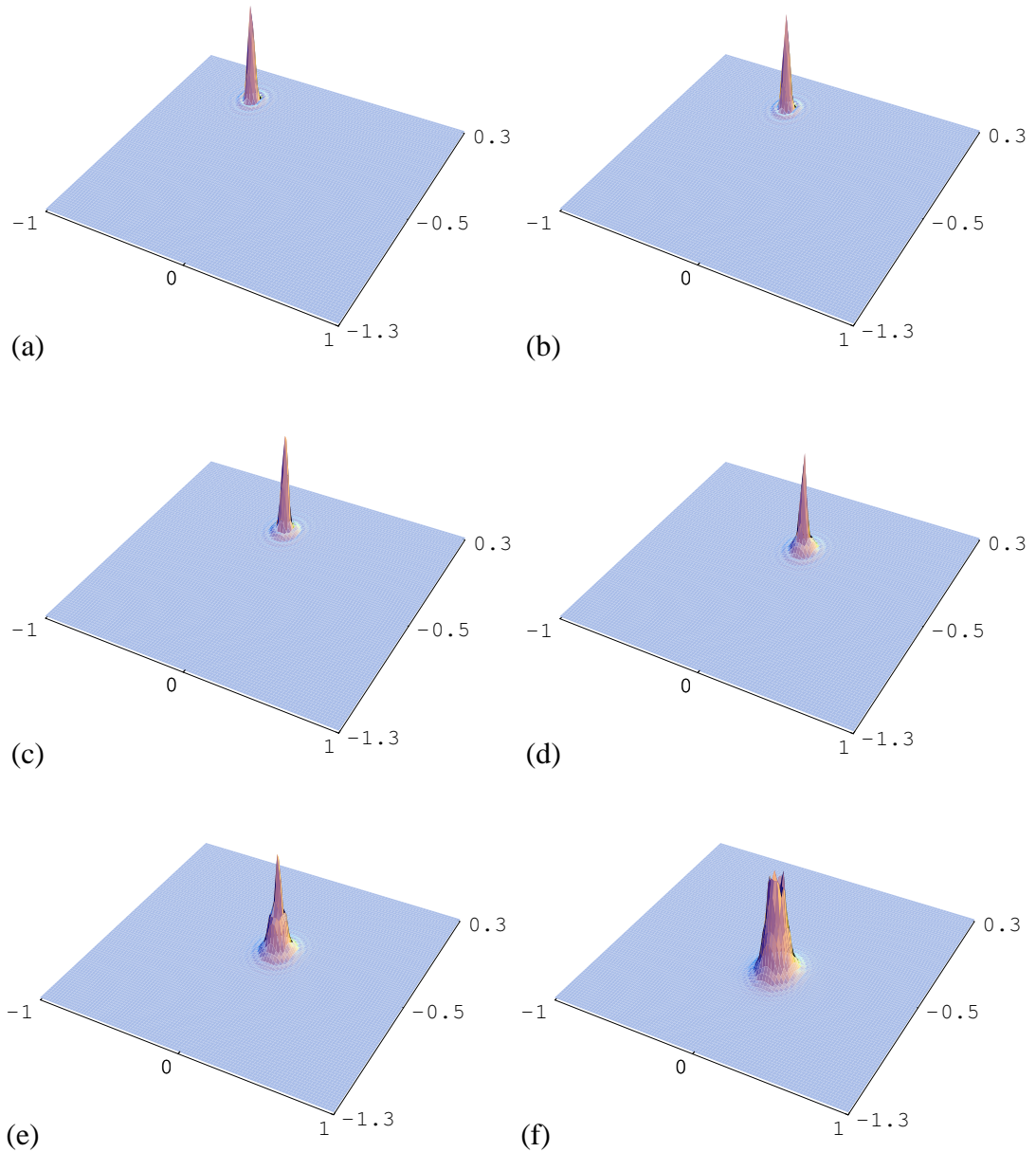
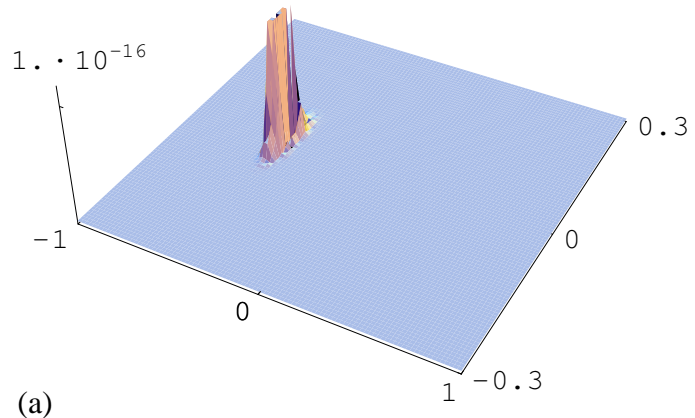


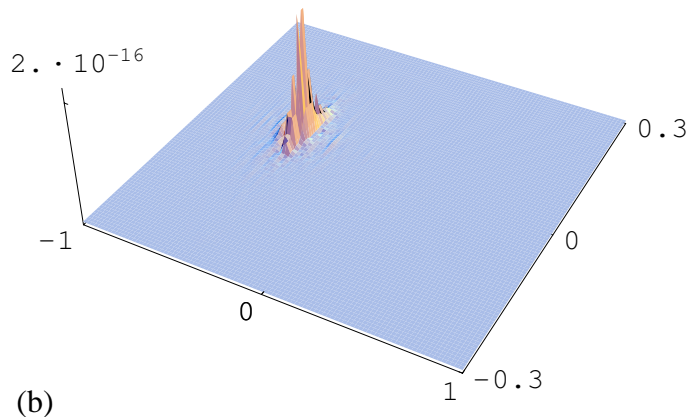
Figure 3.22: Propagation of a fermi wave packet, for  $1.6 \text{ ps}$ , under an approximate uniform constant magnetic field  $B = 0.4T$ .

be implemented in the computational method by propagating the initial wave function forward in time by an amount  $\Delta t$  and then propagating it backward in time by an amount  $-\Delta t$ . Theoretically, the final wave function after propagation is identical to the initial wave function. If errors accumulate throughout the computational method, then the phase or the amplitude of the wave function would have varied. This comparison imposed a very stringent test on the stability of the method and numerical accuracy.

For simple cases with a fine grid, the initial wave function can be reproduced with almost machine precision, a relative error of less than  $10^{-15}$ , see Figures 3.23 and 3.24. For more complicated cases, large space or applied magnetic field, the initial wave function can be reproduced to within a relative error of  $10^{-8}$ . The time propagation of the wave packet illustrates this phenomena, where the wave packet is seen to spread, reflect and translate (under a magnetic field) to a final state; and then recombine and move back to its original position under time reversal, see Section 4.1.5 for a detailed analysis.

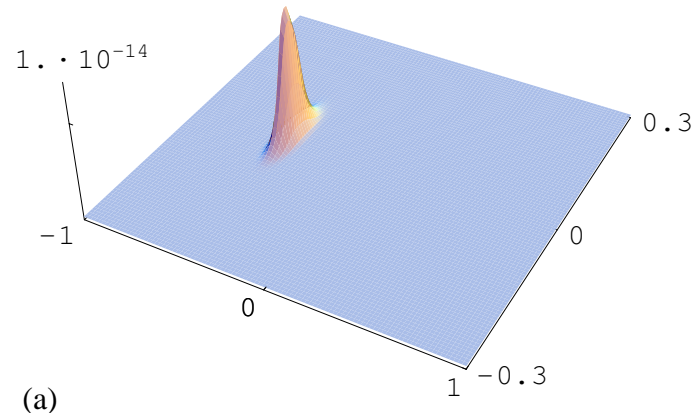


(a)

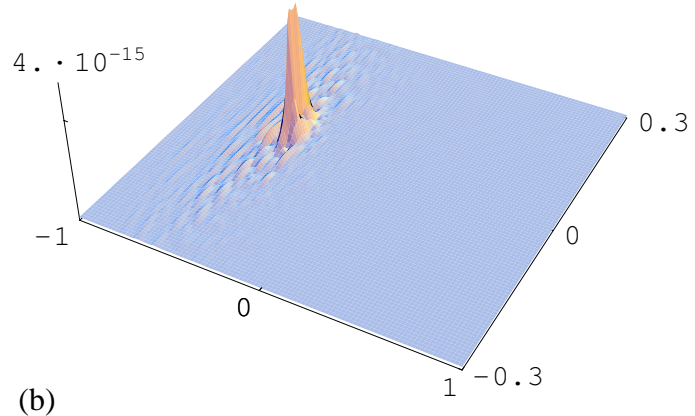


(b)

Figure 3.23: Comparison of the forward and backward propagation of the wave function to the initial wave function, (a) Gaussian wave packet (b) fermi wave packet.



(a)



(b)

Figure 3.24: Relative error for the forward and backward propagation of a (a) Gaussian and (b) fermi wave packet under the influence of an approximate uniform constant magnetic field.

# **Chapter 4**

## **Systems studied and results**

The theoretical model and computer code presented in previous chapters allow many systems to be studied from simple propagation in free space to propagation through complicated devices with applied magnetic fields. The computer program provides complete quantum mechanical information about the system under study, including its transient behaviour. These results were analysed using different techniques, depending on the information required. The theory behind the analysis is presented in this chapter where it is applicable.

As the theoretical model and computer code developed, more complicated systems were able to be studied with confidence that the results obtained accurately reflected reality. The last couple of systems studied provide insight into device design and uses. The results were previously unknown and should prove useful for further experimental advancement.

### **4.1 Double barrier**

The double barrier, as shown in Figure 4.1, is a simple nano-device that exhibits many of the features of electron transport in nano-devices. The transmission, reflection and tunnelling of the wave packet are the most fundamental aspects demonstrated. Slow moving components of the wave function are also trapped by the barriers, which then proceed to

tunnel out of the device. The most interesting phenomena is the resonant tunnelling of the electron, which is discussed more thoroughly in Section 4.1.3.

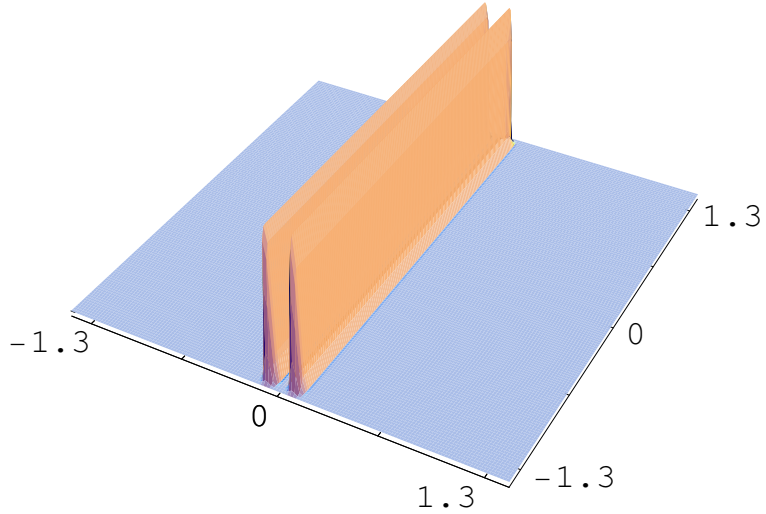


Figure 4.1: Double barrier potential of height 0.082 eV, barrier spacing 160 nm with spatial size 2.6  $\mu\text{m}$  in both the  $x-$  and  $y-$  dimensions.

For the following calculation, the prototype device is taken to be approximately 220 nm in length (outer edges of the barriers), while the spatial grid is chosen to be 2.6  $\mu\text{m}$  long and 2.6  $\mu\text{m}$  wide to accommodate the wave packet throughout the tunnelling. The height of the double barrier, for the results depicted in Figures 4.2 and 4.3, is 0.082 eV. The initial energy of the electron wave packet is chosen to be 0.082 eV. The momentum spread is assumed to be 10% in both  $x-$  and  $y-$  dimensions. The centre of the initial wave packet is set sufficiently away from the potential barriers to ensure that the entire wave function has negligible interaction with the potential at time  $t = 0$ .

Figure 4.2 illustrates the time evolution of the electron wave packet through the double barrier. Initially, the wave packet moves toward the right with time as a free wave. At time approximately 0.8 ps, one starts to observe the distortion in the wave packet caused by its interaction with the potential. At about 1.2 ps, a significant portion of the wave packet is reflected by the barriers. Further along in time one can also clearly see the formation of a trapped wave packet between the two potential barriers and its gradual decay.

Another illustration of the time evolution of the system is shown in Figure 4.3, where the wave function is given in momentum space. At time 0 to 0.4 ps, the momentum contri-

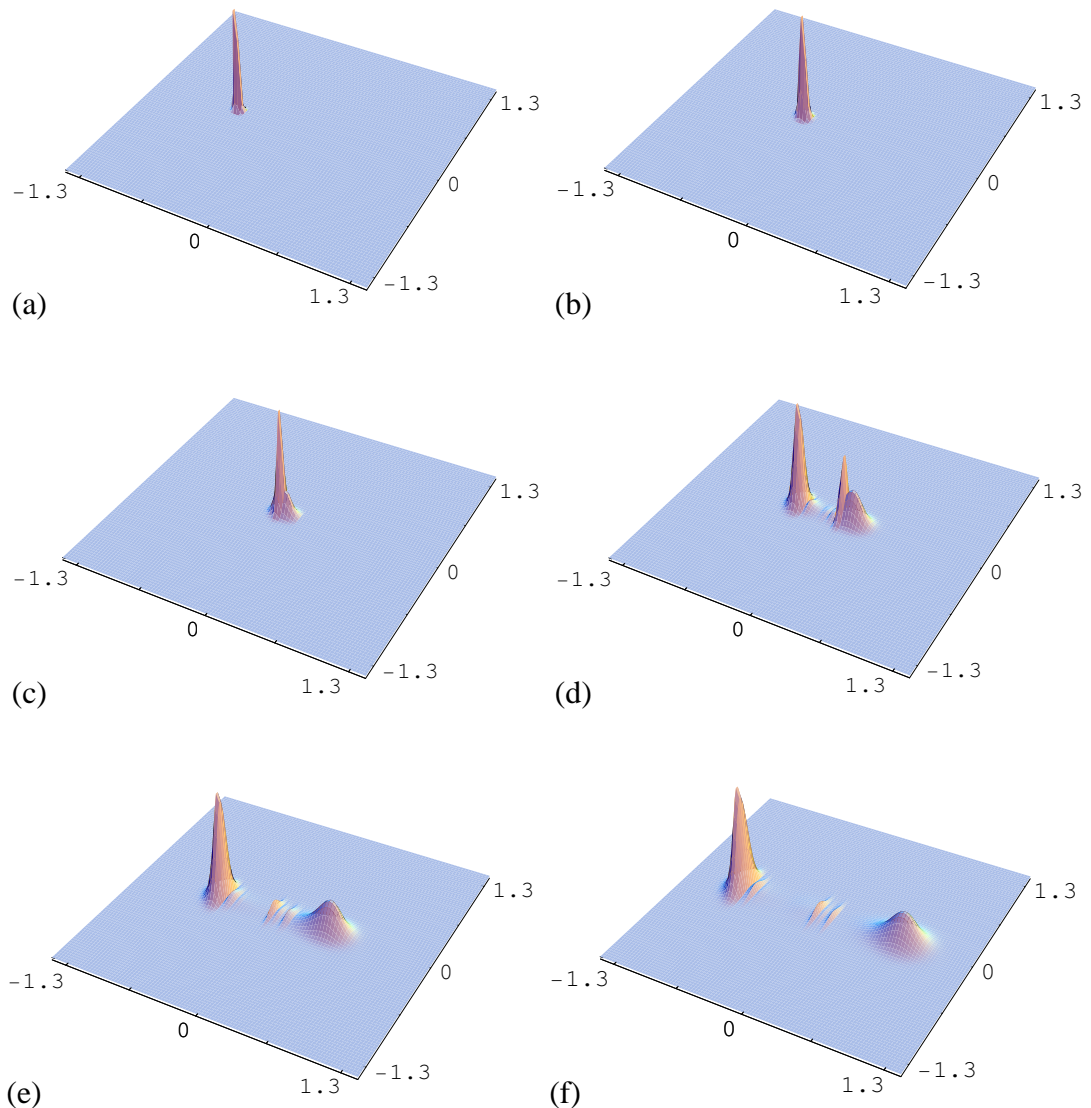


Figure 4.2: Propagation through the double barrier depicted in Figure 4.1. (a) is the initial wave function,  $t = 0$  (b) is the propagated wave function at  $0.4 \text{ ps}$ ; (c)  $0.8 \text{ ps}$ ; (d)  $1.2 \text{ ps}$ ; (e)  $1.6 \text{ ps}$  and (f) at  $2.0 \text{ ps}$ .

bution is a Gaussian centered at  $p_x = 4.0 \times 10^{-26} \text{ kg m s}^{-1}$  and  $p_y = 0$ . At time  $0.8 \text{ ps}$ , a much wider spread in the momentum wave function including negative components is observed. This corresponds to the compression in the spatial wave function shown in Figure 4.2. A significant part of the wave function has negative momentum in the  $x$ -direction due to the increasing reflected flux. At  $1.2 \text{ ps}$ , the positive and negative parts of the wave function in momentum space are well separated, representing transmission and reflection respectively. Note that there is a small part of the wave function with near-zero momentum, which represents the trapped states.

The effect of increasing the height of the double-barrier is shown in Figure 4.4 and Figure 4.5. As expected, complete transmission is observed for sufficiently low barriers. As the height of the barriers approaches the incident energy, part of the wave packet is reflected, part of the wave packet tunnels through the barriers, and the rest is temporarily trapped between the two barriers, see Figure 4.6. The ratio of the three parts and their relative phases depend entirely on the structure of the potential and the initial energy value. For sufficiently high barriers, a complete reflection is achieved.

### 4.1.1 Transmission coefficient

The code produces the final wave function  $\psi(x, y, t)$  at time  $t$  from the initial wave function. From this, the transmission ( $T$ ) and reflection ( $R$ ) can be computed in a number of ways. The most obvious is the amount of wave function on either side of the potential. This has a direct physical correspondence. However, this direct method means that the wave function needs to be spatially separated from the potential to gain an accurate transmission coefficient. Also, components of the wave function still inside the device will not be included in the value, resulting in  $T + R \neq 1$ .

Another method is to transform the real space wave function to momentum space and evaluate the amount of the wave function with forward momentum and backward momentum. This is the preferred method, as it is easier to implement (need only compute those components with forward and backward momentum) and the results for  $T$  and  $R$  converge much quicker than the direct method.

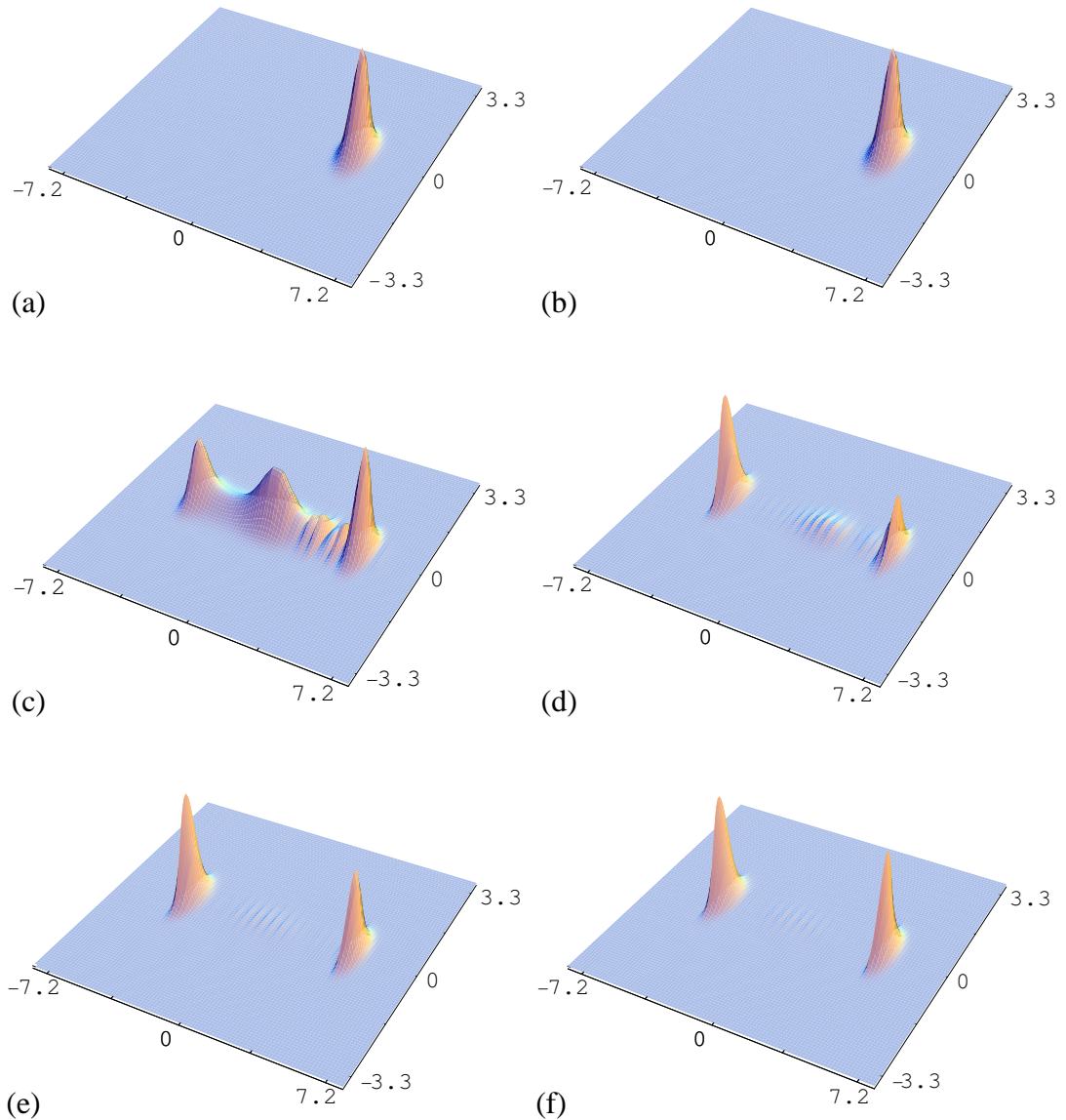


Figure 4.3: Momentum space propagation for the wave function propagation shown in Figure 4.2. The coordinate units shown are  $10^{-26} \text{ kg m s}^{-1}$ , where  $7.2 \times 10^{-26} \text{ kg m s}^{-1}$  is the maximum momentum in the  $x-$  dimension and  $3.3 \times 10^{-26} \text{ kg m s}^{-1}$  is the maximum momentum in the  $y-$  dimension.

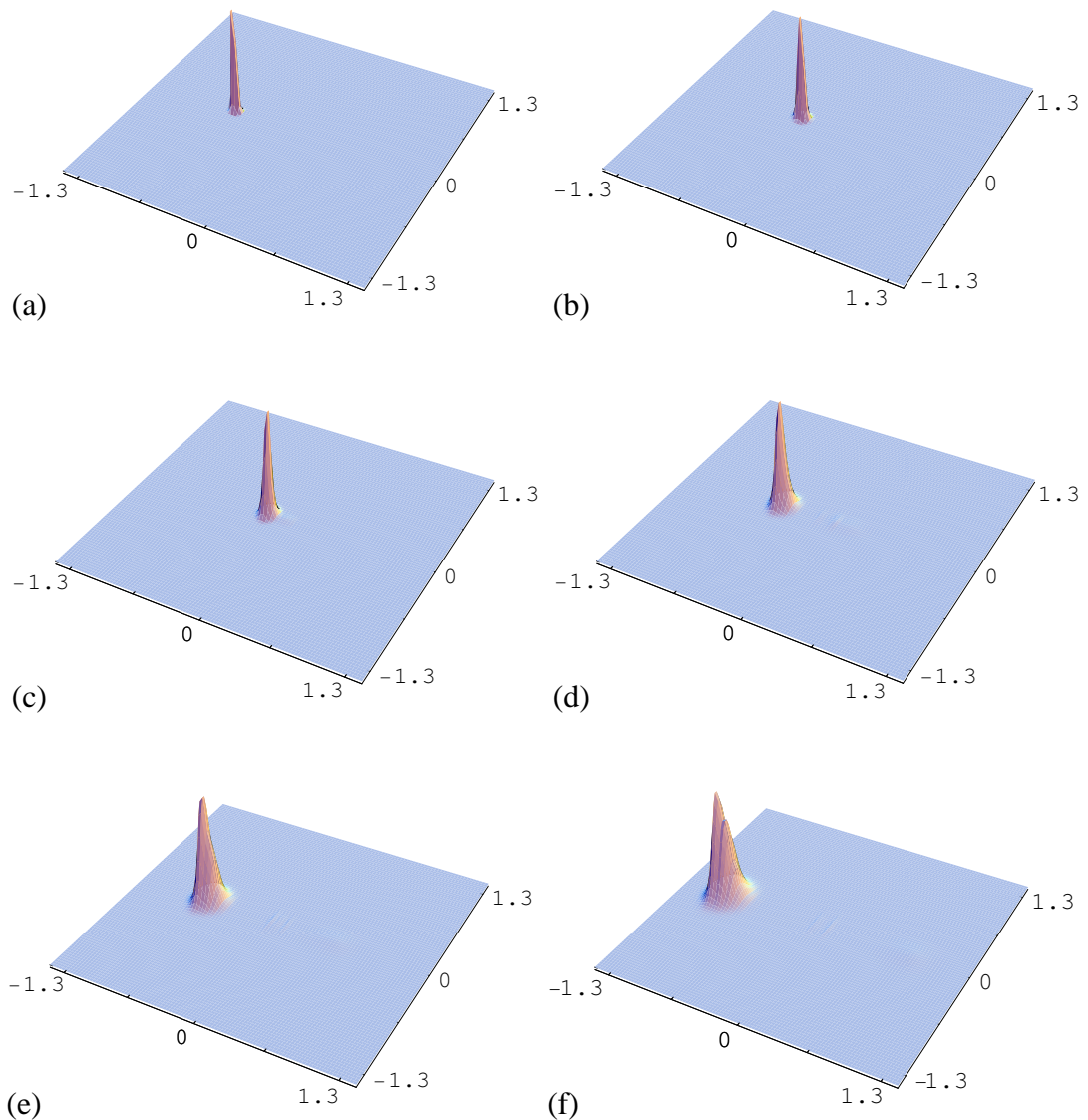


Figure 4.4: Propagation through a double barrier similar to that depicted in Figure 4.1, except the potential barrier height is 0.11 eV. (a) is the initial wave function,  $t = 0$  (b) is the propagated wave function at 0.4 ps; (c) 0.8 ps; (d) 1.2 ps; (e) 1.6 ps and (f) at 2.0 ps.

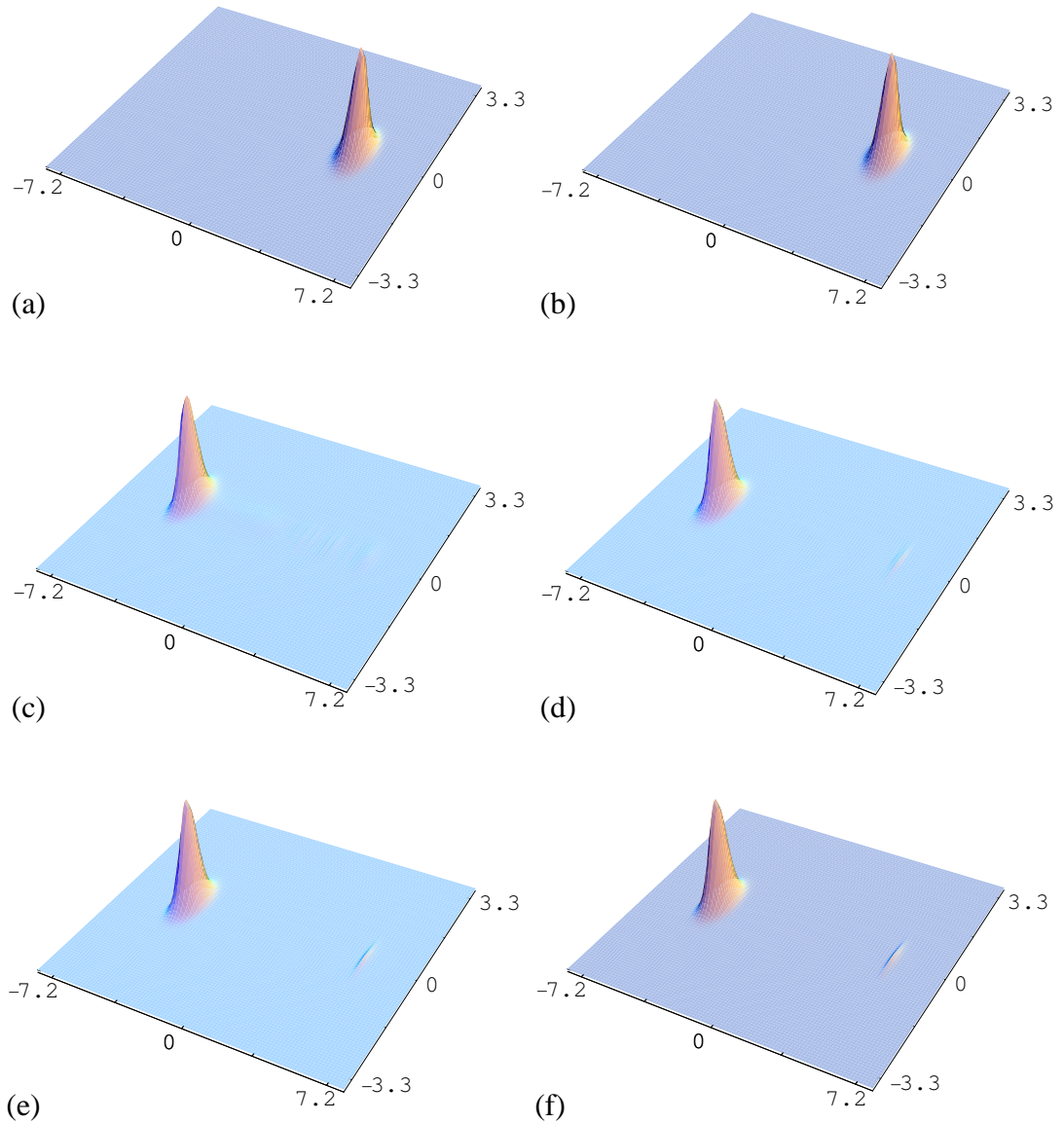


Figure 4.5: Momentum space propagation for the wave function propagation shown in Figure 4.4. The coordinate units shown are  $10^{-26} \text{ kg m s}^{-1}$ , where  $7.2 \times 10^{-26} \text{ kg m s}^{-1}$  is the maximum momentum in the  $x-$  dimension and  $3.3 \times 10^{-26} \text{ kg m s}^{-1}$  is the maximum momentum in the  $y-$  dimension.

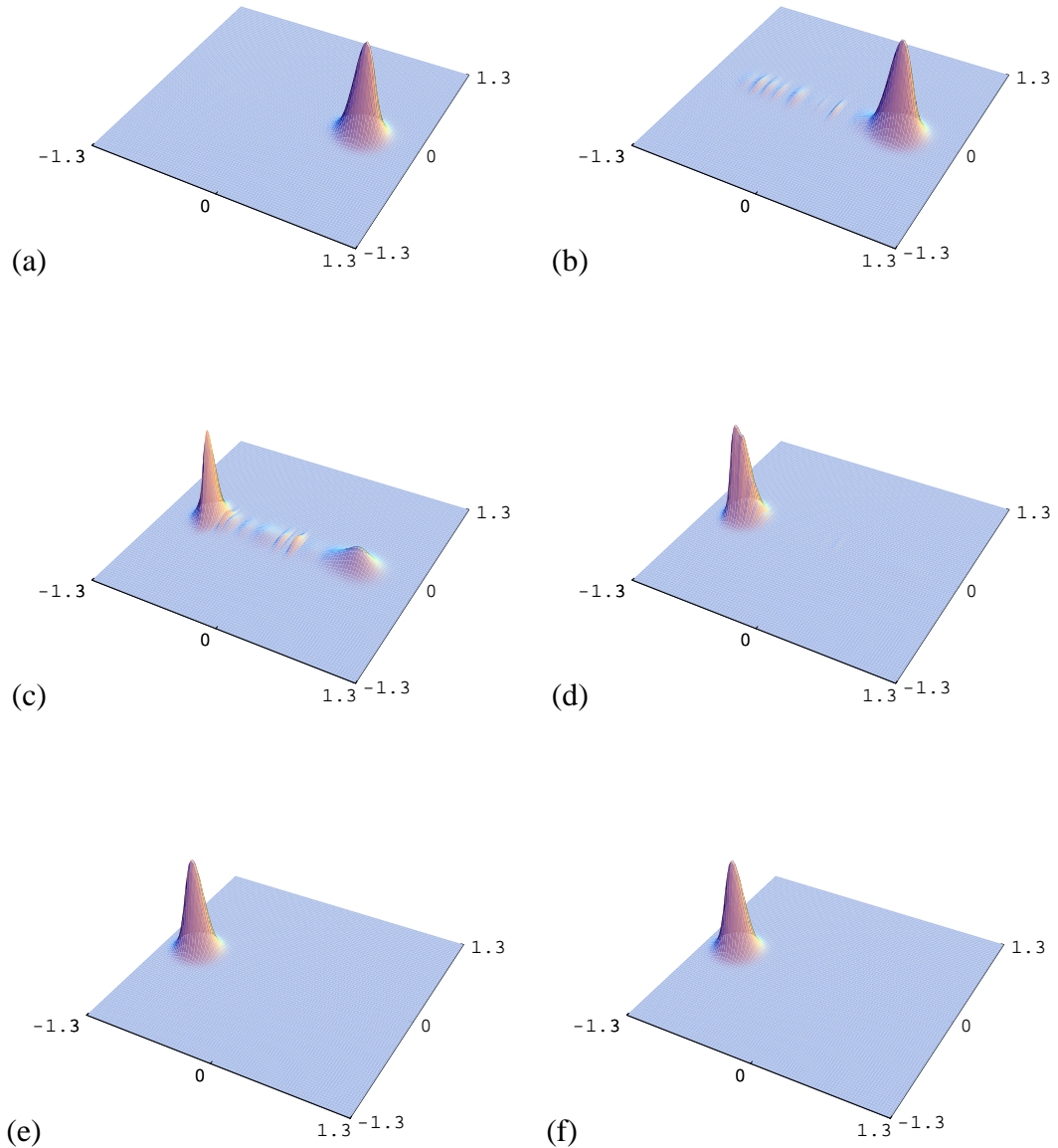


Figure 4.6: Final wave function for propagation through a double barrier with varying height. For these calculations, the wave function had median energy 0.082 eV and was propagated from left to right. The extent of the propagation space is  $-1.3 \mu m$  to  $1.3 \mu m$ . The potential height of and transmission through the double barrier was: (a) 0.027 eV and 1.0; (b) 0.054 eV and 0.96; (c) 0.082 eV and 0.36; (d) 0.11 eV and 0.0081 (e) 0.14 eV and  $8.4 \times 10^{-6}$  (f) 0.16 eV and  $7.3 \times 10^{-8}$ .

Take, for example, a long quantum wire with a resonant cavity or quantum transistor in the middle (see Sections 4.5 and 4.4 for more details). The long quantum wire may extend the entire spacial domain thus, the wave function never leaves the wire. However, once the wave packet has passed the resonant cavity or quantum transistor, it will no longer reflect so that the transmission and reflection coefficients will not change. By using the momentum space method to compute the transmission and reflection coefficients, once the wave packet has passed the area of interest, the components with forward and reverse momentum will give the transmission and reflection coefficients. However, if the real space method is used, you need to determine the amount of wave function on each side of the potential component of interest. Since the potential component of interest may be rather complicated (eg. multiple resonant cavities or bends and corners), writing a general algorithm to determine the amount on either side can be difficult. For this reason, the momentum space method was used for all computations performed during the studies for this thesis.

While the transmission and reflection calculated from the momentum space wave function will not add to 1, they will add to a constant, since

$$\int |\Psi(x,y)|^2 dx dy = 1 \quad (4.1)$$

$$= \int \Psi^*(x,y)\Psi(x,y) dx dy \quad (4.2)$$

$$= C \int \Psi^*(p'_x, p'_y) \exp(-i p'_x x - i p'_y y) \times \Psi(p_x, p_y) \exp(i p_x x + i p_y y) dp_x dp_y dp'_x dp'_y dx dy \quad (4.3)$$

$$= C \int \Psi^*(p'_x, p'_y) \Psi(p_x, p_y) \times \delta(p_x - p'_x) \delta(p_y - p'_y) dp_x dp_y dp'_x dp'_y \quad (4.4)$$

$$= C \int \Psi^*(p_x, p_y) \Psi(p_x, p_y) dp_x dp_y \quad (4.5)$$

which results in

$$\int \Psi^*(p_x, p_y) \Psi(p_x, p_y) dp_x dp_y = \frac{1}{C}. \quad (4.6)$$

The normalisation can be carried out numerically producing reliable transmission and reflection coefficients.

### 4.1.2 Momentum spectrum

Often, it is desirable to know what the transmission of each momentum state is. From the previous section, such information could be obtained by propagating many wave packets with very small momentum spread. Such wave packets would have large spatial distribution and thus require a large numerical grid to support the calculation. A better way is to compare the final momentum distribution with the initial momentum distribution (Yiu & Wang 1996). If  $\Psi_i(p_x, p_y)$  is the Fourier transform of the initial wave function and  $\Psi_f(p_x, p_y)$  is the Fourier transform of the final wave function, then the transmission amplitude  $T(p_x, p_y)$  is given by

$$T(p_x, p_y) \Psi_i(p_x, p_y) = \Psi_f(p_x, p_y), \quad (4.7)$$

where appropriate division for each  $p_x$  and  $p_y$  will produce the amplitude of transmission for that momentum state. If the transmission amplitude of one dimension is required, integration of the other dimension prior to the amplitude calculation yields the desired result

$$T(p_x) \int_y \Psi_i(p_x, p_y) dy = \int_y \Psi_f(p_x, p_y) dy. \quad (4.8)$$

Numerically, great care must be taken not to divide by zero or numbers effectively zero (due to computer precision). This can be overcome by discarding momentum states which are considered too small

$$T(p_x, p_y) = \frac{\Psi_f(p_x, p_y)}{\Psi_i(p_x, p_y)} \text{ for } |\Psi_i(p_x, p_y)| > \delta, \quad (4.9)$$

for some small number  $\delta$ .

The results produced will be for a range of momentum values but not all values. To obtain a larger range, the code can be run for several different initial wave function momentum and spreads, with the results combined together. This allows the characteristics of the device to be analysed with a small number of calculations.

Figure 4.7 shows the  $x-$  dimension momentum spectrum for propagation through a double barrier. As expected, momentum states with less energy than the barrier height do not transmit through the double barrier. For momentum states with considerably greater

energy than the barrier height, near perfect transmission results. Momentum states close in energy to the barrier height transmit to varying amounts with a resonant spike clearly evident at  $4.03 \times 10^{-26} \text{ kg m s}^{-1}$ . This momentum state aligns with an energy level of the system (in this case a double barrier) and resonantly propagates through the double barrier, as described further in Section 4.1.3.

### 4.1.3 Resonant tunnelling

The resonant tunnelling of the wave packet through the double barrier is due to the quantisation of states between the barriers. If the energy of the incident electron aligns with an energy level in the device, then it will resonantly tunnel through the device unhindered.

From Figure 4.7, it can be seen that resonant tunnelling occurs for an initial wave function peak momentum of approximately  $4.03 \times 10^{-26} \text{ kg m s}^{-1}$ . The resonant tunnelling is investigated further in Figure 4.8, which compares the propagation of a wave packet for resonant and non-resonant tunnelling. A small change in the initial energy of the wave packet causes the wave packet to go from almost zero transmission to almost complete transmission.

Such resonant tunneling can be utilised to build electronic components such as diodes and transistors (Alferov 2001). However, such phenomena can also result in a device being inoperable, as the electrons may be able to pass through the device undesirably.

### 4.1.4 Effects of magnetic fields

The transport of 2D electrons under the influence of an external magnetic field has attracted considerable interest recently, showing a range of interesting phenomenon with promising novel applications. For example, it has been used to probe nano-structured devices for impurities (Koonen et al. 2000), to study quantum ratchets (Christensson et al. 1998, Linke et al. 2000), quantum chaos (Narevich et al. 2000), and to understand the interference of different electronic paths (Entin & Mahmoodian 2000). They have also been proposed as a possible mechanism (when combined with a single electron transistor)

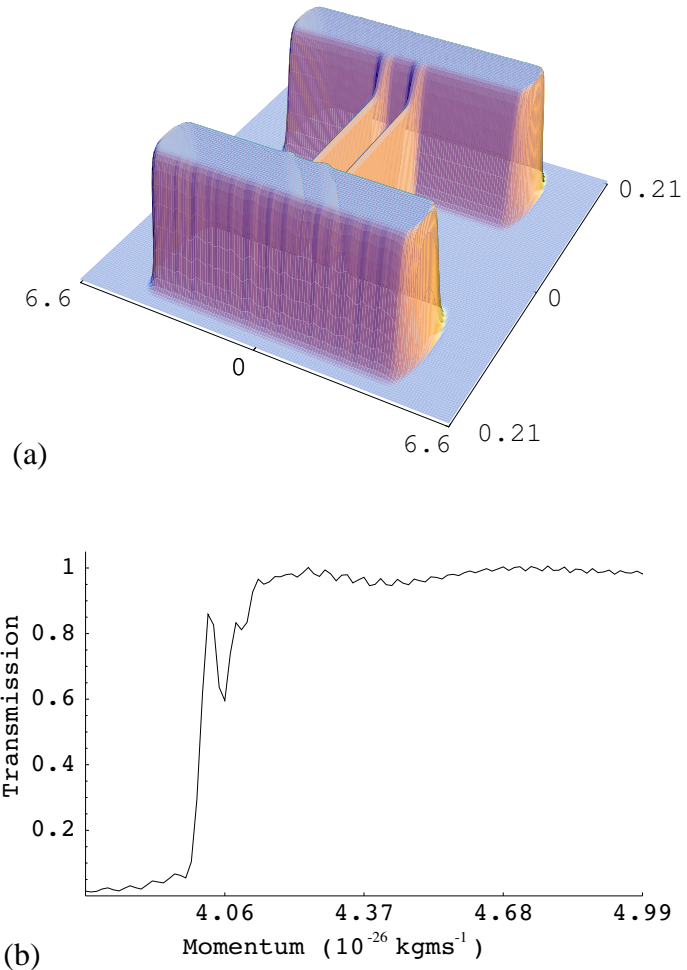


Figure 4.7: (a) Doubler barrier formed by walls with a potential height of  $0.11\text{ eV}$ , while the double barrier is of height  $0.081\text{ eV}$ ; (b) Momentum spectrum for the double barrier. The wave function peak momentum was  $4.00 \times 10^{-26}\text{ kg m s}^{-1}$  with a momentum spread of 20% in both the  $x-$  and  $y-$  dimensions. The momentum distribution of the initial and final wave functions were integrated over  $p_y$  to provide information about the  $x-$  dimension propagation.

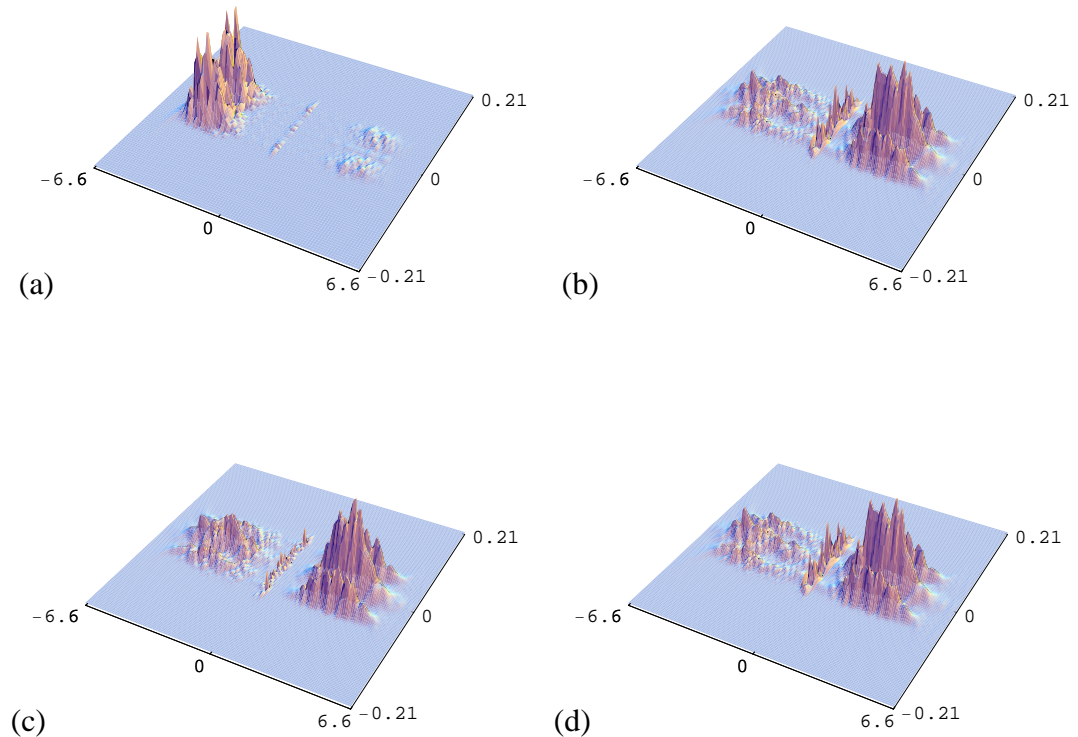


Figure 4.8: Comparison of resonant and non-resonant tunnelling. The initial momentum of each wave function is (a)  $3.97 \times 10^{-26} \text{ kg m s}^{-1}$ , (b)  $4.03 \times 10^{-26} \text{ kg m s}^{-1}$ , (c)  $4.06 \times 10^{-26} \text{ kg m s}^{-1}$  and (d)  $4.13 \times 10^{-26} \text{ kg m s}^{-1}$ . The transmission for each of these cases is (a) 0.057, (b) 0.87, (c) 0.80 and (d) 0.97.

to allow the spin of an electron to be determined on the qbit in a quantum computer (Kane et al. 2000).

While many experiments have been performed, a fully quantum mechanical model to describe the various systems involving external magnetic fields has not been available, especially for non-uniform and time-varying fields. Many classical and semi-classical models have been developed (Gallagher et al. 2000, Koonen et al. 2000, Linke et al. 2000, Narevich et al. 2000), but these fail to capture the full quantum nature of the physical systems at the nano-meter scale. As an example, Koonen et al. (2000) used a rather crude model in the analysis of their experimental data, which artificially cuts off parts of a wave function blocked by an electric potential. In their paper, they called for a more sophisticated model to help building a detailed picture of the shape and size of the density fluctuation in a 2D electron gas.

As expected, the propagation of a Gaussian wave function through a double barrier with an applied magnetic field produces circular paths, with the reflected components of the wave function curving in the opposite direction to the transmitted wave function.

As is clearly depicted in Figure 4.9 and Figure 4.10, the amount of the wave function transmitted is affected by the magnetic field. Energy components originally propagating in the  $x$ - dimension are rotated into the  $y$ - dimension. Consequently, the  $x$ - component, which causes tunnelling through the device, can be different to the case with no applied magnetic field. The extreme case occurs when the wave function completely reverses its propagation while between the barriers. In this case, with no increase in barrier height, the wave function completely reflects.

### 4.1.5 Time reversal

The Chebyshev propagation scheme allows the propagation of an arbitrary wave function forward in time to a final state. By reversing the time, that final state can also be propagated backward using exactly the same propagation scheme. If the numerical error is being introduced at each term in the summation or time step in the propagation, then the forward and backward propagation wave function should be considerably different to the

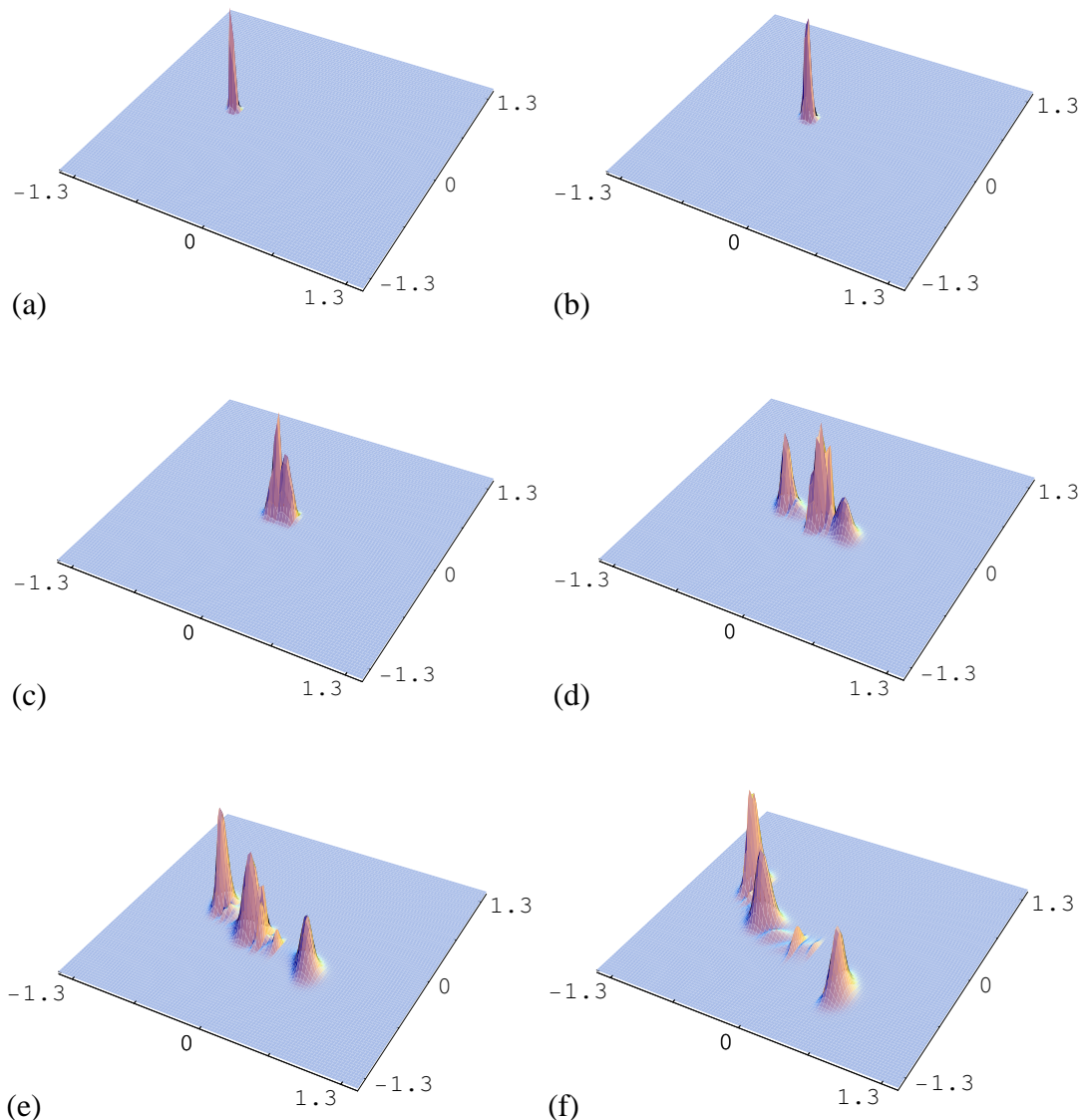


Figure 4.9: Propagation through the double barrier depicted in Figure 4.1 with a strong applied magnetic field of  $0.4 \text{ T}$ . (a) is the initial wave function,  $t = 0$  (b) is the propagated wave function at  $0.4 \text{ ps}$ ; (c)  $0.8 \text{ ps}$ ; (d)  $1.2 \text{ ps}$ ; (e)  $1.6 \text{ ps}$  and (f) at  $2.0 \text{ ps}$ .

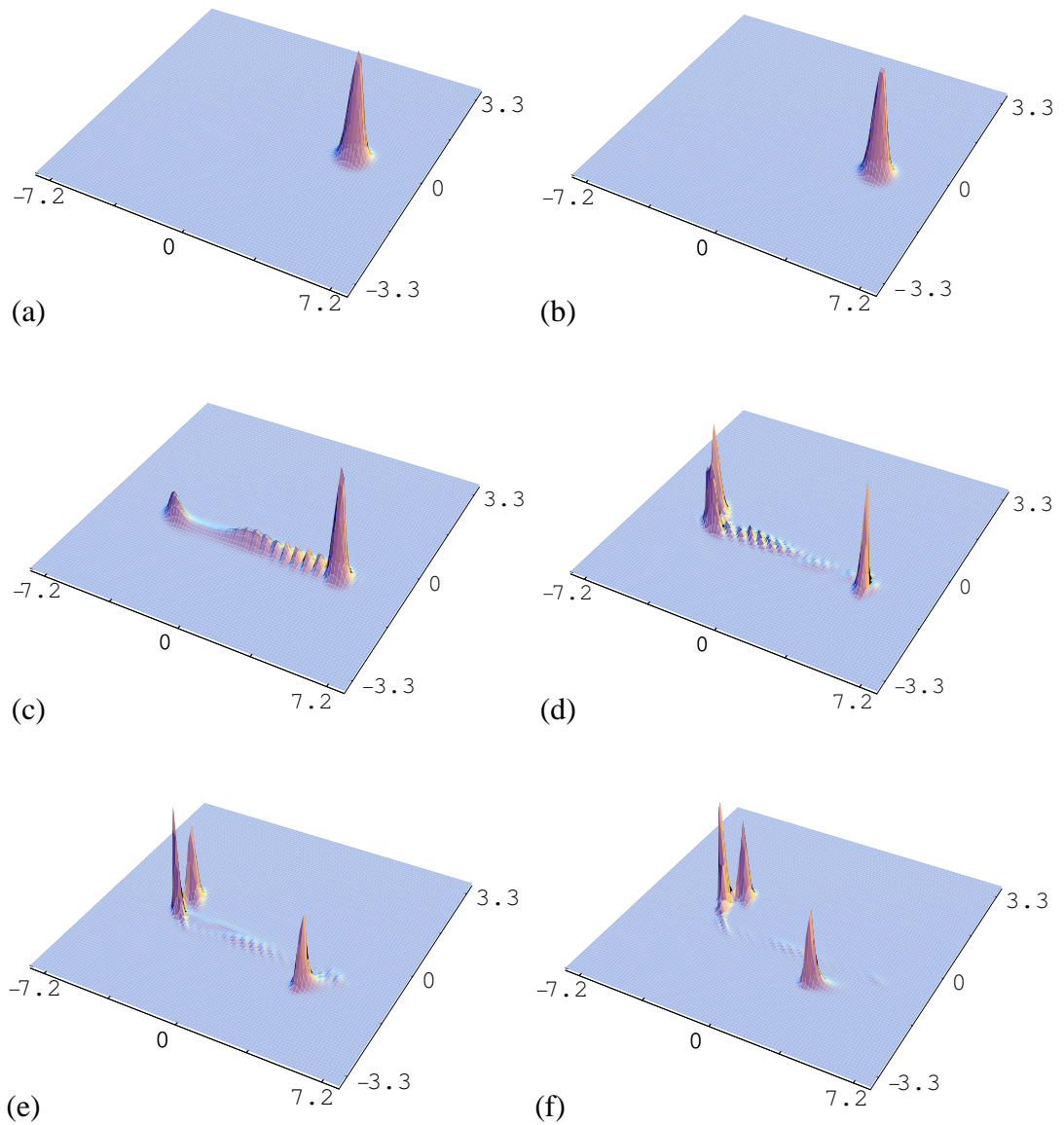


Figure 4.10: Momentum space propagation for the wave function propagation shown in Figure 4.9. The coordinate units shown are  $10^{-26} \text{ kg m s}^{-1}$ , where  $7.2 \times 10^{-26} \text{ kg m s}^{-1}$  is the maximum momentum in the  $x-$  dimension and  $3.3 \times 10^{-26} \text{ kg m s}^{-1}$  is the maximum momentum in the  $y-$  dimension.

initial wave function.

Figures 4.11 and 4.12 demonstrate how the initial wave function is reproduced upon forward and then reverse propagation. This process poses a very strong test of the accuracy and numerical stability of the Chebyshev propagation scheme.

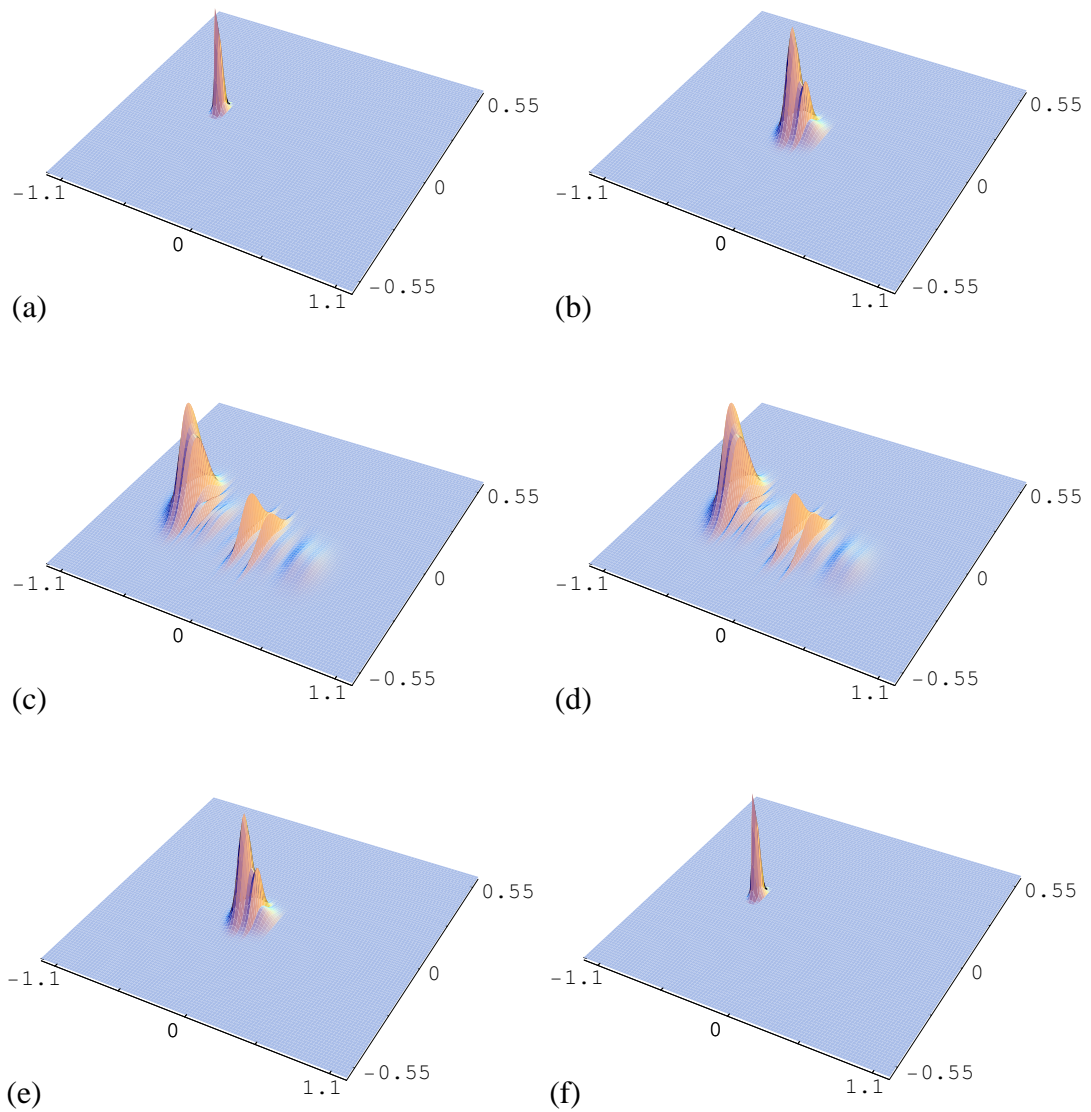


Figure 4.11: Propagation of the wave packet to a final state and then back to the initial state under time reversal. This is under a strong applied magnetic field of  $0.4\text{ T}$  and a double barrier electrostatic potential.

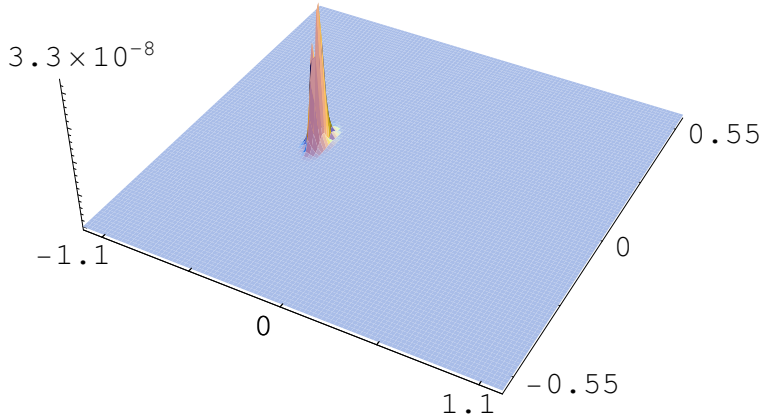


Figure 4.12: Relative error between initial wave function and the wave function propagated forward and then backward in time. This is for the propagation displayed in Figure 4.11.

## 4.2 Nano-rings

Nano-rings are ring shaped potentials which allow the wave function to travel around each arm of the ring and then interfere at the outlet port. By altering the length of each arm or applying a magnetic field, constructive or destructive interference can be achieved. Such devices have been suggested as possible ways to detect the spin of an atomic electron (Josephs-Franks et al. 2000) in a silicon substrate and has been suggested for use in a quantum computer similar to that proposed by Kane (1998).

### 4.2.1 Electron propagation in a nano-ring

As a prototype case, consider a nanometre scale ring structure shown schematically in Figure 4.13(a) with the confinement potential depicted in Figure 4.13(b). Electron transport between the source and the drain is dependent on quantum waves propagating around the ring and undergoing interference with reflections from the potential barriers. These barriers can be raised or lowered by changing the negative voltage applied to the metal gates, as shown in Figure 4.13(b).

The height of the potential walls is chosen to be 1.0 eV, while the space spanned by the potential is  $1.06 \times 0.53 \mu m$ . The incoming electron has a dominant energy of 0.82 eV

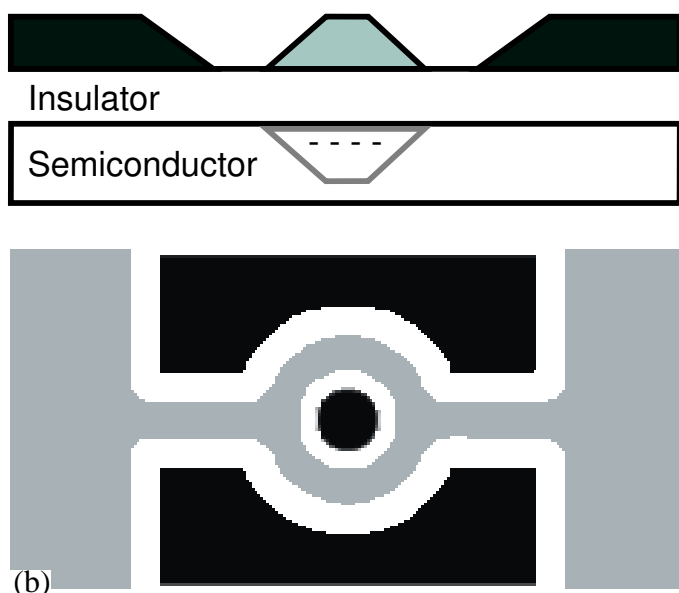
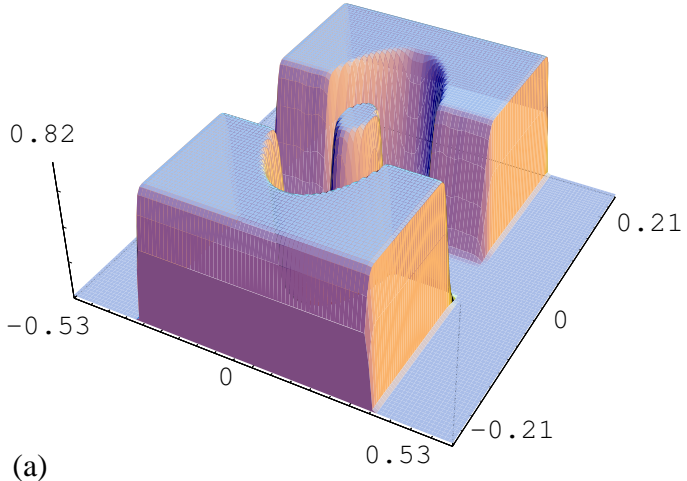


Figure 4.13: (a) The side and top view of the device. The dark grey regions are negatively charged metal gates and the light grey area is positively charged. (b) The confinement potential. The middle metal gate (i.e. the light grey area) is biased positively to induce conduction electrons in the semiconductor layer. The side and central gates (i.e. the dark grey area) are biased negatively to confine the conduction electrons in a narrow tunnel.

with a spread in momentum of 7.5%. The width of the propagation channel is  $0.11 \mu m$  and the radius of the ring is also  $0.11 \mu m$ . The total time of propagation is  $0.41 ps$ , which was equally divided into 6 time steps of  $0.068 ps$ .

The propagation of the wave function is shown in Figure 4.14. Plot (a) is the initial wave function with (b)-(f) showing the wave function at the end of each time step. As shown, the wave function travels along, hits the middle pole of the ring, part of the wave function reflects from the pole with the rest propagating around it.

Figure 4.15 shows the error between the wave function propagated forward in time and the wave function propagated backward in time to the same position. This error is the difference between the two wave functions divided by the maximum value of the forward propagated wave function. Plot (a) is the error between the initial wave function and the returned wave function. Plots (b)-(f) show the error between the forward wave function and the wave function propagated back to the same position. As can be seen the error is about  $10^{14}$  times smaller than the amplitude of the corresponding wave function, indicating that the propagation scheme is extremely accurate and self consistent.

Throughout the propagation, the relative change in the norm of the wave function and the relative change in energy of the system were both in the order of  $10^{-14}$ . The comparison with the known solution of free space propagation was also extremely good and the error was approximately  $10^{-16}$ , which is of the order of the machine accuracy (double precision). The addition of a non-zero potential introduces negligible error, but the computational time and working arrays increase due to the requirement of a finer grid.

### 4.2.2 The Aharonov-Bohm ring

As an electron passes through an Aharonov-Bohm ring (depicted in Figure 4.16), its wave function explores both arms of the ring and then interfere to produce a transmission. By applying a magnetic field, the transmission can be made to undergo oscillations, as shown in Figure 4.17, where the frequency is determined by the geometry of the device.

Figures 4.18 and 4.19 show the effect the magnetic field has on the wave function as it

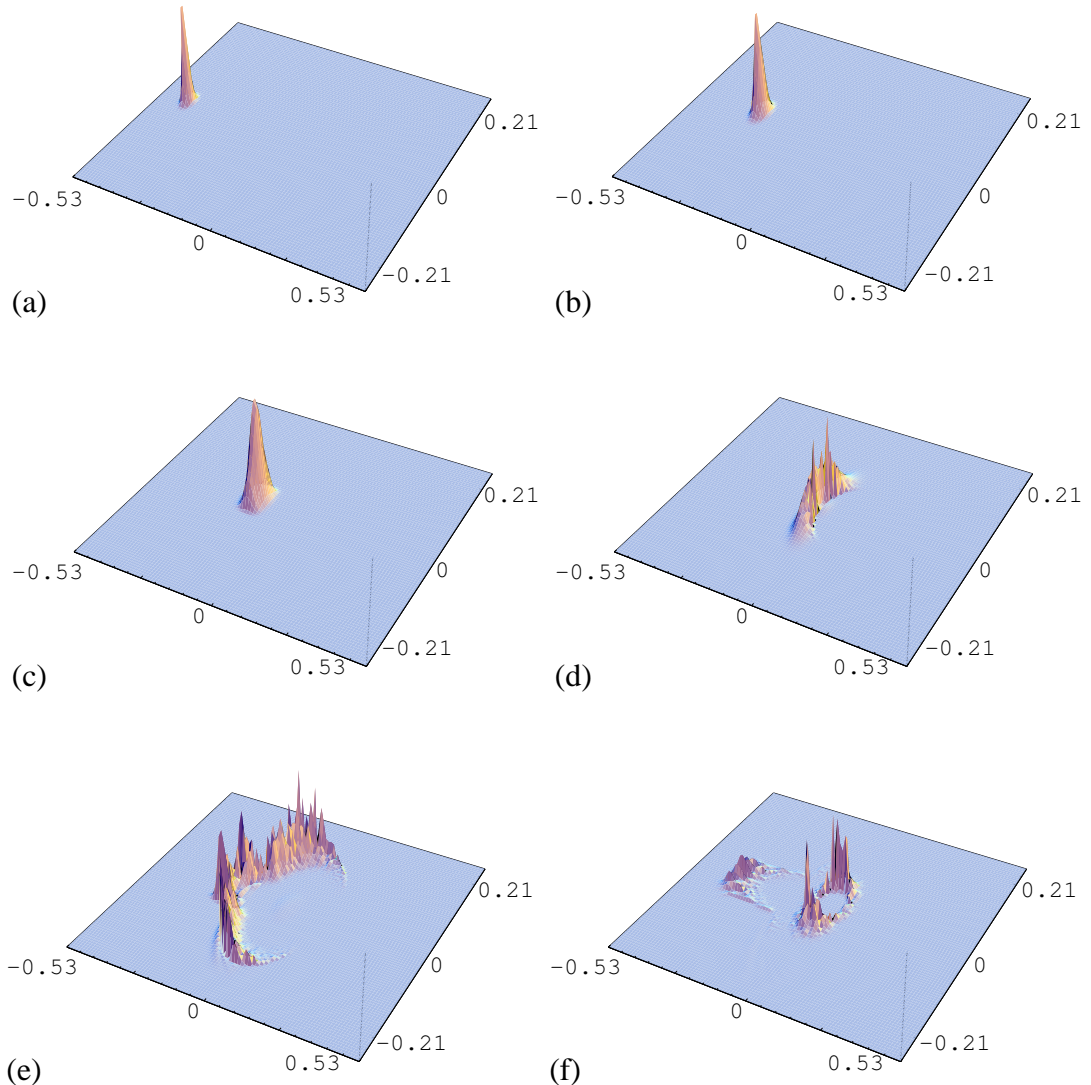


Figure 4.14: Propagation of the wave function through the potential. (a) Initial wave function. (b)-(f) Wave function at the end of each time step.

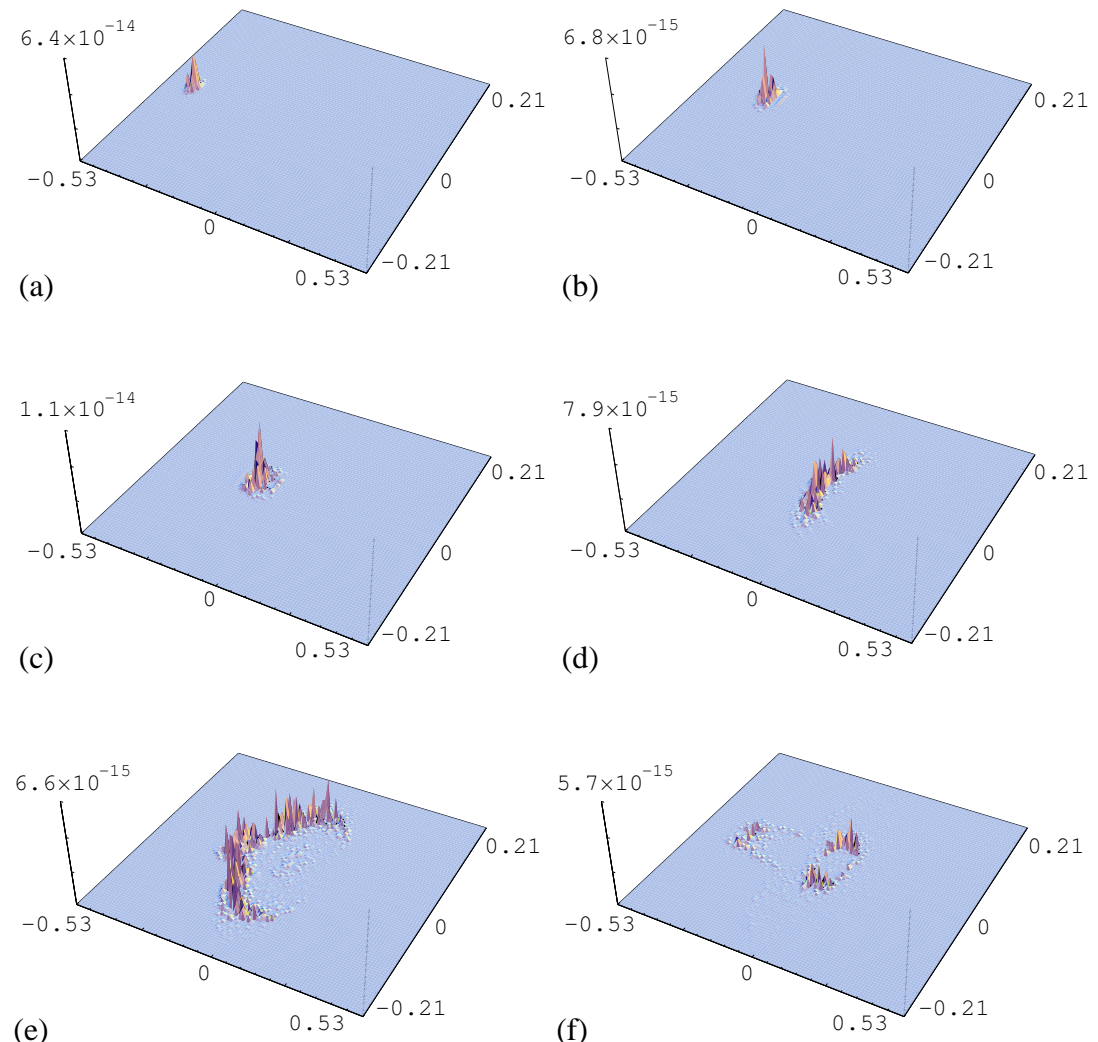


Figure 4.15: Error between forward and reversed propagation. (a) Error between the initial and the final time-reversed wave function. (b)-(f) Error between the wave function at the end of each time step and the wave function propagated backwards to the same time.

propagates through the device. The magnetic field can cause more of the wave packet to enter the ring, rather than reflecting off the central pillar of the potential, as the comparison between Figure 4.18(c) and 4.19(c) demonstrate. Understanding the phase relationship between the electron and the transmission will allow such devices to be constructed and used with accuracy. The results presented demonstrate how the computational method developed allows the effects of an external field (in this case, magnetic) to be studied in great detail.

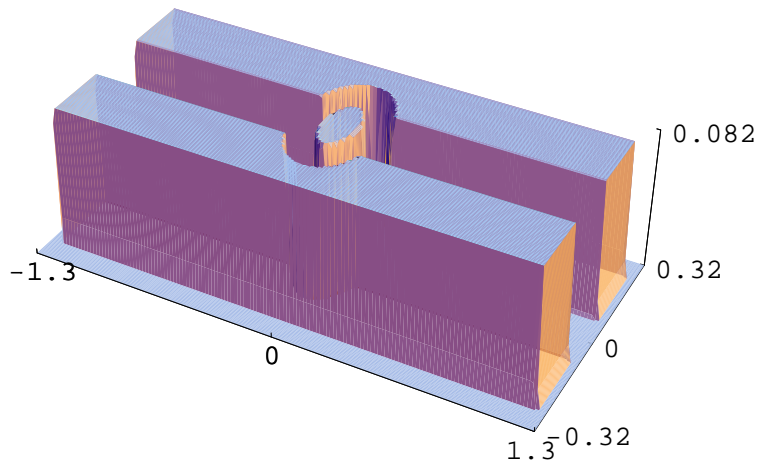


Figure 4.16: Ring potential used to study Aharanov Bohm oscillations.

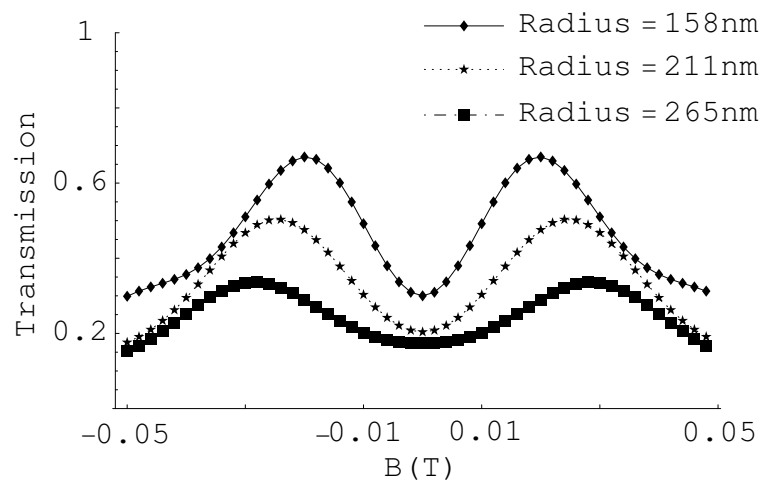


Figure 4.17: Aharonov Bohm oscillations for the transmission of an electron through a ring with an applied magnetic field, varying between  $-0.05T$  to  $0.05T$ . Such oscillations are in line with those seen experimentally (van der Wiel. et al. 2001).

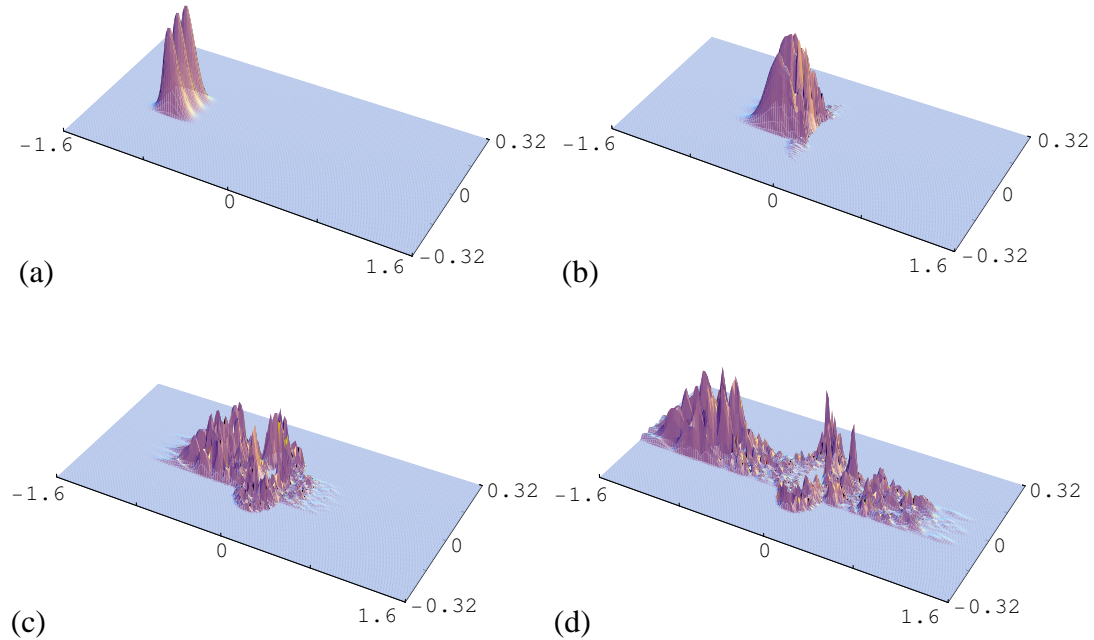


Figure 4.18: Propagation of an electron through the ring potential with no magnetic field applied.

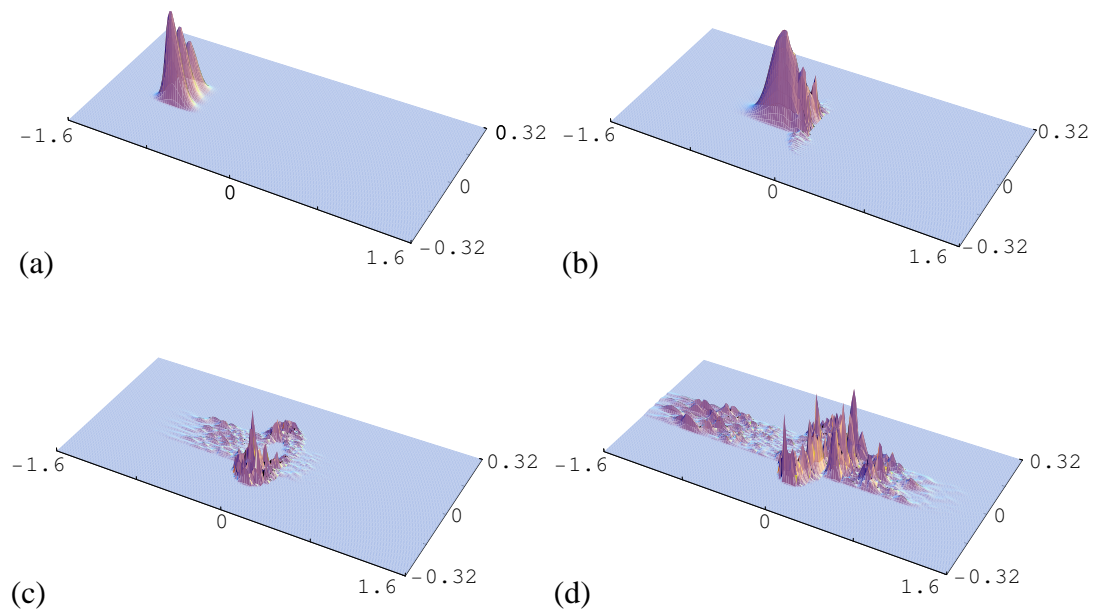


Figure 4.19: Propagation of an electron through the ring potential with an applied magnetic field of  $0.018T$ .

## 4.3 Quantum wire

As the name suggests, a quantum wire is a potential that resembles a wire. That is, electrons are effectively constrained to movement in one dimension, along the wire. The geometry of the quantum wires greatly effects the transport properties through the wire, with vast difference in the conductance for seemingly small changes in geometry or incident electron energy. Various aspects of quantum wires have been studied and the results are presented below.

### 4.3.1 Length

The length of a quantum wire, as might be expected, has little effect on the propagation of an incident electron. Once the wave function enters the wire, there is no mechanism for reflection or scattering. Consequently, that component of the wave function in the wire, with a positive momentum, will continue to propagate through the wire unobstructed. However, if the wire is shorter than the spatial spread of the electron wave packet, then tunnelling of the electron through the device becomes likely. This can lead to resonant states between the point contacts and resonant propagation, much like the double barrier discussed in Section 4.1.3.

To demonstrate how little the length of the quantum wire effects propagation, Figure 4.20 shows the transmission for three different width wires as the length of the wire increases. For a quantum point contact (zero length wire) the transmission is greatest, as the electron can tunnel through the potential barrier since it is very thin. However, once the wire is lengthened, the wave function is no longer able to tunnel through the barrier and the transmission stabilises. Potentials and final wave functions for two wires (with  $0.042\mu m$ ) of different lengths are shown in Figures 4.21 and 4.22. Both quantum wires produce a transmission coefficient of 0.4023. The peak energy of the initial wave function is  $0.054\text{ eV}$  and is initially positioned  $0.15\mu m$  away from the potential.

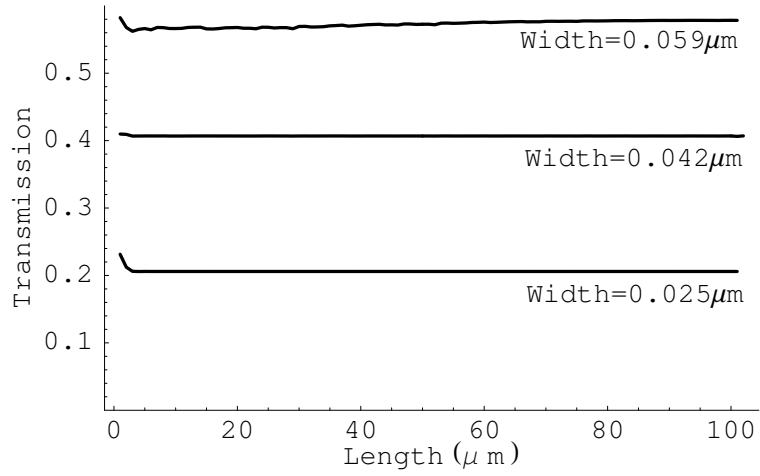


Figure 4.20: Transmission through wires of three different widths. As the length of the wire is increased, the transmission becomes constant.

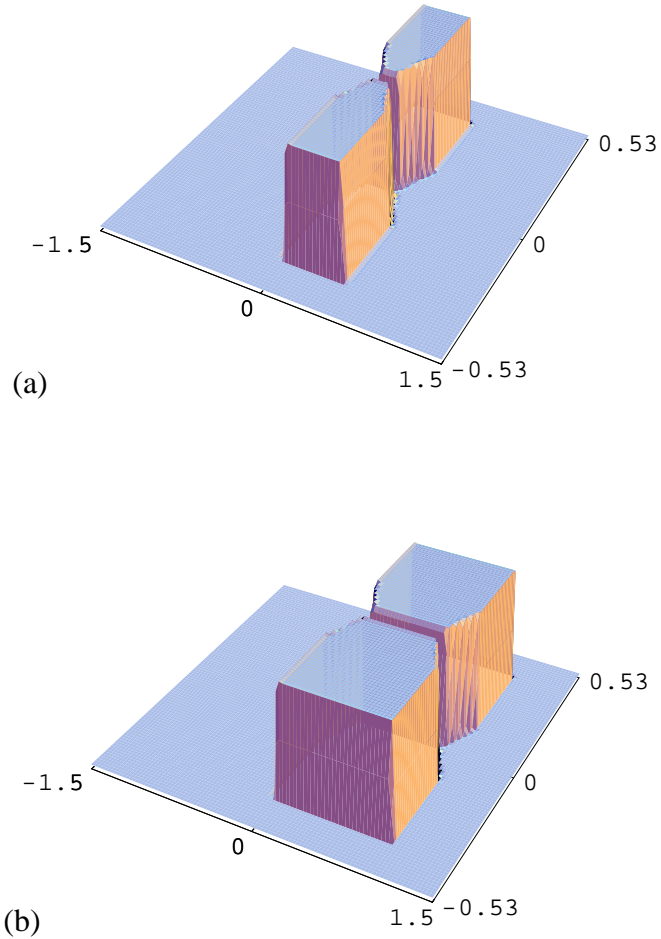
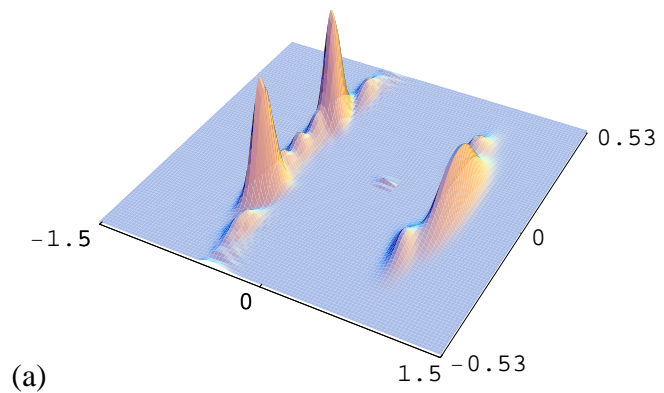
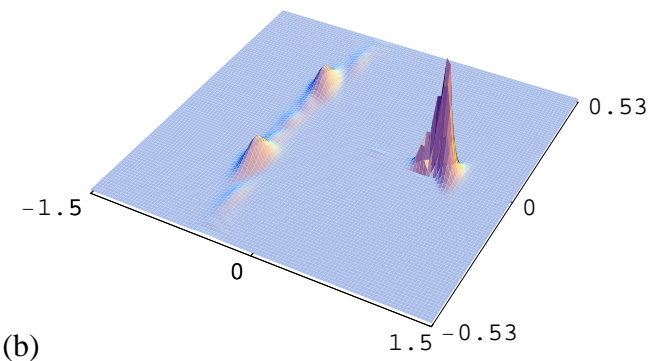


Figure 4.21: (a) Short quantum wire with flange, length of wire without flange is  $0.21 \mu m$  and the potential height is  $0.11 eV$ . (b) Long quantum wire with flange, length of wire without flange is  $0.74 \mu m$ .



(a)



(b)

Figure 4.22: (a) Final wave function after propagation through the short quantum wire. The final transmission coefficient is 0.4023. (b) Final wave function after propagation through the long quantum wire. The final transmission coefficient is 0.4023.

### 4.3.2 Width and quantised conductance

The conduction of electrons through quantum wires has been demonstrated theoretically and experimentally to be highly dependent on the width of the wire. As the wire becomes wider, more quantised energy levels become available for transport. As each level aligns with the energy of the incoming electron, a jump in conductance is observed. Eventually, the wire becomes large enough that effectively there exist a continuum of states within the wire and the electron will propagate with little or no geometric effects - the classical limit.

#### Conductance

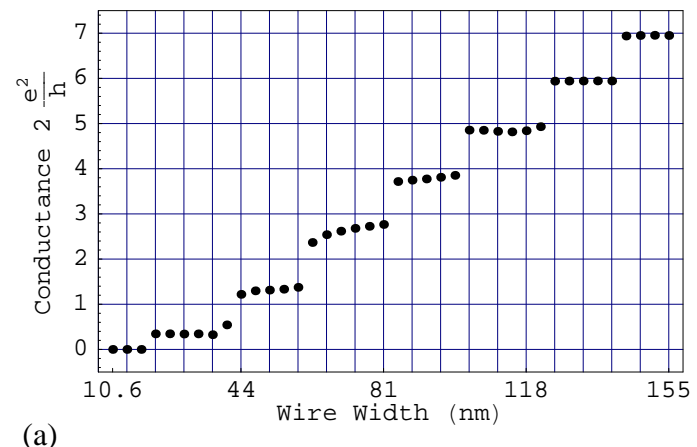
Experimentally, the main quantity measured is the conductance  $G = 1/\mathcal{R}$  where  $\mathcal{R}$  is the resistance of the device. This measures the ability of the current to flow through the device. Current is an average measure of electron drift through a device and is not readily applicable to devices with low electron densities. Consequently, a formulation for the conductance is required that refers to the transmission of individual electrons.

A standard method to analyse such devices was developed using the Landauer formulation (Ferry & Goodnick 1997, Gold 1988)

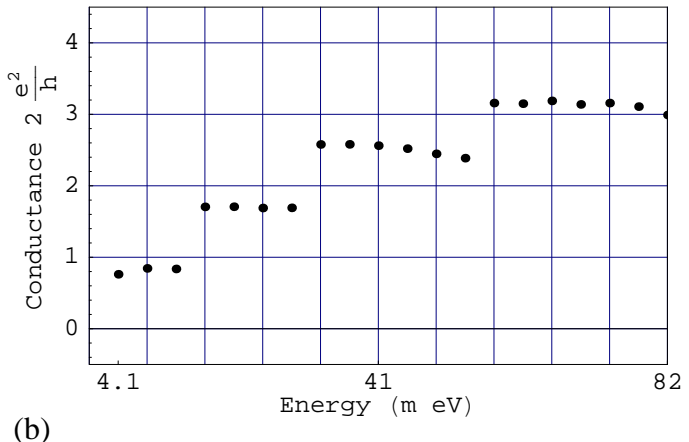
$$G = \frac{I}{V} = \left( \frac{2e^2}{h} \right) \frac{T}{1-T} = \left( \frac{2e^2}{h} \right) \frac{T}{R} = \frac{2e^2}{h} N T , \quad (4.10)$$

where  $N = \text{Int}[2W/\lambda_f]$  is the integer number of modes across the quantum wire,  $\lambda_f$  is the Fermi-wavelength,  $T$  is the transmission coefficient, and  $W$  is the width of the wire (Datta 1995). This formula applies to a single one-dimensional channel (quantum wire) where a two terminal measurement is made, that is, the potential drop across the source and drain. As more channels become available for transport, the conductance changes by precisely  $2e^2/h$  giving rise to the characteristic conductance curves, see Figure 1.7.

It is found that the model and computational code were able to reproduce the conductance quantisation as observed experimentally (van Wees et al. 1988, Kane et al. 1998) and predicted theoretically by time independent models (van Wees et al. 1988, Szafer & Stone 1989, Csontos & Xu 2000), as shown in Figure 4.23.



(a)



The results shown in Figure 4.23(a) were calculated for a wire of  $211.7\text{ nm}$  in length and flange angle of  $18^\circ$  with an incident energy of  $0.054\text{ eV}$ , corresponding to a Fermi-wavelength  $\lambda_f \approx 21\text{ nm}$ . As anticipated by previously studies, the conductance changes as a stepping function with respect to the wire width. The results shown in Figure 4.23(b) were calculated for a wire  $106\text{ nm}$  in length,  $18^\circ$  of flange angle, and constant width of  $100\text{ nm}$ . Again, quantised conductance including a dip-like structure between adjacent plateaus were obtained, as were also observed by Csontos & Xu (2000).

In the calculation, the initial electron wave function is a Gaussian wave packet with a small spread in its energy (approximately 5%). As the wave packet enters the quantum wire, components of the wave packet will propagate through different available channels. As the central momentum aligns with a particular channel, a slight peak in transmission is observed, and as it moves away, a slight dip occurs. These effects are reflected in the conductance presented in Figure 4.23 as they relate by Equation 4.10.

### 4.3.3 Flange angle

One area of quantum wires where little or no experimental research has been performed is the connection of quantum wires to the classical leads. Experimentally, this is difficult as it requires new devices to be constructed for each shape or modification required to study. The theoretical investigation, consequently, has also been slow to develop in this area. This section studies what happens as the flange connecting the quantum wire is slowly opened and how the transmission is affected.

An example confinement potential  $\mathcal{V}(x,y)$  is shown in Figure 4.24, together with the initial electron wave packet before entering the quantum wire. The flange shown here has an angle of  $18^\circ$  and the wire width is  $46.6\text{ nm}$ . The amplitude of the wave packet has been scaled to be visible on the graph with the potential. The potential walls are of finite height, but they are significantly higher than the incident energy of the incoming electron. As a result, leakage from the potential barriers is negligible. For the calculations presented, the potential height is typically  $0.11\text{ eV}$  and the incident energy typically  $0.054\text{ eV}$  with a 5% spread.

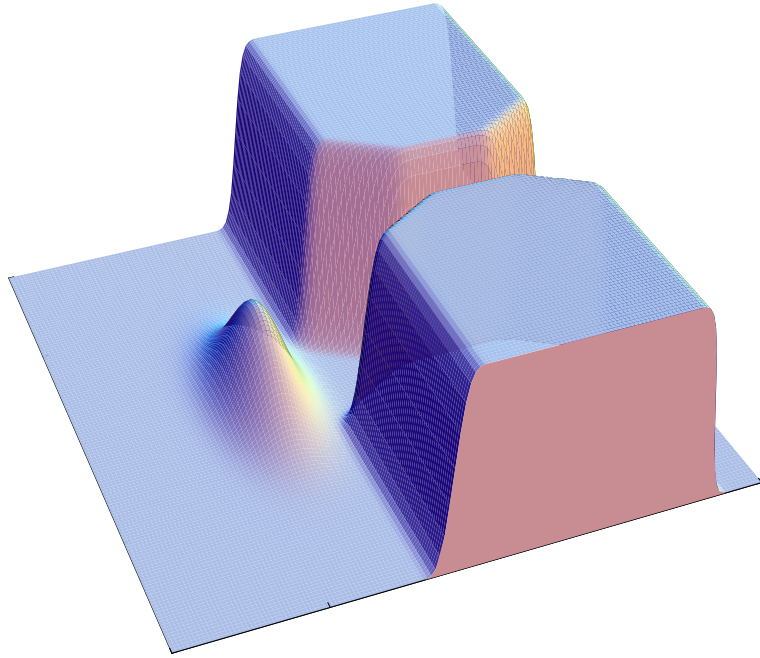


Figure 4.24: Confinement potential and initial wave packet used in the calculations. The wave packet has been scaled to enable visualisation.

Calculations were carried out for a range of flange angles (from  $5^\circ$  to  $85^\circ$ ) and wire widths (from  $14.8 \text{ nm}$  to  $46.6 \text{ nm}$ ). The length of the wire was  $211.7 \text{ nm}$  (with flange) or  $106 \text{ nm}$  (without flange), and the length of the flanges was  $106 \text{ nm}$ . It was found that the transmission behaviour did not change when a longer or shorter wire was examined (see Section 4.3.1). The structures studied here are approximately an order of magnitude smaller than those examined experimentally by Kane et al. (1998). Nevertheless, the underlying physics at work should be equivalent. Transmission coefficients are obtained by integrating the transmitted wave packets in the region to the right of the quantum wire. Great care was taken to ensure that numerical error was minimised. It was also ensured that the final wave packet emerged from the interaction region and the calculated transmission coefficients are independent of the propagation time.

Calculations were carried out using smooth-wall potentials as opposed to hard-wall potentials. The geometry used in the calculations is similar to those shown in Kane et al. (1998) and Sohn et al. (1996) pp. 5-6. The smooth-wall potentials are closer to reality as demonstrated, for example, from self-consistent calculations (Laux et al. 1988).

The main focus of this work is on the behaviour of electron transport in a two-dimensional

nano wire with flanges of different angles. Shown in Figure 4.25 are the calculated conductance as a function of flange angle for three different wire widths and a comparison for a width of 46.6 nm between hard-wall and smooth-wall potentials. The overall behaviour is in agreement with expectation. For example, if the flange angle is small (close to  $0^\circ$ ) the structure is effectively a longer wire without flanges, while a large flange angle (close to  $85^\circ$ ) characterises a short wire without flanges. Consequently, their transmission properties should be similar. This is demonstrated by the results having roughly the same transmission probability for small and large angles. The results also show that a smoothed potential doesn't change the overall shape of the curve.

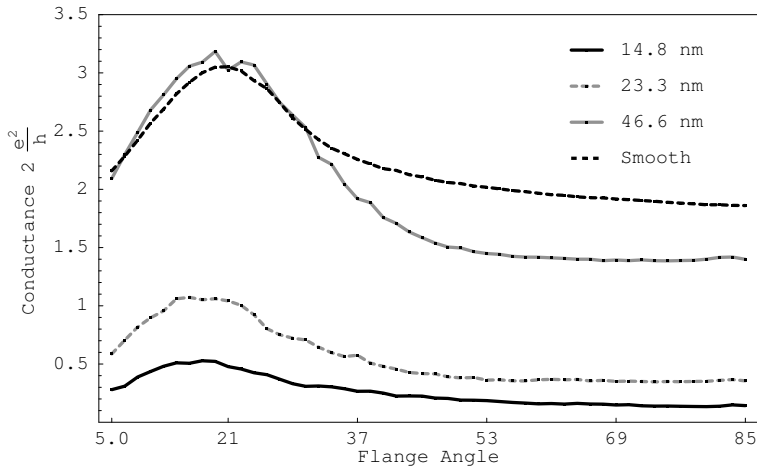


Figure 4.25: Conductance for different flange angles from  $5^\circ$  to  $85^\circ$ . Results for three different wire widths are shown: 14.8 nm; 23.3 nm; 46.6 nm; and 46.6 nm with a smooth-wall potential.

An interesting result is the fact that the maximum transmission does not occur at  $45^\circ$  which this type of symmetry argument suggests. In fact, the flange angle in the nano wire fabricated by Kane et al. (1998) is approximately  $45^\circ$ . The maximum transmission actually occurs at approximately  $18^\circ$  regardless of the wire width or length. It is anticipated that if Kane et al. changed the flange angle in their nano wire, an enhanced transmission would be observed.

By looking at the actual propagation of the wave function for the maximum transmission case and comparing it to the case for a flange angle of  $45^\circ$ , an interesting observation is made (see Figure 4.26 and Figure 4.27). In the  $45^\circ$  case, the wave function has partial reflection from the flange and the wire as expected. However, in the maximum transmission

case, it appears as though the wave packet first reflects from the flange and then resonantly reflects from the inlet after being trapped for a short period of time (in the order of  $0.2\text{ ps}$ ). Such resonance trapping allows the wave packet to re-adjust its momentum components and, as a result, enhances the overall transmission through the wire.

In addition to changing the width of the wire, the energy of the incoming wave packet was also varied to see if the optimal angle is changed. It was found that with double the initial energy ( $0.109\text{ eV}$ ) the peak transmission moved about  $3^\circ$  to the left (i.e. smaller angle). Similarly with half the initial energy ( $0.027\text{ eV}$ ) the peak transmission moved about  $3^\circ$  to the right (i.e. larger angle). For all calculations, the same energy spread of 5% was used, which means that the width of the Gaussian wave packet remains the same. It was also found that increasing the height of the potential (from  $0.109\text{ eV}$  to  $0.163\text{ eV}$ ) did not alter the transmission coefficients in any way.

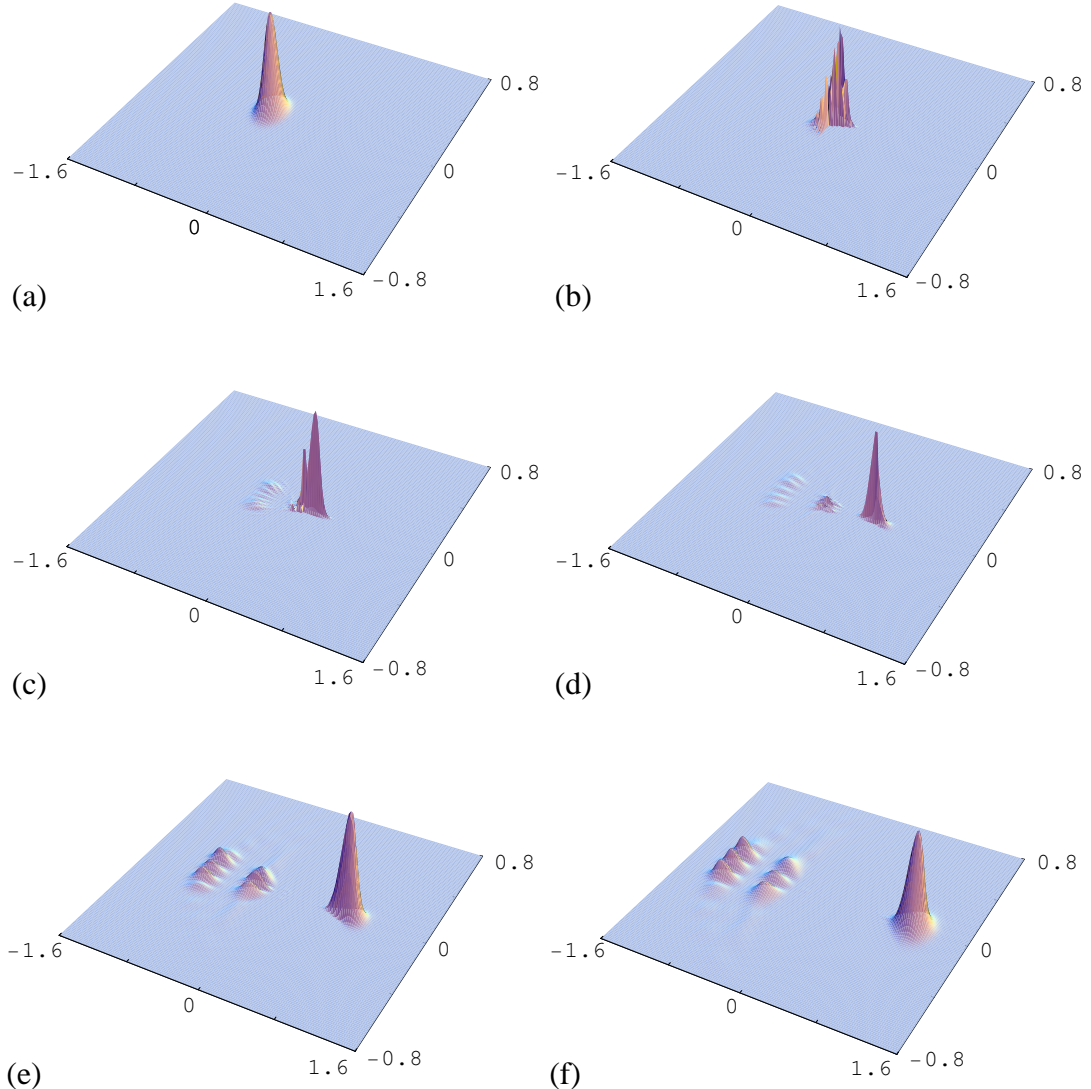


Figure 4.26: Propagation of the electron wave packet for a flange angle of  $18^\circ$ . Top to bottom, left to right  $t = 0, 0.356, 0.712, 1.068, 1.424$  and  $1.78$  ps.

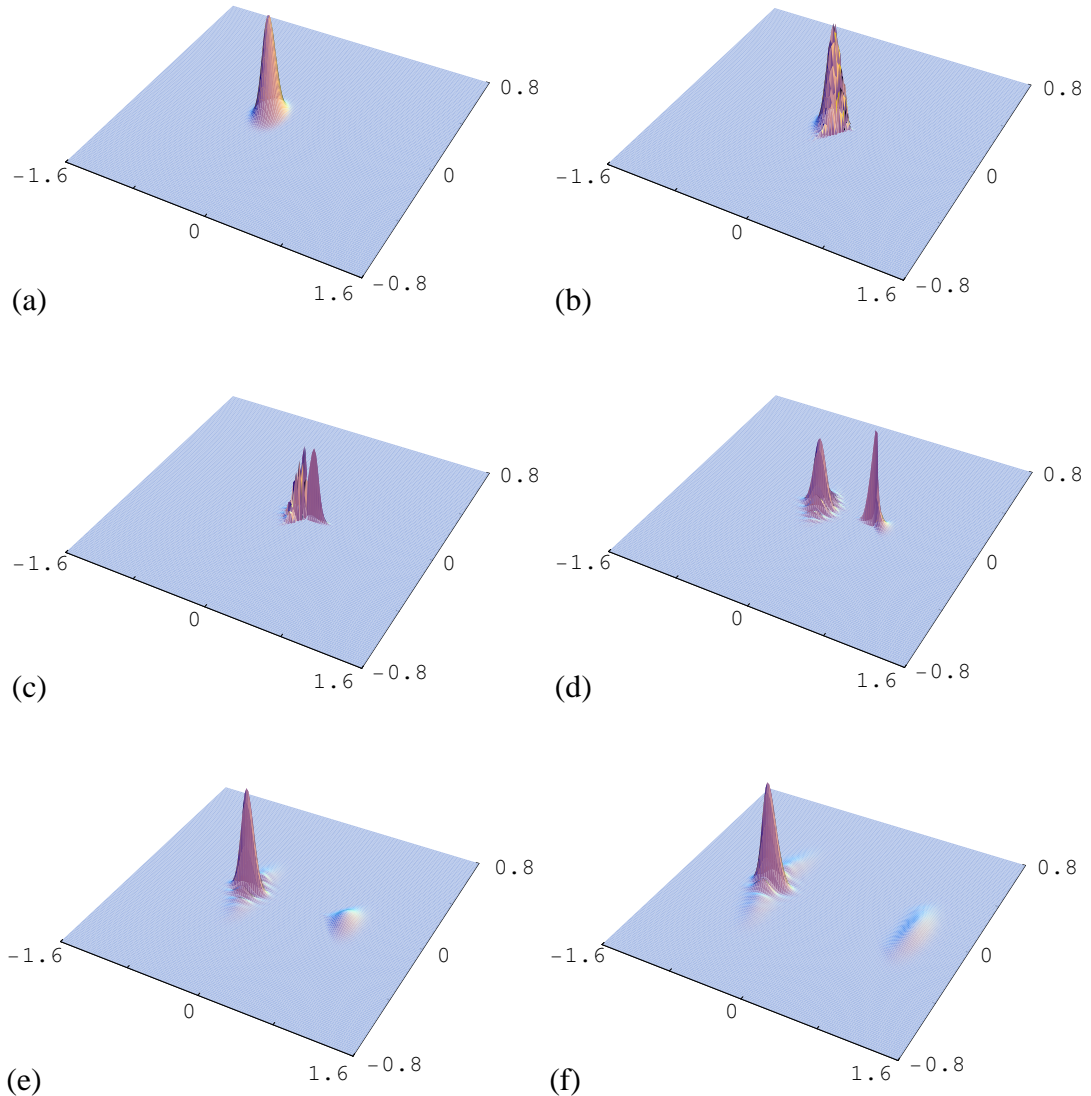


Figure 4.27: Propagation of the electron wave packet for a flange angle of  $45^\circ$ . Top to bottom, left to right  $t = 0, 0.356, 0.712, 1.068, 1.424$  and  $1.78 \text{ ps}$ .

## 4.4 Quantum transistor

The construction of a quantum transistor has generated much interest (Sugaya et al. 2002, Martin et al. 2003, Buehler et al. 2003). Transistors form the basic building blocks of current silicon chips and a reduction in size of the transistor leads directly to a reduction in size and required power of a silicon chip. A quantum transistor is able to alter the phase of a single electron, allowing very small electronic devices to be constructed. Such a device will also have the very low power consumption, as only a single electron will be required to operate it.

The quantum transistor is a simple device which uses interference to prevent or allow transmission. A small gate is added to the side of a quantum wire, which can be adjusted to control the potential depth in the side stub, see Figure 4.28. This in turn changes the phase of part A and part B of the wave function resulting in complete transmission through to complete reflection. The exact potential required for the device to operate correctly is highly dependent on the energy of the transport electron, which can be determined from other device characteristics.

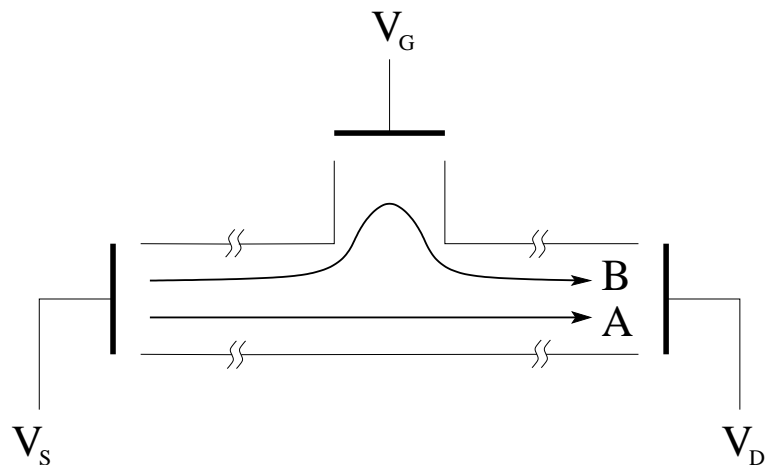


Figure 4.28:  $V_S$  is the source,  $V_D$  is the drain and  $V_G$  is the gate voltage. By reducing the gate voltage, the electron will be drawn into the stub, path A, inducing a phase shift with respect to path B. By tuning the voltage of  $V_G$  the transmission can be altered anywhere between zero and one.

Figure 4.29 shows the quantum transistor potential, while Figure 4.30 shows the final wave function after propagation through the device. Changing the bias on the side gate

clearly acts as a quantum transistor and allows the electrons to be fully transmitted or reflected.

Quantum transistors have been constructed out of carbon nano tubes and have been demonstrated to operate at room temperature (Tans et al. 1998). Their construction out of semiconductor material has also been performed, allowing precise control over single electron flow.

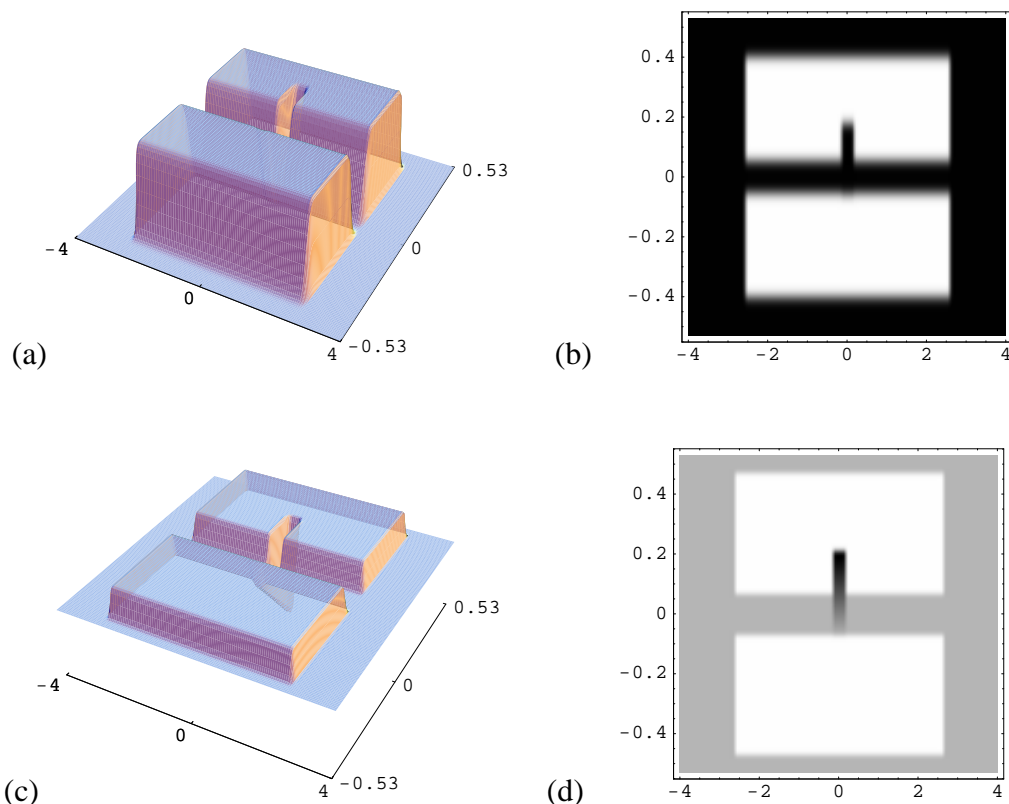
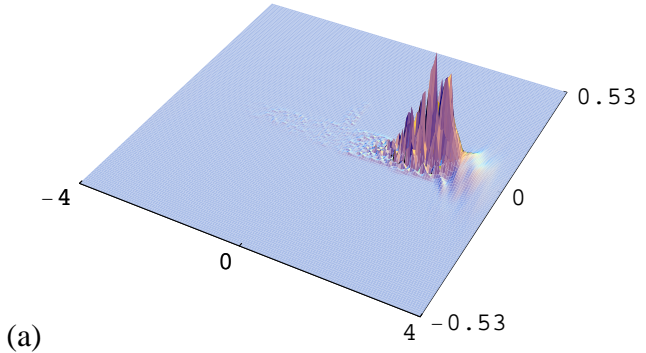
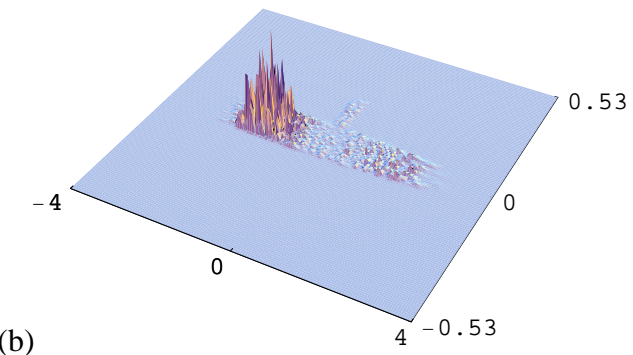


Figure 4.29: (a) Quantum transistor potential with no bias applied to small side gate, (b) is the density plot of the same potential. The potential height is  $0.082 \text{ eV}$  with the total space being  $4.0 \mu\text{m}$  in the  $x-$  dimension and  $0.53 \text{ eV}$  in the  $y-$  dimension. (c) The same quantum transistor potential with a  $-0.22 \text{ eV}$  bias on the small side gate, (d) is the density plot of the same potential, highlighting the effect of the side gate.



(a)



(b)

Figure 4.30: (a) Shows the transmission of the wave function when no side gate bias is applied while (b) demonstrates that nearly the entire wave function is reflected with a  $-0.22$  eV bias on the small side gate. The transmission coefficients are 0.99 and 0.13 respectively.

## 4.5 Resonant cavities

Similarly, the propagation of wave packet along a quantum wire can be greatly altered by the introduction of small resonant cavities. When the wave function enters the cavity, it interferes and can either resonantly reflects or transmits through the cavity (Figure 4.31). By tuning the cavity (changing its length and width) various energy components of the wave function can be reflected (Figure 4.32). By coupling several cavities together a spread of energies can be reflected (Figures 4.33- 4.35). In this way, an energy dependent filtering device can constructed.

Such cavities demonstrate how the  $y-$  dimension of a quantum wire can greatly affects the transmission properties. By careful design and construction, such resonant cavities may be used to remove high energy propagation modes in the quantum wire, allowing one conduction energy level to be studied. By coupling such a wire to further devices the energy of the propagation electrons can be controlled in a very precise way. For example, it will allow a single electron of known energy to be placed onto a quantum dot, allowing greater control in probing the structure of the quantum dot.

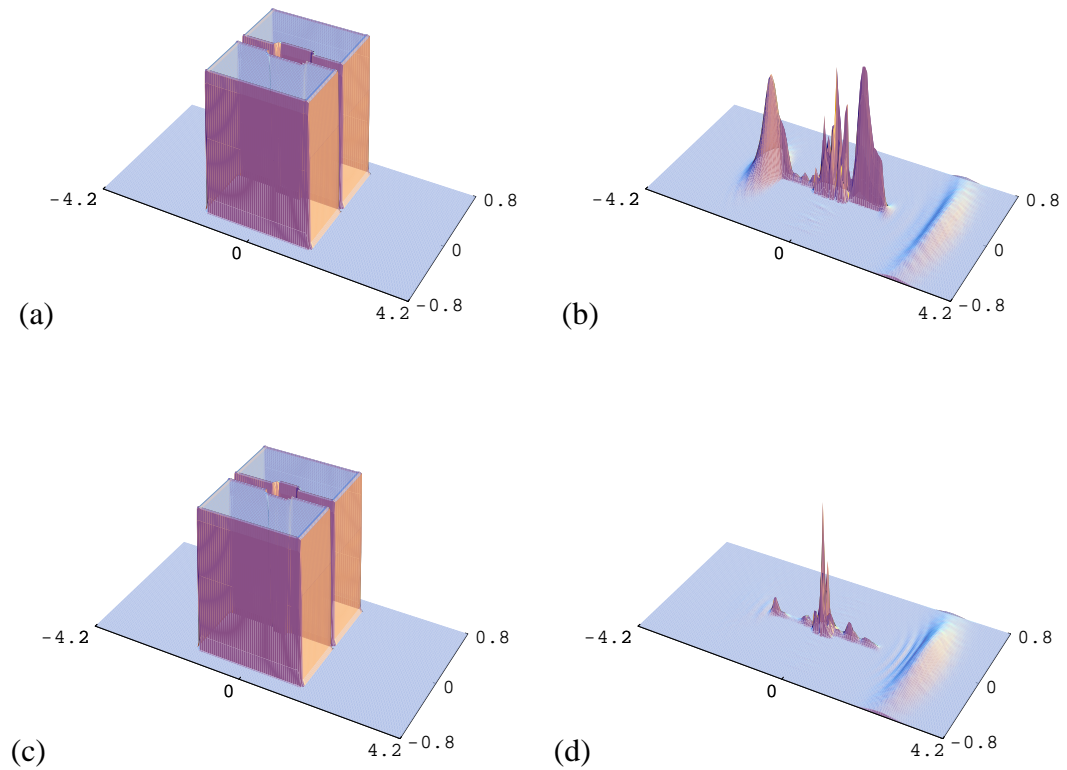


Figure 4.31: Potential and wave function for (a)-(b) minimum transmission  $T = 0.49$  for cavity size  $0.87 \times 0.21 \mu\text{m}$ , and (c)-(d) maximum transmission  $T = 0.89$  for cavity size  $0.58 \times 0.21 \mu\text{m}$ . The wave function had initial energy  $0.0049 \text{ eV}$  and the potential height was  $0.13 \text{ eV}$ . The actual space size is  $8.5 \times 3.2 \mu\text{m}$  which has been cropped to show the region of interest.

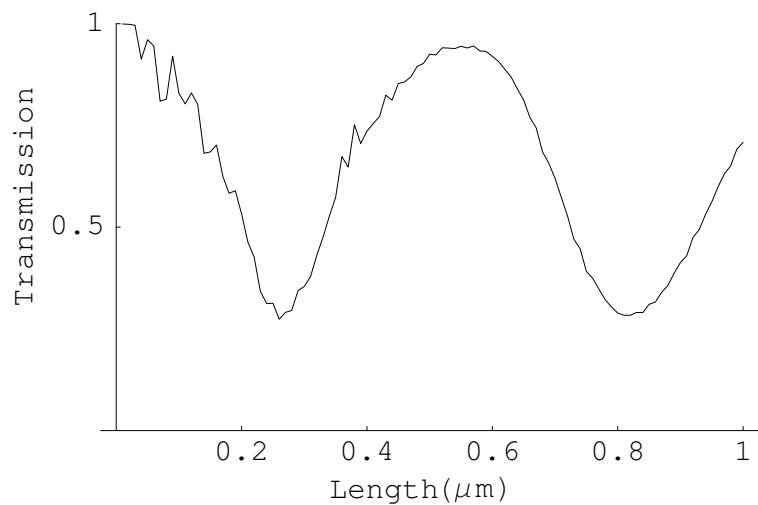


Figure 4.32: Transmission through a single cavity, of width  $0.21 \mu\text{m}$ , as the length of the cavity is increased. The wave function had initial energy  $0.0049 \text{ eV}$  and the potential height was  $0.13 \text{ eV}$ .

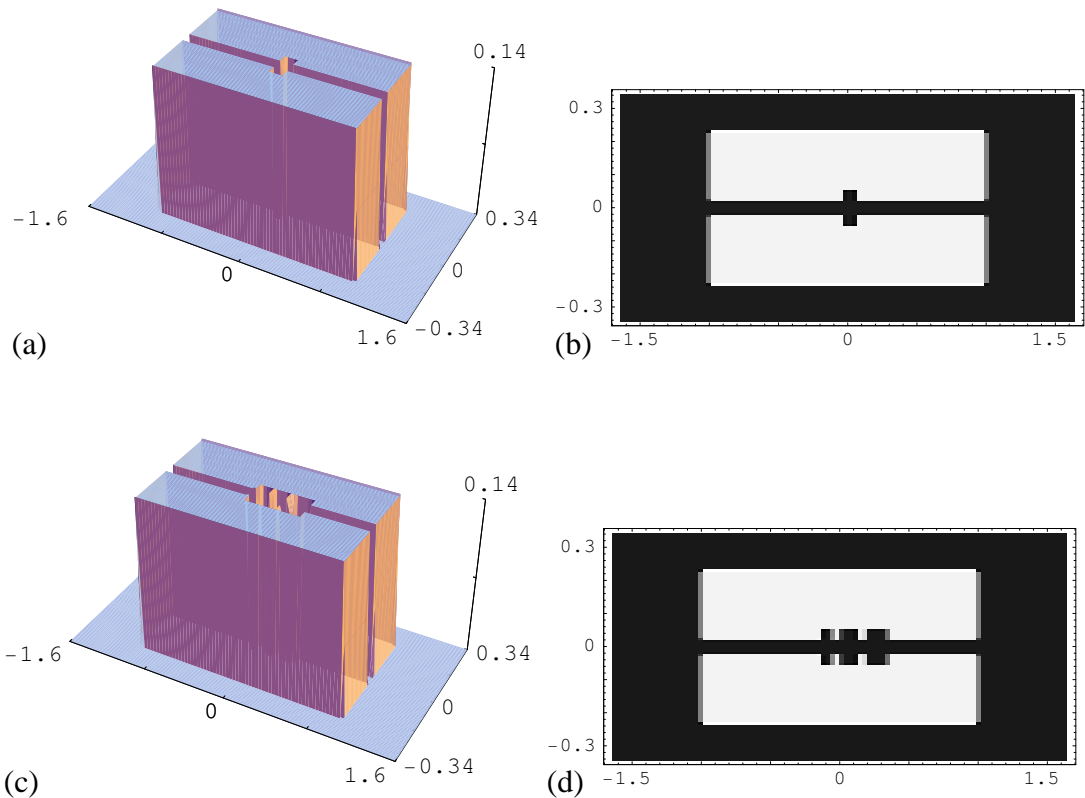


Figure 4.33: Potential with 1 and 3 resonant cavities. The single cavity is  $0.16 \times 0.21 \mu\text{m}$ , while the triples cavities are:  $0.13 \times 0.21 \mu\text{m}$ ;  $0.26 \times 0.21 \mu\text{m}$ ; and  $0.40 \times 0.21 \mu\text{m}$  respectively.

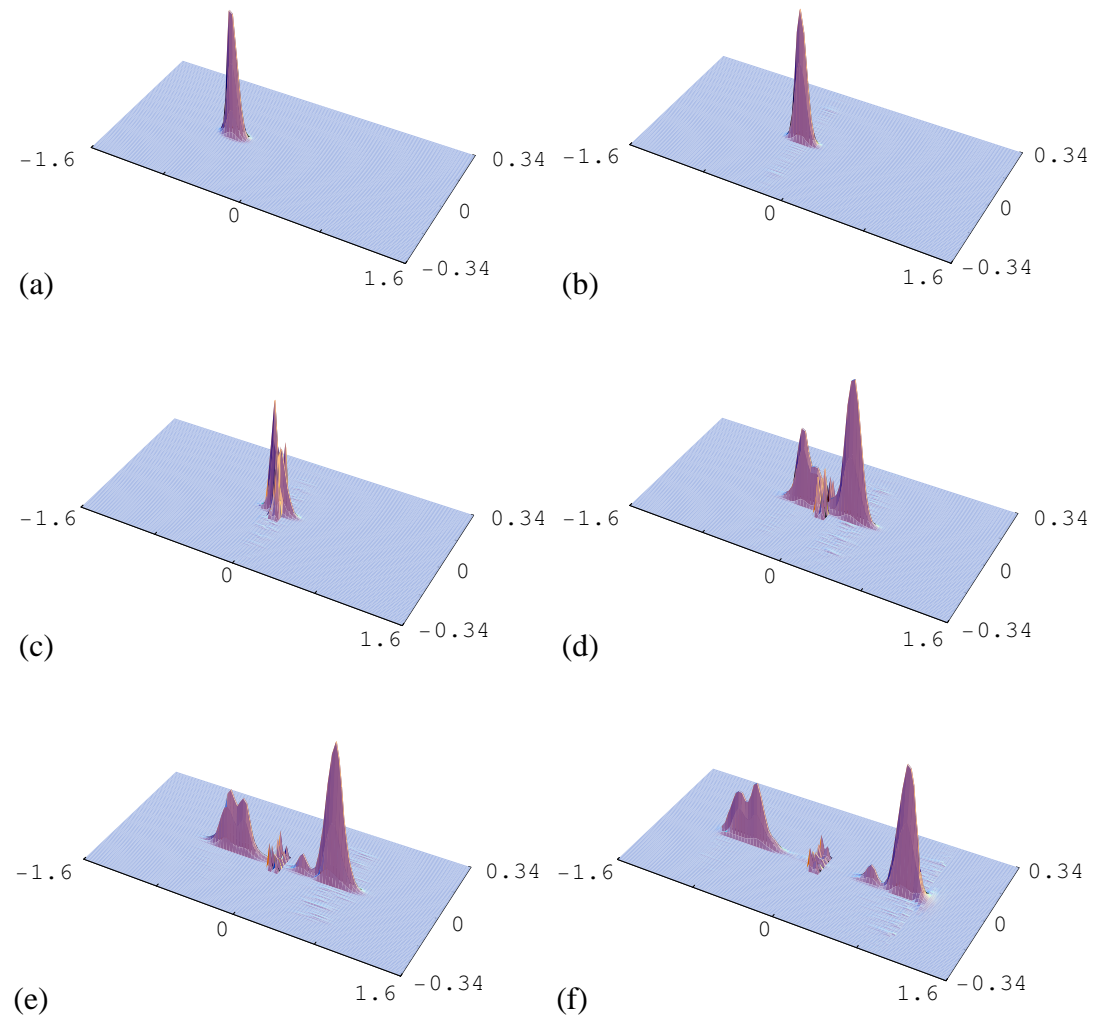


Figure 4.34: Propagation through a single resonant cavity. Approximately 40% of the wave function is resonantly reflected.

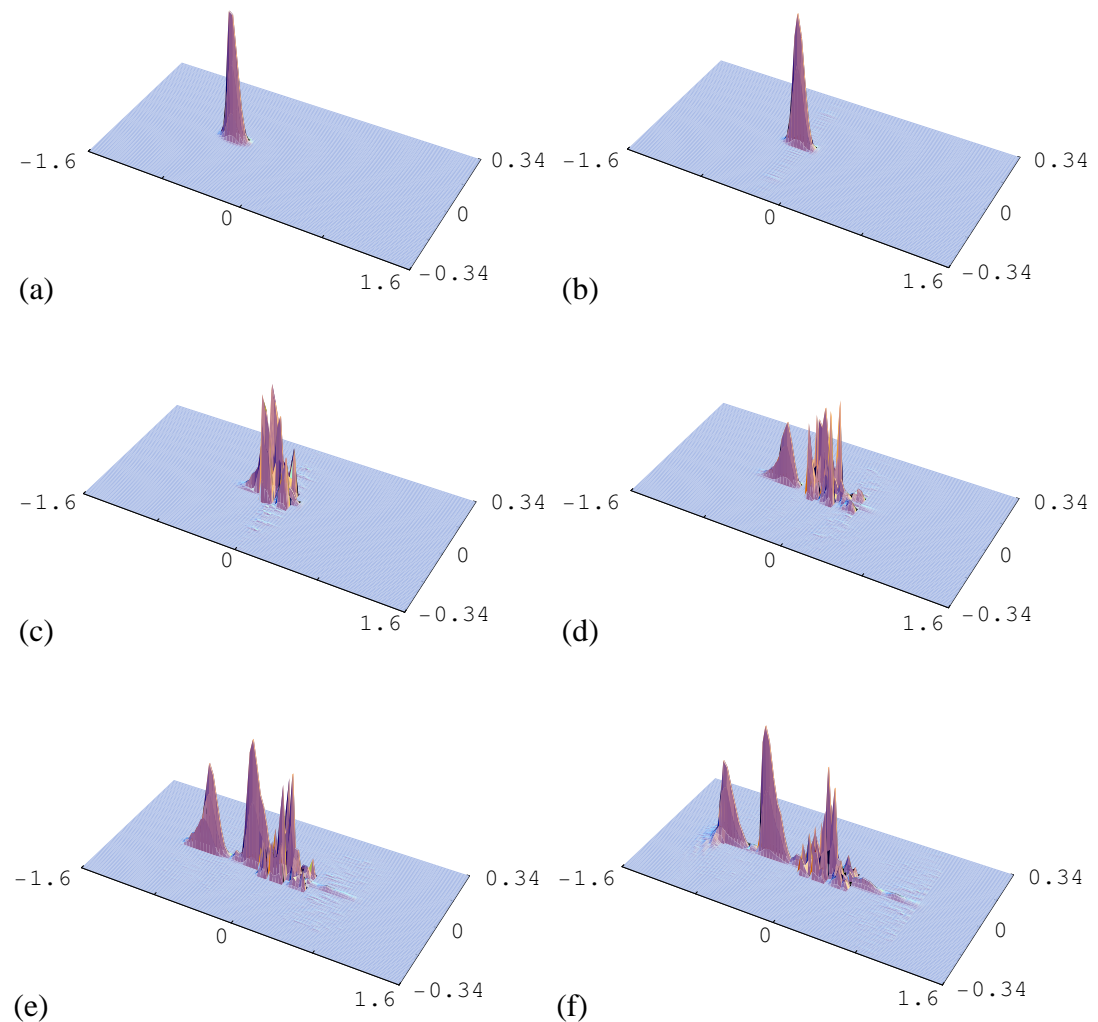


Figure 4.35: Propagation through a triple resonant cavity. Each cavity is tuned to a slightly different energy. Approximately 90% of the wave function is resonantly reflected.

## 4.6 Quantum wire impurity

As an electron propagates through a quantum wire or other quantum devices, impurities will cause the wave function to scatter and dephase. The presence of impurities will alter the conductance of a device, changing its desired properties. With a greater understanding of such impurities, their locations and effects on propagation, devices with greater stability and more reliable properties can be designed. Kim et al. (2002) solved the time independent Schrödinger equation for such impurities in quantum waveguides, modeling the impurities as quantum dots in an electronic potential (which forms the quantum wire). Their work demonstrated how the resonant structures, observed by the transmission through the device, change as the impurity parameters are changed.

The application of a weak magnetic field allows the phase of the electron to be altered without greatly affecting its propagation through the devices. As the electron encounters an impurity, it too will alter the phase. By studying the transmission of a wave packet through a device (which is proportional to conductance) and how it varies as the magnetic field strength is varied, the effects of the impurity can be understood.

Koonen et al. (2000) demonstrated experimentally and semi-classically that for a particular impurity there is a maximum in transmission, demonstrating that the conductance through the device was highly dependent on the location of the impurity. They were able to reproduce the main features of their experimental conductance using a semi-classical wave front (Figure 4.36). Their theoretical model assumed the wave function at the exit of a quantum point contact was of the form

$$\psi_0(0,y) = \left(\frac{2}{W}\right)^{\frac{1}{2}} \cos\left(\frac{\pi y}{W}\right) \text{ for } W/2 \leq y \leq W/2, \quad (4.11)$$

where  $W$  is the width of the quantum point contact at the exit. The wave function is assumed zero elsewhere.

The wave function at any  $x-$  position can be computed using the time independent Green's theorem (Section 2.5.2) with Dirichlet's boundary conditions and a weak applied magnetic field. The impurity is simulated by computing the wave function  $\psi(x,y)$  at the  $x-$  position of the impurity and setting values of the wave function to be zero for

the extent of the impurity. This modified wave function is then propagated through to the detector where the transmission is calculated.

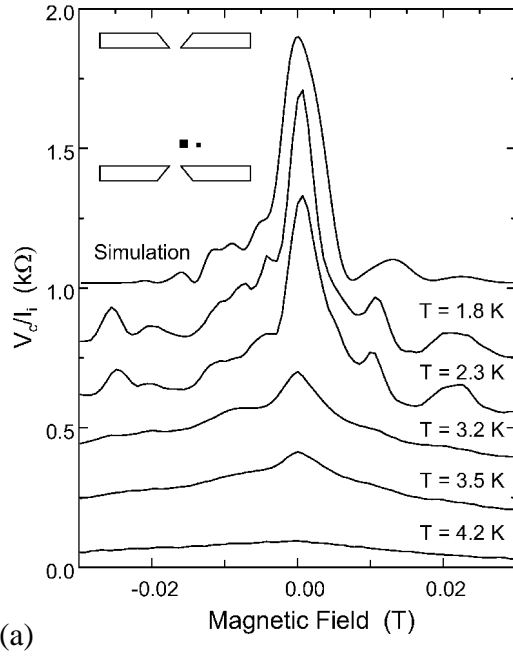
As indicated by Koonen et al. (2000) this wave function cutting method is a very crude method of simulating scattering. Neither diffusive backscattering or forward scattering nor wave function matching at the boundaries is considered. However, as shown in Figure 4.36, the simulated results qualitatively match the experimental results.

By solving the full time dependent Schrödinger equation with the impurity represented by the potential and a weak applied magnetic field, the short comings of the method used by Koonen et al. (2000) are overcome. The results obtained, shown in Figure 4.37-4.39, demonstrate the effects of changing the size and position of the impurity. All three sizes of the impurity demonstrate similar features. However, the off-axis position has a dramatic effect on the conductance. Initially for a slight movement off-axis, the change in transmission is dramatic, though symmetrical. As the impurity scans across the face of the propagating electron, the conductance gradually increases until it is nearly back to its original value, as the propagation electron is no longer sampling it as much in the later case.

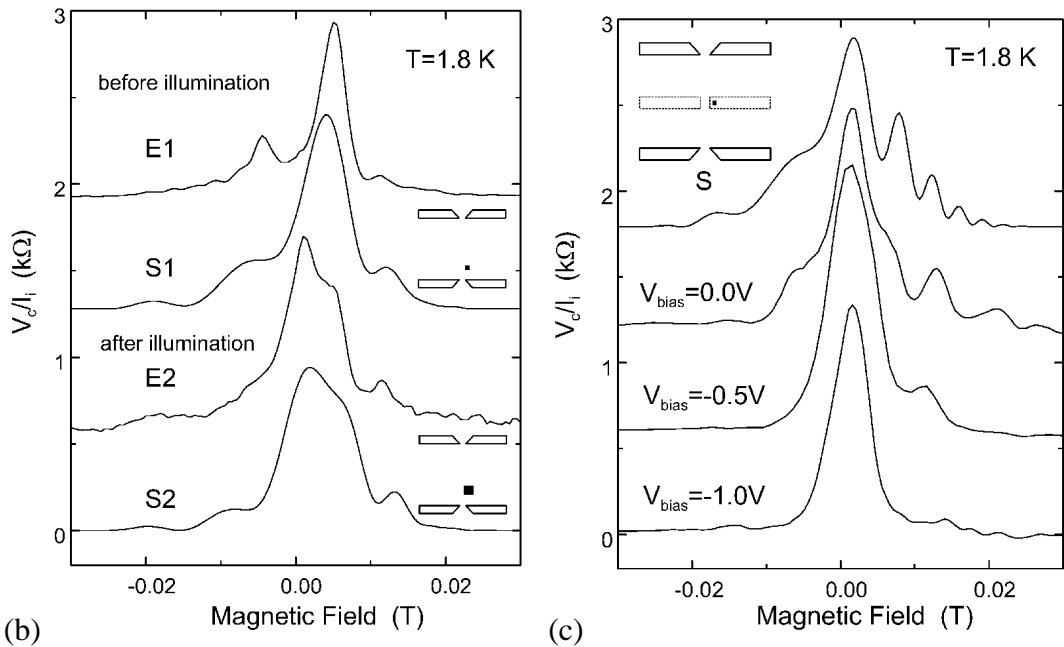
Figure 4.40 and Figure 4.41 show the typical propagation of the electron and its interaction with the impurity. It highlights the dramatic effects that the magnetic field has on the electron transmission and how it allows the potential landscape to be scanned.

The conductance results obtained closely match those obtained by Koonen et al. (2000) experimentally. The smaller bumps and peaks are also reproduced. Differences are mostly due to the imprecise nature of locating the impurity and the initial wave function shape in experiments and matching that to the precise theoretical model (where the location of the impurity is well defined and the initial electron has a Gaussian form).

Through such analysis it can be seen that adjusting the magnetic field strength allows the impurity, its approximate location and its characteristics to be studied. With an appropriately chosen magnetic field, the effects of the impurity can be diminished, resulting in conductance almost identical to the unobstructed wave function.



(a)



(b)

(c)

Figure 4.36: Experimental and semi-classical theoretical results obtained by Koonen et al. (2000). Simulations curves are denoted ‘S’, ‘S1’ and ‘S2’, while the other curves, some denoted ‘E1’ and ‘E2’, are results of experiments for different bias voltages and conditions. The distance between the electron source and detector was  $4.0 \mu\text{m}$  with the impurity between  $0.6 \mu\text{m}$  and  $2.0 \mu\text{m}$  from the electron injection point. The impurity was between  $0.08 \mu\text{m}$  and  $0.42 \mu\text{m}$  off axis. The system was cooled to approximately  $1.8K$  with a wave function width ranging between  $0.08\mu\text{m}$  and  $0.14\mu\text{m}$ .

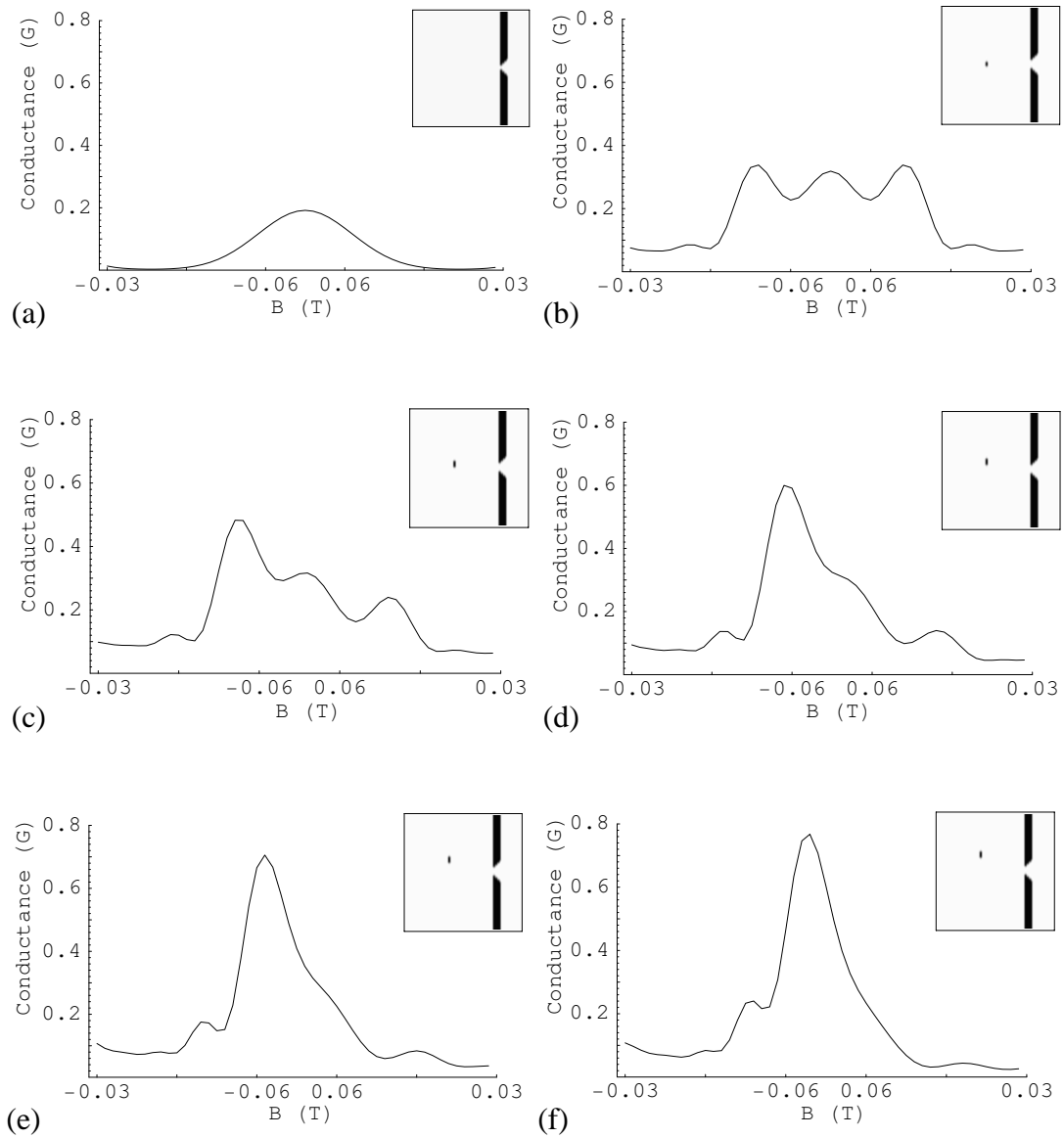


Figure 4.37: Transmission curves as the magnetic field is swept from  $-0.03T$  to  $0.03T$ . The impurity is a small rectangular block of size  $0.074 \times 0.037 \mu\text{m}$ , with potential height  $0.82 \text{ eV}$ , while the electron has mean energy  $0.27 \text{ eV}$ . (a) is the unobstructed conductance (no impurity). (b) the impurity is located on the x- axis ( $y = 0$ ) while (c) is  $0.037 \mu\text{m}$  off axis, (d)  $0.074 \mu\text{m}$  off axis, (e)  $0.111 \mu\text{m}$  off axis and (f)  $0.48 \mu\text{m}$  off axis. For all calculations the slit in the screen is  $0.074 \mu\text{m}$  wide.

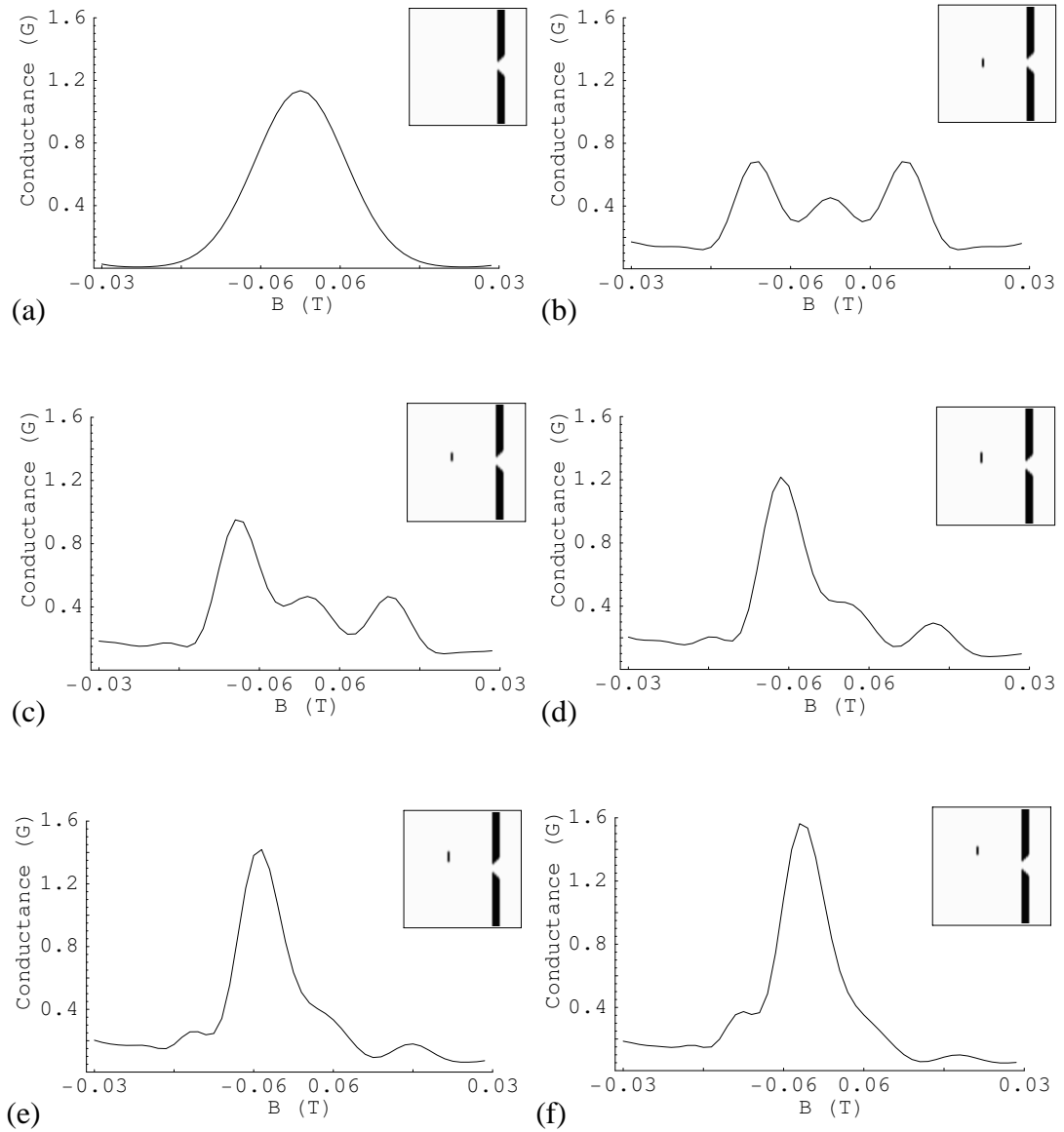


Figure 4.38: Transmission curves as the magnetic field is swept from  $-0.03T$  to  $0.03T$ . The impurity is a small rectangular block of size  $0.074 \times 0.074 \mu\text{m}$ , with potential height  $0.82 \text{ eV}$ , while the electron has mean energy  $0.27 \text{ eV}$ . (a) is the unobstructed conductance (no impurity). (b) the impurity is located on the  $x$ -axis ( $y = 0$ ) while (c) is  $0.037 \mu\text{m}$  off axis, (d)  $0.074 \mu\text{m}$  off axis, (e)  $0.111 \mu\text{m}$  off axis and (f)  $0.148 \mu\text{m}$  off axis. For all calculations the slit in the screen is  $0.074 \mu\text{m}$  wide.

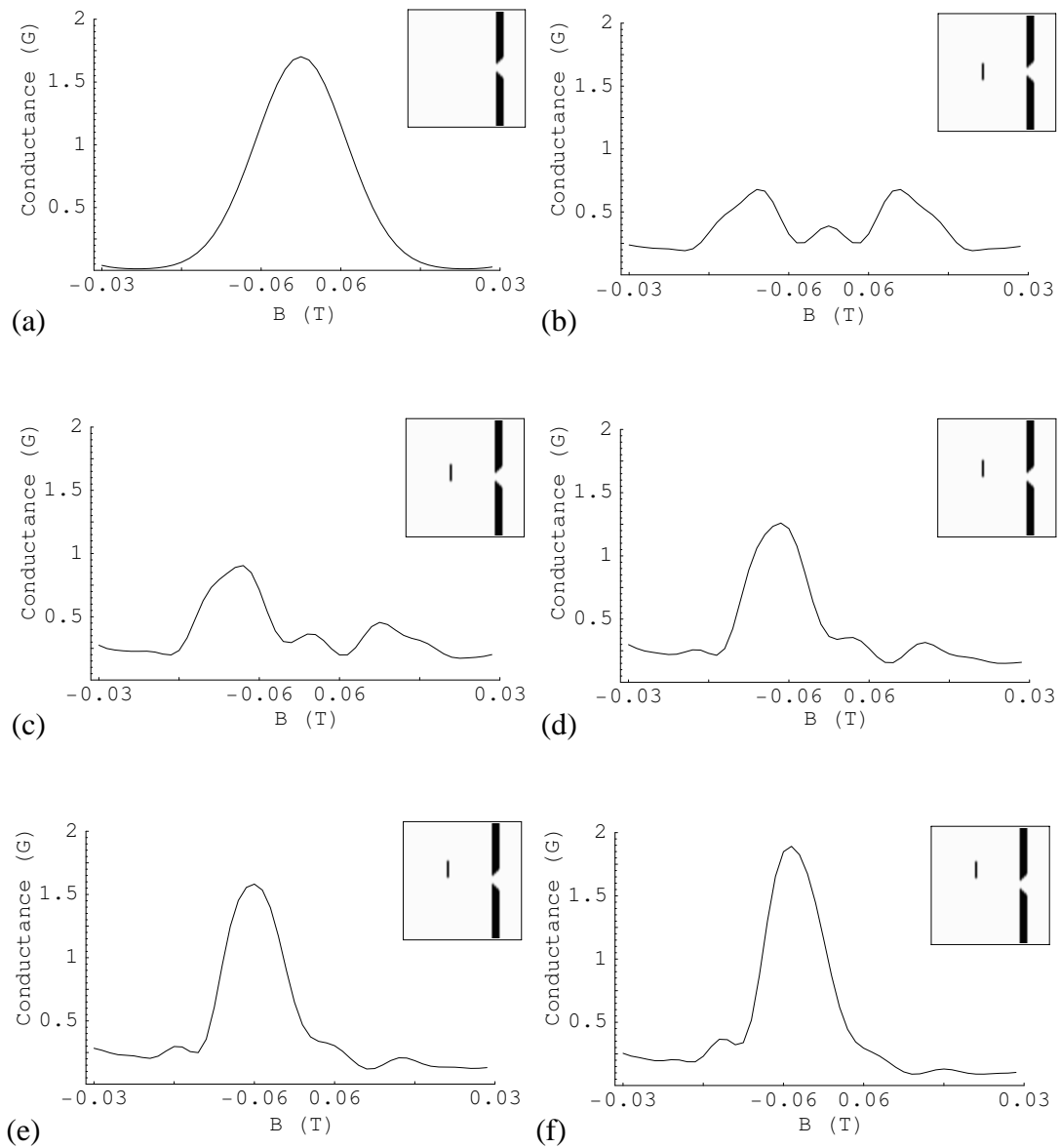


Figure 4.39: Transmission curves as the magnetic field is swept from  $-0.03T$  to  $0.03T$ . The impurity is a small rectangular block of size  $0.074 \times 0.15 \mu\text{m}$ , with potential height  $0.82 \text{ eV}$ , while the electron has mean energy  $0.27 \text{ eV}$ . (a) is the unobstructed conductance (no impurity). (b) the impurity is located on the x- axis ( $y = 0$ ) while (c) is  $0.037 \mu\text{m}$  off axis, (d)  $0.074 \mu\text{m}$  off axis, (e)  $0.111 \mu\text{m}$  off axis and (f)  $0.48 \mu\text{m}$  off axis. For all calculations the slit in the screen is  $0.074 \mu\text{m}$  wide.

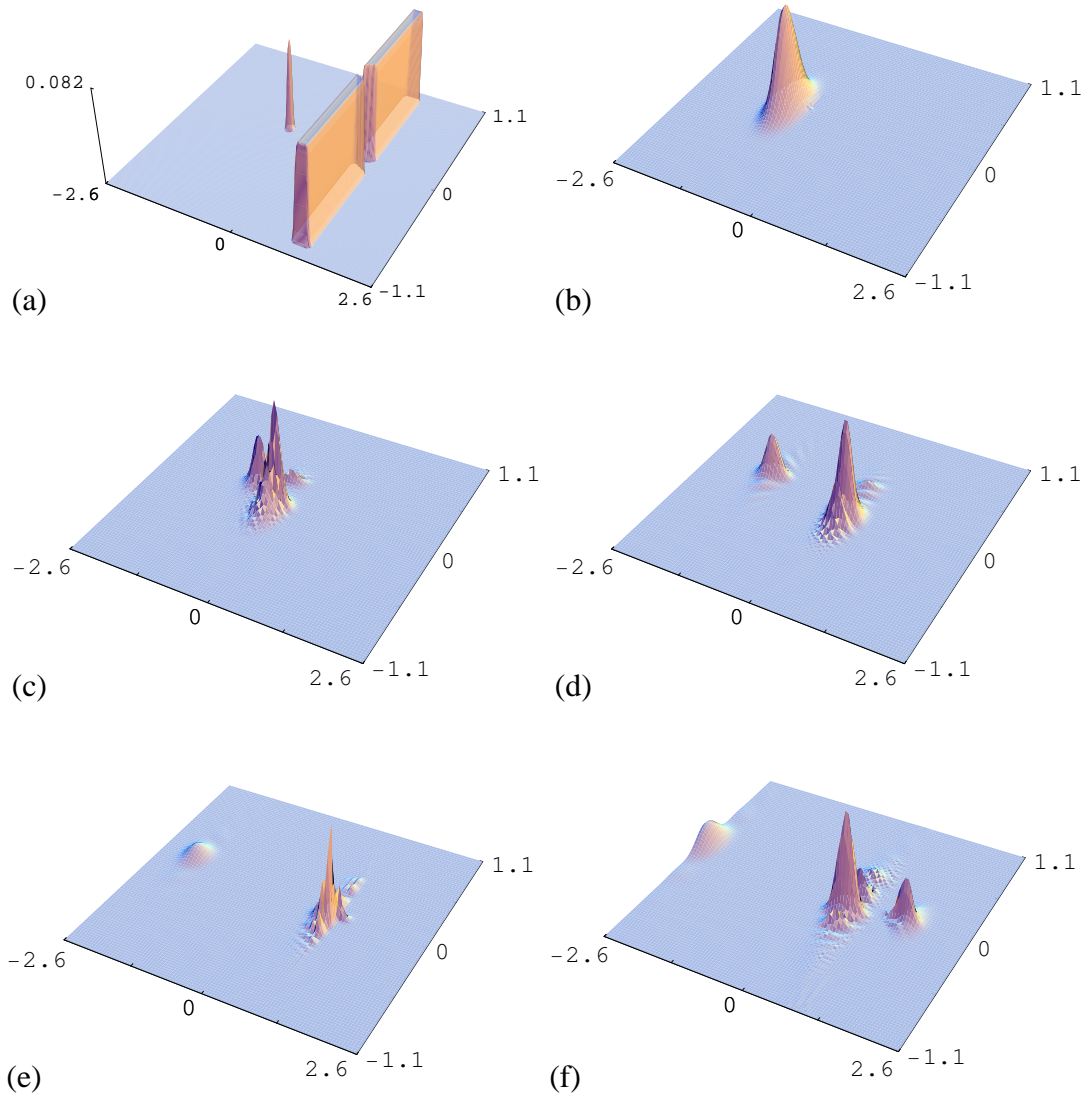


Figure 4.40: Typical propagation probing the impurity. No magnetic field is applied, hence only the central component of the wave function is sampled. The impurity is  $0.074 \times 0.15 \mu\text{m}$  in size with the slit in the screen  $0.074 \mu\text{m}$  wide. (a) Shows the potential while (b)-(f) show the propagation.

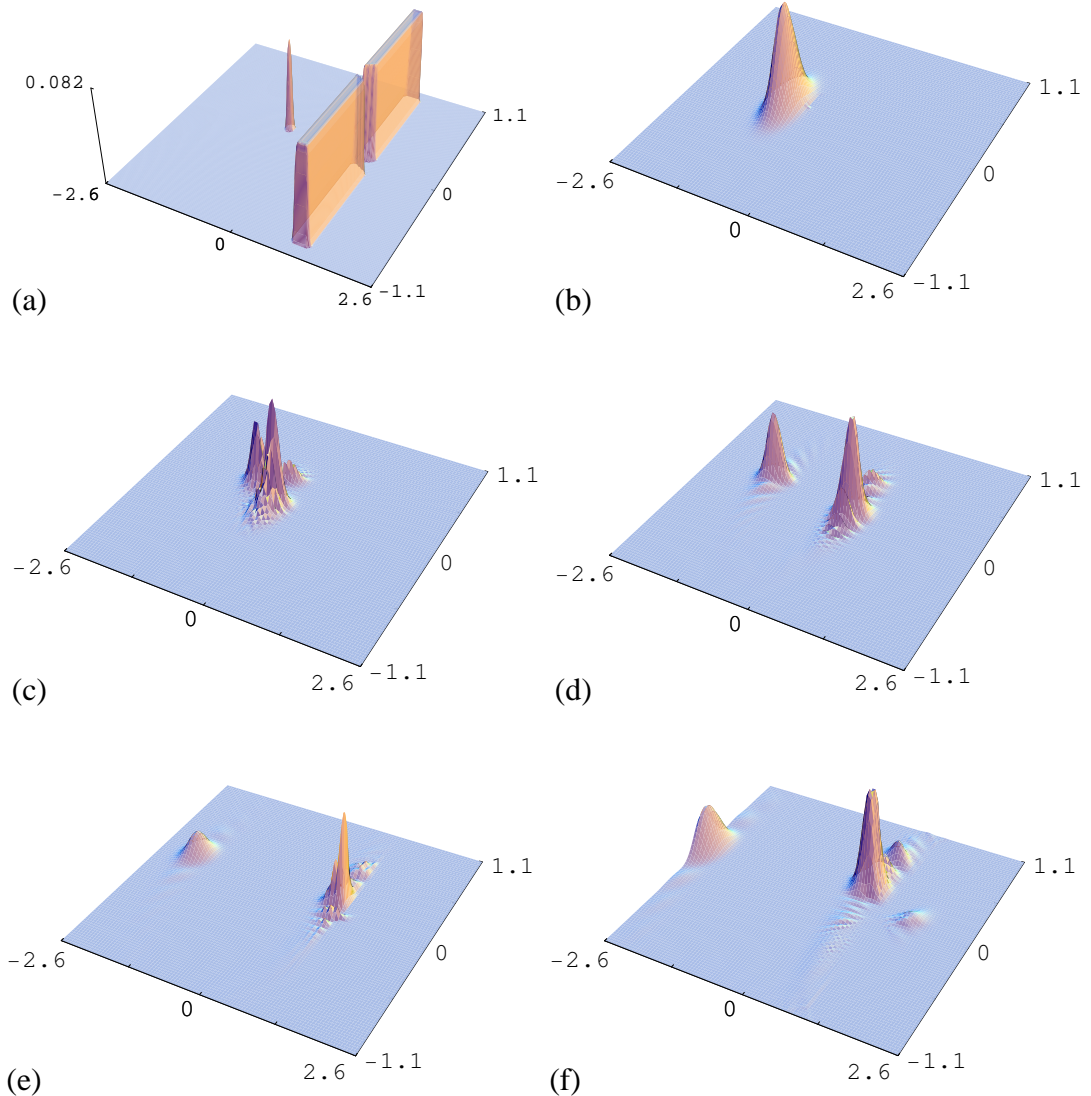


Figure 4.41: Typical propagation probing the impurity. A magnetic field of  $-0.0132T$  is applied. The portion of the transmitted wave function sampled by the screen has changed due to the wave function being swung by the magnetic field. The impurity is  $0.074 \times 0.15 \mu\text{m}$  in size with the slit in the screen  $0.074 \mu\text{m}$  wide. (a) Shows the potential while (b)-(f) show the propagation.

# Chapter 5

## Positron-hydrogen scattering

The general nature of the theoretical model and computational method outlined in this thesis, allows studies of many other physical systems. As an example, the same Chebyshev-Fourier scheme was applied to study positron-hydrogen scattering.

This chapter is largely reproduced from a paper by Wang et al. (1999). The numerical results were obtained using a modified version of the code developed in this thesis and formed a major component of an Honours Thesis for Riste (1998).

### 5.1 Multi-electrons

The inclusion of multiple electrons is a logical progression for studying single electron transport. There are several ways that such a development can be taken. A fully four dimensional Hamiltonian could be used, increasing the memory requirements of the computer code to over 13 *terabytes* (for roughly  $500 \times 500 \times 500 \times 500$  grid), beyond currently available resources. An equivalent increase in computational time also results.

Moving to a full 4 dimensional model may also have computational difficulties. When the electrons move close to each other, the system energy can become unbounded. Since the Chebyshev propagation scheme assumes the energy is bounded, it may prove to be inadequate. The limitation may be partially overcome by adopting a soft-core type approach,

whereby the unbounded energy can be dealt with in a reasonable fashion; however the memory and computational requirements still stand.

A second method worth considering is to assume that the two electrons are independent and treat them as two separate 2 dimensional wave functions, with an appropriate Hamiltonian. Such calculations would need to be performed self consistently using small time steps and it should only double or triple the memory requirements. Since many small time steps would be used, the benefit of the Chebyshev propagation scheme would be reduced.

Following is an application of the Chebyshev propagation scheme to two electrons, each only in 1 dimension, requiring only a two dimensional Hamiltonian. This treatment encapsulates the full quantum information of the 1 dimensional electrons.

## 5.2 Background

Positron-hydrogen scattering involves four possible processes, i.e. elastic scattering, atomic excitation, atomic ionisation, and positronium formation. As a member of the class of three-body Coulomb problems, this study is of fundamental importance in atomic physics. It is also important because it involves interactions of matter with antimatter and thus has applications in cosmology and astrophysics.

Over the past decades, extensive studies have been conducted for a similar three-body Coulomb system, i.e. electron-hydrogen scattering, but much less work has been done for the positron-hydrogen system. This is mainly due to the lack of an appropriate positron source, which has only recently become feasible to provide collisional data. Positron-hydrogen scattering is also a more challenging theoretical problem because of the extra channel of reaction, i.e. the positronium formation. This section of the study examines positron-hydrogen collision processes by numerically solving the time dependent Schrödinger equation.

A scattering event is clearly a time dependent process. During such an event, two particles approach each other, interact, and then separate. In the case where the event is

on an atomic scale and is fully quantum mechanical in nature, the system wave function of the particles will evolve as the collision takes place in accordance with the time dependent Schrödinger equation. Nevertheless, nearly all reported theoretical studies of electron/positron scattering from atoms utilise a time independent approach, for example, the convergent-close-coupling method (Bray & Stelbovics 1995, Bray & Stelbovics 1997, Ryzhikh & Mitroy 1997), the distorted-wave Born approximation method (Madison et al. 1995, Wang et al. 1995), the convergent R-matrix method (Bartschat et al. 1996), the intermediate energy R-matrix method (Scott et al. 1997), the Hyperspherical-coordinates method (Yang et al. 1996), the convergent J-matrix method (Konovalov & McCarthy 1995) and the Faddeev method (Faddeev & Markuriev 1993, Kvitsinsky & Hu 1996).

The kernel of these methods is built around a set of stationary scattering states that are independent of time. Over the past half a century, considerable and continuous progress has been made in developing very sophisticated time independent methods, which can now describe a wide range of experimental findings. However, there are many mathematical difficulties inherent in the time independent approaches, for example, the difficulty in handling the boundary conditions of continuum states in electron-atom collisions due to the long-range Coulomb interactions. These difficulties are of such magnitude that formal time independent scattering theory has not yet led to a universally-valid computational method for the ionisation problem (McCarthy 1996, Bray 1997). Moreover, the time independent approach provides little information on the transient state of the system during the scattering process.

On the other hand, the time dependent approach has a more natural correspondence to reality, i.e. starting from an initial state of the system and following the events through time. It gives a direct solution of the quantum equations of motion and consequently has many distinct advantages over the traditional time independent methods. For example, it provides information on transient behaviours and allows direct visualisation of the collision process, where one can “watch” the electron and atom wave packet evolving in time and in space; it handles continuum states, ionisation, resonance and post-collision interaction in the most natural way and is thus free of the difficulties encountered by the time independent approaches; as an initial value problem, it is also comparatively easy to implement, flexible, and versatile in treating a large variety of quantum many-body

problems. It is therefore expected to resolve some serious discrepancies between existing theories and experiments. This chapter examines s-wave positron-hydrogen scattering by numerically propagating the positron-hydrogen system wave function in time through the collision region.

Some progress has been made in developing and applying the simpler schemes to problems in the field of atomic physics, including the calculation of electron impact ionisation of hydrogen (Bottcher 1985), FOD, Stark shift and lifetime of hydrogen (Hermann & J. Fleck 1988), split operator scheme, two-electron atom energies (Zhang et al. 1994), split operator scheme, atomic autoionisation (Schultz et al. 1994), FOD, photoionisation (Dehnen & Engel 1995), split operator scheme, s-wave electron scattering from hydrogen (Ihra et al. 1995), split operator scheme, electron detachment from H- (Kazansky & Taulbjerg 1996), split operator scheme, and e-H scattering (Pindzola & Robicheaux 1996), Taylor expansion, (Pindzola & Schultz 1996), SOD method.

Larkin et al. (1998) studied the positron-hydrogen system using the split operator scheme. Their study was based on a linear one-dimensional model (i.e. the only scattering directions possible are forward or backward). This one-dimensional model is not the same as the well known S-wave model, or the Temkin-Poet model, where only the first term in the partial wave expansion is retained. The S-wave model can be readily expanded to include the other partial waves systematically until convergence is achieved, while the linear one-dimensional model cannot be extended to obtain a full solution of the system unless all six dimensions are included in the calculation.

It is very encouraging that the above calculations were found to be in fairly good agreement with results from time independent models and/or experimental data. Nevertheless, there is a general deep concern about the accuracy of the final system wave function obtained by the time dependent schemes, since errors accumulated over the many time steps may cause severe distortion of the wave packets. This prompted the adoption of the most accurate scheme up to date, i.e. the Chebyshev scheme, for this investigation on the S-wave positron-hydrogen scattering.

## 5.3 Theory

In the S-wave Temkin-Poet model (Temkin 1962, Poet 1978, Poet 1980, Poet 1981), all angular dependence is neglected and the time dependent Schrödinger equation of the S-partial wave is given by

$$i \frac{\partial}{\partial t} \psi^S(r_1, r_2, t) = \left( -\frac{1}{2} \frac{\partial^2}{\partial r_1^2} - \frac{1}{2} \frac{\partial^2}{\partial r_2^2} + \frac{1}{r_1} - \frac{1}{r_2} - \frac{1}{r_>} \right) \psi^S(r_1, r_2, t), \quad (5.1)$$

where  $r_1$  and  $r_2$  are the distances of the positron and the electron relative to the nucleus respectively,  $r_>$  refers to the greater of  $r_1$  and  $r_2$ ,  $\psi^S(r_1, r_2, t)$  is the S-wave function and the system Hamiltonian

$$H = -\frac{1}{2} \frac{\partial^2}{\partial r_1^2} - \frac{1}{2} \frac{\partial^2}{\partial r_2^2} + \frac{1}{r_1} - \frac{1}{r_2} - \frac{1}{r_>}. \quad (5.2)$$

Assuming the hydrogen atom is initially in the ground state, its wave function is then given by

$$\Psi_H(r_2) = r_2 \exp(-r_2). \quad (5.3)$$

The positron is assumed to be sufficiently far away from the hydrogen atom so that initially it can be represented by a wave packet for a free particle, i.e.

$$\psi_{e^+}(r_1) = \exp\left(\frac{-(r_1 - a)^2}{4\sigma}\right) \exp(i k r_1), \quad (5.4)$$

where  $a$  defines the starting position of the positron,  $k$  is the dominant momentum of the positron wave packet, and  $\sigma$  is the inverse of the momentum spread in the initial positron wave packet. Combining the two expressions gives the initial wave function for the positron-hydrogen system:

$$\psi(r_1, r_2, t=0) = r_2 \exp\left(-r_2 + i k r_1 - \frac{(r_1 - a)^2}{4\sigma}\right). \quad (5.5)$$

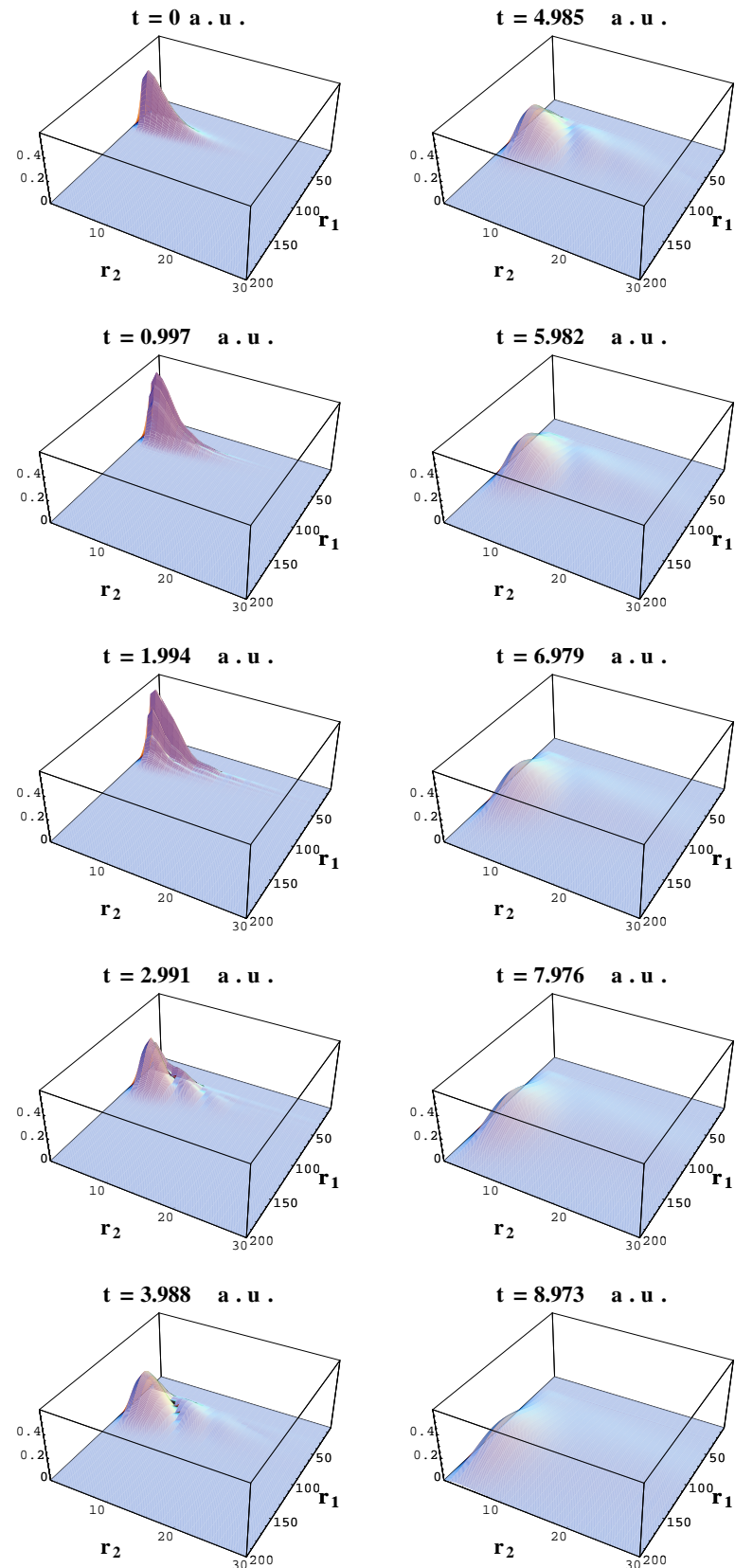


Figure 5.1: Time evolution of the positron-hydrogen system wave function through the collision interaction. The dominant energy of the incident positron is 3.4 a.u.

## 5.4 Results

Figure 5.1 illustrates the time evolution of this wave function under the influence of positron-electron, positron-nucleus and electron-nucleus interactions. These time dependent wave functions were obtained by propagating the wave function in time according to Equation 5.1. The wave function is initially observed moving toward the nucleus of the hydrogen atom, then being scattered by the interaction potentials between the three particles, and finally moving away from the interaction region.

This simulation was carried out for a dominant incident energy of 3.4 *a.u.* with a 5% spread in momentum, which is well above the positronium formation threshold and also the ionisation energy of hydrogen. Therefore, it was expected that significant changes in the profile of the system wave function in the  $r_2$  direction would result (i.e. the electron coordinate), representing a finite probability in finding the electron at greater distances from the nucleus. This is in accordance with the finite amplitudes of excitation and ionisation of the hydrogen atom at this energy. The enhancement of the larger distance amplitude along the  $r_1 = r_2$  line can be interpreted as partially due to the formation of positronium.

It is not possible to determine with any certainty that positronium formation occurred at any particular stage purely by investigation of s-wave wave functions, because the angular positions of the two particles could not be known in this model. It was possible that even if the two particles were at the same radius, they could have been on opposite sides of the nucleus. Further work with the inclusion of other partial waves will resolve the issue of how much of the amplitude along the  $r_1 = r_2$  line was referred to positronium formation and how much of the amplitude was due to both particles moving away from the nucleus.

The scattering of a positron from a hydrogen atom by numerically solving the time dependent Schrödinger equation has also been examined. Two approximations are used. The first is a Chebyshev polynomial expansion of the time evolution operator and the second a partial wave expansion of the initial wave function, of which only the S-wave term is retained. It was found that the time dependent behaviour of the propagating wave function during and after the interaction matched expectations qualitatively.

# **Chapter 6**

## **Conclusion**

Developed in this thesis is a novel theoretical model and computational scheme to solve the time dependent Schrödinger equation, which describes transient behaviour of nano structured quantum systems. It provides a very powerful tool to model, for example, the propagation of electrons through arbitrarily shaped quantum waveguides. This scheme can be readily applied to examine many different types of quantum phenomena. Of interest are conductance fluctuation in nano wires, the connection of nano wires to external leads, resonant tunnelling through barriers, effects of magnetic fields and many more.

By solving the time dependent Schrödinger equation, complete quantum mechanically information of the system under study is obtained at all times and values for appropriate measurable quantities of interest can be extracted. Stringent tests on the accuracy of solutions were carried out, including conservation of norm and energy, time reversal propagation, and comparison with exact solutions in the case of free space propagation with and without a uniform external magnetic field. This model is readily applied to nano structures with arbitrarily complex boundaries, has been demonstrated to be applicable to electron-positron scattering, and has been investigated as applicable to time dependent potentials.

The computer code has evolved into a sophisticated program allowing the study of many varied devices, reproducing experimental and previous theoretical results. New devices were studied with many new and original results produced. These included:

- Quantum transistor
- Resonant cavities and energy dependent devices
- Quantum impurity scanning
- Quantum wire connections and flange angles
- Electron transport under an external magnetic field

The Chebyshev-Fourier computational scheme developed in this thesis is fast, efficient and able to run on multiple processors through the use of MPI (message passing interface). With excellent scaling over multiple processors, the code can be used to study large systems in great detail. The application of a negative complex potential at the boundary of the numerical grid was shown to effectively absorb a propagating wave packet with negligible reflection. The nature of this absorption was investigated in great depth, along with the possible errors that it can introduce. Such an investigation had not previously been undertaken in the context of single time-step propagators. With algorithmic optimisations, such as the complex absorbing boundaries and a wave function splitting algorithm, the computer code produced has been demonstrated to be general purpose, allowing the study of quantum dynamical problems in a wide range of systems.

The results obtained for the quantum wire flange angle were new, novel and unexpected. It was found that the way in which a nano wire is connected to the external electron sources can greatly affect the transmission properties of the wire. The optimal flange angle for maximum transmission was found to be approximately  $18^\circ$  with a small shift due to a change in the initial energy of the electron. With further study of this resonance behaviour, additional increase in transmission may be achieved, perhaps even to 100%. To accomplish this, non-linear shaped flanges may need to be considered.

The application of the code to solve the impurity scanning problem, with a fully quantum mechanical method, improved on the semi-classical methods previously used and demonstrated the possibilities and capabilities of the computer code. The results obtained, previously only studied using semi-classical methods, closely matched those obtained experimentally. With a refined impurity potential, it is foreseen that the experimental results

could be reproduced with greater detail. Such analysis will require closer collaboration with those performing the experiments.

With the adaption of the code to run on multiple processors and the commissioning of large super computers, it is anticipated that the model and computational code developed could be readily adapted to solve more complicated systems involving several connected nano-devices. With minor modifications (and a massive increase in computational requirements) the code could be extended to model the full 4D time dependent Schrödinger equation representing two 2D electrons. Alternatively, the code could be extensively modified to use self-consistent propagation to interact more 2D electrons (with only modest increases in computational requirements). The ability to solve the multi-electron systems allows far greater insight into nano structured devices with closer ties to those ultimately required by the commercial semi-conductor industry.

# Appendix A

## Format of input file

```
#  
#      Input file description and default values. It contains all the  
#      variables that can be set as the input of the model.  
#  
#  
#      Atomic unit conversion factors:  
#  
#          Time:      1 a.u. = 2.41888E-17 s  
#          Energy:    1 a.u. = 27.2114 eV  
#          Distance: 1 a.u. = 5.29177E-11 m  
#          Momentum: 1 a.u. = 1.99285E-24 kg m/s  
#          Magnetism: 1 a.u. = 2.35050E+5 T  
#  
#  
#      Possible prime factored values for n < 2000 (for speed of FFT)  
#  
#      0,1,2,3,4,5,6,7,8,9,10,12,14,15,16,18,20,21,24,25,27,28,30,32,35,  
#      36,40,42,45,48,49,50,54,56,60,63,64,70,72,75,80,81,84,90,96,98,100,  
#      105,108,112,120,125,126,128,135,140,144,147,150,160,162,168,175,  
#      180,189,192,196,200,210,216,224,225,240,243,245,250,252,256,270,  
#      280,288,294,300,315,320,324,336,343,350,360,375,378,384,392,400,  
#      405,420,432,441,448,450,480,486,490,500,504,512,525,540,560,567,  
#      576,588,600,625,630,640,648,672,675,686,700,720,729,735,750,756,  
#      768,784,800,810,840,864,875,882,896,900,945,960,972,980,1000,1008,  
#      1024,1029,1050,1080,1120,1125,1134,1152,1176,1200,1215,1225,1250,  
#      1260,1280,1296,1323,1344,1350,1372,1400,1440,1458,1470,1500,1512,  
#      1536,1568,1575,1600,1620,1680,1701,1715,1728,1750,1764,1792,1800,  
#      1875,1890,1920,1944,1960,2000  
#
```

```

#
# Any real or integer values may be entered as expressions using one
# the predefined constants:
#
#      pi      = 3.141592653589793238462643383279502884197
#      boltzk = 1.380658d-23
#      h       = 6.6260755d-34
#      hbar    = h/2.0d0/pi
#      masse   = 9.1093898d-31
#      nm      = 1.0d-9
#      chargee = 1.60217733d-19
#      ev      = chargee
#      aut     = 2.41888d-17
#      aue     = 27.2114*ev
#      aus     = 5.29177d-11
#      aup     = 1.99285d-24
#      aub     = 2.35050d5
#      c       = 2.99792458d8
#      mu0    = 4.0d0*pi*1.0d-7
#
# For example, to define the mass of the wave function:
#
#      mass
#      0.067*masse
#
# or, to define the space size:
#
#      spacesize
#      100000.0*aus 100000.0*aus
#
#
# Any lines which the interpreter does not understand are ignored.
#
#
# A command consists of a keyword followed by defining values.
#

```

```

#
# Any command not defined in the input file will first be defined
# according to its default value. Then, it will be dynamically
# assigned according to other parameters. For example: if n, p and
# pmax are not defined in the input file, they initial get their
# default values and then get redefined dynamically, dependant on
# other defined variables.
#
# The following were defined
#
#      space size
#      10000.0*aus 10000.0*aus
#
#      initialwavefn
#      gaussian
#
#      initialenergy
#      1.5d-3*aue
#
# The following computations are performed in s_derive_parameters()
#
#      p          =  (/ sqrt(2.0d0*mass*initialenergy), 0.0d0 /)
#      pspread     =  pspread*sqrt(sum(p**2))
#      wavefnwidth =  hbar/pspread
#      pmax        =  pmax + sqrt(-2.0d0*log(cutoff)/wavefnwidth**2
#                                *hbar**2)
#      gridspacing =  pi/pmax*hbar
#      n           =  int(spacesize/gridspacing)+1
#      n(1)         =  f_factorprime(n(1))
#      n(2)         =  f_factorprime(n(2))
#      gridspacing =  spacesize/dble(n-1)
#      pmax        =  pi/gridspacing*hbar
#      pspacing    =  2.0d0*parameters%pmax / dble(n)
#
# which dynamically define various required variables. It is
# suggested that the minimum number of definitions be placed in the
# input file allowing the computer code to dynamically set all
# other required variables.
#

```

```

#
#      Allowed variables, a brief description and their default values.
#

datadir          # Directory where all output will be placed
<text>           #      maxlen=50
#      default:  data/

basename         # Base name of all output to be produced
<text>           #      maxlen=50
#      default:  wavefn.

chkpntfile       # Base name of the checkpoint file
<text>           #      maxlen=50
#      default:  cps_chkpt.

initialwavefn    # Shape of initial wavefunction
<text>           #      'gaussian' or 'fermi'
#      default:  gaussian

optimisation     # Type of complex potential to use
<text>           #      'splitwavefn' or 'exponential' or 'gaussian'
#      or 'linear' or 'freespace' or
#      or 'theoreticalfreespace'or 'none'
#      default:  none

potsmoothtype   # How to smooth the potential
<text>           #      'poisson' or 'gaussblur' or 'none'
#      default:  none

comppotpos        # Where to put the complex potential
<logical> <logical> <logical> <logical>
#      xmin edge, xmax edge, ymin edge, ymax edge
#      default:  .true. .true. .true. .true.

smooth           # Number of gridpoints to smooth the potential
<integer> <integer> #      x- and y- dimension
#      default:  32 32

extraboundary    # Amount of extra boundary to add
<integer> <integer> #      x- and y- dimension
#      default:  2 2

mass              # Mass of the wave function
<real>            #      mass
#      default:  6.67d-2*masse

fermienergy       # Fermi energy of the initial wave function
<real>            #      fermi energy
#      default:  0.0

```

```

temperature          # Temperature of the initial wave function
<real>              # temperature
                      # default:  0.01

initialenergy       # Initial energy of the wave function
<real>              # energy
                      # default:  0.0

p                  # Initial momentum of the wave function
<real> <real>      # x- and y- components
                      # default: 0.0 0.0

pspread             # Initial spread of the wave function
<real> <real>      # x- and y- components as a percentage of p
                      # default:  0.05 0.05

pmax               # Maximum momentum supported by the grid
<real> <real>      # x- and y- components
                      # default:  0.0 0.0

accuracyfactor     # Increased accuracy in each dimension
<real> <real>      # x- and y- increase factor (multiples pmax)
                      # default:  1.0 1.0

eigenfactor         # Increase eigen energy in Chebyshev expansion
<real>              # multiplicative factor
                      # default:  1.25

position            # Starting position of the wave function
<real> <real>      # x- and y- coordinates
                      # default:  0.0 0.0

wavefnwidth         # Spread of the wave function
<real> <real>      # x- and y- spread
                      # default:  0.0 0.0

t                  # Propagation time
<real>              # time
                      # default:  0.0

n                  # Number of grid points
<integer> <integer> # x- and y- grid points
                      # default:  0 0

distance            # Propagation distance
<real>              # distance
                      # default:  1.0d4*aus

gridspacing         # Distance between grid points
<real> <real>      # x- and y- gridspacing
                      # default:  0.0 0.0

```

```

maxgridspacing      # Maximum distance between grid points
<real> <real>      #   x- and y- max gridspacing
#   default:  0.0 0.0

pspacing           # Momentum spacing between momentum grid points
<real> <real>      #   x- and y- momentum spacing
#   default:  0.0 0.0

spacesize          # Size of space
<real> <real>      #   x- and y- size
#   default:  2.0d4*aus 2.0d4*aus

timesteps          # Number of timesteps to break propagation into
<integer>         #   number of time steps
#   default:  1

chkpntfreq         # Frequency to checkpoint (number of time steps)
<integer>         #   frequency in terms of time steps
#   default:  1

tstep               # Size of each timestep
<real>             #   time step size
#   default:  0.0

plotnumber          # Number of wavefunction to save to disk
<integer>          #   number
#   default:  0

plotpointnum        # Number of grid points to save to disk
<integer> <integer> #   x- and y- points
#   default:  0 0

plotcomplex         # Include complex potential when saving to disk
<logical>          #   save complex
#   default: .true.

plotwfn             # Save the wave function to disk
<logical>          #   save wave function
#   default: .true.

plotwfnp            # Save the momentum of the wave function to disk
<logical>          #   save momentum wave function
#   default: .true.

plotpot              # Save the potential to disk
<logical>          #   save potential
#   default: .true.

potrange             # Range of the potential
<real> <real>      #   min and max of potential
#   default:  0.0 0.0

```

```

tranrefl          # Output transmission and reflection coefficients
<logical>
#      output coefficients
#      default: .true.

potbound          # Bounds of the space
<real> <real> <real> <real>
#      xmin, xmax, ymin, ymax
#      default: 0.0 0.0 0.0 0.0

speccutoff        # Cutoff of the momentum spectrum
<real>
#      minimum momentum
#      default: 0.01

tspectrum         # Compute and save the transmission spectrum
<logical>
#      transmission spectrum
#      default: .true.

espectrum         # Compute and save the energy spectrum
<logical>
#      energy spectrum
#      default: .true.

pspectrum         # Compute and save the momentum spectrum
<logical>
#      momentum spectrum
#      default: .true.

conductance       # Compute and save the conductance
<logical>
#      conductance
#      default: .true.

primefactorn     # Ensure n is a multiple of prime factors
<logical>
#      prime factors
#      default: .true.

externale         # External electric field across potential
<real>
#      magnitude of electric field
#      default: 0.0

externalb         # External magnetic field
<real>
#      magnitude of magnetic field
#      default: 0.0

gauge             # Magnetic vector potential gauge
<text>
#      '(-y,0,0)' or '(-y,x,0)' or '(x-y,x-y,0)'
#      default: (x-y,x-y,0)

omegal            # The Lomar frequency for magnetic field
<real>
#      lomar frequency
#      default: 0.0

```

```

#
#      The following variables allow the definition of various shaped
#      potentials
#
potfn          # Arbitrary function as the potential
<integer>     # Potential object number
<real>         # Minimum of function
<real>         # Maximum of function
<function>     # Fortran90 style function

circle          # Defines a circle (annulus) for the potential
<integer>     # Potential object number
<real> <real>   # x- and y- coordinates of centre
<real>         # Radius of circle
<real>         # Width of circle boundary
<real>         # Potential height of the circle

fillcircle      # Filled circle for the potential
<integer>     # Potential object number
<real> <real>   # x- and y- coordinates of centre
<real>         # Radius of circle
<real>         # Potential height of the circle

ellipse         # Ellipse (annulus) for the potential
<integer>     # Potential object number
<real> <real>   # x- and y- coordinates of centre
<real> <real>   # Major and minor axes
<real>         # Width of elipse boundary
<real>         # Potential height of the ellipse

fillellipse     # Filled ellipse for the potential
<integer>     # Potential object number
<real> <real>   # x- and y- coordinates of centre
<real> <real>   # Major and minor axes
<real>         # Potential height of the ellipse

line            # Line for the potential
<integer>     # Potential object number
<real> <real>   # x- and y- coordinates of line end
<real> <real>   # x- and y- coordinates of line end
<real>         # Width of line
<real>         # Potential height of the line

```

```

ramp                      # Ramp for the potential
<integer>                 # Potential object number
<real> <real>             # x- and y- coordinates of line end
<real> <real>             # x- and y- coordinates of line end
<real>                     # Width of line
<real>                     # Minimum height of ramp
<real>                     # Maximum height of ramp

polygon                    # Polygon (border)
<integer>                 # Potential object number
<real>                     # Width of polygon boundary
<real>                     # Potential height of polygon
<real> <real>             # x- and y- coordinates of first polygon point
...
<real> <real>             # x- and y- coordinates of polygon points
<real> <real>             # x- and y- coordinates of first polygon point

fillpolygon                # Filled polygon
<integer>                 # Potential object number
<real>                     # Potential height of polygon
<real> <real>             # x- and y- coordinates of first polygon point
...
<real> <real>             # x- and y- coordinates of polygon points
<real> <real>             # x- and y- coordinates of first polygon point

end                       # End of description file (required)

```

# Bibliography

- Akis, R. & Ferry, D. K. (2001), ‘Quantum waveguide array generator for performing fourier transforms: Alternate route to quantum computing’, *App. Phys. Lett.* **79**, 2823–2825.
- Alamo, J. A. D., Eugster, C. C. & Hu, Q. (1998), ‘Electron waveguide devices’, *Superlattices and Microstructures* **23**(1), 121–137.
- Alferov, Z. I. (2001), ‘Nobel lecture: The double heterostructure concept and its applications in physics, electronics, and technology’, *Rev. Mod. Phys.* **73**, 767–782.
- Amemiya, K. (1999), ‘Electron transport in quantum wires with tunneling barrier in magnetic fields’, *J. Phys. Soc. Jpn.* **68**, 567.
- Amemiya, K. & Kawamura, K. (1995), ‘Analysis of the hall effect in terms of magneto-focusing in quantum dots’, *J. Phys. Soc. Jpn.* **64**, 1245.
- Asker, A. & Cakmak, A. S. (1978), ‘Explicit integration method for the time-dependent schrödinger equation for collision problems’, *J. Chem. Phys.* **68**, 2794.
- Balakrishnan, N., Kalyanaraman, C. & Sathyamurthy, N. (1997), ‘Time-dependent quantum mechanical approach to reactive scattering and related processes’, *Physics Reports* **280**, 79–144.
- Barticevic, Z., Fuster, G. & Pacheco, M. (2002), ‘Effect of an electric field on the bohm-aharonov oscillations in the electronic spectrum of a quantum ring’, *Phys. Rev. B* **65**, 193307 1–4.
- Bartschat, K., Hudson, E., Scott, M., Burke, P. & Burke, V. (1996), ‘Convergent r matrix with pseudostates calculation for e-he collisions’, *Phys. Rev. A* **54**, R998–R1001.

- Beck, T. L. (2000), ‘Real-space mesh techniques in density-functional theory’, *Rev. Mod. Phys.* **72**, 1041–1080.
- Bertoni, A., Bordone, P., Brunetti, R., Jacoboni, C. & Reggiani, S. (2000), ‘Quantum logic gates based on coherent electron transport in quantum wires’, *Phys. Rev. Lett.* **84**, 5912–5915.
- Bottcher, C. (1985), ‘Numerical calculations on electron impact ionisation’, *Adv. At. Mol. Phys.* **35**, 209–254.
- Braun, M., Meier, C. & Engel, V. (1996), ‘Nanosecond wave-packet propagation with the split-operator technique’, *Comp. Phys. Comm.* **93**, 152.
- Bray, I. (1997), ‘Close-coupling theory of ionization: Success and failures’, *Phys. Rev. Lett.* **78**, 4721–4724.
- Bray, I. & Stelbovics, A. (1995), ‘Calculation of electron scattering on hydrogenic targets’, *Adv. At. Mol. Opt. Phys.* **35**, 209–254.
- Bray, I. & Stelbovics, A. (1997), ‘Electron-impact excitation of the 3d state of hydrogen at 54.4eV’, *J. Phys. B* **30**, L493–L497.
- Buehler, T. M., Reilly, D. J., Brenner, R., Hamilton, A. R., Dzurak, A. S. & Clark, R. G. (2003), ‘Correlated charge detection for readout of a solid-state quantum computer’, *App. Phys. Lett.* **82**(4), 577–579.
- Buffington, G. D., Madison, D. H., Peacher, J. L. & Schultz, D. R. (1999), ‘Lattice, time-dependent approach for electron-hydrogen scattering’, *J. Phys. B: At. Mol. Opt. Phys.* **32**, 2991–3001.
- Carini, J., Lonergan, J., Murdock, D., Trinkle, D. & Yung, C. (1997), ‘Bound states in waveguides and bent quantum wires. i. applications to waveguide systems’, *Phys. Rev. B* **55**, 9842–9851.
- Cerjan, C. & Kulander, K. C. (1991), ‘Efficient time propagation for finite difference representations of the time-dependent schrödinger equation’, *Comp. Phys. Comm.* **63**, 529–537.
- Child, M. (1991), ‘Analysis of a complex absorbing barrier’, *Molecular Physics* **72**, 89.

- Christensson, L., Linke, H., Omling, P., Lindelof, P. E., Zozoulenko, I. V. & Berggren, K. F. (1998), ‘Classical and quantum dynamics of electrons in open equilateral triangular billiards’, *Phys. Rev. B* **57**(19), 12306–12313.
- Clark, I. & Bracken, A. (1996), ‘Bound states in tubular quantum waveguides with torsion’, *J. Phys. A* **29**, 4527–4535.
- Cohen-Tannoudji, C., Diu, B. & Laloë, F. (1977), *Quantum Mechanics*, Vol. 1, John Wiley and Sons and Hermann.
- Csontos, D. & Xu, H. Q. (2000), ‘Effects of boundary roughness on the conductance of quantum wires’, *Appl. Phys. Lett.* **77**, 2364–2366.
- Csontos, D. & Xu, Q. (2002), ‘Characteristics of electron transport through vertical double-barrier quantum-dot structures: Effects of symmetric and asymmetric variations of the lateral confinement potentials’, *Phys. Rev. B* **66**, 205317 1–12.
- Datta, S. (1995), *Electronic transport in mesoscopic systems*, Cambridge University Press.
- Dehnen, R. & Engel, V. (1995), ‘Wave-packet dynamics and photoionization in the coulomb potential’, *Phys. Rev. A* **52**, 2288–2294.
- Elliot, S. R. (1998), *The Physics and Chemistry of Solids*, John Wiley and Sons.
- Entin, M. & Mahmoodian, M. (2000), ‘Aharonov-bohm effect in mesoscopic ring in a nonstationary magnetic field’, *J. Phys.: Condens. Matter* **12**, 6845–6850.
- Faddeev, L. & Markuriev, S. (1993), *Quantum Scattering Theory for Several Particle Systems*, Kluwer: Boston.
- Feit, M. D., Fleck, J. A. & Steiger, A. (1982), ‘Solution of the schrödinger equation by a spectral method’, *J. Comp. Phys.* **47**, 412.
- Ferry, D. K. & Goodnick, S. M. (1997), *Transport in nanostructures*, Cambridge University Press.
- Fonseca, L. R. C., Korotkov, A. N. & Likharev, K. K. (1996), ‘Accuracy of the singel-electron pump using an optimized step-like rf drive waveform’, *Appl. Phys. Lett.* **69**(13), 1858–1860.

Frigo, M. (1999), A fast fourier transform compiler, *in* ‘ACM SIGPLAN Conference on Programming Language Design and Implementation’.

Frigo, M. & Johnson, S. G. (1997), The fastest fourier transform in the west, Technical report, Massachusetts Institute of Technology.

Frigo, M. & Johnson, S. G. (1998), Fftw: An adaptive software architecture for the fft, *in* ‘1998 ICASSP conference proceedings’.

Frohne, H. R., Meleenan, M. J. & Datta, S. (1989), ‘An efficient method for the analysis of electron waveguides’, *J. Appl. Phys.* **66**, 2699.

Führer, M. S., Kim, B. M., Durkop, T. & Brintlinger, T. (2002), ‘High-mobility nanotube transistor memory’, *Nano Letters* **2**(7), 755–759.

Gallagher, B. L., Kubrak, V., Rushforth, A. W., Neumann, A. C., Edmonds, K. W., Main, P. C., Henini, M., Marrows, C. H., Hickey, B. J., Thoms, S. & Dahlberg, D. E. (2000), ‘2d electron gas in non-uniform magnetic fields’, *ACTA Physica Polonica A* **98**, 217–230.

Gilbert, M. J., Akis, R. & Ferry, D. K. (2002), ‘Magnetically and electrically tunable semiconductor quantum waveguide inverter’, *App. Phys. Lett.* **81**, 4284–4286.

Gold, A. (1988), ‘Scattering time and single-particle relaxation time in a disordered two-dimensional electron gas’, *Phys. Rev. B* **38**(15), 10798–10811.

Goldberger, M. & Watson, K. (1964), *Collision Theory*, Wiley, New York.

Golub, G. H. & Loan, C. G. V. (1989), *Matrix Computations*, Johns Hopkins.

Gray, S. K. & Balintkurti, G. G. (1997), ‘Quantum dynamics with real wave packets, including application to three-dimensional reactive scattering’, *J. Chem. Phys.* **108**, 950–962.

Gu, B., Sheng, W. & Wang, J. (1998), ‘Oscillatory magneto-conductance in quantum waveguides with lateral multi-barrier structures’, *Int. J. Mod. Phys. B* **12**, 653–661.

Harris, J., Akis, R. & Ferry, D. K. (2001), ‘Magnetically switched quantum waveguide qubit’, *App. Phys. Lett.* **79**, 2214–2215.

- Hayamizu, Y., Yoshita, M., Watanabe, S., Pfeiffer, H. A. L. & West, K. (2002), ‘Lasing from a single-quantum wire’, *App. Phys. Lett.* **81**, 4937–4939.
- Hermann, M. R. & J. Fleck, J. (1988), ‘Split-operator spectral method for solving the time-dependent schrödinger equation in spherical coordinates’, *Phys. Rev. A* **38**, 6000–6012.
- Hines, C. (2000), Electron transport under time-dependent Hamiltonians, PhD thesis, Department of Physics, UWA.
- Ihra, W., Draeger, M., Handke, G. & Friedrich, H. (1995), ‘Time-dependent approach to electron scattering and ionization in the s-wave model’, *Phys. Rev. A* **52**, 3752–3762.
- Jensen, H. D. & Martinis, J. M. (1992), ‘Accuracy of the electron pump’, *Phys. Rev. B* **46**(20), 13407–13427.
- Jin, G., Wang, Z., Hu, A. & Jiang, S. (1999), ‘Quantum waveguide theory of serial stub structures’, *J. Appl. Phys.* **85**, 1597–1608.
- Josephs-Franks, P. W., Reed, R. P. & Pakes, C. I. (2000), ‘Small area, low-inductance niobium squid for the detection of single atomic spin-flips’, *Physica B* **280**, 540–541.
- Kane, B. E. (1998), ‘A silicon-based nuclear spin quantum computer’, *Nature* **393**, 133–137.
- Kane, B. E., McAlpine, N. S., Dzurak, A. S., Clark, R. G., Milburn, G. J., Sun, H. B. & Wiseman, H. (2000), ‘Single-spin measurement using single-electron transistors to probe two-electron systems’, *Phys. Rev. B* **61**, 2961–2972.
- Kane, B., Facer, G., Dzurak, A., Lumpkin, N., Clark, R., Pfeiffer, L. & West, K. (1998), ‘Quantised conductance in quantum wires with gate-controlled width and electron density’, *Appl. Phys. Lett.* **72**, 3506–3508.
- Kane, B., Pfeiffer, L. N. & West, K. W. (1995), ‘High mobility gaas heterostructure field effect transistor for nanofabrication in which dopant-induced disorder is eliminated’, *Appl. Phys. Lett.* **67**, 1262–1264.
- Kastner, M. A. (1993), ‘Artificial atoms’, *Physics Today* pp. 24–31.

Katine, J. A., Eriksson, M. A., Adourian, A. S., Westervelt, R. M., Edwards, J. D., Lupu-

Sax, A., Heller, E. J., Campman, K. L. & Gossard, A. C. (1997), ‘Point contact conductance of an open resonator’, *Phys. Rev. Lett.* **79**(24), 4806–4809.

Kazansky, A. & Taulbjerg, K. (1996), ‘Quantum wavepacket study of electron detachment from  $h^-$  by electron impact’, *J. Phys. B* **29**, 4465–4475.

Kim, C. S., Roznova, O. N., Satanin, A. M. & Stenberg, V. B. (2002), ‘Interference of quantum states in electronic waveguides with impurities’, *J. of Exp. and Theo. Phys.* **94**(5), 992–1007.

Kittel, C. (1986), *Introduction to Solid State Physics*, Wiley, New York.

Knipp, P. A. & Reinecke, T. L. (1996), ‘Boundary-element method for the calculation of electronic states in semiconductor nanostructures’, *Phys. Rev. B* **54**, 1880.

Konovalov, D. & McCarthy, I. (1995), ‘Convergent j-matrix calculation of electron-helium resonances’, *J. Phys. B* **28**, L139–L145.

Koonen, J. J., Buhmann, H. & Molenkamp, L. W. (2000), ‘Probing the potential landscape inside a two-dimensional electron gas’, *Phys. Rev. Lett.* **85**, 2473–2476.

Kouwenhoven, L. (1998), ‘Quantum dots’, *Physics World* **11**, 35–39.

Kouwenhoven, L., Austing, D. & Tarucha, S. (2001), ‘Few-electron quantum dots’, *Rep. Prog. Phys.* **64**, 701–736.

Kroes, G. J. & Neuhauser, D. (1996), ‘Performance of a time-independent scattering wave packet technique using real operators and wave functions’, *J. Chem. Phys.* **105**, 8690–8698.

Kvitsinsky, A. & Hu, C. (1996), ‘Resonances and excitations of  $n = 2$  levels in  $e^- + h$  scattering via the faddeev approach’, *J. Phys. B* **29**, 2059–2077.

Lang, N. D. & Avouris, P. (1998), ‘Oscillatory conductance of carbon-atom wires’, *Phys. Rev. Lett.* **81**(6), 3515–3518.

Larkin, J. M., Eberly, J. H., Lappas, D. G. & Grobe, R. (1998), ‘Numerical study of positron-hydrogen scattering’, *Phys. Rev. A* **57**, 2572–2577.

Laux, S. E., Frank, D. J. & Stern, F. (1988), ‘Quasi-one-dimensional electron states in a

split-gate gaas/algaas heterostructure’, *Surf. Sci.* **196**, 101.

Linke, H., Sheng, W. D., Svensson, A., Lofgren, A., Christensson, L., Xu, H. Q. & Om-

ling, P. (2000), ‘Asymmetric nonlinear conductance of quantum dots with broken inversion symmetry’, *Phys. Rev. B* **61**, 15914 – 15926.

Luttinger, J. M. (1963), ‘An exactly soluble model of a many fermion system’, *J. Math.*

*Phys.* **4**, 1154–1162.

Lyons, D. M., Ryan, K. M., Morris, M. A. & Holmes, J. D. (2002), ‘Tailoring the optical

properties of silicon nanowire arrays through strain’, *Nano Letters* **2**(8), 811–816.

Macias, D., Brouard, S. & Muga, J. G. (1994), ‘Optimization of absorbing potentials’,

*Chem. Phys. Lett.* **228**, 672–677.

Madison, D., Schroeder, J., Bartschat, K. & McEachran, R. (1995), ‘Second-order

distorted-wave calculation for electron-copper scattering’, *J. Phys. B* **28**, 4841–4851.

Martin, I., Mozyrsky, D. & Jiang, H. W. (2003), ‘A scheme for electrical detection of

single-electron spin resonance’, *Phys. Rev. Lett.* **90**(1).

Martinis, J. M. & Nahum, M. (1994), ‘Matrological accuracy of the electron pump’, *Phys.*

*Rev. Lett.* **72**(6), 904–907.

McCarthy, I. (1996), ‘The electron-atom ionisation problem’, *Aust. J. Phys.* **49**, 219–229.

McCullough, E. A. & Wyatt, R. E. (1971), ‘Dynamics of the collinear  $h + h_2$  reaction. i.

probability density and flux’, *J. Chem. Phys.* **54**, 3578.

Midgley, S. & Wang, J. B. (2000), ‘Complex absorbing potential and chebyshev propaga-

tion scheme’, *Phys. Rev. E* **61**, 920–925.

Narevich, R., Prange, R. E. & Zaitsev, O. (2000), ‘Square billiard with a magnetic flux’,

*Phys. Rev. E* **62**, 2046–2059.

Naulleau, P., Goldberg, K. A., Anderson, E. H., Attwood, D., Batson, P., Bokor, J., Den-

ham, P., Gullikson, E., Harteneck, B., Hoef, B., Jackson, K., Olynick, D., Rekawa,

S., Salmassi, F., Blaedel, K., Chapman, H., Hale, L., Mirkarimi, P., Soufli, R.,

- Spiller, E., Sweeney, D., Taylor, J., Walton, C., O'Connell, D., Tichenor, D., Gwyn, C. W., Yan, P. Y. & Zhang, G. (2002), 'Sub-70 nm extreme ultraviolet lithography at the advanced light source static microfield exposure station using the engineering test stand set-2 optic', *J. Vac. Sci. Technol.* **60**(6), 2829–2833.
- Neuhauser, D. & Baer, M. (1990), 'A new accurate (time independent) method for treating three-dimensional reactive collisions: The application of optical potentials and projection operators', *J. Chem. Phys.* **92**, 3419.
- Nikolic, K. & Sodan, R. (1998), 'Electronic transport in quantum waveguide systems with attached stubs', *Phys. Rev. B* **58**, 9631–9634.
- Normand, J.-M. (1980), *A Lie Group: Rotations in Quantum Mechanics*, North-Holland, Amsterdam.
- O'Brien (1999). Private Conversation.
- Olendski, O. & Mikhailovska, L. (2002), 'Bound-state evolution in curved waveguides and quantum wires', *Phys. Rev. B* **66**, 035331 1–8.
- Pang, T. & Louie, S. G. (1990), 'Negative-donor centers in semiconductors and quantum wells', *Phys. Rev. Lett.* **65**(13), 1635–1638.
- Pindzola, M. S. & Robicheaux, F. (1996), 'Total ionization cross section for electron-hydrogen scattering using a time-dependent close-coupling method', *Phys. Rev. A* **54**, 2142–2145.
- Pindzola, M. S. & Schultz, D. R. (1996), 'Time-dependent close-coupling method for electron-impact ionization of hydrogen', *Phys. Rev. A* **53**, 1525–1536.
- Poet, R. (1978), 'The exact solution for a simplified model of electron scattering by hydrogen atoms', *J. Phys. B: Atom. Molec. Phys.* **11**, 3081–3093.
- Poet, R. (1980), 'Symmetrically coupled differential equations in scattering i. model electron-hydrogen collisions', *J. Phys. B: Atom. Molec. Phys.* **13**, 2995–3008.
- Poet, R. (1981), 'A method of including continuum states in the close-coupling formulation', *J. Phys. B: Atom. Molec. Phys.* **14**, 91–101.

- Popov, I. & Popova, S. (1996), ‘Eigenvalues and bands imbedded in the continuous spectrum for a system of resonators and a waveguide - solvable model’, *Phys. Lett. A* **222**, 286–290.
- Rau, A. R. P. & Unnikrishnan, K. (1996), ‘Evolution operators and wave functions in a time-dependent electric field’, *Phys. Lett. A* **222**, 304–308.
- Riss, U. & Meyer, H.-D. (1995), ‘Reflection-free complex absorbing potentials’, *J. Phys. B: At. Mol. Opt. Phys.* **28**, 1475–1493.
- Riste, N. (1998), A Time Dependent Approach to Positron-Hydrogen Scattering, PhD thesis, Department of Physics, UWA.
- Robinson, I. K., Bennett, P. A. & Himpel, F. J. (2002), ‘Structure of quantum wires in au/si(557)’, *Phys. Rev. Lett.* **88**, 096104 1–4.
- Ryzhikh, G. & Mitroy, J. (1997), ‘Positron scattering from atomic sodium’, *J. Phys. B* **30**, 5545–5565.
- Saito, M., Takats, M., Okada, M. & Yokoyama, N. (1992), ‘Analysis of the angular distribution of electrons injected through a quantum point contact by use of a green’s function with a weak-magnetic-field approximation’, *Phys. Rev. B* **46**, 13220–13233.
- Schult, R. L., Ravenhall, D. G. & Wyld, H. W. (1989), ‘Quantum bound states in a classically unbound system of crossed wires’, *Phys. Rev. B* **39**, 5476–5479.
- Schultz, D., Bottcher, C., Madison, D., Peacher, J., Buffington, G., Pindzola, M., Gorczyk, T., Gavras, P. & Griffin, D. (1994), ‘Time-dependent approach to atomic autoionization’, *Phys. Rev. A* **50**, 1348–1458.
- Scott, M., Burke, P., Bartschat, K. & Bray, I. (1997), ‘Near-threshold electron impact ionization of atomic hydrogen’, *J. Phys. B* **30**, L309–L315.
- Seideman, T. & Miller, W. (1991), ‘Calculation of the cumulative reaction probability via a discrete variable representation with absorbing boundary conditions’, *J. Chem. Phys.* **96**, 4412–4422.
- Sohn, L. (1998), ‘A quantum leap for electronics’, *Nature* **394**, 131–132.

Sohn, L., Kouwenhoven, L. P. & Schön, G. (1996), *Mesoscopic Electron Transport*, Kluwer Academic Publishers.

Sugaya, T., Bird, J. P., Ogura, M., Sugiyama, Y., Ferry, D. K. & Jang, K. Y. (2002), ‘Quantum-interference characteristics of a 25 nm trench-type ingaas/inalas quantum-wire field-effect transistor’, *App. Phys. Lett.* **80**(3), 434–436.

Szafer, A. & Stone, A. D. (1989), ‘Theory of quantum conduction through a constriction’, *Phys. Rev. Lett.* **62**, 300–303.

Tachibana, H. & Totsuji, H. (1996), ‘Characteristics of a quantum waveguide’, *J. Appl. Phys* **79**, 7021–7028.

Tal-Ezer, H. & Kosloff, R. (1984), ‘An accurate and efficient scheme for propagating the time dependent schrödinger equation’, *J. Chem. Phys.* **81**, 3967.

Tanner, B. (1995), *Introduction to the Physics of Electrons in Solids*, Cambridge University Press.

Tans, S. J., Verschueren, A. R. M. & Dekker, C. (1998), ‘Room-temperature transistor based on a single carbon nanotube’, *Nature* **393**, 49–52.

Taylor, J. (1972), *Scattering Theory: Quantum Theory of Nonrelativistic Collisions*, Wiley, New York.

Temkin, A. (1962), ‘Nonadiabatic theory of electron-hydrogen scattering’, *Physical Review* **126**, 130–142.

ter Haar, D. (1975), *Problems in Quantum Mechanics*, Pion: London.

van der Wiel., W. G., Nazarov, Y. V., Franceschi, S. D., Fujisawa, T., Elzerman, J. M., Huizinga, E. W. G. M., Tarucha, S. & Kouwenhoven, L. P. (2001), Electro-magnetic aharonov-bohm effect in a 2-d electron gas ring.

van Wees, B. J., van Houten, H., Beenakker, C. W. J., Williamson, J. G., Kouwenhoven, L. P., van der Marel, D. & Foxen, C. T. (1988), ‘Quantized conductance of point contacts in a two-dimensional electron gas’, *Phys. Rev. Lett.* **60**, 848–850.

- Varshini, Y. (1998), ‘Simple wavefunction for an impurity in a parabolic quantum dot’, *Superlattices and Microstructures* **23**, 145–149.
- Vibók, A. & Balint-Kurt, G. (1992), ‘Reflection and transmission of waves by a complex potential - a semiclassical jeffreys-wentzel-kramers-brillouin treatment’, *J. Chem. Phys* **96**, 7615–7622.
- Wang, C. K. (1997), ‘The effects of width variation on the quasi-bound states in a ballistic quantum channel with bends’, *Physica B* **229**, 240–248.
- Wang, J. B. & Midgley, S. (1999), ‘Quantum waveguide theory - a direct solution to the time-dependent schrödinger equation’, *Phys. Rev. B* **60**, 13668–13675.
- Wang, J. B., Riste, N., Midgley, S., Stelbovics, A. T. & Williams, J. F. (1999), ‘Time-dependent approach to positron-hydrogen scattering’, *Aust. J. Phys.* **52**, 595–602.
- Wang, J. B. & Scholz, T. (1998), ‘Time-dependent approach to scattering by chebyshev-polynomial expansion and the fast-fourier-transform algorithm’, *Phys. Rev. A* **57**, 3554–3559.
- Wang, J., Williams, J., Stelbovics, A., Furst, J. & Madison, D. (1995), ‘Coherent excitation of the singlet-triplet mixed 1s4f state of helium’, *Phys. Rev. A* **52**, 2885–2900.
- Wang, Y., Wang, J. & Guo, H. (1994), ‘Magnetoconductance of a stadium-shaped quantum dot: A finite-element-method approach’, *Phys. Rev. B* **49**, 1928–34.
- Webb, R. (1998), ‘Breakdown of the independent electron picture in mesoscopic samples at low temperatuires: the hunt for the unicorn’, *Superlattices and Microstructures* **23**, 969–980.
- Whittington, M. A., Traub, R. D. & Jefferys, J. G. R. (1995), ‘Recurrent excitatory postsynaptic potential induced by synchronized fast cortical oscillations’, *Nature* **373**, 612–615.
- Xu, H. Q. & Gu, B. (2001), ‘Phase property of the transmission through a quantum dot’, *J. Phys.:Condens. Matt.* **13**, 3599–3606.
- Yang, Z., Bao, C. & Lin, C. (1996), ‘Hyperspherical approach to three-electron atomic systems’, *Phys. Rev. A* **53**, 3934–3945.

Yanson, A., Bollinger, G., Vandenbrom, H., Agrait, N. & Vanruitenbeek, J. (1998), ‘Formation and manipulation of a metallic wire of single gold atoms’, *Nature* **395**, 783–785.

Yiu, C. & Wang, J. (1996), ‘Efficient method for calculating the transmission coefficient of two-dimensional quantum wire structures’, *J. Appl. Phys.* **80**, 4208–4210.

Zhang, L., Feagin, J., Engel, V. & Nakano, A. (1994), ‘Electron-pair wave packets’, *Phys. Rev. A* **49**, 3457–3462.